Investigation of the Mott transition with metastable Helium atoms

Cécile Carcy

université PARIS-SACLAY

INSTITUT d'OPTIQUE GRADUATE SCHOOL ParisTech

NNT : 2019SACLO014

Thèse de doctorat

Investigation of the Mott transition with He* atoms

Thèse de doctorat de l'Université Paris-Saclay
préparée à l'Institut d'Optique

Ecole doctorale n°572 Ondes et Matière (EDOM)
Spécialité de doctorat : Physique Quantique

Thèse présentée et soutenue à Palaiseau, le 19 Novembre 2019, par

CÉCILE CARCY

Composition du Jury :

Nicolas Pavloff Professeur, Université Paris-Sud (Laboratoire de Physique Théorique et Modèles Statistiques - LPTMS)	Président
Hélène Perrin Chercheur CNRS, Université Paris-13 (Laboratoire de Physique des Lasers - LPL)	Rapporteur
Chiara Fort Chercheur, Université de Florence (European Laboratory for Non-linear Spectroscopy - LENS)	Rapporteur
Chris Vale Chercheur, Swinburne University (Center of Quantum and Optical Science - CQOS)	Examinateur
Guido Pupillo Professeur, Université de Strasbourg (Institut de Science et d'Ingenierie Supramoleculaire - ISIS)	Examinateur
David Clément Maitre de Conférence, Institut d'Optique (Laboratoire Charles Fabry - LCF)	Directeur de thèse
Denis Boiron Professeur, Institut d'Optique (Laboratoire Charles Fabry - LCF)	Co-directeur de thèse

Remerciements

Ce manuscript décrit les résultats de trois années de thèse d'un point de vu purement scientifique. Mais une thèse, c'est bien plus que cela. Ce sont trois années pendant lesquelles je me suis levée, j'ai pris mon vélo pour rejoindre le labo et passé un nombre conséquent d'heures à essayer des percer des mystères de la physique. Ce sont en tout:

$$N_{\text{heure}} \approx 35 \text{ h} \times (53-5) \text{ semaines} \times 3 \text{ ans} \times \eta_{\text{motivation}} \approx 25000 \text{ h} \times \eta_{\text{motivation}} \quad (1)$$

Le paramètre inconnu de cette équation, $\eta_{\text{motivation}}$ traduit le fait que le nombre d'heures passées au labo dépend généralement fortement de la motivation du thésard. Cette motivation peut être personnelle (intérêt du thésard pour son sujet, volonté de faire bien les choses ou d'avancer rapidement...), mais elle peut aussi venir de son entourage.

Dans mon cas personnel, ce facteur $\eta_{\text{motivation}}$, bien qu'il ait subit quelques fluctuations lors de la dernière année de thèse, a dans son ensemble été assez élevé. Et cela pour une raison simple: car j'ai eu l'occasion durant cette thèse de travailler et de cotoyer des personnes formidables qui ont été un vrai soutien lorsque la motivation venait à flancher. Si ce manuscrit est le manuscrit de Cécile Carcy, il est en fait le fruit d'un travail en équipe, sans lequel tout ca n'aurait été possible.

Alors, forcément, au moment même où j'écris ces remerciements, une personne en premier me vient en tête. David, pour être honnête, je t'ai détesté à certains moments de ma thèse (par exemple lorsque tu m'as fait reprendre des données pendant que je rédigeais), mais au final, je n'aurais pas pu espérer avoir un meilleur maitre de thèse que toi. Tu as toujours été là quand il fallait et a su comprendre (et faire avec) ma facon de travailler. Ma motivation, elle vient en partie de la tienne car ce genre de choses sont généralement contagieuses. Ta bonne humeur permanente, ta compréhension, ton encadrement exeptionnel (ce n'est clairement pas toujours le cas), ton envie de transmettre tes passions, la physique mais pas que cela, ont permis de rendre ces nombreuses heures passées au labo agréables. C'est aussi grâce à toi qu'il y a toujours eu dans l'équipe une ambiance de travail très sympatique et amicale au fil des arrivées et des départs. Alors un grand MERCI pour tout!

Lors de ma thèse, j'ai eu l'occasion de travailler au sein de l'équipe avec des nombreuses personnes: Rockson Chang, Hugo Cayla, Marco Mancini, Antoine Ténart, et Gaëtan Hercé. Je vous remercie tout d'abord pour avoir réussi à me supporter! Ce fut un plaisir de travailler avec chacuns d'entre vous, au fil des galères et des succès. Vous êtes aussi les acteurs majeurs de la bonne ambiance dans le groupe, au travail et en dehors. J'ai aussi eu l'occasion de travailler, lors de la rédaction d'articles, avec Thomas Bourdel et Alain Aspect. Toujours de très bon conseils, ils nous ont grandement aidé, et je les remercie pour cela. Finalement, je remercie Tommaso Roscilde, avec qui j'ai découvert la Mécanique Quantique il y a 7 ans (!!!) à l'ENS de Lyon et qui a fourni durant ma thèse des simulations numériques complexes et nous a grandement aidé à comprendre la physique de la transition de Mott et ses inconnus.

De manière générale, je tiens à remercier tous les thésards qui sont passés par le groupe optique atomique. Ce fut agréable pendant ces années de partager quelques moments pendant les pauses ou au déjeuner (même s'il est vrai que j'ai un peu fait bande à part), et les nombreuses soirées en dehors du travail. De manière générale, je voudrais remercier toutes les personnes avec qui j'ai pu travailler ou que j'ai cotoyé à l'Institut.

Pour finir, je voudrais tout particulièrement remercier mes collocs (Anais, Vincent et Adrien) pour avoir partagé 2 ans de thèse sous le même toit. Vous avez été d'un grand soutien. Il est temps pour nous de voler désormais de nos propres ailes mais j'ai vraiment apprecié ces deux années passées avec vous.

Anima **S**ana **I**n **C**orpore **S**ano (ASICS), merci à toute la bande @AsicsFrontRunner. La thèse, c'est comme un marathon. Les sessions "fractionné" du Mercredi ont été pour moi un vrai entrainement mental à la résistance, et un moyen de me vider l'esprit. Merci aussi à la bande @OutTrip pour tous ces weekends d'escapade nature et sportifs.

Contents

Introduction

Quantum mechanics arose at the beginning of the 20th century from the building and solving of some problems that the classical mechanics was failing to describe, starting from the very nature of light and massive particles. While the classical mechanics is based on a particle description of matter, L. de Broglie developed the idea of the particle-wave duality, *i.e*, the fact that matter can also be described as a wave, which was confirmed a few years later by the experiment of Davidson and Germer [1] on the electronic diffraction. Under this formalism, to every particle of mass m, one can assign a wavelength through $\lambda = h/mv$ where v refers to the speed of the particle. When two identical particles are well separated in space, their wavepackets do not overlap and the system made by the particles can be described with the classical mechanics. On the contrary, as soon as the particles are close together, the wavepackets interfere and the particles are indistinguishable, a situation that can only be described with the tools of the quantum mechanics.

This situation can be generalized to a macroscopic ensemble of bosonic particles such as a gas at the thermal equilibrium. In this case, the extension of the wavepackets is given by the thermal de Broglie wavelength $\lambda_{dB} = \frac{h}{\sqrt{2\pi m k_B T}}$ and the system forms, as soon as the inter-particle distance is of the order of (or smaller than) λ_{dB}, a unique macroscopic wave with a uniform phase over the entire system. This is the well-known phenomenon of Bose Einstein Condensation (BEC phase) that can be reached by increasing the density or decreasing the temperature of the gas. This phenomenon is a purely quantum statistical effect that can be derived considering the Bose-Einstein distribution, which characterizes the energy levels occupation of indistinguishable bosonic particles (at the thermodynamic limit). At low temperature (or high density), the population of the excited states saturates and all the atoms accumulate in the single particle lowest-energy state (condensate mode) of the system, as a consequence of which the lowest-energy state becomes macroscopically populated.

Beside the Bose-Einstein condensation, the quantum interferences are at the origin of many quantum effects such as the bosonic bunching evidenced in the Hanbury Brown and Twiss (HBT) experiment [2, 3] or, in quantum optics, in the behavior of single particles systems, such as illustrated by the Hong-Ou-Mandel (HOM) experiment [4, 5].

These effects derive from the correlations between the interfering particles. The Bose-Einstein condensate can be revealed trough the measurement of the one-particle correlation function while the HBT effect shows up in the two-particle correlations. We insist here on the fact that the properties of these correlations can be recast from the quantum statistics of ideal particles.

The interaction in many-body systems

When the particles are interacting, the interactions are at the origin of the appearance of new correlations that enrich the physics and are at the origin of very peculiar behaviors. For instance, interactions are at the origin of the appearance of superfluid properties in BECs. They can also drive a class of phase transitions, called the quantum phase transitions that can occur at $T = 0$. An emblematic example of such a transition is the Mott transition that separates a conductor phase to an insulator phase in some periodic systems.

The interaction between the atoms can often be treated using mean-field (MF) theories. Using a

Hartree-Fock approximation which consists in writing the many-body wavefunction as a product of single-particle wavefunctions, one is left with a single particle problem that is usually easy to solve. This method is for instance used to derive the Gross-Pitaevskii equation in the case of an interacting Bose-Einstein condensate [6]. However, at the mean-field level, all the correlations between individual quantum particles are neglected.

As a result, certain properties of many-body interacting systems can not be accounted for by the mean-field theories, requiring the use of beyond mean-field theories. An emblematic example can be found in the collision between two condensates: two-body collisions are at the origin of the creation of correlated atomic pairs with opposite momenta (due to the conservation of the momentum) [7]. This phenomenon can not be accounted for by usual mean-field theories because there exists nothing such as a correlation between the momentum of 2 particles at the MF level. These systems are referred to as N body systems or strongly-interacting systems.

Although strongly interacting systems can not be solved analytically, these systems can be characterized by the measurement of the correlations between the atoms. The understanding of the way the particles are correlated provides a deep insight into the microscopic mechanisms at stake.

The Bose-Hubbard model

In this thesis, we will investigate an emblematic example of strongly interacting system: an ensemble of bosonic particles trapped into a periodic potential and interacting with repulsive interactions. This system is described by the Bose-Hubbard Hamiltonian and it is characterized by three energy scales (see Fig. 1): the on-site energy U, the tunneling energy J (kinetic term) and the temperature T.

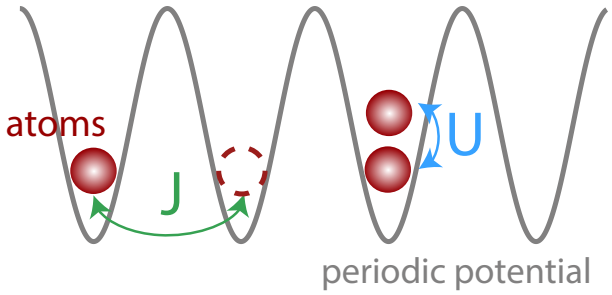

Figure 1: **Bosonic particles trapped into a periodic potential.**

At $T = 0$, when the system is in its ground state, a phase transition separates a conductor when $J \gg U$ (SuperFluid SF phase) and an insulating phase for $J \ll U$ (Mott Insulator MI). Contrary to a classical transition where the interplay between the kinetic energy and the temperature is controlling the state of the system, this transition, referred to as the Mott transition, occurs at $T = 0$ and is driven by the competition between the kinetic energy and the repulsive interactions, that is, by the ratio U/J. When the interactions become very strong, the particles tend to avoid each other in order to minimize the energy of the system and thus they localize at the lattice sites. At $T > 0$, when increasing the temperature of a superfluid, the system undergoes a classical transition towards a thermal state, usually referred to as Normal Fluid (NF). If nowadays, the phase diagram is globally known, some open questions remain unsolved, more particularly in the vicinity the quantum critical point of the Mott transition.

Cold atoms experiments as quantum simulators

A few years after the production of the first Bose Einstein Condensate in the second half of the 90's [8, 9], cold atoms appeared to be a very good platform to investigate the Mott transition experimentally. In fact, the ability to produce, using the interaction between the light and the matter, arbitrary potentials for neutral atoms, combined to the possibility to access the ground state of the system by transferring a BEC to a periodic optical potential (usually called optical lattice) allowed for the

creation of the Mott insulator state in the Bloch group in 2002 [10]. But more than that, the high tunability of the cold atom experiments allows to explore a large area of the Bose-Hubbard phase diagram and investigate it using many different tools. Using optical imaging, one can access for instance the position of the atoms by taking an in-situ image [6]. Other experiments, based on the detection of the particles after a long time-of-flight, allow for the detection of particles in the momentum-space [6]. The two approaches are complementary (due to Heisenberg relation): some measurements like the observation of the ordering in the Mott phase or the presence of defects requires the in-situ imaging while the investigation of the temperature, the coherence or the excitations of the system are better suited in the momentum-space.

One extraordinary capability of cold atom experiments is the possibility to detect the atoms in the momentum- or the position-space at the single atomic level, and thus to access observables at the microscopic level. From the distribution of individual particles, it is indeed possible, provided the signal to noise ratio is good enough, to compute the correlation functions at any order.

^{4}He* experiment

In our experiment, we produce metastable Helium-4 (^{4}He*) Bose-Einstein condensates trapped in an optical harmonic trap. By transferring the atoms to a 3D optical lattice, we are investigating the 3D Bose-Hubbard Hamiltonian. This is the main purpose of this thesis. The originality of our experiment relies on the use of a specific atom: the Helium atom in the metastable state that lies 20eV above the ground state. Thanks to their high internal energy, the He* atoms can be detected with an electronic detection after a long time-of-flight. As a result, the momentum distribution of the lattice gases can be measured in 3D and with the single-atom resolution, which is challenging to obtain with usual optical imaging techniques.

The single atom detection allows for the measurement of the particle correlations in the momentum space, which reveals to be very interesting when studying quantum phase transitions. Quantum critical points are for instance characterized by a change in the excitation spectrum of the system and their signatures usually appear in the momentum space through the relation dispersion of the excitations. Among them, pairing mechanisms of particles with opposite momenta ($k/-k$) are an archetype of such momentum correlations and appear for instance in the case of the quantum depletion in the BEC phase. These correlations are due to the presence of interactions between the particles and need to be distinguished from the correlations induced by the quantum statistics such as bosonic bunching, that can also be investigated in cold atoms experiments [11].

Ouline of the thesis

This thesis is organized in six chapters. The first one 1 is an introduction to the physics of the Mott transition and its investigation with cold atoms. The second chapter 2 will be dedicated to some reminders about the concept of coherence in quantum systems and its link with the correlation measurements. In the third chapter 3, we will focus on the description of the He* experiment, notably by introducing the measurement of the momentum distribution at the single atomic level, with a special emphasis on the conditions required to access the momentum-space. The fourth chapter 4 deals with the establishment of the Bose-Hubbard phase diagram, and more precisely with the identification of its boundaries and the implementation of a thermometry method to be able to relate the properties of the clouds probed to their positions in the phase diagram. In the fifth chapter 5, we are studying the residual phase coherence present in the Mott insulator states and restored by particle-hole excitations . Finally, the last chapter 6 is about the measurement of the second-order and third-order correlation functions deep in the Mott insulator phase. We will show that these correlations are of HBT-type. A similar measurement has been also carried out in the thermal part of a superfluid and on increasing the temperature and exhibits features which are beyond the usual framework associated with HBT-type experiments.

1. The Mott Transition

1.1 A bit of history

The understanding of the atomic structure and the development of the quantum mechanics formalism at the beginning of the 20^{th} century pushed the physicists to investigate the stability of matter and to develop a formalism to describe solids that are composed of atoms tightly bounded together. Contrary to amorphous solids characterized by an irregular arrangement of atoms, the crystalline solids are made of an assembly of atoms organized with a periodic structure. Besides this apparent simplicity, they can carry different properties. For instance, some materials are good electrical conductors (referred to as a metals) and others are insulators.

The band theory, developed in the late 20's by Bethe, Sommerfeld, and Bloch is the first successful theory providing us with an understanding of metals, insulators and the transition. According to this theory, free electrons can delocalize over the crystal made by the periodic assembly of the positive ions. The effect of the ions is to create onto the electrons a periodic potential that is at the origin of a band structure for the energy levels of the free electrons. The distinction between conductors and insulators was then based on the filling of the electronic bands: for an insulator, the conduction band (first energy band above the highest energy band totally filled) is empty, whereas it is not the case for a conductor. Besides explaining the electrical conductivity, this theory enables to understand for instance the optical absorption of metals. However, in 1937, Boer and Verwey [12] found that some transition metal oxides with a partially filled d-electron band, such as NiO, were insulators, although expected to be metallic according to the band theory. Ten years later, in 1949, Mott derived the first model to understand the insulating character of NiO, pointing out the effect of the strong Coulomb repulsion between the electrons [13]. For his study of the electrical conductivity in many-body systems, Sir Neville Mott was awarded, with J. van Vleck and Anderson, the Nobel Prize in Physics in 1977. He also gave his name to this class of insulators:

Mott insulators are materials that should conduct the electricity according to the band theory but are insulators because of the strong repulsion between the electrons.

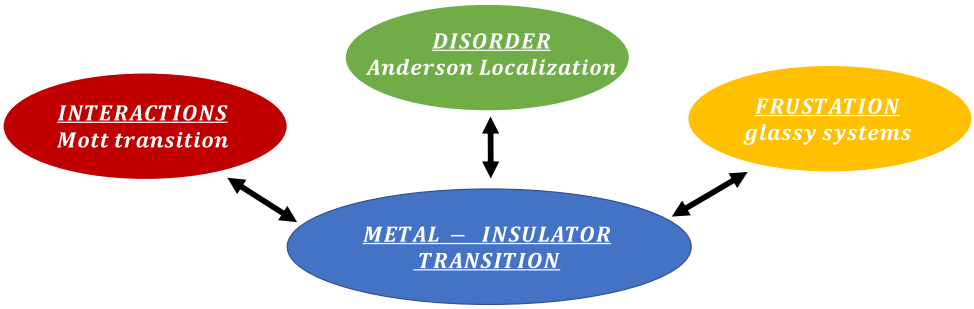

Figure 1.1: **Schematics of the Metal-Insulator transitions.** A metal to insulator transition can be driven by different parameters like the presence of strong repulsive interactions, the presence of strong disorder or frustration.

Note that the existence of strong repulsive interactions is not the only parameter that can be at the origin of localization phenomena. Anderson has been co-awarded with Mott the Nobel Prize for his study of the effect of disorder on the localization of electrons and the appearance of disorder-induced insulators. Metal-insulator transitions can also be driven by the presence of frustration (Fig. 1.1).

Even if there has been a lot of progress in the understanding of these phases as well as the mechanisms that drive the transition, there are today numerous questions opened. By adding some other degrees of freedom like doping, other phases with exotics behaviors can appear, complexifying a lot the phase diagram. Among them, the well cited example of the high-T_c superconductor phase is still the object of intense research. From the late 60's, some theoretical models have been proposed to explain these transitions, like the generic Hubbard model. However, analytic or numerical resolutions of these models are hardly possible for a large number of electrons (large here being only a few dozens, which means much less than the Avogrado number!), which explains why the investigation has turned towards experiments.

One possible platform to study these systems are cold atoms. They offer the possibility to recreate some specific Hamiltonian in a tunable way, allowing to explore a lot of phase transitions. They also provide a large panel of measurement methods that render possible some measurements that would be impossible to carry out with bulk systems.

In 1979, Fisher et al. published an article in which the behaviour of bosonic particles moving into a periodic potential was studied [14]. He demonstrated that in the presence of strong repulsive interactions, the bosonic particles were localizing at the lattice sites [14], forming a bosonic Mott insulator. The first experimental realization of the Mott transition with cold atoms has been realized with bosons in 2002 in the group of I.Bloch [10].

In this thesis, we will deal with the bosonic Mott transition. More precisely, I am presenting the first experimental realization of this transition with metastable He^* atoms. The properties of this specific atom allow us to access for the first time some quantities like momentum correlation functions that were hardly accessible in other experiments, providing complementary measurements to the ones carried out so far.

1.2 The Bose-Hubbard model

In this section, we describe a system made of bosonic interacting particles hopping through a lattice potential. We will show that depending on some parameters, the ground state of the system is either a conductive state or a localized one as predicted by M.Fisher et al. in [14]. A more detailed description of this system can be in found for instance in [15].

1.2.1 The three-dimensional Bose-Hubbard Hamiltonian

For simplicity, we consider a 3D lattice potential with a cubic symmetry of lattice spacing d[1] :

$$V(\vec{r}) = V_0 \left[\cos^2(\frac{k_d}{2}\, x) + \cos^2(\frac{k_d}{2}\, y) + \cos^2(\frac{k_d}{2}\, z)\right] \tag{1.1}$$

where $k_d = \frac{2\pi}{d}$ is the associated wavevector and V_0 is the lattice amplitude. Note that V_0 is generally given in unit of the recoil energy: $V_0 = s\, E_r$ with $E_r = \frac{h^2}{8md^2}$ and m the mass of the particles.

The interaction potential between the particles writes: $U_{int}(\vec{r_1}, \vec{r_2})$.

The Hamiltonian of the system made of N particles is consequently given by:

$$\hat{\mathcal{H}} = \underbrace{\sum_{i=1}^{N} \frac{\vec{p_i}^2}{2m} + \sum_{i=1}^{N} V(\vec{r_i})}_{\hat{\mathcal{H}}_{\text{band}}} + \underbrace{\sum_{i}^{N}\sum_{j>i}^{N} U_{\text{int}}(\vec{r_i}, \vec{r_j})}_{\hat{\mathcal{H}}_{\text{int}}} \tag{1.2}$$

The band Hamiltonian

Here we solve the band Hamiltonian $\hat{\mathcal{H}}_{\text{band}}$ that describes an ensemble of ideal particles in the lattice potential. The particle are independent and we are left with solving a one-body problem. Furthermore, as the three directions of space are decoupled, we will consider only one direction (x).

We are consequently interested in solving the problem parametrized by the following Hamiltonian:

$$\hat{\mathcal{H}}_{\text{band}} = \frac{\hat{p}^2}{2m} + V_0 \cos^2(\frac{k_d}{2}\, \hat{x}) \tag{1.3}$$

The eigenfunctions $\psi_q(x)$ of this Hamiltonian are the Bloch's functions. According to the Bloch's theorem, they can be written as the product of a plane wave and a periodic function u_q (with the same periodicity as the lattice one) [16]:

$$\psi_q(x) = e^{iqx} u_q(x) \tag{1.4}$$

with q belonging to the first Brillouin zone $q \in \left[-\frac{k_d}{2}; \frac{k_d}{2}\right]$ and u_q verifying the equation:

$$\left[\frac{(\hat{p} + \hbar q)^2}{2m} + V_0 \cos^2(\frac{k_d}{2}\, \hat{x})\right] u_q(x) = E(q) u_q(x) \tag{1.5}$$

Because of the periodicity of $u_q(x)$, q, called the quasi-momentum, can be restricted to the first Brillouin zone.

The resolution of this equation can be done numerically and the Bloch's functions and the energy bands indexed by the number n (by increasing energy) are obtained for all the quasi-momenta in the first Brillouin zone (Fig. 1.2). Note that in the case of the 3D optical lattice, the energy spectrum is given by the sum of the energies along each direction of the lattice. However, in this case, the first excited band corresponds to the sum of two lowest 1D energy bands plus one first excited 1D band.

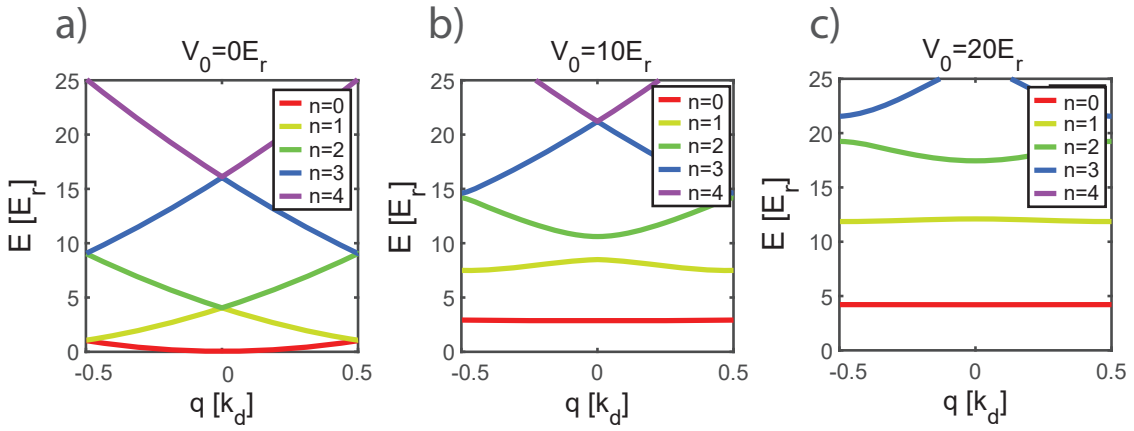

Figure 1.2: **Energy bands for different lattice depths. a)** $V_0 = 0\,E_r$. **b)** $V_0 = 10\,E_r$. **c)** $V_0 = 20\,E_r$. In the absence of a lattice ($V_0 = 0\,E_r$), the energy bands are obtained by folding up the usual free particle parabola into the first Brillouin zone. When a lattice is present, a gap ΔE is opening between the fundamental band and the first excited one of about $\Delta E \approx V_0/2$.

The lattice amplitude must be increased up to about $V_0 \approx 2.2\,E_r$ for a gap in the energy spectrum to appear, contrary to the 1D case where a gap opens as soon as a lattice amplitude is present.

Actually, one can use the periodicity of Bloch's functions on the quasi-momentum to write them as a sum of lattice site localized functions called the Wannier functions w:

$$\psi_{n,q}(x) = \left(\frac{d}{2\pi}\right)^{1/2} \sum_j w_{n,j}(x) e^{-ijdq} \tag{1.6}$$

verifying the relation: $w_{n,0}(x - jd) = w_{n,j}(x)$ where j refers to the index of the lattice site. The Wannier functions for the fundamental band $w_{0,0} = w$ are plotted in Fig. 1.3.

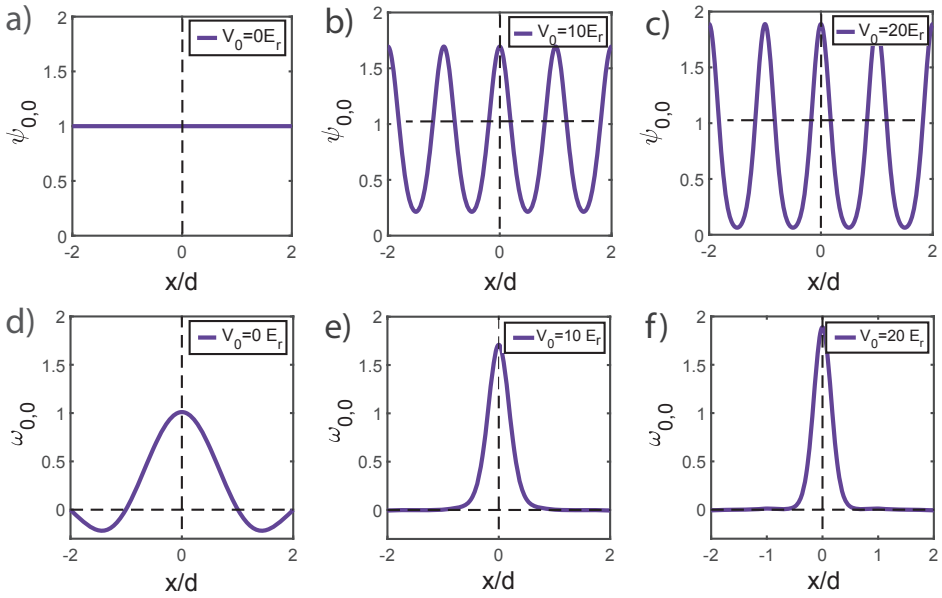

Figure 1.3: **The Bloch and the Wannier functions for the fundamental band.** When the lattice amplitude V_0 increases, the Bloch functions become more and more peaked around the lattice sites (a-c), which translates for the Wannier functions in a sharpening (d-f).

[1]Similar results would be obtained with other geometries.

When dealing with indistinguishable quantum particles, it is often convenient to describe the systems with the formalism of the second quantification. We consequently introduce the creation $\hat{a}_n(q)^\dagger$ (resp. annihilation $\hat{a}_n(q)$) operator that creates (resp.annihilates) a particle in the Bloch wave $\psi_{n,q}(x)$. Given that $\hat{\mathcal{H}}_{\text{band}}$ is diagonal in the Boch function basis:

$$\hat{\mathcal{H}}_{\text{band}} = \sum_n \int_{-\frac{k_d}{2}}^{+\frac{k_d}{2}} E_n(q)\hat{a}_n^\dagger(q)\hat{a}_n(q)dq \tag{1.7}$$

Translating in the second quantization formalism the change of basis given in Eq. 1.6:

$$\hat{a}_n^\dagger(q) = \left(\frac{d}{2\pi}\right)^{1/2} \sum_j \hat{b}_{n,j}^\dagger e^{ijdq} \tag{1.8}$$

leads to the following expression for the band Hamiltonian:

$$\hat{\mathcal{H}}_{\text{band}} = \sum_n \sum_{j,j'} J_n(j-j')\hat{b}_{n,j}^\dagger \hat{b}_{n,j'} \tag{1.9}$$

where $\hat{b}_{n,j}^\dagger$ (resp. $\hat{b}_{n,j}$) is the creation (resp. annihilation) operator that creates (resp.annihilates) a particle in the Wannier function centered in the lattice site indexed by j and the band n, and $J_n(j)$ is given by:

$$J_n(j) = \int w_{n,j}^*(x)\left(\frac{\hat{p}^2}{2m} + V(x)\right) w_{n,0}(x)dx = \frac{d}{2\pi}\int_{-\pi/d}^{\pi/d} dq E_n(q)e^{-ijdq} \tag{1.10}$$

Written under the form given in Eq. 1.9, $\hat{\mathcal{H}}_{\text{band}}$ is easy to interpret: it describes the hops, within a band n, of an atom from the site j to the site j'. The probability is governed by the coefficient J which only depends on the band n and on the distance between the two sites j and j'.

Since we want to study the ground state properties of the system, we suppose that no higher band than the lowest energy one is populated. Of course, this is valid for $V_0 \gtrsim 2.2\,E_r$, value at which a gap is opening between the lowest energy band and the other ones in the energy spectrum of the 3D band Hamiltonian. Furthermore, for $V_0 \geq 3\,E_r$, the hopping events between non adjacent sites can be neglected and we will consider only hops between neighboring sites ($\sum_{<j,j'>}$) with a constant $J_0(1) = -J$ (to have J positive).

Finally:

$$\hat{\mathcal{H}}_{\text{band}} = -J \sum_{<j,j'>} \hat{b}_j^\dagger \hat{b}_{j'} \tag{1.11}$$

The variation of J as a function of V_0 is represented in Fig. 1.4. When the lattice depth increases, it becomes more difficult for the particles to tunnel from one lattice site to another one.

The interaction term

In the formalism of the second quantification, the two-body interaction term $\hat{\mathcal{H}}_{\text{int}}$ writes [17]:

$$\hat{\mathcal{H}}_{\text{int}} = \frac{1}{2}\int d\vec{r}\int d\vec{r'} U_{\text{int}}(\vec{r},\vec{r'})\hat{\Psi}^\dagger(\vec{r})\hat{\Psi}^\dagger(\vec{r'})\hat{\Psi}(\vec{r'})\hat{\Psi}(\vec{r}) \tag{1.12}$$

with $\hat{\Psi}^\dagger(\vec{r})$ the creation field operator that creates a particle in $\vec{r}$:

$$\hat{\Psi}(\vec{r}) = \sum_j w_j(\vec{r})\hat{b}_j = \sum_j w_0(\vec{r}-\vec{r}_j)\hat{b}_j. \tag{1.13}$$

Here, we suppose that the particles interact with a repulsive short-range interaction of contact type:

$$U_{\text{int}}(\vec{r_1} - \vec{r_2}) = g\delta(\vec{r_1} - \vec{r_2}) \tag{1.14}$$

Furthermore, as we saw in the previous subsection, the Wannier functions are sharpening when increasing the lattice depth. The overlap between the Wannier functions centered on different lattice sites becomes increasingly negligible. We consequently only consider the on-site interactions. Taking into account this hypothesis:

$$\hat{\mathcal{H}}_{\text{int}} = \frac{U}{2}\sum_j \hat{n}_j(\hat{n}_j - 1) \tag{1.15}$$

with $U = g\left[\int w^4(x)dx\right]^3$ and $\hat{n}_j = \hat{b}_j^\dagger \hat{b}_j$ is the number of particles in the site j.

Remark: In order to derive the expression of the parameters U and J, we used the Wannier functions calculated from the band Hamiltonian, that is to say for the case when the particles are not interacting. In the presence of repulsive interactions, the Wannier wavefunctions broaden. However, this broadening is generally not taken into account (except in metrology experiments like in the case of the atomic clocks) since very weak, especially when working with a few particles per lattice site, which will be the case in this thesis [18].

Summary

We have just shown that provided the lattice amplitude is not too low ($V_0 \gtrsim 3\,E_r$), the physics of interacting (repulsive interactions) bosons moving in a periodic potential and restricted to the lowest energy band is captured by the Hamiltonian:

$$\boxed{\hat{\mathcal{H}}_{\text{BH}} = \underbrace{-J\sum_{i\neq j}\hat{b}_i^\dagger \hat{b}_j}_{\text{kinetic term}} + \underbrace{\frac{1}{2}U\sum_i \hat{n}_i(\hat{n}_i - 1)}_{\text{interaction term}}} \tag{1.16}$$

This Hamiltonian is called the **Bose-Hubbard Hamiltonian** [19]. It depends only on two parameters that are the interaction term U and the hopping term J. The variation of these parameters as a function of the lattice amplitude is given in Fig. 1.4.

Note that in the Hamiltonian of Eq. 1.16, all the lattice sites are equivalent, and the system is homogeneous. This homogeneity can be broken by the presence of an additional potential that varies in space, as it is the case when investigating the Mott transition with trapped cold atoms (see §.1.3). We will discuss the effect of this trapping potential in §.1.3, for the moment we concentrate the discussion on the homogeneous Bose-Hubbard model.

1.2.2 The superfluid to Mott insulator transition

In this section, we consider the ground state of the homogeneous Bose-Hubbard Hamiltonian. We take the simple case where N particles can move in a lattice of $M = N/\bar{n}$ lattice sites where $\bar{n} \in \mathbb{N}$ is the average lattice filling, that is to say the mean number of atoms per lattice site $\bar{n} = \langle \hat{n}_i \rangle$ (since the system is homogeneous, this value is independent on the lattice site). There are two energy scales in the problem: the hopping energy J that characterizes the kinetic energy of the particles in the lattice potential and the interaction energy term U which gives the particles on-site interaction. Besides the apparent simplicity of this Hamiltonian, its exact resolution is challenging. In fact, an analytic solution exists only for the two extreme cases:

U/J → 0: Perfect Superfluid (SF)

In this limit, the bosons are not interacting. As mentioned in §.1.2.1, the single-particle ground state of lowest energy is the Bloch wavefunction of quasi-momentum $q = 0$. The ground state of the whole

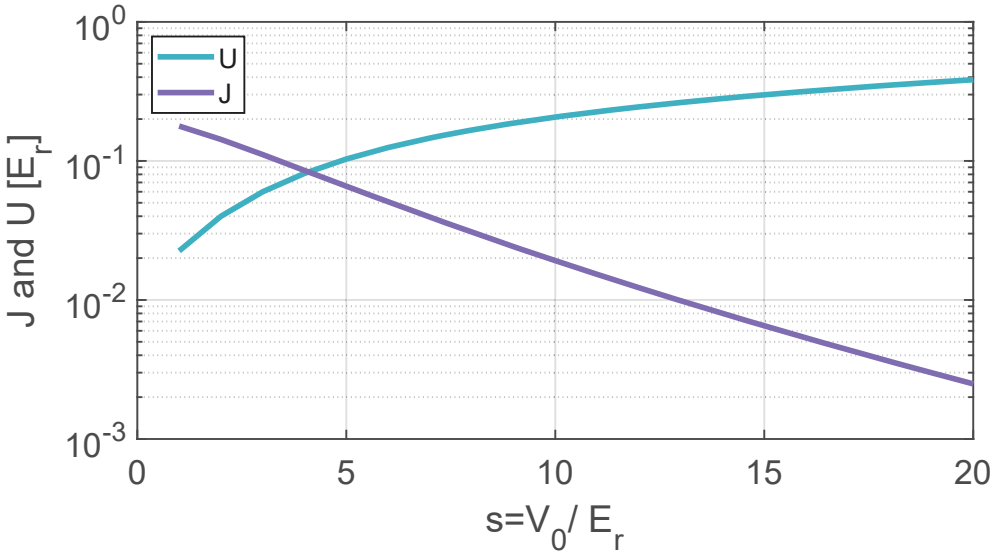

Figure 1.4: **Numerical values computed for J and U as a function of the lattice depth V_0 for Helium atoms and d = 775 nm (see §.3.1).** When the lattice depth increases, J decreases exponentially as it becomes more difficult for the particles to tunnel from one site to another one. Meanwhile, the on-site energy term U increases due to the tightening of the Wannier wavefunctions.

system containing N particles (canonical ensemble description) is the product of the single particle ground state:

$$|\Psi_0\rangle = \frac{1}{\sqrt{N!}}(\hat{a}^\dagger(q=0))^N|0\rangle = \frac{1}{\sqrt{N!}}\left(\frac{1}{\sqrt{M}}\sum_{j=1}^{M}\hat{b}_j^\dagger\right)^N|0\rangle \tag{1.17}$$

In the thermodynamic limit ($N \to \infty$, $M \to \infty$ and $\frac{N}{M} = \bar{n}$), the many-body wavefunction $|\Psi_0\rangle$ becomes equivalent to a coherent state (linked to the creation operator $\hat{a}^\dagger(q=0)$) with the same average number of particles N: $|\Psi_{\text{coh}}\rangle \propto e^{\sqrt{N}\hat{a}^\dagger(q=0)}|0\rangle$. By using the relation between the creation operator linked to the Bloch's functions ($\hat{a}^\dagger(q=0)$) and the one linked to the creation of a particle in the site j ($\hat{b}_j^\dagger$):

$$|\Psi_0\rangle \approx |\Psi_{\text{coh}}\rangle \propto \prod_{j=1}^{M} e^{\sqrt{\bar{n}}\hat{b}_j^\dagger}|0\rangle \propto \prod_{j=1}^{M}|\alpha_j\rangle \tag{1.18}$$

where $|\alpha_i\rangle$ refers to a coherent state linked to the site j and of amplitude $\alpha_j = \sqrt{\bar{n}}e^{i\phi}$. In other words, the many-body wavefunction $|\Psi_0\rangle$ can be written as a product of local coherent states defined on each lattice site j.

With this representation of the ground state, one can derive some characteristic properties:

- By analogy with the BEC theory, we can define on each lattice site j the matter-wave field as the expectation value of the creation operator:

$$\psi_j = \left\langle \Psi_0|\hat{b}_j^\dagger|\Psi_0\right\rangle \approx \left\langle \Psi_{\text{coh}}|\hat{b}_j^\dagger|\Psi_{\text{coh}}\right\rangle = \sqrt{\bar{n}}e^{-i\phi}. \tag{1.19}$$

  The fact that this quantity is different from zero implies off-diagonal long range order, characteristics given by Penrose and Onsager to the presence of a condensate phase [20]. In the discrete system of lattice sites, long-range order is characterized by the first-order correlation function $C^{(1)}(j,j') = \left\langle \hat{b}_j^\dagger\hat{b}_{j'}\right\rangle$:

$$\left\langle \hat{b}_j^\dagger\hat{b}_{j'}\right\rangle \underset{|\vec{r}_j-\vec{r}_{j'}|\to+\infty}{\longrightarrow} \alpha_j^*\alpha_{j'} \tag{1.20}$$

- The probability to find n particles in a lattice site is characterized by a Poisson statistics with $\sigma_n = \sqrt{\bar{n}}$:

$$p(n) \approx \frac{\bar{n}^n}{n!} e^{-\bar{n}} \tag{1.21}$$

U/J $\to \infty$: Perfect Mott insulator (MI)

The Hamiltonian then reduces to:

$$\hat{\mathcal{H}}_{\mathrm{BH}} = \frac{1}{2} U \sum_i \hat{n}_i(\hat{n}_i - 1) \tag{1.22}$$

The ground state wavefunction is consequently a Fock state:

$$|\Psi_0\rangle_{MI} = \frac{1}{\sqrt{N!}} \prod_{j=1}^{M} \left(\hat{b}_j^\dagger\right)^{\bar{n}} |0\rangle \tag{1.23}$$

- Because of the strong repulsive interactions, the particles localize on the lattice sites, with a filling of $n_0 = \bar{n} = \frac{N}{M}$ particles per lattice site and $\sigma_n = 0$. This state is the bosonic **Mott Insulator** predicted by M.Fisher [14].

- In this case, $\psi_j = \left\langle \Psi_0 | \hat{b}_j^\dagger | \Psi_0 \right\rangle = 0$ and there is no long-range order:

$$C^{(1)}(j, j') = \left\langle \hat{b}_j^\dagger \hat{b}_{j'} \right\rangle \underset{|\vec{r}_j - \vec{r}_{j'}| \to +\infty}{\longrightarrow} 0 \tag{1.24}$$

The Mott phase transition

A phase transition manifests generally as a brutal change in the properties of the system when varying a parameter. They can be intriguing in the sense that systems do not necessarily go to a phase that possesses the intrinsic symmetry of the problem. This notion of symmetry breaking is remarkably important in quantum physics to understand the phase transitions. To capture the change in the symmetry of the system, each transition is characterized by an order parameter that takes a non zero value only in the ordered phase and drops to zero at the transition point. In the present case of the Mott transition, the order parameter is given by the matter wave field $\psi_i = \left\langle \Psi_0 | \hat{b}_j^\dagger | \Psi_0 \right\rangle$. Although the Bose-Hubbard Hamiltonian is invariant under a phase change (if $|\psi\rangle$ is an eigenvector of the Hamiltonian, $|\psi\rangle\, e^{i\theta}$ is also one), the condensate chooses spontaneously at the transition a particular phase uniform over the cloud : $\psi(\vec{r}) = |\psi(\vec{r})| e^{i\phi}$ (which corresponds to the breaking of the $U(1)$ symmetry).

Phase transitions are usually driven by the fluctuations induced by the competition of different energy scales present in the system, here the competition of the kinetic energy with the interaction energy, which is usually parametrized by the ratio U/J. As represented in Fig. 1.5, a phase transition occurs at the critical point $(U/J)_c$ at which the ground state of the system changes suddenly from a Superfluid to a Mott Insulator. In 3D and in the thermodynamic limit, the transition is expected to occur for a critical ratio $(U/J)_c^{MF} = 34.8$ for $\bar{n} = 1$ (the general formula applying to any dimension is $(U/J)_c = 5.8\, z$ where z corresponds to the number of nearest neighbors for $\bar{n} = 1$ and $(U/J)_c = 4z\bar{n}$ for $\bar{n} \gg 1$) according to mean-field theories [14, 22, 23] and $(U/J)_c^{QMC} = 29.3\,(2)$ from Quantum Monte Carlo (QMC) calculations [24]. These methods will be discussed §.1.2.3.

Up to now, we only considered systems with a commensurable lattice filling $\bar{n} = n_0$, thus fixing the chemical potential μ (the number of atoms). However, the properties of the system depend strongly on the lattice filling. To characterize that, the full phase diagram $(\mu/U, J/U)$ is represented in Fig. 1.6 (extracted from [14]). The chemical potential μ is determining the filling in the Mott insulator phase.

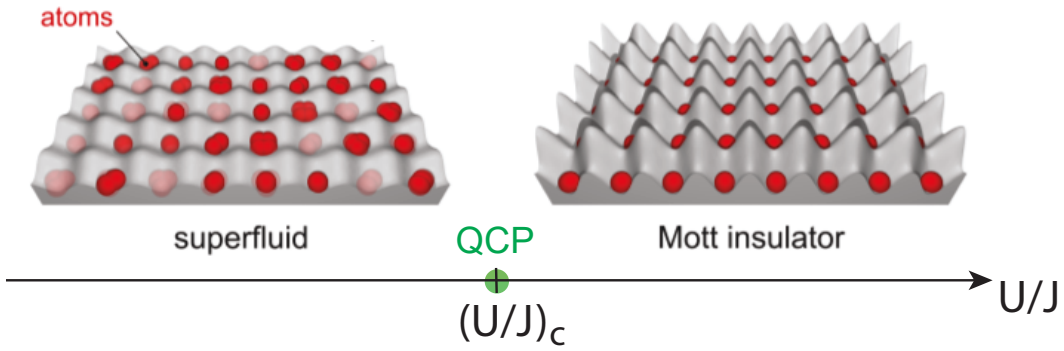

Figure 1.5: **Sketch of the Superfluid and the Mott insulating phases.** The system undergoes a phase transition at the quantum critical point (QCP) for $U/J = (U/J)_c$ between a Mott insulating phase and a superfluid phase. Adapted from [21].

For an homogeneous system, the average filling[2] $\bar{n}$ stays constant whatever U/J ($\bar{n} = N/M$). The behavior of the system when changing U/J is consequently given by the iso-filling lines that are shown as dashed lines in Fig. 1.6. More particularly, we see that for an homogeneous system, the Mott transition only appears for commensurable fillings. Besides, the critical value $(U/J)_c$ at which the transition is happening increases with the lattice filling.

In the next section, we will see that even if the Mott transition phase diagram is well known from a qualitative point of view, getting quantitative results like the exact location of the transition or the state of the system around the Quantum Critical Point (CQP) reveals difficult.

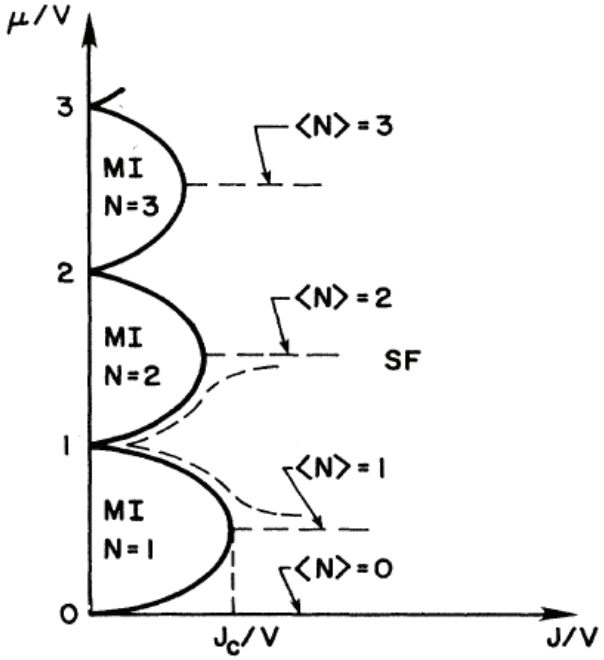

Figure 1.6: **Phase diagram of the Mott transition at T = 0 as a function of J/U and μ/U.** Diagram extracted from [14].

The quantum critical point (QCP)

Similarly to classical phase transitions, the critical point of a quantum phase transition is of particular interest because of the universal scaling behaviors that the systems exhibit, with the characteristic

[2]Careful: In Fig. 1.6, the filling is written $\langle N \rangle$, whereas in this thesis, N refers to the total number of atoms.

scaling exponents determined by the basic properties of the system, such as the symmetry and the dimensionality [25].

More precisely, if we define $m(\vec{r})$ as the order parameter of the transition, then $\langle m(\vec{r})\rangle = 0$ in the disordered phase. However, on approaching the critical point, the order parameter (or its fluctuation) develops short-range correlations:

$$C^{(1)}(\vec{r},\vec{r'}) = \left\langle m(\vec{r})m(\vec{r'})\right\rangle \propto e^{-|\vec{r}-\vec{r'}|/\xi} \tag{1.25}$$

with increasing correlation length ξ. For infinite and homogeneous systems, this correlation length is algebraically diverging at the transition. If we note g the parameter that drives the transition, then:

$$\xi \propto |g - g_c|^{-\nu} \tag{1.26}$$

with ν the critical correlation length exponent that depends only on the universality class of the transition. Because of the divergence of the correlation length, the system is left with no characteristic length. The behavior of the system is consequently scale invariant (in the sense that the system behave in the same way at any length scale). As a result, all the observables depend, via power laws with universal exponents, on some experimental parameters (as it is the case for ξ in Eq. 1.26).

In Tab. 1.1, we are giving the corresponding parameters in the specific case of the Mott transition.

Parameters	Expression in the case of the Mott transition
Ordered phase	SF
Disordered phase	MI
Order parameter $m(\vec{r})$	$\psi_j = \left\langle \hat{b}_j^\dagger \right\rangle$
$C^{(1)}(\vec{r},\vec{r'})$	$C^{(1)}(i,j) = \left\langle \hat{b}_j^\dagger \hat{b}_i \right\rangle$
g	U/J
ν	$\nu = 0.6717\,(1)$ (numerical computation [26])

Table 1.1: **Parameters associated to the Mott transition.**

The measurement of these scaling laws are particularly important since they are universal and usually hard to compute.

1.2.3 Short review of some theoretical approaches for the Bose-Hubbard Hamiltonian

Up to know, we limited the investigation on the properties of the SF and MI phases in the trivial cases where $U = 0$ or $J = 0$. We would like to extend the investigation to the other cases, and provide a full description across the Mott transition.

In the presence of interaction and tunnel coupling, the BH Hamiltonian is not diagonal in either the Bloch's wavefunction basis or the Fock state one. The difficulty in solving exactly the BH Hamiltonian, and more generally, the Hamiltonian relative to systems with large numbers of interacting particles relies on the fact that, because of the interaction term, the Hamiltonian of the system is not a sum of one-particle Hamiltonian.

The approximate methods

When the interactions between the particles are weak, they can be treated at the mean-field level. For instance, in the BEC theory, one usually performs a Hartree-Fock mean field-theory which consists

in factorizating the N-particle wavefunction into a symmetrized product of the single-particle wavefunctions, and leads to the Gross-Pitaevski equation [6]. In lattice systems, the effect of interactions between the atoms is enhanced and one has to use more refined mean-field theories.

Different methods have been developed in order to account for some properties of the lattice gases. They generally apply to a limited region of the phase diagram. Among them:

- The methods that considers the fluctuations, on top of the mean-field solution, induced by the perturbative parameters (either the interaction or the tunneling parameter), generally up to the quadratic order. One can cite the Bogoliubov theory [22] (see later for the derivation) or the site-decoupled mean-field approaches [27] in the superfluid regime. In the Mott insulator phase, the strong-coupling methods can be used [28, 29].

- The mean-field variational methods like the Gutzwiller one where the ground state of the system is found by minimizing the system energy using the Gutzwiller ansatz [30]. Its range of application covers all the transition (although very approximate around the transition point) and is quite accurate to estimate some physical quantities like the in-situ density, for which it has been used in the present work. For this reason, its derivation is shortly explained below.

The Gutzwiller method:

This method consists in writing the many-body ground state function as a product of on-site wavefunctions $|\phi_j\rangle$ developed on the Fock state basis. The Gutzwiller ansatz is defined as [30]:

$$|\Psi_G\rangle = \prod_{j=1}^{M} |\phi_j\rangle = \prod_{j=1}^{M} \sum_{n_j=0}^{\infty} f_j(n_j) \, |n_j\rangle \tag{1.27}$$

This ansatz has the property to converge towards the exact ground state of the system for $U/J \to \infty$ and $U/J \to 0$, (see §.1.2.2). More precisely, by comparison with Eq. 1.18 and Eq. 1.23, we find:

- $U/J \to \infty$: The on-site wavefunction $|\phi_j\rangle$ is a Fock state, meaning $f_j(n_j) = \delta_{n_j,n_0}$.

- $U/J \to 0$: $|\phi_j\rangle$ is a coherent state. The $f_j(n_j)$ are consequently the coefficients corresponding to the projection of a coherent state on the corresponding Fock state basis.

In order to find the best variational estimate for the ground state in the intermediate cases, one has to calculate the Free energy corresponding to $|\Psi_G\rangle$:

$$\left\langle \hat{\mathcal{H}}_{\mathrm{BH}} \right\rangle_{|\Psi_G\rangle} - \mu \left\langle \hat{N} \right\rangle_{|\Psi_G\rangle} = -J \sum_{<i,j>} \alpha_i^* \alpha_j + \sum_j \sum_{n_j=0}^{\infty} \left[\frac{U}{2} n_j(n_j - 1) - \mu n_i \right] |f_j(n_j)|^2 \tag{1.28}$$

and minimize it with the help of the variational parameters that are the $f_j(n_j)$ coefficients defined in Eq. 1.27, with the condition $\langle n_j \rangle = \sum_{n_j=0}^{\infty} |f_j(n_j)|^2 \, n_j = \bar{n}$.

From the value of the $f_j(n_j)$ coefficients, one can calculate quantities like the density profile or the condensate fraction defined as the ratio of the number of atoms in the single particle ground state as compared to the total number of atoms.

The Quantum Monte Carlo algorithm

The only method able to solve exactly the BH Hamiltonian in 3D is the Quantum Monte Carlo method (QMC).

The idea of this method, pointed out in 1949 [31], is based on a stochastic approach to solve quantum problems. More precisely, when trying to calculate the ground state of a quantum system with a large number of particles N that can carry many degrees of freedom D, one is usually confronted to

the computation of expectation values that can be written as an integral over $N \times D \gg 1$ dimensions. Instead of calculating the integral over the $N \times D \gg 1$ dimensional phase space, Quantum Monte Carlo methods only consider random points on this phase space to evaluate the integrals.

Because of the complexity of the algorithm and the fact that its numerical computation takes usually far more time than the usual mean-field approaches, they are not used in the daily basis. However, as showed in §.4, they can be used in order to be compared with experimental data.

For the purpose of this work, we collaborated with two theoretician researchers that provided us QMC calculations: Giuseppe Carleo (Flatiron Institute, New-York) and Tommaso Roscilde (Ecole Normale Supérieure de Lyon). They are both using the Worm algorithm, following the scheme of Pollet [32]. The idea of this method relies on the calculation of the partition function $Z = \mathrm{Tr}\left\langle e^{-\beta\mathcal{H}}\right\rangle$ through stochastic methods. From that, the two-particle correlation function $C^{(1)}(i,j) = \left\langle \hat{b}_i^\dagger \hat{b}_j \right\rangle$ is deduced, giving access to the density distribution of the lattice gases as well as the momentum distribution (see §.2.2).

Excitation in the different phases

One important property that can be investigated using the mean-field theories discussed in the former section are the excitations hosted by the different phases. In fact, a signature of a quantum phase transition usually lies in an abrupt change in the excitation spectrum of the system at the transition point. In the case of the Mott transition:

- In the SF phase, the lowest energetic excitations are gapless sound waves (Goldstone mode relative to the continuous broken symmetry[3]). They are usually referred to as the Bogolibov excitations.
- In the Mott phase, there are two gapped excitations: particles and holes. Because of the atom number conservation, these two modes are coupled and give rise to particle-hole excitations.

Bogoliubov excitations:

In the Superfluid phase, not too close to the transition, the interaction term can be treated with the perturbation theory. A standard approach, also used in order to treat the effect of weak interactions in a harmonically trapped BEC, consists in using the Bogoliubov approximation [22].

At $U = 0$, all the atoms are in the lowest single-particle energy state of the system, *i.e*, in the Bloch wave, which implies that $\left\langle \hat{a}^\dagger(q=0)\hat{a}(q=0)\right\rangle = N$. Because of the interaction, some atoms leave the ground state and occupy higher quasi-momentum states. The Bogoliubov approximation consists in replacing the operators $\hat{a}^\dagger(q=0)$ and $\hat{a}(q=0)$ by $\sqrt{N_{BEC}}$ with N_{BEC} the number of atoms in the condensate. The amplitude of the other modes are treated as small fluctuations and expended to quadratic order. The detailed derivation of the Bogoliubov method can be found in [22, 33]. Here we will give only the major steps in the reasoning. Furthermore, we consider only the case of a 1D homogeneous system containing N particles.

The first step consists in writing the Hamiltonian of the system (written in Eq. 1.2) in the quasi-momentum basis using the relation between creation operator of an atom in site j ($\hat{b}_j^\dagger$) and in the quasi-momentum q ($\hat{a}^\dagger(q)$):

$$\hat{b}_j^\dagger = \frac{1}{\sqrt{N}} \sum_j \hat{a}^\dagger(q) e^{iqx} \tag{1.29}$$

[3]There exists also a gapped excitation mode called the Higgs amplitude mode that is present in the SF phase close to the transition.

$$\hat{\mathcal{H}}_{\mathrm{BH}} = \sum_q E(q)\hat{a}^\dagger(q)\hat{a}(q) + \frac{1}{2}\frac{U}{N}\sum_{q',q'',q'''} \hat{a}^\dagger(q'-q''')\hat{a}^\dagger(q''+q''')\hat{a}(q'')\hat{a}(q') \tag{1.30}$$

which simplifies after performing the Bogoliubov approximation:

$$\hat{\mathcal{H}}_{\mathrm{BB}} = -\frac{1}{2}Un_0N_0 - \frac{1}{2}\sum_q (E(q)+Un_0) + \frac{1}{2}\sum_q \left(\hat{a}^\dagger(q), \hat{a}(-q)\right) \times \begin{bmatrix} E(q)+Un_0 & Un_0 \\ Un_0 & E(q)+Un_0 \end{bmatrix} \begin{pmatrix} \hat{a}(q) \\ \hat{a}(-q)^\dagger \end{pmatrix} \tag{1.31}$$

The Hamiltonian can then be diagonalized by using the Bogoliubov transformation which consists in making the change of variable:

$$\begin{pmatrix} \hat{\beta}_q \\ \hat{\beta}^\dagger_{-q} \end{pmatrix} = \begin{bmatrix} u_q & v_q \\ v_q^* & u_q^* \end{bmatrix} \begin{pmatrix} \hat{a}(q) \\ \hat{a}(-q)^\dagger \end{pmatrix} \tag{1.32}$$

with $\hat{\beta}_q$ and $\hat{\beta}^\dagger_q$ that follow the usual commutation relations of creation and annihilation operators. The Hamiltonian writes:

$$\hat{\mathcal{H}}_{\mathrm{BB}} = \hat{\mathcal{H}}_0 + \sum_q \hbar\omega_q \hat{\beta}^\dagger_q \hat{\beta}_q \tag{1.33}$$

where

$$\hat{\mathcal{H}}_0 = -\frac{1}{2}Un_0N_0 + \frac{1}{2}\sum_q [\hbar\omega_q - (\epsilon_q + Un_0)] \tag{1.34}$$

$$\hbar\omega_q = \sqrt{E(q)^2 + 2Un_0E(q)} \tag{1.35}$$

$$|v_q|^2 = |u_q|^2 - 1 = \frac{1}{2}\left(\frac{E(q)+Un_0}{\hbar\omega_q} - 1\right) \tag{1.36}$$

The ground state of the system is consequently defined as the vacuum state for the $\hat{\beta}_q$ operators, often called the quasi-particle operators.

Under the Bogoliubov approximation, the excitation spectrum of the system is continuous and given by the dispersion relation written in Eq. 1.35. This dispersion relation is usual in condensed matter physics and characterized by two regimes: the phononic regime and the free particle regime.

- At low q, the dispersion relation is linear, $\hbar\omega_q \approx \sqrt{2Un_0E(q)} \approx \hbar q\sqrt{\frac{Un_0}{m^*}}$ with m^* the effective mass defined by $E(q) = \frac{\hbar^2q^2}{2m^*} + o(q^3)$. According to Eq. 1.32, the creation of a quasi-particle with an energy $\hbar\omega_q$ corresponds to the creation and the destruction of two waves at quasi-momentum q and $-q$, thus explaining the term phonon mode. We will see a bit further in the manuscript that these phonon modes could be detected via the $q/-q$ correlation signal induced.
- The excitations at large q are particle-like because $\hbar\omega_q \approx E(q)$. In this case, the quasi-particles are the real particles.

To summarize, when the interaction between the atoms increases, the population of the atoms in the condensate decreases and higher quasi-momentum components get populated.

Remark: Provided an object is dragged at a speed $v < c$ where $c = \mathrm{Min}_q(\omega_q/q) = \sqrt{\frac{Un_0}{m^*}}$ is the speed of the sound, there is no dissipation in the system due to the fact that no Bogoliubov excitations can be created. This is at the origin of the term "superfluid phase".

Particle-hole excitations

When $J = 0$ and $\bar{n} = n_0 \in \mathbb{N}$, the ground state of the system consists in a perfect array of on-site Fock states with exactly n_0 particles per site. The excitations with the lowest energy correspond to

removing or adding a particle to a certain lattice site j. These are referred as respectively hole or particle excitations.

In our system, the number of particles is fixed. The only allowed excitations are consequently the combination of the two: particles and holes where a particle leaves a site to fill an other site (already filled). The excitation energy, defined as the minimum energy to provide to the system in order to transfer it from the ground state to the first excited state, and that corresponds here to the energy required to remove a particle in one site to put it in an other site is:

$$E^p + E^h = (n_0(n_0-1)+1)\,U - n_0(n_0-1)U = U \tag{1.37}$$

This formula has been derived considering that the interaction energy relative to the presence of n_0 particles in the same lattice site is equal to $n_0(n_0-1)U/2$. The MI phase is consequently gapped with $\Delta \approx U$ in the limit $U \gg J$.

Effect of a finite tunnelling.

The role of the particle-hole excitations can be found considering the effect of a small but finite tunnelling J. The existence of a finite tunnelling has for consequence to couple the $J = 0$ ground state to excited states. The ground state of the system is not an array of Fock states anymore, but an admixture of particle-hole excitations on top of the perfect Mott insulator solution. This can be described using the perturbation theory with J/U as the perturbation parameter. The ground state at the first order perturbation writes:

$$\left|\Psi^{(1)}\right\rangle = |\Psi\rangle_{MI} + \frac{J}{U}\sum_{<i,j>} \hat{b}_i^\dagger \hat{b}_j \,|\Psi\rangle_{MI} \tag{1.38}$$

where the second term translates in mathematical term the presence of particle-holes in the system.

From this equation, one can derive an important consequence of the presence of these particle-holes: the modification of the first order coherence [34].

$$\begin{aligned} C^{(1)}(i,j) = \left\langle \hat{b}_i^\dagger \hat{b}_j \right\rangle_{\left|\Psi^{(1)}\right\rangle} &= C^{(1)}(i,j)_{MI} + {}_{MI}\langle\Psi| \frac{J}{U}\hat{b}_i^\dagger \hat{b}_j \sum_{<h,l>} \hat{b}_l^\dagger \hat{b}_h \,|\Psi\rangle_{MI} + \text{c.c} + \mathcal{O}((J/U)^2) \\ &= \delta_{i,j} n_i + 2\frac{J}{U} n_i(n_j+1) \times (\delta_{i+1,j} + \delta_{i-1,j}) \end{aligned} \tag{1.39}$$

These particle-holes are responsible for the restoration of some short-range coherence in the Mott phase. Within the first order perturbation theory, the particles and holes delocalize on neighboring sites, resulting in a decrease of the first-order correlation $C^{(1)}(i,j)$ over a distance equal to the lattice spacing d. When approaching the transition, the excitations can delocalize over larger distances as it will be seen in §.5.

1.2.4 Solving the BH Hamiltonian with the quantum simulation

Although the approximate or exact numerical methods succeeds in probing some basic properties of the BH Hamiltonian such as the position of the QCP or observables like the density, some others remain out of reach. For instance, beyond the first-order, the investigation of correlation functions has been elusive. In the region close to the QCP, the thermodynamic functions obey some universal scaling relations that are hard to compute and have not been measured in experiments. Furthermore, we limit ourselves to the description of the static properties. But out of equilibrium/relaxation physics is another topic for which theoretical approaches are limited.

To overcome these limitations, one possibility is to use experiments. This approach was initially proposed by R. Feynman in 1982 [35]. In the next section, we will see that an adequate platform in order to study the Bose-Hubbard Model are cold atoms experiments. Cold atoms trapped in an optical lattice are described by the BH Hamiltonian and thus constitute what is called a "quantum simulator" for the BH model.

1.3 Realization of the Bose Hubbard Hamiltonian with cold atoms

To realize the Bose-Hubbard Hamiltonian in an experiment, one obviously needs to create a periodic potential. With quantum gases, such a periodic structure can be implemented using far-detuned laser beams. The idea of using periodic pattern of light as a tool to manipulate neutral atoms appeared in the early 80's with the realization of the Kapitza-Dirac diffraction [36] (predicted by Kapitza and Dirac in 1933 [37]). A beam of sodium was then diffracted by a standing wave of light. This effect, which relies on the particle-wave duality, has been the starting point to many other experiments. One can cite more particularly the experimental realization of the Bragg diffraction, scheme that can be used for the implementation of atomic beamsplitters [38]. Parallel to theses effects, the loading and trapping of atoms into periodic patterns of light enabled the experimental realization of a new physics [39]. By cooling the atoms into the lowest energy band of the optical lattice, other authors managed to investigate quantum effect such as Bloch oscillations [40].
In 1998, Zoller and colleagues demonstrated [41] that the dynamics of atoms loaded into the fundamental band of an optical lattice is perfectly described by the BH Hamiltonian. With the possibility to tune U/J at wish (at least over a broad range in U/J), it is possible to explore the Mott transition. While cooling techniques at that time were based on Raman cooling [40] and direct cooling from the optical lattice [42], they demonstrated in the same article that by loading a BEC into an optical lattice, it is possible to access the ground state of the system without any further cooling.

The experimental confirmation and the first experimental observation of the 3D bosonic Mott transition using cold atoms has been achieved in the group of I. Bloch in 2002 [10]. Note that the investigation of the Mott transition with cold atoms has then been extended to lower dimensions [43, 39] and different geometries among which the triangular [44] and Kagome [45] ones. In 2008, the Mott transition has also been observed in polarized fermionic systems [46].

Here, we propose to review the major advantages and properties of cold atoms that make possible the investigation of the Mott transition:

- By using optical lattices, it is possible to trap atoms in periodic potentials.
- It is possible, by transferring a Bose Einstein Condensate to the lattice potential, to load the atoms in the fundamental band of the optical lattice.
- By varying the power of the lattice beams, U/J can be tuned and one can investigate the MI and the SF phase, as well as the transition point.
- Numerous techniques are available to measure different physical observables. See §.1.3.2.

1.3.1 Optical lattices

The interaction between the light and neutral atoms can be predominantly dissipative or conservative depending on the detuning $\Delta = \omega - \omega_0$ ($\omega/2\pi$ is a laser frequency and $\hbar\omega_0$ the energy difference between the two atomic energy levels coupled by the light) of the light with respect to the atomic transition. The dissipative part (dominant at resonance) can be used to cool the atoms, while the conservative part is generally used to trap the atoms. When the detuning of the light is large, *i.e* $\Delta \gg \Gamma$, with Γ the width of the transition, the dissipative force is negligible and the effect of the light onto the atoms can be described as a shift of their energies by the dipolar potential [47]:

$$V_{\text{dip}}(\vec{r}) = \frac{3\pi c^2}{2\omega_0^3}\left(\frac{\Gamma}{\Delta}\right) I(\vec{r}) \tag{1.40}$$

where $I(\vec{r})$ is the intensity of the light. By shaping the intensity pattern of the light, it is consequently possible to engineer a large variety of potential geometries. Periodic potentials can consequently be

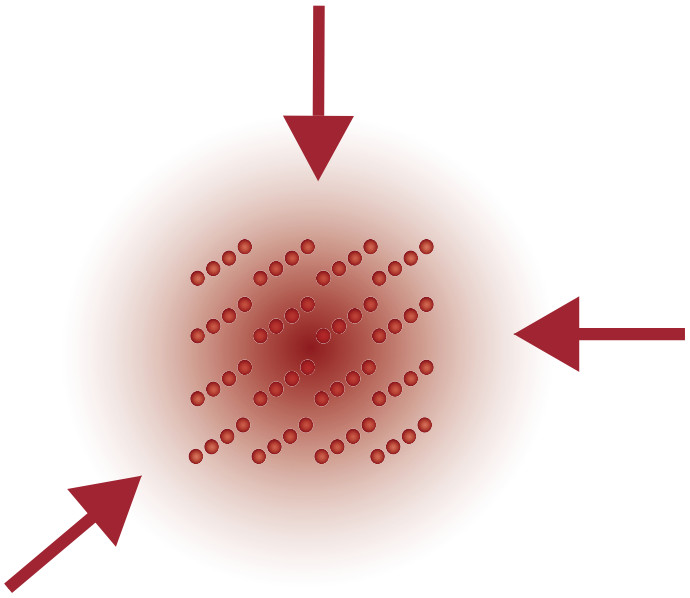

Figure 1.7: **Scheme of a 3D optical lattice.** The red points represent atoms trapped into a cubic 3D optical lattice.

induced using interference phenomena that are responsible for a periodic modulation of the intensity pattern.

More precisely, a 3D square lattice potential is obtained by using 3 pairs of retroreflected laser beams as displayed in Fig. 1.7 (the retroreflected beams are not shown). Because the lattice potential is induced by the light, such a configuration is referred to as an optical lattice. In most of the experimental apparatus, the light beams are laser beams with a gaussian intensity profile. The overall potential writes:

$$V(\vec{r}) = V_0 \left[\cos^2(k_L x) + \cos^2(k_L y) + \cos^2(k_L z)\right] + \frac{m}{2}\omega_{ext}^2 r^2 + \mathcal{O}\left(\frac{r^2}{w_0^2}\right) \tag{1.41}$$

where V_0 is the lattice depth, $k_L = 2\pi/\lambda$ is the laser wavevector, w_0 is the lattice beam waist radius (here we suppose that the lattice beams have the same waist) and ω_{ext} is the external trapping frequency:

$$V_0 = \frac{6\pi\Gamma c^2}{\omega_0^3}\frac{1}{\Delta} \times \frac{2P}{\pi w_0^2} \qquad \omega_{ext}^2 = \frac{8}{m}\frac{V_0}{w_0^2} \tag{1.42}$$

To the desired 3D cubic potential of depth V_0 and of spatial period $d = \lambda/2$, is superimposed a harmonic trapping potential coming from the shape of the gaussian beams. This external trapping is causing the non-homogeneity of the system. This will be discussed in §.1.3.3.

By varying the power P of the laser beams, one can vary at will the lattice depth accordingly ($V_0 \propto P$). Because $U/J = f(V_0)$ (see Fig. 1.8), tuning V_0 offers the possibility to explore the Mott transition.

1.3.2 Experimental techniques to investigate the Mott transition

In order to probe the gas loaded in the optical lattice, different experimental methods are available:

- The in-trap imaging reveals the density profile of the clouds. In the case of a 3D lattice, this method suffers from the problem of the optical imaging integration along the line-of-sight. It

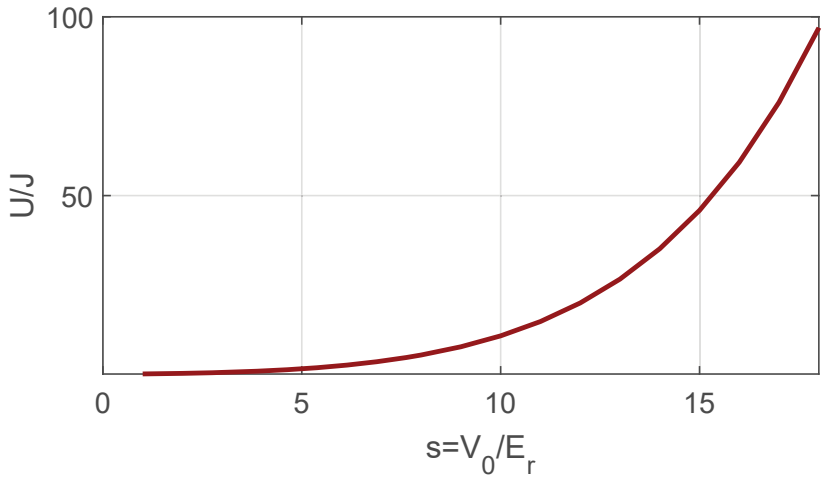

Figure 1.8: **Numerical values computed for the ratio U/J as a function of the lattice depth V_0 with d = 775 nm** (see §.3.1). When the lattice depth increases, U/J increases, going towards a stronger interacting system.

is consequently impossible to measure directly the full three dimensional density. Furthermore, because of the absence of symmetry of revolution, it is not possible to use techniques like the Abel transform to access, from a 2D density measurement, the 3D distribution. In lower geometries, quantum gas microscope experiments [48, 49] as well as the electron microscopy [50] experiments measure the in-situ position of the atoms with a single atom sensitivity. With these approaches, position-space correlation functions can be measured directly. This has led to an impressive number of breakthrough observations over the past decade.

- Probing the position of the atoms after a long time-of- flight enables to access, in some conditions given in §.3, the in-trap momentum distribution of the atoms. Like in the former case, the atoms can be detected via the optical imaging. However, the technique used in quantum gas microscopes can not be directly transferred to the time-of-flight imaging (to be able to detect the atoms, the exposure times used in the quantum gas microscope experiments are very long, about a few hundreds of ms, and is not appropriate for the measurement of the position of the atoms while falling during the time-of-flight, first because the atoms can move a lot on this time scale and because the field of view of the camera is generally limited to few ms). Schmiedmayer and colleagues in Wien also designed a setup from which they can measure, after 50 ms of time-of-flight, the 2D momentum distribution with the single atom resolution. It is based on the use of high numerical aperture optics to detect the fluorescence of atoms illuminated by a light sheet. They also demonstrated the possibility to measure the 3D momentum distribution performing a tomographic measurement [51], even if the actual implementation remains challenging.

- Quantum gases can be probed using spectroscopic techniques. They allow for the measurement of the excitation spectrum [10, 52, 53, 54]. One can cite the techniques of the amplitude modulation (see §.3.1.4) or the Bragg spectroscopy [54].

If the different methods provide complementary information, some properties are easier to measure in the momentum-space domain.

In the present work, we probe the momentum distribution by measuring the density of the clouds after a long time-of-flight. Furthermore, the specificity of our experiment relies on the use of He^* atoms that can be detected by an electronic detection. Thanks to this original way of detecting particles, we can go beyond some limitations associated with optical imaging and measure the momentum distribution in three dimensions and with a single atom sensitivity[55]. This will be discussed in detail in §.3.

1.3.3 Investigation of the Mott transition at finite temperature, with finite size in inhomogeneous gases

For the description of the Bose-Hubbard Hamiltonian and the Mott transition, we only considered infinite (more precisely, considering the size of the system $M \to \infty$) and homogeneous systems at $T = 0$ so far. If the cold atoms are a good testbed for the investigation of the Mott transition, however, the three characteristics mentioned above are not fulfilled. The cold atomic clouds loaded in the optical lattice have a low but finite temperature. Furthermore, because of the external trapping, these systems are not homogeneous and thus finite. Note that if the effect of the finite temperature is clearly a drawback for the experiments, on the contrary, the inhomogeneity allows for the observation of the MI phase. In fact, without an external trapping, such a realization would require to load the optical lattice with an integer number of atoms per lattice site, *i.e.* a fixed total number of atoms $N = n_0 \times M$, which is very challenging [56] when working with large systems (in the experiment, we are working with clouds extending over up to 50 lattice sites).

These differences with respect to the homogeneous systems described so far have to be taken into account for the interpretation of the results obtained in the experiments.

Finite temperature

To characterize the effect of the temperature, the phase diagram is plotted in Fig. 1.9 with the two parameters that are the ratio U/J and T/J (homogeneous system). We see that the superfluid and the Mott insulating phases subsist at low temperature.
When increasing the temperature, the superfluid can undergo a "condensation transition" (in analogy to the BEC theory) towards a thermal phase, usually called the Normal Fluid phase (NF). In this case, the transition is driven by thermal fluctuations, and characterized by the ratio T/J. Because the fluctuations are of thermal origin, the transition is said to be classical. On the contrary, the Mott transition is a quantum phase transition in the sense that it is driven only by some parameters of the Hamiltonian describing the system. In the MI side of the diagram, there is no proper phase transition between the Mott state and the normal state but a smooth crossover with characteristic temperature $T_{\text{melt}} \approx 0.2 \times U/k_B$ [57].

On this diagram, besides the usual phases we have just described, is represented in green the quantum critical region which is the domain of the phase diagram just above the quantum critical point (QCP). This region is particularly interesting for reasons that will be explained later.

In usual experiments, it has been shown that the temperatures achieved were low enough in order to be able to probe the superfluid and the Mott insulator phases [10]. However, the finite temperature could be high enough in order to washed out some properties of the physics at $T = 0$. This is especially the case when trying to characterize the quantum critical point. An understanding of this question is one driving force of the experiment.

Effect of the external trapping: the inhomogeneity and the finite size of the clouds

The inhomogeneity:

Up to now, we have considered homogeneous systems. In the case of cold atom experiments, optical potentials are generally made using (focused) gaussian laser beams. As we saw in §.1.3.1, the inhomogeneous intensity distribution of the gaussian beams creates an additional harmonic potential referred to as the external trapping with:

$$V_{\text{ext}}(\vec{r}) = \frac{1}{2} m \omega_{ext}^2 r^2 \tag{1.43}$$

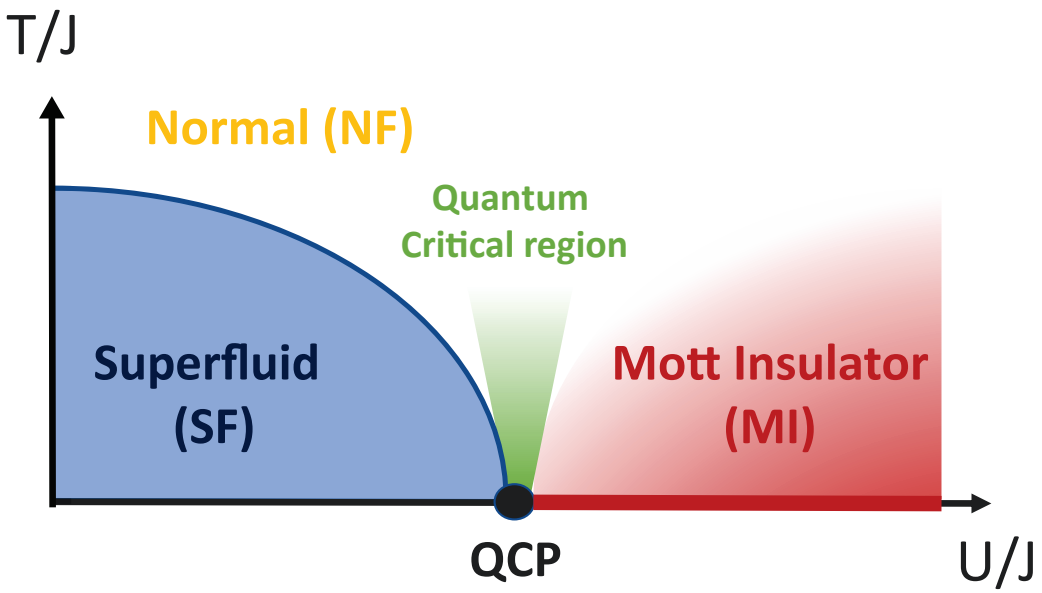

Figure 1.9: **Phase diagram of the Mott transition.** At high temperature, the system is in the normal phase NF (thermal phase). When lowering the temperature at $U/J << (U/J)_c$, the system undergoes a classical (thermal) second-order phase transition towards a SuperFluid phase (SF). When increasing the ratio U/J, the system undergoes a second-order quantum phase transition between the SF phase and the Mott Insulator phase (MI). In the MI side of the diagram, there is no proper phase transition between the Mott state and the normal state but a smooth crossover.

Provided the Local Density Approximation (LDA) applies [58][4], one can deduce the properties of the inhomogeneous system from the homogeneous one by replacing the chemical potential μ by an effective chemical potential:

$$\mu_{\text{eff}}(\vec{r}) = \mu - V_{\text{ext}}(\vec{r}) \tag{1.44}$$

Contrary to the homogeneous systems, the average filling $\bar{n}_j$ on each lattice site j adjusts to follow the variation of the effective chemical potential on the cloud size and consequently depends on the lattice site position. It is maximum at the center of the trap and decreases towards 0 at the edge. A qualitative understanding on the effect of the inhomogeneity on the system composition can be derived from the phase diagram given in Fig. 1.10.

In the superfluid phase, far from the transition, the gas remains entirely superfluid (see the green arrow in the subfigure a). When $U/J = (U/J)_c$ with $(U/J)_c$ referring to the transition point for an homogeneous system with a filling equal to one, a Mott plateau with a filling equals to one appears at the center of the cloud while the rest of the cloud stays superfluid (see the red arrow in the subfigure a). When increasing U/J past this point, the ratio between the MI domain and the superfluid shells decreases. If the ratio U/J reaches the transition point for $\bar{n} = 2$ (in a homogeneous system), then MI shells with filling equal to one and two alternate with superfluid shells, as depicted in Fig. 1.10.b.

Note that from now on, we will write that a cloud is in the Mott phase as soon a MI plateau is present, that is to say for $U/J > (U/J)_c$, and the critical values $(U/J)_c$ are the ones of the homogeneous systems.

The finite size:

[4]Provided the trapping potential varies slowly from one site to another site, the system is locally at thermal equilibrium as demonstrated in [58]. However, a failure of the LDA can be observed around the QCP [59].

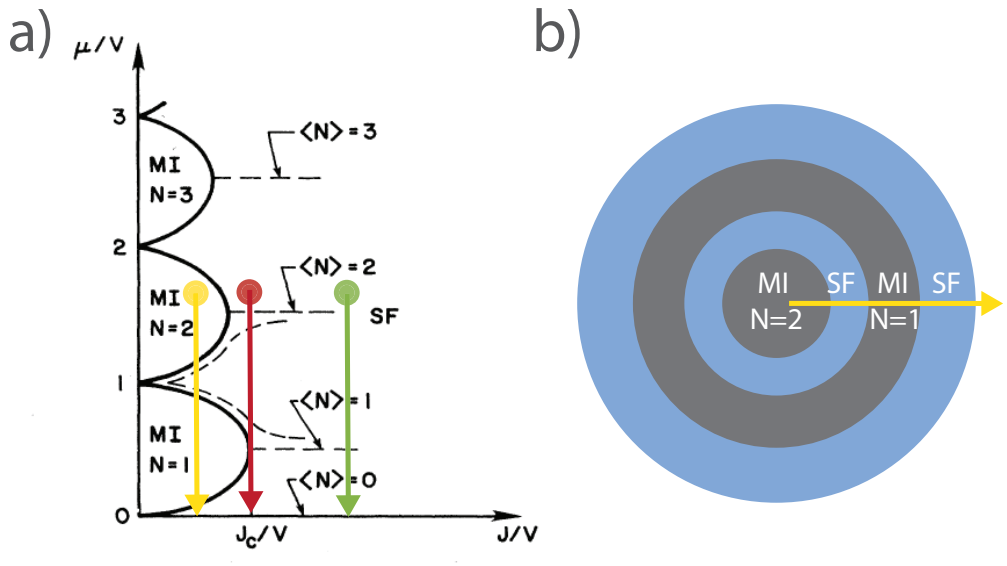

Figure 1.10: **Effect of the external trapping. a)** Phase diagram $\mu/U = f(J/U)$ of the Mott transition (homogeneous system). The arrows indicate the evolution of $\mu_{eff}(r)/U$ from the center of the cloud to the edge. For $J/U \gg (J/U)_c$, the system is entirely superfluid (green arrow). When $J/U = (J/U)_c$ (transition point for a homogeneous Mott insulator with a filling $\bar{n} = 1$), a thin shell at the location where $\bar{n} = 1$ is becoming a Mott insulator with a unit filling while the rest of the cloud stays superfluid (red arrow). For $J/U \ll (J/U)_c$ shells of MI and SF alternate. When increasing even more J/U, the transition point corresponding to a Mott insulator with a filling equal to 2 can be crossed (yellow arrow).**b)** Sketch of the wedding cake structure for a cloud prepared with the parameters μ/U and J/U corresponding to the coordinates of the yellow point in the subfigure a).

With lattice gases, one can also use the Thomas-Fermi approximation in order to get an analytic approximate solution for the shape of the cloud in the superfluid phase and the value of the chemical potential μ. This method consists in minimizing the energy of the particles on single lattice sites neglecting the kinetic energy (as a result, this approximation is not valid for $J \approx U$). One finds similar results than the one derived for a BEC trapped in a harmonic trap:

$$\bar{n}_j = \frac{1}{U}\left(\mu - \frac{1}{2}m\omega_{ext}^2 r_j^2\right) \tag{1.45}$$

with:

$$r_{TF} = \sqrt{\frac{2\mu}{m\omega_{ext}^2}} \quad \text{and} \quad \mu = \left(\frac{15}{16}\frac{(\lambda/2)m^{3/2}NU\omega_{ext}}{\sqrt{2}\pi}\right)^{2/5} \tag{1.46}$$

That is, the superfluid has a parabolic profile of radius given by r_{TF}.

To get a more quantitative density profile, the mean-field theories discussed in §.1.2.3 can be generalized to the inhomogeneous case. More particularly, we will use in this thesis the Gutzwiller approach with taking into account the presence of the external confinement (which only requires to replace μ by μ_{eff} in the BH Hamiltonian and taking into account that the f_j's coefficients do now depend on the lattice site index j).

Consequences:

In both cases, the notion of phase transition has to be reconsider. In fact, the inhomogeneity of the clouds and the finite size of the system leads to dramatic changes in the properties of the system when varying U/J. For instance, because of the finite size, the quantities supposed to diverge at the transition, such as the correlation length ξ (which represents the size over which the first-order correlation function $C^{(1)}(i,j)$ is decaying), are limited by the spatial extent of the cloud. Because

of the inhomogeneity and the possibility that different phases coexist in the Mott phase, the abrupt change of some observables supposed to occur at the transition such as the condensate fraction are washed out. As a result, the transition observed is a crossover and not a true phase transition. A central question is whether it is possible to infer, from measurements carried out with inhomogeneous and finite size clouds, the properties of homogeneous systems (and as a result, of the Mott transition).

What can we learn from the trapped and finite temperature lattice gas clouds?

At lot of work has been devoted over the past few years to take into account the finite size and the inhomogeneity of the clouds, and relate the properties of the Mott transition to the quantities measured in the experiment. More particularly, researchers concentrated on the investigation of the critical point and how the universal laws supposed to be observed at the transition are modified by the presence of the trap. They are referred to as the finite size scaling (FSS) and the trap size scaling (TSS) theories.

If we consider for instance the example of the first-order correlation function $C^{(1)}$, for an infinite homogeneous system, the coherence length is expected to diverge at the condensation transition $\xi \underset{T\to T_c}{\propto} \frac{1}{|T-T_c|^\nu}$ with ν the critical exponent associated to the universality class of the transition. In trapped systems, it can not diverge anymore but it scales at the transition point as L^θ where L refers to the size of the cloud and θ is an exponent which depends only on the critical parameters of the condensation transition [60]. Furthermore, the first-order correlation function is still exhibiting a universal behavior, controlled by $|T - T_c|$ and L^θ where θ is the universal trap exponent and can be written as a function of ν. From a general point of view, this reasoning holds with different observables. [61, 62, 63, 64].

The effect of the temperature close to the QCP has been shown to be less dramatic as we could think for the investigation of the Mott transition. In fact, the quantum critical point is affecting a large portion of the finite temperature phase diagram in a region named the quantum critical region and depicted in green in Fig. 1.9. In this region, the thermodynamic properties are totally controlled by the critical point. For instance, some observables in the quantum critical regime are expected to exhibit a power-law dependence on temperature with exponents descending from the critical exponents at the QCP (a situation that is analog to the effect of the trap) [65]. The question that remains unanswered concern the extension of this region, and whose knowledge is important to state on the ability to probe the associated critical phenomena in usual cold atom experiments.

2. Correlation in Quantum macroscopic systems

When trying to solve a problem where the system is composed of a macroscopic number of particles, we saw in the previous chapter that there exist two situations that are drastically different:

- When the particles are non-interacting or weakly interacting (meaning MF theories can be applied), the wavefunction of the quantum state of the entire system of N particles can be written as a product of single particle wavefunctions:

$$|\Psi\rangle = \prod_i |\psi_i\rangle \tag{2.1}$$

  All the information about the system is contained in the one-particle wavefunction. As a result, correlations between two or more individual particles are not playing any role and can be discarded.

- On the contrary, for strongly interacting systems, such a factorization can not be performed because of the strong correlations between the different particles. A full characterization of these N-body systems thus requires the calculation of the correlation functions up to the order N in the collective degrees of freedom of the many-body system (spatial position, momentum, spin, ..., of the atoms).

This constitutes a strong motivation for the investigation of the Mott transition through the correlation functions.

But before dealing with the specific case of the Mott transition, we will review some properties of the correlation functions, starting with the simple case of the correlation measurements in Optics. This choice is motivated by the importance that the field of Optics had on the development of the theory of correlations and its formalism. In fact, the quest for a quantum interpretation of the Hanbury Brown and Twiss (HBT) effect (which was fully understood in terms of classical optics as demonstrated in the first section of this chapter) is at the origin of the Glauber theory of the photodetection [66] and the explanation of the correlations between individual photons. This formalism has then enabled to derive numerous quantum effects such as the Hong-Ou-Mandel (HOM) effect [4], that could not have been explained using classical physics.

2.1 Introduction to correlation functions

2.1.1 The classical example of the light

First-order correlation

The notion of correlation and its relations to coherence first appeared in optics to describe the properties of the light sources. In optics, the term coherence refers to the tendency that two waves, generated by a source, and separated in time or space, to oscillate in phase, and thus to their possibility to interfere. The coherence of the source can be characterized by the first order correlation

function (auto-correlation of the field in time and/or space):

$$G^{(1)}(\vec{s_1}, t_1; \vec{s_2}, t_2) = \langle E^*(\vec{s_1}, t_1) E(\vec{s_2}, t_2) \rangle \tag{2.2}$$

and the normalized first-order correlation function:

$$g^{(1)}(\vec{s_1}, t_1; \vec{s_2}, t_2) = \frac{G^{(1)}(\vec{s_1}, t_1; \vec{s_2}, t_2)}{\langle E^*(\vec{s_1}, t_1) \rangle \langle E(\vec{s_2}, t_2) \rangle} \tag{2.3}$$

We can differentiate two cases:

- When $\vec{s_1} = \vec{s_2}$, that is to say in the case of a point-like source, $G^{(1)}(\vec{s_1}, t_1; \vec{s_2}, t_2)$ characterizes the temporal coherence of a source.
- When $t_1 = t_2$, $G^{(1)}(\vec{s_1}, t_1; \vec{s_2}, t_2)$ gives information on the spatial coherence of the source, that is to say on the relationship between the field emitted at different locations of an extended source.

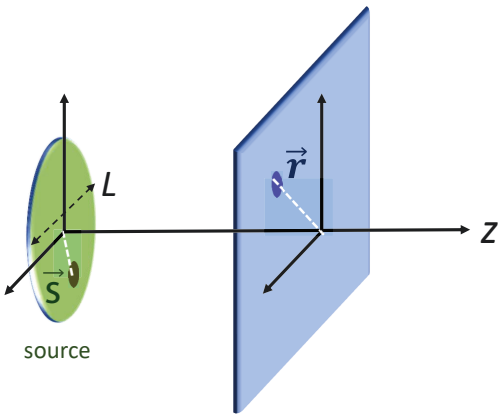

These correlations can be determined in the propagated field. If we consider a monochromatic source of spatial extension L. The amplitude of the field in the Fraunhofer regime ($z \gg L$) and within the paraxial approximation ($r_1 \ll z$) writes:

$$A(\vec{r_1}) = \int_{s_1 \in S} a(\vec{s_1}) e^{i \frac{2\pi}{\lambda z} . \vec{r_1} . \vec{s_1}} d\vec{s_1} \qquad \text{with} \qquad E(\vec{r}, t) = A(\vec{r}) e^{i\omega t} \tag{2.4}$$

and

$$G^{(1)}(\vec{r_1}, \vec{r_2}) = \langle A^*(\vec{r_1}) A(\vec{r_2}) \rangle = \int_{\vec{s_1} \in S} \int_{\vec{s_2} \in S} \langle a^*(\vec{s_1}) a(\vec{s_2}) \rangle \, e^{-i \frac{2\pi}{\lambda z} (\vec{r_1} . \vec{s_1} - \vec{r_2} . \vec{s_2})} d\vec{s_1} d\vec{s_2} \tag{2.5}$$

In the case of a spatially incoherent source, *i.e*, $\langle a^*(\vec{s_1}) a(\vec{s_2}) \rangle = I(\vec{s_1}) \delta(\vec{s_2} - \vec{s_1})$, this relation simplifies:

$$G^{(1)}(\vec{r_1}, \vec{r_2}) = \int_{\vec{s} \in S} I(\vec{s}) e^{-\frac{2\pi}{\lambda z} (\vec{r_1} - \vec{r_2}) . \vec{s}} d\vec{s} = FT[I(\vec{s})] \ (\delta \vec{k} = \frac{2\pi}{\lambda z} (\vec{r_1} - \vec{r_2})) \tag{2.6}$$

meaning that the first-order correlation function measured far away from the source is given by the Fourier transform (FT) of the source intensity distribution (Wiener-Khinchin theorem). $G^{(1)}(\vec{r_1}, \vec{r_2})$ consequently decreases over a distance $l_c^{'} \approx 1/L$. Note that there is an equivalent if considering a temporal incoherent source: $G^{(1)}(t_1, t_2) = FT[I(\omega)]$ where $I(\omega)$ is the spectral density of the source.

In both cases, the knowledge of $G^{(1)}(\vec{r_1}, \vec{r_2})$ allows for the measurement of some properties of the source. For instance, the measurement of the two-point amplitude correlation of a light coming from a distant star has been used in 1920 by Michelson to measure the diameter of the star while for the temporal case, the measurement of $G^{(1)}(t_1, t_2)$ is at the very principle of the Fourier-transform spectrometers.

As $G^{(1)}(\vec{r_1}, \vec{r_2})$ can not be measured directly with basic photodetectors, it is usually deduced using interference effects such as described in Fig. 2.1:

$$I(P) \propto \left\langle |A(\vec{r_1})|^2 \right\rangle + \left\langle |A(\vec{r_2}, t_1)|^2 \right\rangle + 2 \langle A^*(\vec{r_1}) A(\vec{r_2}) \rangle \times \cos \left(\frac{2\pi}{\lambda z'} \vec{X} . (\vec{r_1} - \vec{r_2}) \right) \tag{2.7}$$

With the visibility of the interference pattern $\mathcal{V} = \frac{I_{\max} - I_{\min}}{I_{\max} + I_{\min}}$ given by the normalized first-order correlation $g^{(1)}(\vec{r_1}, \vec{r_2})$.

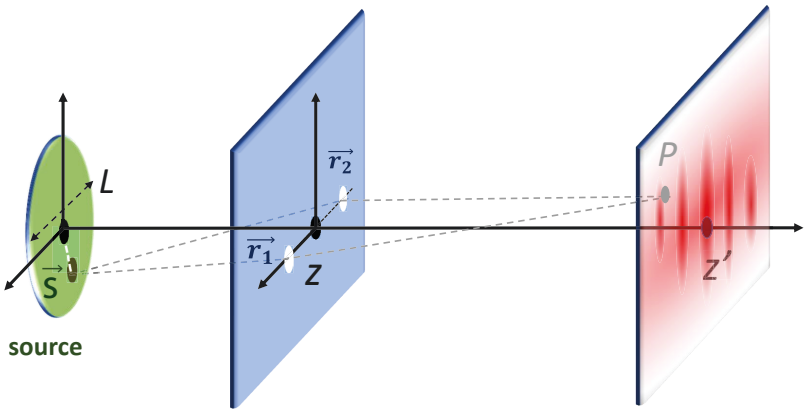

Figure 2.1: **Measurement of the first-order coherence using a double-slit experiment.**

Second-order correlation

But piece of information are also contained in higher-order correlations. That is the solution that Hanbury Brown and Twiss applied in order to circumvent the problem of sensitivity of the first-order coherence measurement to phase disturbances in 1956 [2]. Instead of measuring $G^{(1)}(\vec{r_1}, \vec{r_2})$, they looked at the intensity correlations at two photodetectors situated in $\vec{r_1}$ and $\vec{r_2}$, that is to say they measured the second-order correlation function:

$$G^{(2)}(\vec{r_1}, \vec{r_2}) = \langle A^*(\vec{r_1})A(\vec{r_1})A^*(\vec{r_2})A(\vec{r_2})\rangle = \langle I(\vec{r_1})I(\vec{r_2})\rangle \tag{2.8}$$

$$g^{(2)}(\vec{r_1}, \vec{r_2}) = \frac{\langle I(\vec{r_1})I(\vec{r_2})\rangle}{\langle I(\vec{r_1})\rangle \langle I(\vec{r_2})\rangle} \tag{2.9}$$

In the case of a spatially incoherent source, the amplitudes of the field in $\vec{r_1}$ and $\vec{r_2}$ are given by the sum of the field emitted by the different elementary emitters. These sources are fluctuating independently but with the same statistics. As a consequence of the central limit theorem, the field in $\vec{r_1}$ and $\vec{r_2}$ is fluctuating with a gaussian statistics and one can show that [67]:

$$\langle I(\vec{r_1})I(\vec{r_2})\rangle = \langle I(\vec{r_1})\rangle \langle I(\vec{r_2})\rangle + \langle A^*(\vec{r_1})A(\vec{r_2})\rangle \langle A^*(\vec{r_2})A(\vec{r_1})\rangle \tag{2.10}$$

which leads to:

$$\begin{aligned} g^{(2)}(\vec{r_1}, \vec{r_2}) = 1 + \left|g^{(1)}(\vec{r_1}, \vec{r_2})\right|^2 &= 2 \quad \text{for} \quad |\vec{r_1} = \vec{r_2}| \\ &\geq 1 \quad \text{for} \quad |\vec{r_1} - \vec{r_2}| \lesssim l_c \\ &= 1 \quad \text{for} \quad |\vec{r_1} - \vec{r_2}| \gg l_c \end{aligned} \tag{2.11}$$

with $l_c = l_c'/\sqrt{2}$ the typical decay length of the $g^{(2)}$ function. In the case of an incoherent source, the second-order correlation writes as a function of the first-order correlation function.

In fact, the normalized second-order correlation function $g^{(2)}(\vec{r_1}, \vec{r_2})$ can be seen as an indicator of the probability to measure a photon in $\vec{r_2}$ considering there is one in $\vec{r_1}$ and normalized by the probability corresponding to the case where the two events are independent. The results of Eq. 2.11 implies that the probability to find two photons close together ($\vec{r_1} \to \vec{r_2}$) is higher than finding two bosons separated apart ($\vec{r_1} - \vec{r_2} \to \infty$). The bosons group together! The properties that $g^{(2)}(\vec{r_1}, \vec{r_2}) > 1$ refers to as the bosonic bunching. This effect comes entirely from the quantum statistics, and in this case, the bosonic statistics. For instance, if we repeat the same experiment using fermionic particles instead of bosonic ones, we would have found $g^{(2)} < 1$, which can not be derived using a classical treatment to solve the problem. To extend the notion of coherence to different other systems, a quantum treatment is necessary [66].

2.1.2 From the classical to the quantum description

The quantum treatment of the light describes radiations in terms of photon mode occupation. These modes appear when developing on the plane waves basis (the plane waves are characterized by their frequency and polarization) the light field. Under this formalism, one can write any light field [68]:

$$\hat{\vec{E}}(\vec{r},t) = \sum_l i\vec{\epsilon}_l \mathcal{E}_l \left[e^{i\vec{k}_l.\vec{r}}\hat{a}_l - e^{-i\vec{k}_l.\vec{r}}\hat{a}_l^\dagger \right] e^{-i\omega_l t} = \hat{\vec{E}}^{(+)}(\vec{r},t) + \hat{\vec{E}}^{(-)}(\vec{r},t) \tag{2.12}$$

with $\hat{a}_l$ and $\hat{a}_l^\dagger$ the annihilation and creation operators of a photon in the mode l. They satisfies the usual commutation relations:

$$\left[\hat{a}_l, \hat{a}_{l'}^\dagger\right] = \delta_{ll'} \qquad [\hat{a}_{l'}, \hat{a}_l] = 0 \tag{2.13}$$

The Hamiltonian then writes:

$$\hat{\mathcal{H}}_{\text{light}} = \sum_l \hbar\omega_l \left(\hat{n}_l + \frac{1}{2}\right) \tag{2.14}$$

with $\hat{n}_l = \hat{a}_l^\dagger \hat{a}_l$ the number operator (the energy of the system is the sum of the energy of a photon times the number of photons in each mode.)

If we apply this formalism to the example of Fig. 2.1 considering a single mode radiation, the probability to measure a photon in $\vec{r_1}$ and a photon in $\vec{r_2}$ simultaneously writes:

$$P\left(\vec{r_1},\vec{r_2}\right) = \|\hat{a}(\vec{r_2})\hat{a}(\vec{r_1})\,|\psi\rangle\,\|^2 = \left\langle \psi|\hat{a}^\dagger(\vec{r_1})\hat{a}^\dagger(\vec{r_2})\hat{a}(\vec{r_2})\hat{a}(\vec{r_1})|\psi\right\rangle = \left\langle \hat{a}^\dagger(\vec{r_1})\hat{a}^\dagger(\vec{r_2})\hat{a}(\vec{r_2})\hat{a}(\vec{r_1})\right\rangle \tag{2.15}$$

where $|\psi\rangle$ is the incoming light field.

The quantum analog of the classical second-order correlation function writes:

$$G^{(2)}(\vec{r_1},t_1;\vec{r_2},t_2) = \left\langle \hat{a}^\dagger(\vec{r_1},t_1)\hat{a}^\dagger(\vec{r_2},t_2)\hat{a}(\vec{r_2},t_2)\hat{a}(\vec{r_1},t_1)\right\rangle \tag{2.16}$$

$$g^{(2)}(\vec{r_1},t_1;\vec{r_2},t_2) = \frac{G^{(2)}(\vec{r_1},t_1;\vec{r_2},t_2)}{\rho(\vec{r_1},t_1)\rho(\vec{r_2},t_2)} \tag{2.17}$$

where $\rho(\vec{r_1},t_1) = \left\langle \hat{a}^\dagger(\vec{r_1},t_1)\hat{a}(\vec{r_1},t_1)\right\rangle$ is the photon density. This definition can be generalized to any order.

Remark: One needs to pay attention to the order of the creation and annhilation operators for the definition of the correlation functions. In quantum mechanics, the detection of a photon in a certain mode corresponds to its annihilation by the detector (Glauber theory [66]). The correlation functions have consequently to be written with the normal order, *i.e*, with the creation operators on the left and the annihilation operators on the right as shown in Eq. 2.16.

In the case of the detection of the two photons, for $\vec{r_1} = \vec{r_2}$, $\hat{a}^\dagger(\vec{r_1}) = \hat{a}^\dagger(\vec{r_2}) = \hat{a}^\dagger$.

$$\begin{aligned} g^{(2)}(\vec{r_1} = \vec{r_2}) = \frac{\left\langle \hat{a}^\dagger\hat{a}^\dagger\hat{a}\hat{a}\right\rangle}{\left\langle \hat{a}^\dagger\hat{a}\right\rangle^2} &= \frac{\left\langle \hat{a}^\dagger\hat{a}\right\rangle^2 + \left\langle (\hat{a}^\dagger\hat{a})^2\right\rangle - \left\langle \hat{a}^\dagger\hat{a}\right\rangle^2 - \left\langle \hat{a}^\dagger\hat{a}\right\rangle}{\left\langle \hat{a}^\dagger\hat{a}\right\rangle^2} \\ &= 1 + \frac{\sigma_{\overline{N}}^2 - \overline{N}}{\overline{N}^2} \end{aligned} \tag{2.18}$$

where $\overline{N} = \left\langle \hat{a}^\dagger\hat{a}\right\rangle$ is the average number of photons and σ_N its variance. The bunching amplitude consequently depends on the atom number fluctuations of the source trough $\sigma_{\overline{N}}$.

One can consider different examples:

- *Thermal light:* The probability distribution of photon numbers is given by a Bose-Einstein distribution resulting in $\sigma_{\overline{N}} = \overline{N}^2 + \overline{N}$ [69] and leading to $g^{(2)}(0) = 2$.

- *Coherent light:* This is the case of the classical sources such as lasers. The probability distribution is a Poisson distribution characterized by $\sigma_{\overline{N}} = \overline{N}$ and $g^{(2)}(0) = 1$.

- *Fock states:* Fock states are number states, resulting in $\sigma_{\overline{N}} = 0$ and $g^{(2)}(0) = 1 - 1/\overline{N}$. They anti-bunch! This is an example of a non-classical state in the sense that it would not have been possible to obtain $g^{(2)}(0) < 1$ with a classical description of the light.

2.1.3 Correlation functions

The definition of the correlation functions can be generalized to higher orders $n \in \mathbb{N}$ and $n > 1$[1]:

$$G^{(n)}(\vec{r_1}, t_1; ...; \vec{r_n}, t_n) = \left\langle \hat{a}^\dagger(\vec{r_1}, t_1)....\hat{a}^\dagger(\vec{r_n}, t_n)\hat{a}(\vec{r_n}, t_n)....\hat{a}(\vec{r_1}, t_1) \right\rangle \tag{2.19}$$

$$g^{(n)}(\vec{r_1}, t_1; ...; \vec{r_n}, t_n) = \frac{G^{(n)}(\vec{r_1}, t_1; ...; \vec{r_n}, t_n)}{\prod_{j=1}^{n} G^{(1)}(\vec{r_1}, t_1; \vec{r_1}, t_1)} \tag{2.20}$$

For $n = 1$ we define:

$$G^{(1)}(\vec{r_1}, t_1; \vec{r_2}, t_2) = \left\langle \hat{a}^\dagger(\vec{r_1}, t_1)\hat{a}(\vec{r_2}, t_2) \right\rangle \tag{2.21}$$

$$g^{(1)}(\vec{r_1}, t_1; \vec{r_2}, t_2) = \frac{G^{(1)}(\vec{r_1}, t_1; \vec{r_2}, t_2)}{\{n(\vec{r_1}, t_1)n(\vec{r_2}, t_2)\}^{1/2}} \tag{2.22}$$

The correlation functions verify the following properties:

- Similarly to the classical case, $|g^{(1)}(\vec{r_1}, t_1; \vec{r_2}, t_2)| \leq 1$.

- The only state verifying $|g^{(n)}(\vec{r_1}, t_1; ...; \vec{r_n}, t_n)| = 1 \ \forall n$ is a coherent state. This serves as a definition of a fully coherent field.

- In some specific cases, it is possible to decompose the correlation functions at order $n > 1$ as a polynomial sum of the first-order correlation function $g^{(1)}$. That is for instance what we found calculating the intensity correlation between two spatially incoherent sources in Eq. 2.11. This is called the **Wick theorem**.

Remark: We have considered here implicitly the case where the system is in a pure state $\mid \Psi\rangle$. However, the information about a system can be limited to the knowledge of the statistical distribution of the different states, *i.e*, when the system is in a mixed state. It is for instance the case of an ensemble of thermal particles. Then, it is more convenient to use the formalism of the density matrix which allows to calculate the expectation values of operators whatever the initial state of the system. The correlation functions can then be computed using the definition of the statistical average of any operators $\hat{O}$ within the density matrix formalism:

$$\left\langle \hat{O} \right\rangle = Tr\left\{ \hat{\rho}\hat{O} \right\} \tag{2.23}$$

2.1.4 Wick's theorem

The Wick theorem can be easily understood considering its classical version, which is in this case, a pure classical statistical effect. In fact, if we consider u_1,...,u_{2n} N gaussian random variables (*i.e*, with a probability distribution given by a gaussian function), then the N-order moments $\langle u_1...u_{2n}\rangle$ can be written [70] as a function of all the combinations of second order moments (here $\langle\rangle$ refers to a

[1] In general, one can define the n^{th} correlation order $G^{(n)}(\vec{r_1}, t_1; ...; \vec{r_n}, t_n; \vec{r_{n+1}}, t_{n+1}; ...; \vec{r_{2n}}, t_{2n})$ where the indices of the annihilation operators are different from the creation operators. In the experiment, the only measurable correlation functions are the one given in the text.

statistical average):

$$\langle u_1 ... u_{2n} \rangle = \sum_P \langle u_j u_i \rangle \langle ... \rangle \langle u_m u_k \rangle \tag{2.24}$$

where $\sum_P$ refers to the summation over all possible distinct grouping of the $2n$ variables in pairs.

The Wick theorem:

When considering a system characterized by a gaussian density matrix, that is to say when $\hat{\rho} \propto exp\left(-\sum_\alpha \gamma_\alpha \hat{a}_\alpha^\dagger \hat{a}_\alpha\right)$*, then high-order products of creation and annihilation operators can be factorized into all possible products of only two operators* [71].

This theorem was demonstrated by G.Wick in 1950 in a different context [72]. Its demonstration is beyond reach of this manuscript. However, a simplified approach by Gaudin in the case of thermal systems (that is to say for the case where the density operator is given by the Boltzmann distribution) is given in [73].

In mathematical terms, this means that provided the applicability of the theorem:

$$\left\langle \hat{\Psi}_1 ... \hat{\Psi}_{2n} \right\rangle = \left\langle \hat{\Psi}_1 ... \hat{\Psi}_2 \right\rangle \left\langle \hat{\Psi}_3 ... \hat{\Psi}_4 \right\rangle ... \left\langle \hat{\Psi}_{2n-1} ... \hat{\Psi}_{2n} \right\rangle + \text{permutations} \tag{2.25}$$

where the $\hat{\Psi}_i$ are equal to one of the annihilation operators $\hat{a}_i$.

Applied to the normalized correlation functions $g^{(n)}(\vec{r_1}, t_1; ...; \vec{r_n}, t_n)$ defined in the former section, one finds:

$$g^{(n)}(\vec{r_1}, t_1; ...; \vec{r_n}, t_n) = \frac{\prod_{i,j} G^{(1)}(\vec{r_i}, t_i; \vec{r_j}, t_j)}{\prod_i n(\vec{r_i}, t_i)^{1/2}} \tag{2.26}$$

and considering that $G^{(1)}(\vec{r_i} = \vec{r_j}, t_i = t_j) = n(\vec{r_i}, t_i)$, we find that: for $\vec{r_1} = \vec{r_2} ... = \vec{r_n}$ and $t_1 = t_2 ... t_n$:

$$\begin{aligned} &g^{(n)} = n! \quad \text{for} \quad \vec{r_1} = \vec{r_2} ... = \vec{r_n} \quad \text{and} \quad t_1 = t_2 ... t_n \\ &g^{(n)} < n! \quad \text{In the other cases (Cauchy-Schwartz inequality)} \end{aligned} \tag{2.27}$$

This effect is called the bunching in the sense that the probability that the particles are detected in the same mode (here temporal and spatial modes) is higher than the product of the independent probabilities.

Applicability of the theorem

Since a gaussian density matrix has the non diagonal elements null, a pre-requisite for the Wick's theorem to apply is the absence of coherence between the states associated to the creation and the annihilation operators. Note that this statement is dependent of the choice of the basis where the operators are written: a density matrix can be diagonal in a specific basis and not in another one.

- In the case of a thermal ensemble, the density matrix ρ_T is given by the Boltzmann distribution:

$$\rho_T = \frac{e^{-\beta \mathcal{H}_0}}{Tr\left\{e^{-\beta \mathcal{H}_0}\right\}} \tag{2.28}$$

  where $\mathcal{H}_0 = \sum_j \hbar \omega_j \hat{a}_j^\dagger \hat{a}_j$. The density matrix is consequently gaussian in the degrees of freedom associated to $\{\hat{a}_i\}$ and the Wick theorem applies. One finds:

$$g^{(2)}(\vec{r_1}, t_1; \vec{r_2}, t_2) = 1 + |g^{(1)}(\vec{r_1}, t_1; \vec{r_2}, t_2)|^2 \tag{2.29}$$

  that is to say the same result as found in Eq. 2.11 and obtained with a classical treatment.

- If the state of the system is a coherent state $|\alpha\rangle$:

$$\hat{\rho}_{coh} = |\alpha\rangle \langle\alpha| \propto \sum_n \sum_m \frac{\alpha^n \alpha^{*m}}{\sqrt{n!m!}} |n\rangle \langle m| \tag{2.30}$$

  and is consequently not gaussian, so the Wick's theorem does not apply. This is for instance the case for the laser light.

One important conclusion of this paragraph is that under the applicability of the Wick theorem, all the information is encoded in the first-order correlation function but strong correlations associated to statistics appear and give rise to $g^{(2)}(\vec{r_1} = \vec{r_1}; t_1 = t_2) = 2$ (bosonic bunching).

Contrary to the case of the light field, the case of bosonic (matter) particles is more complex in the sense that the particles can interact. The interactions are at the origin of strong correlations between the particles, and of different origin than the pure statistical one we have mentioned so far.

2.2 Correlation measurements in the context of the lattice gases

In this section, we are investigating the correlation functions related to systems described by the Bose-Hubbard Hamiltonian. For the purpose of clarity, we define:

- $C^{(1)}(i,j) = \left\langle \hat{b}_i^\dagger \hat{b}_j \right\rangle$ the first-order correlation function in the position-space. We remind that $\hat{b}_j^\dagger$ is the creation operator associated to adding a particle in the lattice site labeled by j. The normalized corresponding correlation function is: $c^{(1)}(i,j)$. Note that this correlation function is discrete since it is defined only at the position of the lattice sites.
- $G^{(1)}(\vec{k},\vec{k'}) = \left\langle \hat{a}^\dagger(\vec{k})\hat{a}(\vec{k'}) \right\rangle$ refers to the first-order momentum-space correlation function with $\hat{a}^\dagger(\vec{k})$ the creation operator of a particle with a momentum $\vec{k}$.

The annihilation operator $\hat{a}(\vec{k})$ is linked to $\hat{b}_j$ by the formula (V refers to the volume of quantization):

$$\hat{a}(\vec{k}) = \frac{1}{\sqrt{V}} \sum_j e^{-i\vec{k}.\vec{r_j}} \hat{b}_j \tag{2.31}$$

In the experiment, as it will be developed in the next chapter, we access the momentum distribution of the lattice gases with a single atom sensitivity. We can thus measure directly:

- The momentum density:
$$\rho(\vec{k}) = \left\langle \hat{a}^\dagger(\vec{k})\hat{a}(\vec{k}) \right\rangle$$
- The high-order correlation functions $G^{(n)}(\vec{k_1};...;\vec{k_n})$ with $n \geqslant 2$. More precisely, in this manuscript, we only consider the second and third-order correlations:
$$G^{(2)}(\vec{k_1},\vec{k_2}) = \left\langle \hat{a}^\dagger(\vec{k_1})\hat{a}^\dagger(\vec{k_2})\hat{a}(\vec{k_1})\hat{a}(\vec{k_2}) \right\rangle$$
$$G^{(3)}(\vec{k_1},\vec{k_2},,\vec{k_3}) = \left\langle \hat{a}^\dagger(\vec{k_1})\hat{a}^\dagger(\vec{k_2})\hat{a}^\dagger(\vec{k_3})\hat{a}(\vec{k_3})\hat{a}(\vec{k_2})\hat{a}(\vec{k_1}) \right\rangle$$

Remark.
One needs to pay attention to the difference between the correlation functions of order n, $G^{(n)}$, and the density-density correlations of the same order:

$$G^{(n)}_{\text{dens-dens}}(\vec{k_1},...,\vec{k_n}) = \left\langle \hat{\rho}(\vec{k_1})...\hat{\rho}(\vec{k_2}) \right\rangle = \left\langle \hat{a}^\dagger(\vec{k_1})\hat{a}(\vec{k_1})...\hat{a}^\dagger(\vec{k_n})\hat{a}(\vec{k_n}) \right\rangle \tag{2.32}$$

$G^{(n)}$ and $G^{(n)}_{\text{dens-dens}}$ only differ by the auto-correlation terms of the form $\left\langle \hat{a}^\dagger(\vec{k_1})\hat{a}(\vec{k_2}) \right\rangle \delta(\vec{k_2} - \vec{k_1})$.
Experiments that access only the momentum-space densities measure $G^{(n)}_{\text{dens-dens}}$. As we will in §.3, our detection scheme is analog to the single photon detection mentioned earlier: the detection of a metastable atom corresponds to its destruction (in the sense that the atom is not in the metastable state anymore.). The correlation function measured in the experiment are consequently, according to the Glauber theory, the correlation functions $G^{(n)}$ written with the normal order.

2.2.1 Periodicity of the correlation functions

Because of Eq. 2.31, the operators $\hat{a}(\vec{k})$ are periodic with a periodicity given by the reciprocal lattice defined by the vectors $\vec{K} = k_d \times (n_x\vec{u}_x + n_y\vec{u}_y + n_z\vec{u}_z)$ where $(n_x;n_y;n_z) \in \mathbb{Z}^3$ and $(\vec{u}_x,\vec{u}_y,\vec{u}_z)$ are the 3 directions of the optical lattice. As a result, all the correlation functions are periodic with the periodicity of the reciprocal lattice and one can limit their investigation to the first Brillouin zone (that is to say in the quasi-momentum basis).

In the two next sections, we will treat the case of an infinite and homogeneous system. The effect of the finite size as well as the shape of the real in-situ density distribution will be discussed in the last paragraph.

2.2.2 First-order correlation

Following Eq. 2.31, the first order correlation $G^{(1)}(\vec{k_1},\vec{k_2}) = \left\langle \hat{a}^\dagger(\vec{k}_1)\hat{a}(\vec{k}_2)\right\rangle$ writes:

$$G^{(1)}(\vec{k_1},\vec{k_2}) = \left\langle \hat{a}^\dagger(\vec{k}_1)\hat{a}(\vec{k}_2)\right\rangle = \frac{1}{V}\sum_{j,i} e^{-i(\vec{k}_2.\vec{r}_j-\vec{k}_1.\vec{r}_i)}\left\langle \hat{b}_i^\dagger\hat{b}_j\right\rangle = \frac{1}{V}\sum_{j,i} e^{-i(\vec{k}_2.\vec{r}_j-\vec{k}_1.\vec{r}_i)}C^{(1)}(i,j) \quad (2.33)$$

In the experiment, one can not measure directly the first-order correlation $G^{(1)}(\vec{k_1},\vec{k_2})$ (besides the density). However, the measurement of the density distribution gives information about the spatial first-order correlation in the lattice potential through:

$$\boxed{\rho(\vec{k}) = \left\langle \hat{a}^\dagger(\vec{k})\hat{a}(\vec{k})\right\rangle = \frac{1}{V}\sum_{j,i} e^{-i\vec{k}.(\vec{r}_j-\vec{r}_i)}\left\langle \hat{b}_i^\dagger\hat{b}_j\right\rangle = \frac{1}{V}\sum_{j,i} e^{-i\vec{k}.(\vec{r}_j-\vec{r}_i)}C^{(1)}(i,j)} \quad (2.34)$$

In the case of an homogeneous system with an average filling $\bar{n}$, we saw in §1.2.2:

$$\begin{aligned} C^{(1)}(i,j) &= \bar{n} \qquad \text{for a lattice superfluid in the limit } U/J \to 0 \\ &= \delta_{i,j}\bar{n} \qquad \text{for a Mott insulator in the limit } U/J \to \infty \end{aligned} \quad (2.35)$$

As a results:

$$\begin{aligned} G^{(1)}(\vec{k_1},\vec{k_2}) &= \frac{\bar{n}}{V}\delta(\vec{k}_1)\delta(\vec{k}_1) \qquad \rho(\vec{k}) = \frac{\bar{n}}{V}\times\delta(\vec{k}) \qquad \text{for } U/J \to 0 \\ G^{(1)}(\vec{k_1},\vec{k_2}) &= \frac{\bar{n}}{V}\delta(\vec{k}_1-\vec{k}_2) \qquad \rho(\vec{k}) = \frac{\bar{n}}{V} \qquad \text{for } U/J \to \infty \end{aligned} \quad (2.36)$$

The situation described here is completely analog with the diffraction of a light through a grating. If the initial state is fully spatially coherent, the momentum distribution displays sharp peaks located at the reciprocal lattice nodes $\vec{K} = k_d \times (n_x\vec{u}_x + n_y\vec{u}_y + n_z\vec{u}_z)$. These peaks are absent if the source is incoherent. Like in optics, the coherence of the lattice gas can be determined by looking at the contrast of the momentum peaks.

This is one of the signals that M.Greiner and colleagues [10] used to demonstrate the first experimental realization of the Mott transition with cold atoms in 2002 (see Fig. 2.2). On the images, one can identify the two regimes discussed: for low values of U/J (graph b), the momentum distribution has a periodic structure characterized by sharp peaks while at high U/J, the peaks are not visible anymore (graph h). All the distributions here are modulated by a large function because in experiment, as it will be derived in §.3.3, we are measuring $\tilde{\rho}(\vec{k}) = \rho(\vec{k}) \times |\tilde{\omega}(\vec{k})|^2$. Since the Wannier functions are always present as a multiplying factor in front of all the correlation functions, they disappear with the normalization. Furthermore, they do not contain any physical information so we choose not to include them in the definition of the correlation functions.

Quantum depletion in the SF phase

To go beyond these two limiting cases, one can concentrate on the evolution of the momentum distribution for increasing U/J in the superfluid phase. One can identify in graphs from b) to f) different contributions to the momentum distribution:

- The *condensed atoms* are the atoms that are in the single-particle lowest energy mode of the lattice system, that is to say atoms in the Bloch wave with a quasi-momentum $q = 0$. They represent the coherent part of the system and are at the origin of the sharp momentum peaks.
- The *depletion* which represents the atoms that occupy higher quasi-momentum states due to the finite temperature of the lattice gas or the interactions. They represent the wide background present below the sharp peaks and are at the origin of the decrease of the peaks contrast. The characteristics of the depletion far from the transition can be derived using the Bogoliubov theory, already mentioned in §.1.2.3.

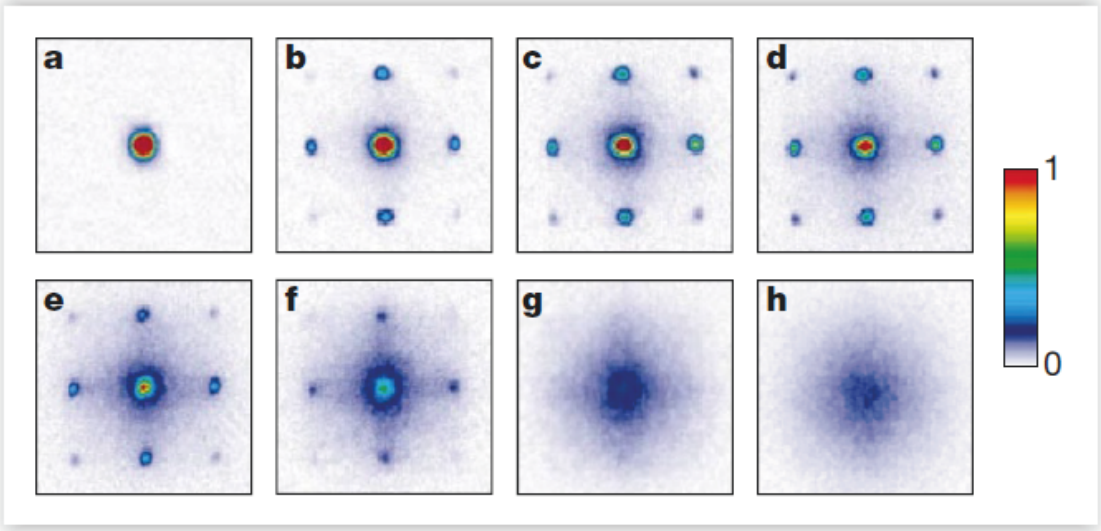

Figure 2.2: **Evolution of the momentum distribution across the Mott transition**. Measured momentum distribution obtained with Rb atoms loaded into the fundamental band of a 3D optical lattice. The different images correspond to different lattice amplitudes and are obtained by optical imaging. The momentum distribution evolves from a pattern with very sharp peaks situated at the reciprocal lattice nodes deep in the SF phase to a wide monotonic distribution in the MI phase. **a)** $s = 0$. **b)** $s = 3$. **c)** $s = 7$. **d)** $s = 10$. **e)** $s = 13$. **f)** $s = 14$ **g)** $s = 16$. **h)** $s = 20$. Data extracted from [10].

More precisely, one can evaluate the modification of the first-order correlation function using the Bogoliubov transformation given in Eq. 1.32 in the quasi-momentum basis.
If we assume that the quasi-particle operators are statistically independent, that is to say $\left\langle \hat{\beta}^\dagger_{\vec{k}_1} \hat{\beta}_{\vec{k}_2} \right\rangle = \delta_{\vec{k}_1,\vec{k}_2} \rho_{qp}(\vec{k}_1)$ with $\rho_{qp}(\vec{k}_1) = 1/\left(e^{\hbar\omega_k/k_BT} - 1\right)$ the density of quasi-particles:

$$\begin{aligned}\left\langle \hat{a}^\dagger(\vec{k}_1)\hat{a}(\vec{k}_2)\right\rangle_{BB} &= \left\langle \left(u_{\vec{k}_1}\hat{\beta}^\dagger_{\vec{k}_1} - v_{\vec{k}_1}\hat{\beta}_{-\vec{k}_1}\right)\left(u_{\vec{k}_2}\hat{\beta}_{\vec{k}_2} - v_{\vec{k}_2}\hat{\beta}^\dagger_{-\vec{k}_2}\right)\right\rangle + \delta_{\vec{k}_1=\vec{k}_2=0}\left\langle \hat{a}^\dagger(k_1=0)\hat{a}(k_1=0)\right\rangle \\ &= \delta_{\vec{k}_1=\vec{k}_2} u^2_{\vec{k}_1}\rho_{qp}(\vec{k}_1) + \delta_{\vec{k}_1=\vec{k}_2} v^2_{\vec{k}_1}\left[1+\rho_{qp}(\vec{k}_1)\right] + N_{BEC}\,\delta_{\vec{k}_1=\vec{k}_2=0}\end{aligned} \tag{2.37}$$

where N_{BEC} refers to the number of atoms in the ground state.
As a result:

$$G^{(1)}_{BB}(\vec{k_1},\vec{k_2}) = \delta_{\vec{k}_1=\vec{k}_2}\left[v^2_{\vec{k}_1} + u^2_{\vec{k}_1}\right]\rho_{qp}(\vec{k}_1) + \delta_{\vec{k}_1=\vec{k}_2} v^2_{\vec{k}_1} + N_{BEC}\delta_{\vec{k}_1=\vec{k}_2=0} \tag{2.38}$$

and

$$\boxed{\rho_{BB}(\vec{k}) = \underbrace{\left[v^2_{\vec{k}} + u^2_{\vec{k}}\right]\rho_{qp}(\vec{k}_1)}_{\text{Thermal depletion}} + \underbrace{v^2_{\vec{k}}}_{\text{Quantum depletion}} + N_{BEC}\,\delta(\vec{k})} \tag{2.39}$$

where the expressions of $u_{\vec{k}}$ and $v_{\vec{k}}$ can be found in §.1.2.3. These functions are decreasing with k and extend over the whole BZ. They are consequently responsible for the presence of the high momentum component visible on the momentum distributions displayed in Fig. 2.2. Because of the temperature, or the interactions, the number of atoms in the condensate decreases to fill higher momentum states: these effects are respectively referred to as the quantum and the thermal depletion (with the different contributions indicated in Eq.2.39). To characterize the depletion, one can use the condensate fraction f_c which corresponds to the ratio between the number of atoms in the condensate compared to the total number of atoms:

$$f_c = \frac{N_{BEC}}{N} \tag{2.40}$$

As the amplitudes of $u_{\vec{k}}$ and $v_{\vec{k}}$ are increasing when getting close to the transition (Careful, the Bogoliubov theory is only valid far from the transition), the condensate fraction decreases and goes to zero at the transition point for homogeneous and infinite systems (this comes from the fact that the condensate fraction is proportional to the modulus of the order parameter ψ).

Particle-hole excitations in the Mott insulator phase

Starting from the perfect Mott insulator ($J = 0$) at $T = 0$ and reintroducing some tunnelling (see graph g), the momentum distribution gets periodically modulated (this effect should be visible by removing the Wannier contribution to the distribution). This is an effect of particle-hole excitations appearing in the Mott phase for a finite tunneling J and already discussed in §1.2.3. At the first-order in the perturbation theory, the ground state of the system writes:

$$\left|\Psi^{(1)}\right\rangle = |\Psi\rangle_{MI} + \frac{J}{U}\sum_{<i,j>} \hat{b}_i^\dagger \hat{b}_j \,|\Psi\rangle_{MI} \tag{2.41}$$

Introducing this expression in Eq. 2.34:

$$\rho_{PH}(\vec{k}) = \rho_{MI}(\vec{k}) + \sum_{<j,i>} e^{-i\vec{k}.(\vec{r}_j - \vec{r}_i)} \times \frac{2J}{U} n_i \,(n_j + 1) \tag{2.42}$$

with the summation that is limited to neighboring sites.
This generalizes in 3D and one finds:

$$\boxed{\rho_{PH}(\vec{k}) = \rho_{MI}(\vec{k}) \left[1 - 2(n_0 + 1)\frac{E(\vec{k})}{U}\right]} \tag{2.43}$$

with $E(\vec{k}) = -2J\sum_{i=x,y,z} \cos(k_i\, d)$ the single particle dispersion relation (within the tight-binding approximation).

When a finite tunnelling is present in the Mott insulator, some short-range first-order coherence is restored. At the first-order in the perturbation theory, that is too say when $J/U \ll 1$, the coherence extends over neighboring sites, and is at the origin of the periodic modulation of the momentum distribution on top of the flat distribution of the perfect Mott insulator. This effect has already been seen in some experiments [74, 34], but only investigated in the high U/J limit and in 3D through indirect signals like the visibility of the interference pattern [75]. In §.5, we investigate the momentum distribution of a Mott insulator on approaching the transition. In this regime, beyond first-order perturbation approaches are available to take into account the delocalization of particle-holes over increasing distances.

2.2.3 Higher-order correlation functions

Correlation in the SF phase

Non interacting systems

First, we consider the case where $U = 0$, that is to say the case of an ideal gas trapped into the optical lattice. We saw in §.1 that the Hamiltonian of the system reduces to the kinetic part (in the absence of the external trapping potential) and is diagonal in the quasi-momentum basis:

$$\hat{\mathcal{H}} = \hat{\mathcal{H}}_{\text{band}} = \sum_{\vec{k}} E(\vec{k})\hat{a}^\dagger(\vec{k})\hat{a}(\vec{k}) \tag{2.44}$$

with $E(\vec{k})$ given by the band structure.

In this situation, one can distinguish two cases:

- **At $T = 0$** only the quasi-momentum $\vec{k} = 0$ is populated. We saw in §.1.2.2 that the state of the system can be approximated in the thermodynamic limit as a product of on-site coherent state. Because of that,

$$\boxed{g^{(n)}_{SF}(\vec{k}_1, \vec{k}_2) = 1 \qquad \forall n \in \mathbb{N}} \tag{2.45}$$

- **When $k_B T \gtrsim 4J$** (when the temperature is of the order of the lowest-energy band width), then a lot of quasi-momentum modes are populated thermally, that is to say that the density operator is given by the gaussian Boltzmann distribution $\hat{\rho} \propto e^{-\beta \hat{\mathcal{H}}_{\text{band}}}$. In this case, the Wick theorem applies. As a consequence, the high-order correlation functions can be written as a sum of all the combinations of first-order correlation functions. For instance, the expression of $g^{(2)}_{th}$ and $g^{(3)}_{th}$ are:

$$\boxed{g^{(2)}_{th}(\vec{k}_1, \vec{k}_2) = 1 + \left| g^{(1)}_{th}(\vec{k}_1, \vec{k}_2) \right|^2} \tag{2.46}$$

$$\boxed{\begin{aligned} g^{(3)}_{th}(\vec{k}_1, \vec{k}_2, \vec{k}_3) = 1 &+ \left| g^{(1)}_{th}(\vec{k}_1, \vec{k}_2) \right|^2 + \left| g^{(1)}_{th}(\vec{k}_1, \vec{k}_3) \right|^2 + \left| g^{(1)}_{th}(\vec{k}_2, \vec{k}_3) \right|^2 \\ &+ 2\mathcal{R}\left\{ g^{(1)}_{th}(\vec{k}_1, \vec{k}_2)\, g^{(1)}_{th}(\vec{k}_1, \vec{k}_3)\, g^{(1)}_{th}(\vec{k}_2, \vec{k}_3) \right\} \end{aligned}} \tag{2.47}$$

with the remarkable values:

$$g^{(2)}_{th}(\vec{k}_1 = \vec{k}_2) = 2! = 2 \qquad g^{(3)}_{th}(\vec{k}_1 = \vec{k}_2 = \vec{k}_3) = 3! = 6 \tag{2.48}$$

Interacting system within the Bogoliubov theory

Within the Bogoliubov approximation, the Hamiltonian of the system is diagonal and quadratic in the quasi-particle operator basis and the modes are supposed to be statistically independant. As a result, the Wick theorem applies (in the quasi-particle basis). To compute the expression of the second-order correlation function $G^{(2)}_{BB}(\vec{k_1}, \vec{k_2}) = \left\langle \hat{a}^\dagger(\vec{k}_1)\hat{a}^\dagger(\vec{k}_2)\hat{a}(\vec{k}_1)\hat{a}(\vec{k}_2) \right\rangle$ within the Bogoliubov approximation, one needs to develop this expression on the quasi-particle operators basis as done for the first-order correlation function in §2.2.2. For $\vec{k}_1 \neq 0$ and $\vec{k}_2 \neq 0$, there are 6 terms non null:

$$\begin{aligned} G^{(2)}_{BB}(\vec{k_1}, \vec{k_2}) = &\, u^2_{\vec{k}_1} u^2_{\vec{k}_2} \left\langle \hat{\beta}^\dagger_{\vec{k}_1} \hat{\beta}^\dagger_{\vec{k}_2} \hat{\beta}_{\vec{k}_1} \hat{\beta}_{\vec{k}_2} \right\rangle \\ &+ u^2_{\vec{k}_1} v^2_{\vec{k}_2} \left\langle \hat{\beta}^\dagger_{\vec{k}_1} \hat{\beta}_{-\vec{k}_2} \hat{\beta}_{\vec{k}_1} \hat{\beta}^\dagger_{-\vec{k}_2} \right\rangle \\ &+ u_{\vec{k}_1} v_{\vec{k}_2} u_{\vec{k}_2} v_{\vec{k}_1} \left\langle \hat{\beta}^\dagger_{\vec{k}_1} \hat{\beta}_{-\vec{k}_2} \hat{\beta}^\dagger_{-\vec{k}_1} \hat{\beta}_{\vec{k}_2} \right\rangle \\ &+ u_{\vec{k}_1} v_{\vec{k}_2} u_{\vec{k}_2} v_{\vec{k}_1} \left\langle \hat{\beta}_{-\vec{k}_1} \hat{\beta}^\dagger_{\vec{k}_2} \hat{\beta}_{\vec{k}_1} \hat{\beta}^\dagger_{-\vec{k}_2} \right\rangle \\ &+ u^2_{\vec{k}_2} v^2_{\vec{k}_1} \left\langle \hat{\beta}_{-\vec{k}_1} \hat{\beta}^\dagger_{\vec{k}_2} \hat{\beta}^\dagger_{-\vec{k}_1} \hat{\beta}_{\vec{k}_2} \right\rangle \\ &+ v^2_{\vec{k}_2} v^2_{\vec{k}_1} \left\langle \hat{\beta}_{-\vec{k}_1} \hat{\beta}_{-\vec{k}_2} \hat{\beta}^\dagger_{-\vec{k}_1} \hat{\beta}^\dagger_{-\vec{k}_2} \right\rangle \end{aligned} \tag{2.49}$$

The Wick theorem for the quasi-particle operators allows to simplify this expression. Since the calculation is long, we are only considering a simple case $T = 0$ ($\rho_{qp}(\vec{k}) = 0$). We find:

$$G^{(2)}_{BB,T=0}(\vec{k_1}, \vec{k_2}) = v^2_{\vec{k}_2} v^2_{\vec{k}_1} + v^4_{\vec{k}_1}\, \delta(\vec{k}_1 - \vec{k}_2) + u^2_{\vec{k}_1} v^2_{\vec{k}_1}\, \delta(\vec{k}_1 + \vec{k}_2) \tag{2.50}$$

and for $\vec{k}_1, \vec{k}_2 \neq 0$:

$$\boxed{g^{(2)}_{BB,T=0}(\vec{k_1}, \vec{k_2}) = 1 + \delta(\vec{k}_1 + \vec{k}_2) + \delta(\vec{k}_1 - \vec{k}_2) + \frac{\delta(\vec{k}_1 + \vec{k}_2)}{v^2_{\vec{k}_1}}} \tag{2.51}$$

As a result, the interactions are at the origin of the appearance of strong two-body correlations, even at $T = 0$. Here, these correlations are due to the quasi-particles pairs $(\vec{k}, -\vec{k})$ and gives a bunching for $\vec{k}_1 = \vec{k}_2$ and $\vec{k}_1 = -\vec{k}_2$.

Remark:
The extra bunching factor $\delta(\vec{k}_1 + \vec{k}_2)/v^2_{\vec{k}_1}$ is the usual term that one finds in the presence of correlated $k/-k$ pairs. It can be understood easily by considering for instance N_k quasi-particle in the mode $\vec{k}$. In the momentum space, this means that N_k particles have a momentum $\vec{k}$ and the same number with a momentum $-\vec{k}$. The number $\vec{k}/\vec{k}$ pairs one can form is $N_k(N_k - 1)$ (because a particle can not pair with itself) while the number $\vec{k}/-\vec{k}$ is N_k^2 resulting in an enhancement by a factor N_k. Normalized to the total number of pairs, this results in an enhancement by a factor $1/n_k$ with $n_k = N_k/N = v^2_{\vec{k}}$ the population of the mode k. When the population n_k is small, this gives rise to a high $k/-k$ bunching amplitude as found in Eq. 2.51. Note that in a different experimental configuration, a similar signal of bunching $k/-k$ of correlated atom forming a pair was observed after the collisions of BEC [76].

Correlations in the Mott phase

Unit filling Mott at T=0 and $J = 0$

In the case of a unitary filling, there is no on-site interaction and the Hamiltonian of the system is the one given in Eq. 2.44. However, because of the strong interactions, the system is not in the pure state $|\vec{q}\rangle = 0$, but in a statistical mixture of quasi-momentum states expending over the whole Brillouin zone, and with no phase coherence. This case is consequently similar to the non-interacting and high temperature limit, with the difference that here the modes are not thermally populated but uniformly populated (corresponding to an infinite effective temperature). In this case, the Wick theorem also applies and we find exactly the same results as written in Eq. 2.46, Eq. 2.48 and Eq. 2.47.
For instance the normalized second-order correlation function of a perfect Mott insulator is given by:

$$\boxed{g^{(2)}_{MI}(\vec{k}_1, \vec{k}_2) = 1 + \left| g^{(1)}_{MI}(\vec{k}_1, \vec{k}_2) \right|^2} \tag{2.52}$$

Mott insulator at T=0 and J finite

Following up what has been done for the first-order correlation function to take into account the particle-hole correction to the first-order in the perturbation theory, the derivation of the second-order correlation function requires the knowledge of the on-site spatial correlation function $C^{(2)}(i, j, s, t)$:

$$\begin{aligned} C^{(2)}(i,j,s,t) &= \left\langle \hat{b}_i^\dagger \hat{b}_j^\dagger \hat{b}_s \hat{b}_t \right\rangle_{|\Psi^{(1)}\rangle} \\ &= C^{(2)}_{MI}(i,j,s,t) + \frac{J}{U} \sum_{<h,l>} {}_{MI}\langle \Psi | \, \hat{b}_i^\dagger \hat{b}_j^\dagger \hat{b}_s \hat{b}_t \hat{b}_l^\dagger \hat{b}_h \, | \Psi \rangle_{MI} + c.c + \mathcal{O}\left(J/U\right) \end{aligned} \tag{2.53}$$

In the sum over $\langle h, l \rangle$, several terms are non-null. As the calculation is quite long, it is not developed here. At the end, one finds [77]:

$$\begin{aligned} G^{(2)}_{PH}(\vec{k_1}, \vec{k_2}) =& G^{(2)}(\vec{k_1}, \vec{k_2}) - \rho_{MI}(\vec{k_1})\rho_{MI}(\vec{k_2}) 2 \frac{E(\vec{k_1}) + E(\vec{k_2})}{U} \\ & \times \left[(n_0 + 1) \times (1 + \delta(\vec{k_1} - \vec{k_2})) - \frac{1}{N}(2n_0^2 + 3n_0 + 1) \right] \end{aligned} \tag{2.54}$$

with n_0 the lattice filling.

The second order normalized correlation function:

$$g^{(2)}_{PH}(\vec{k_1},\vec{k_2}) = \frac{g^{(2)}_{MI}(\vec{k_1},\vec{k_2})}{\left(1-2\frac{n_0+1}{U}E(\vec{k_1})\right)\left(1-2\frac{n_0+1}{U}E(\vec{k_2})\right)} - \frac{2\frac{E(\vec{k_1})+E(\vec{k_2})}{U}\times\left[(n_0+1)\times(1+\delta(\vec{k_1}-\vec{k_2}))-\frac{1}{N}(2n_0^2+3n_0+1)\right]}{\left(1-2\frac{n_0+1}{U}E(\vec{k_1})\right)\left(1-2\frac{n_0+1}{U}E(\vec{k_2})\right)} \tag{2.55}$$

which gives, to the first order in J/U:

$$\boxed{g^{(2)}_{PH}(\vec{k_1},\vec{k_2}) = g^{(2)}_{MI}(\vec{k_1},\vec{k_2}) - 2\frac{E(\vec{k_1})+E(\vec{k_2})}{NU}\times(2n_0^2+3n_0+1)} \tag{2.56}$$

In the experiment, for $n_0 = 1$, $M \approx 20$ and $U/J \approx 50$, the correction term on the right of the equation does not exceed few percents.

2.2.4 Shape and size of the peaks

In the previous section, we considered homogeneous and infinite systems. As a result, the diffraction peaks as well as the bunching peaks were characterized by delta functions. For finite systems and/or inhomogeneous, like in most of the cold atoms experiments, the peaks have a certain width which provides information about the system, one example of which has been seen in the derivation of coherence in optics (§2.1.1).

First-order coherence

The first order correlation function $G^{(1)}(\vec{k_1},\vec{k_2})$ is linked to the in-situ field operator by a Fourier transform (FT):

$$G^{(1)}(\vec{k_1},\vec{k_2}) = \int_{\vec{r}_1}\int_{\vec{r}_2} e^{-i(\vec{k}_1.\vec{r}_1-\vec{k}_2.\vec{r}_2)}\left\langle\psi^\dagger(\vec{r}_1)\psi(\vec{r}_2)\right\rangle \tag{2.57}$$

Note that here, we use a continuous description as we want to concentrate of the shape of the correlation peaks in the first BZ.

$G^{(1)}$ can be linked to the in-situ density distribution in two cases:

- *For a perfectly coherent superfluid:* that is to say when the coherence extends over the whole cloud, then $\left\langle\psi^\dagger(\vec{r}_1)\psi(\vec{r}_2)\right\rangle = \sqrt{n(\vec{r}_1)}\sqrt{n(\vec{r}_2)}$ resulting in:

$$G^{(1)}(\vec{k_1},\vec{k_2}) = FT[\sqrt{n}](\vec{k_1})\times FT[\sqrt{n}](\vec{k_2}) \quad \text{and} \quad \rho(\vec{k}) = \left|FT[\sqrt{n}](\vec{k})\right|^2 \tag{2.58}$$

$$g^{(1)}(\vec{k_1},\vec{k_2}) = 1 \tag{2.59}$$

- *For a perfectly incoherent system (such as a perfect MI or a thermal gas of bosons without interactions):* $\langle\psi(\vec{r}_1)\psi(\vec{r}_2)\rangle = \delta(\vec{r}_1-\vec{r}_2)n(\vec{r}_1)$

$$G^{(1)}(\vec{k_1},\vec{k_2}) = FT[n](\vec{k_2}-\vec{k_1}) \quad \text{and} \quad \rho(\vec{k}) = \rho(\vec{k}=0) \tag{2.60}$$

$$g^{(1)}(\vec{k_1},\vec{k_2}) = FT[n](\vec{k_2}-\vec{k_1})/\rho(\vec{k}=0) \tag{2.61}$$

and in both the cases, the width the first-order correlation peak is supposed to be of the order of the inverse of the system size, $\delta(k) \approx 1/L$ with L the size of the cloud.

Second-order coherence

In this case, it is more complicated to state. However, when the Wick theorem applies, the second-order correlation functions can be calculated from $g^{(1)}$. Since $g^{(2)}(\vec{k_1},\vec{k_2}) \propto |g^{(1)}(\vec{k_1},\vec{k_2})|^2$, the second order correlation peaks typically decreases $\sqrt{2}$ faster than the first order correlation peaks.

Thermal gas of bosons without interactions

One specific case we will treat in this manuscript and for which the in-situ density distribution is straighforward to get is the case of a *thermal cloud*. In fact, the density distribution is given by the Boltzmann factor:

$$n(\vec{r}) \propto \exp\left\{-\left(\frac{1}{2}m\omega_{ext}^2 r^2\right)/k_B T\right\} \tag{2.62}$$

that is to say that the in-trap density is gaussian with a RMS size $s = \sqrt{\frac{k_B T}{m\omega_{ext}^2}}$.

At high temperature, the De Broglie wavelength is so small that one can consider that the cloud is totally incoherent $\left\langle \psi^\dagger(\vec{r}_1)\psi(\vec{r}_2)\right\rangle = \delta(\vec{r}_1 - \vec{r}_2)n(\vec{r}_1)$. Using Eq. 2.61:

$$g_{th}^{(1)}(\vec{k_1},\vec{k_2}) = e^{-\frac{(\vec{k_1}-\vec{k_2})^2}{2(1/s)^2}} \tag{2.63}$$

The application of the Wick theorem provides the expression of the second order correlation function:

$$g_{th}^{(2)}(\delta\vec{k} = \vec{k_1} - \vec{k_2}) = 1 + e^{-2\frac{(\delta\vec{k})^2}{2(1/s)^2}} \tag{2.64}$$

In this thesis, in the case where the correlation peaks are decreasing with a gaussian shape, we choose to define the two-body correlation length l_c such as:

$$g_{th}^{(2)}(\delta k) = 1 + e^{-2(\delta k/l_c)^2} \tag{2.65}$$

which means that for a thermal gas, $l_c = \sqrt{2}/s$ and only depends on the temperature. Such a decrease has already been measured in a hot harmonically trapped cloud [3]. In §.6.4, we are investigating the case of the thermal part of a lattice superfluid below and above the condensation transition. In particular, we will see that in this situation, the physics is a bit more complicated as the depletion is an admixture of the thermal depletion and the quantum depletion, and that are not possible to separated out experimentally. Both of them should be at the origin of the presence of a bunching in the second-order correlation, that are, a priori, not characterized by the same correlation length. Furthermore, it is not obvious that in this situation, the quantum and the thermal depletion could be treated separately in order to predict the shape of the bunching peaks.

Comparison between a Mott insulator and a thermal gas:

A thermal gas as well as a perfect Mott insulator are very similar in their momentum distribution (first-order correlation) and both of them display a periodic second-order bunching. However, one way to differentiate them consists in looking at the precise shape of the bunching peaks. In fact, a thermal gas has a gaussian in-situ density profile, with a width independent on the number of atoms while a Mott insulator is characterized by a uniform in-situ density (if we suppose that it is made of only one Mott plateau and we neglect the SF or thermal shells) that strongly depends of the number of atoms (due to the incompressibility of the Mott state). Since the bunching peak shape (within the applicability of the Wick theorem) is given by the Fourier transform of the in-situ density, they can be distinguished from each other by monitoring the evolution of the peaks shape as a function of the total number of atoms N (see §.6).

3. Measurement of the momentum distribution at the single atom level

The specificity of cold atom experiments working with He* atoms relies on the possibility to use an electronic detection to probe the quantum gases. This electronic detection, performed after a long time of expansion of the quantum gases, allows, provided some conditions detailed in §.3.3, to access the three dimensional momentum distribution of the trapped gas, and this, with a single atom sensitivity. There is no equivalent of such a detection that has been found in order to access this single atom sensitivity in the momentum space with usual optical imaging. This paves the way towards the investigation of the Mott transition trough correlation measurements.

In this chapter, we will describe the metastable He* experiment, and describe the different experimental steps that lead to the production of the lattice gases starting from a Bose Einstein Condensate. The readers that are interested to get a full description of the experimental sequence used to produce He* BECs are invited to read the PhD manuscripts [78, 79, 80] of previous PhD students. A summary of the experimental cycle is also given in the appendix. The second part will be dedicated to the probing of the gas in the momentum space.

3.1 A brief summary of the experimental setup

3.1.1 A BEC of He* atoms

The first BECs of ^{4}He* (bosonic isotope) atoms have been produced simultaneously in 2001 in the group of Denis Boiron, Chris Westbrook and Alain Aspect at the Institut d'Optique [81] and in the group of Michele Leduc and Claude Cohen-Tannoudji at Collège de France [82]. The cooling and the condensation of He* have been made possible by the existence of optical transitions separating the metastable state 2^3S_1 to the 2^3P as shown in the energy level diagram given in Fig. 3.1. Furthermore, the long lifetime of the metastable state 2^3S_1, of the order of 8 000 s, makes it suitable for the use in cold atoms experiments for which the duration of the experimental sequence is of the order of few seconds (a BEC can be produced each 7 s in our experiment).

A major advantage of the use of the metastable Helium atom relies on its large internal energy: the energy level 2^3S_1 is situated at about 20 eV from the ground state. This energy is far larger than what needed to extract an electron from a metal (which is typically of the order of a few eV), and which is the condition to fulfill to be detected electronically. More precisely, the Helium detector is composed of a metallic plate (Micro Channel Plate MCP) on which the atoms are falling after a long time-of-flight. When a metastable atom hits the plate, it can extract one electron. This electronic signal is then amplified and coupled to a mesh of metallic wires called the delay lines. By monitoring the electronic signal at the ends of these delay lines, it is possible to reconstruct the 3 dimensional position of the atoms. This will be explained in detail in §.3.2.

Note that an other characteristic of the metastable atoms lies on the existence of penning collisions (inelastic), process where two metastable atoms have enough energy to ionize one of them. This two-body decay process is enhanced by the presence of a light close to the resonance and by the presence

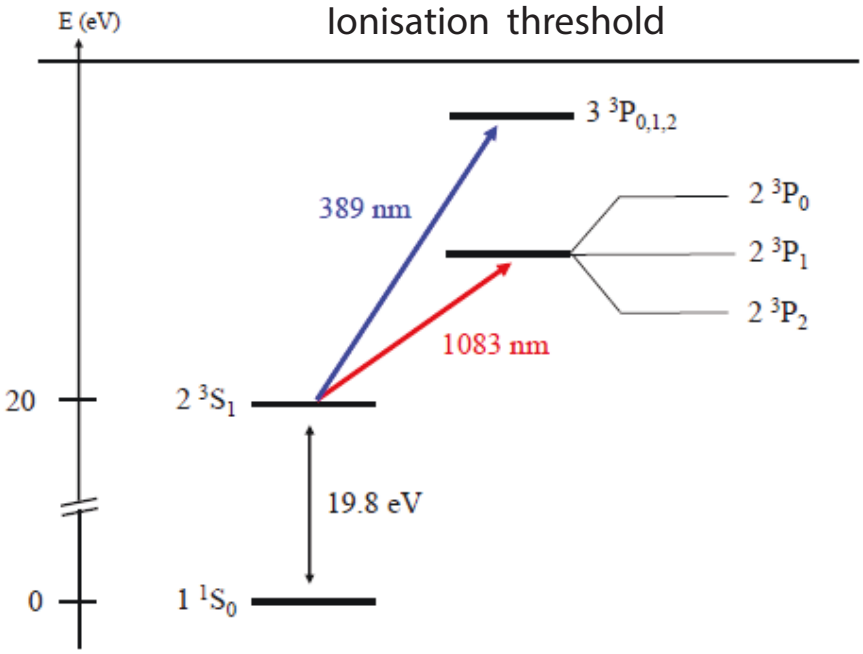

Figure 3.1: **Energy levels of ^{4}He.** The metastable Helium atom He* we consider is the He atom in the triplet state 2^3S_1. In the presence of a magnetic field, this energy level is split into the 2^3S_1, $m_J = \{-1, 0, 1\}$ levels where m_J refers to the projection of the total angular momentum along the quantization axis. To cool the atoms, we use the optical transition at $\lambda = 1083\,\text{nm}$ separating the 2^3S_1 state to the 2^3P state (more precisely the two transitions 2^3S_1 - 2^3P_2 and 2^3S_1 - 2^3P_1).

of a spin mixture [83].

At the end of the cooling and the evaporation sequence, a BEC is produced in the science chamber (SC):

- The BEC is trapped into a crossed optical dipole trap (ODT) with a harmonic confinement of the order of $(\omega_x, \omega_y, \omega_z) = 2\pi \times (100, 400, 400)\,\text{Hz}$. The optical trap is made from a 20W fiber laser at $\lambda = 1550\,\text{nm}$.

- The power of the ODT laser is stabilized in order to increase the stability in the atom number.

- By varying the optical dipole trap depth, the number of atoms in the BEC can be adjusted from a few hundreds to almost 10^6.

- In the optical trap, the atoms are spin polarized in the $m_J = +1$ sublevel of the 2^3S_1 state in order to decrease the effect of the Penning collisions (the Penning rate between $m_J = +1$ and $m_J = +1$ states is 4 orders of magnitude lower than for the collisions between two $m_J = 0$ atoms due to the spin conservation rule [83]).

Note that in the experiment, besides the electronic detection, atoms can be detected via usual optical imaging techniques. More precisely, a BEC can be imaged in-situ or up to 18 ms of time-of-flight by absorption imaging. This is for instance used to measure the number of atoms in the BEC (see Fig. 3.2).

3.1.2 A 3D cubic optical lattice

A sketch of the implementation of the optical lattice on the apparatus is given in Fig. 3.3.

It is made from the sum of three standing waves, generated by three identical retroreflected laser beams with the following characteristics:

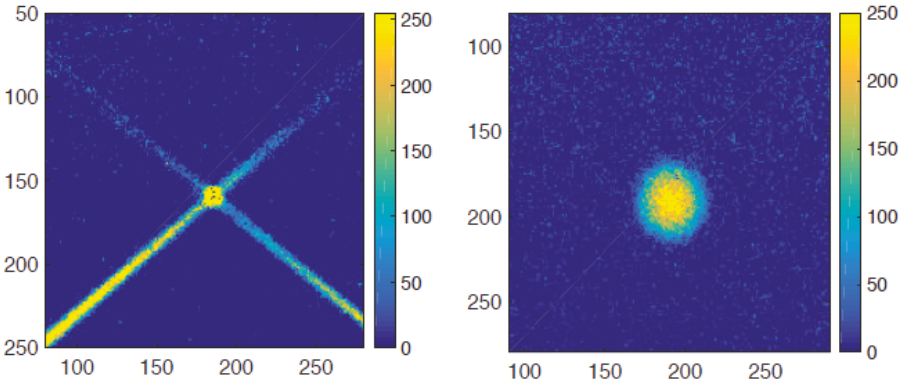

Figure 3.2: **A He* BEC trapped in a crossed optical trap. a)** Atoms trapped in the crossed optical trap and imaged with an absorption imaging technique. **b)** Image of a BEC after $t_{tof} = 10\,\text{ms}$ of time-of-flight from which one can extract the number of atoms N.

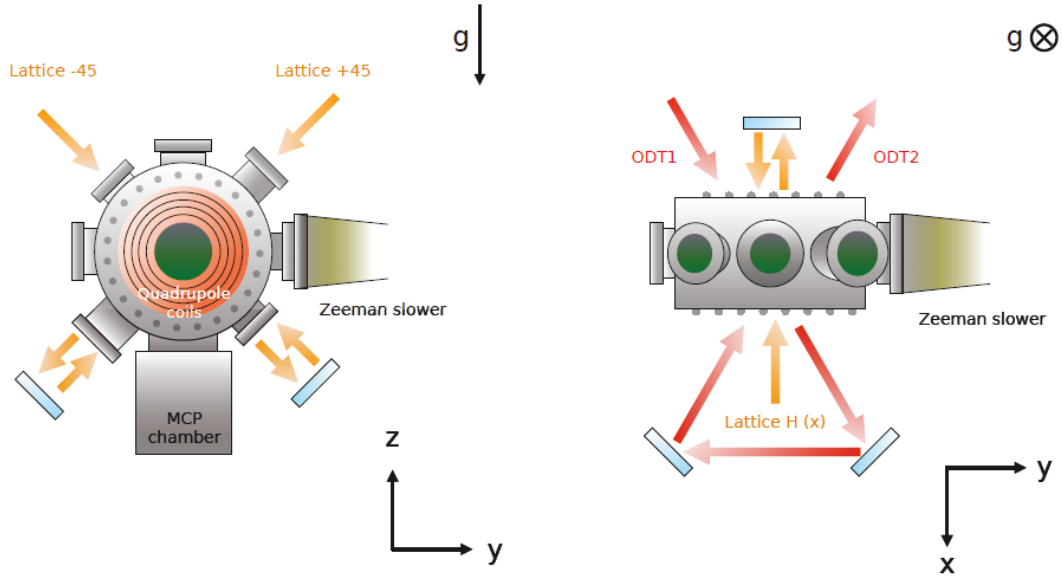

Figure 3.3: **Lattice beam setup.** Two of the lattice beams are oriented at ±45° from the horizontal direction and one is horizontal and perpendicular to the former two.

- The lattice beams are coming from a narrow linewidth 15 W fiber laser at $\lambda = 1550\,\text{nm}$, which corresponds to a detuning of the order of the THz with the nearest optical transition. Consequently, even at high power, the spontaneous scattering is negligible. The total power of the laser is split in 3 in order to get 3 independent beams that are used to generate the optical lattice along the 3 spatial directions.

- The beams are crossing each other perpendicularly, forming a 3D cubic lattice. In this configuration, the lattice period d is equal to the half of the wavelength, *i.e*, $d = \lambda/2 = 775\,\text{nm}$ and the recoil energy $E_r = \hbar^2 k^2/2m = \hbar\omega_r$ with $\omega_r = 2\pi \times 20\,\text{kHz}$.

- Each beam is detuned by 20 MHz from each other so as the atoms do not see the possible interferences between the different beams.

- The lattice beams are crossing at the center of the BEC in order to get an optimal transfer between the ODT and the optical lattice.

- The 3 lattice beams are power stabilized independently. This is done by sending on high speed photodiodes about 1% of the power going through the experiment (and before entering the science

chamber) and injecting the signal from the photodiode in a feedback loop (PID controllers made by Marco Mancini, a former post-doc on the experiment). This enables to compensate possible power fluctuations or drifts coming from the laser or from the transmission of the different optical elements. It is essential in order to determine with precision the lattice depth of the optical lattice along the different directions.

- Using the parameters (the mass m and the interaction coefficient $g = 4\pi\hbar^2 a_{sc}/m$ where $a_{sc} = 7.5\,\text{nm}$ is the $m_J = 1 - m_J = 1$ two-body scattering length) of the helium atom and $d = 775\,\text{nm}$, the critical values $(U/J)_c^{MF} = 34.8$ and $(U/J)_c^{QMC} = 29.3(2)$ correspond respectively to a lattice amplitude $V_{0,c}^{MF} = 14\,E_r$ and $V_{0,c}^{QMC} = 13.5\,E_r$.

- The external trapping frequencies resulting from the gaussian shape of the lattice beams are the same along the different directions and equal to $\omega_{\text{ext}} = 2\pi \times 95\sqrt{V_0}\,\text{s}^{-1}$ or $\omega_{\text{ext}} = 2\pi \times 140\sqrt{V_0}\,\text{s}^{-1}$ depending on the data sets (in the course of the thesis, the waist size of the lattice beams has been changed in order to reach $V_0 = 18\,E_r$, necessary to explore the Mott transition).

3.1.3 Loading of the BEC into the optical lattice potential

Experimental sequence

The transfer of the BEC from the ODT to the optical lattice potential is done by ramping down the ODT beams power while increasing the power in the lattice beams. The experimental sequence is depicted in Fig. 3.4.

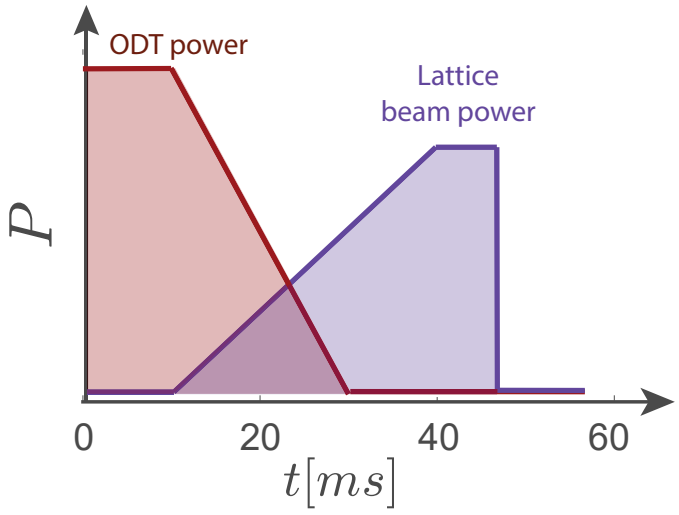

Figure 3.4: **Loading of the BEC from the ODT to the optical lattice potential.** To transfer the atoms from the ODT to the lattice potential, the ODT power is decreased linearly in 20 ms. Meanwhile, the power of the lattice beams is increased with a rate $\Gamma \approx 0.35\,E_r/\text{ms}$. In usual experiments, the lattice is kept for 5 ms and then switched off at the beginning of the time of flight.

The adiabaticity: theoretical considerations

The Bose-Hubbard Hamiltonian describes bosonic particles in the lowest energy band of a periodic potential. As a consequence, the experimental realization of the BH model with ultracold atoms requires the gas to remain in the lowest energy state when the optical lattice is loaded. If the loading is too fast, higher bands can be populated. This time-dependent Hamiltonian problem is well known in quantum mechanics. It leads to the adiabaticity theorem, demonstrated in

[84], which gives some restrictions over the variation of the time-dependent Hamiltonian for the system to stay in the ground state during the non stationary process.

Adiabatic theorem: *Let's consider $\phi_\lambda(t)$ the eigenvalues of $H(t)$ and suppose that the system is in $\phi_\lambda(t)$ at t. The system remains in $\phi_\lambda(t+dt)$ after dt if:*

$$\langle \phi_{\lambda'}(t)|dH/dt|\phi_\lambda(t)\rangle \,| \ll |E_{\lambda'}(t) - E_\lambda(t)|^2/\hbar \tag{3.1}$$

In our system, the situation is more complicated since the expression of the many-body state is not known. Because of this complexity, the adiabaticity is experimentally tested. However, it is possible to find some orders of magnitude of the loading time to use. From the different energy scales present in the system, one can define different time scales:

$$\tau_{band} = \hbar/(V_0/4) \qquad \tau_U = \hbar/U \qquad \tau_{\omega_{ext}} = \hbar/\omega_{ext} \qquad \tau_J = \hbar/J \tag{3.2}$$

The two first ones are related to the time scales corresponding respectively to the transfer from the first to the second band and to the creation of a particle-hole deep in the superfluid and in the Mott insulator regime. The two others are linked to the presence of an external trapping. $\tau_{\omega_{ext}}$ is the time related to the change in the zero point energy of the lattice site trapping and τ_J represents the time needed in order for the atoms to redistribute over the cloud size to adapt to the change in the external potential. For the Helium atoms, and for $V_0 \in [5:18]\, E_r$, the order of magnitude of the different energies are:

$$V_0 \sim E_r \qquad U \sim 0.1\, E_r \qquad J \sim 0.01\, E_r \qquad \hbar\omega_{ext} \sim 0.005\, E_r \tag{3.3}$$

The limiting time scales are thus the ones given by τ_J and $\tau_{\omega_{ext}}$ that are both of the order of 10 ms.

In the experiment, we are ramping up the lattice beams such as $dt/dV_0 = 2.85\,\mathrm{ms}/E_r$. As a result, the lattice is ramped up over more than 10 ms for all the lattice amplitudes investigated in this thesis. Furthermore, after the loading, a waiting time of 5 ms is applied before cutting the lattice trap at the beginning of the time-of-flight. This duration is equal to a few times the tunneling time τ_J (see Fig. 3.5) which normally ensures that the atoms had time to redistribute over the cloud before the TOF. Note that a more careful investigation of the adiabaticity criteria can be found in [85].

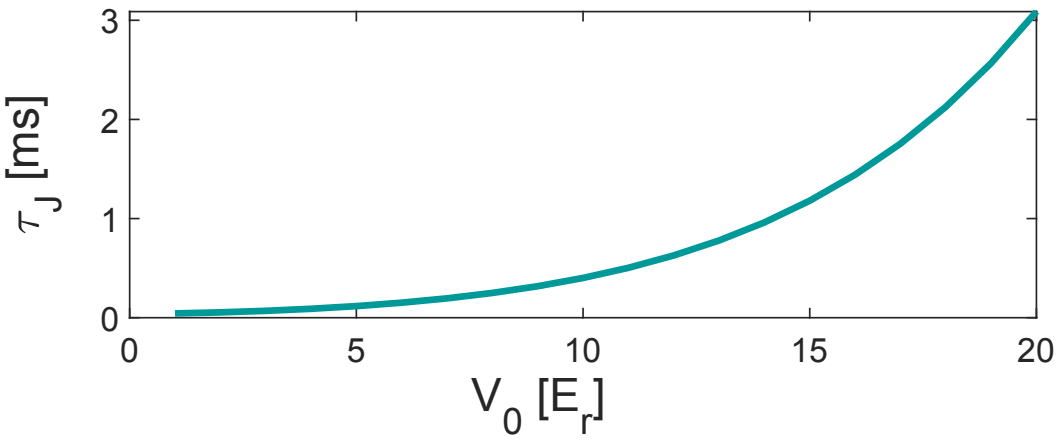

Figure 3.5: **Tunneling time scale τ_j.** Values of the tunneling time τ_J as a function of the lattice depth.

Remark about the shape of the loading ramp:
Any discontinuity during the loading sequence can be at the origin of a non adiabatic process.

This explains why most of the experiments use s-shape ramps with a smooth variation of the lattice amplitude at the begin and at the end of the loading. However, as we did not notice any difference concerning the adiabaticity (the method to check the adiabaticity is mentioned in the next paragraph) when performing this type of ramp or linear ramps, we choose to ramp up linearly the lattice power. The advantage of such a technique is that the ramp performed is always the same, whatever the lattice amplitude chosen to work with. The ramp is just stopped when the working lattice depth is reached.

The adiabaticity: in the experiment

In order to fine tune the parameters of the loading ramp and to check the quality of the adiabaticity, a ramping up and down sequence is performed. This method consists in loading the cloud from the ODT to the optical lattice and transferring it back to the ODT trap, with the time-reversed ramp as depicted in Fig. 3.6. If the loading is perfectly adiabatic, one gets at the end of the sequence a Bose Einstein Condensate similar, in terms of the atom number and the temperature, to the initial one. The parameters we are tuning are:

- The ramping up speed of the optical lattice. We found that the best value is about $dV_0/dt = 0.35\, E_r/\text{ms}$.
- The ramping down time of the ODT trap. It is generally set to about 15 ms.
- The delay τ_{delay} between the beginning of the lattice ramp and the ODT ramp. It is generally set to about 3 ms.
- The holding time in the lattice, generally set to 5 ms.

In the experiment, a loss of about 20% of the atoms is observed after performing this sequence. After investigation, we found that these atoms are lost at the beginning of the transfer when the ODT is switched off, probably due to a non perfect overlap between the ODT trap and the lattice trap. However, no heating is visible, which is a good indication that the loading is adiabatic with a good approximation. An other method explained in §.4 provides a similar conclusion.

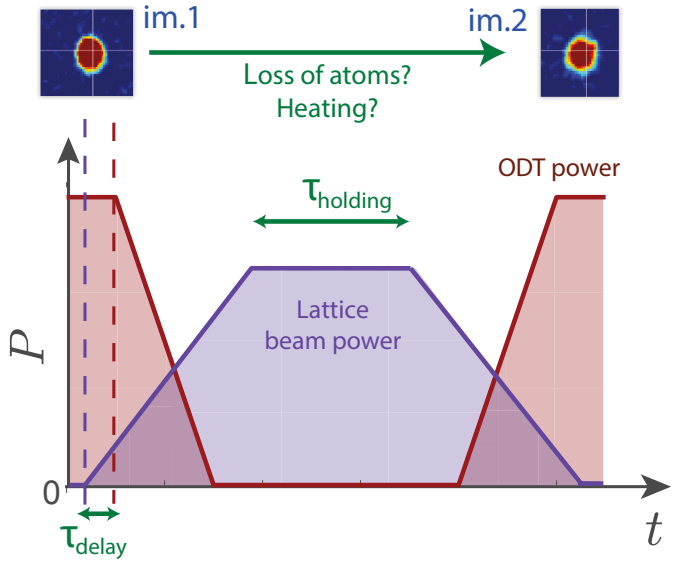

Figure 3.6: **Sequence to test the goodness of the transfer from the ODT to the lattice trap.** An image (im.2) of the BEC is taken after transferring it to the optical lattice and back to the ODT. This image is compared to the image of the BEC taken without performing the transfer to the optical lattice (im.1). From the comparison of the two images, one can deduce the loss of atoms induced by the loading or see if there is some heating happening during the transfer. We perform this sequence with varying the different parameters that are the ramping speed of the optical lattice, the ramping down duration of the ODT trap, the delay between the start of the lattice loading and the decrease of the ODT and finally the waiting time in the lattice. The best parameters are found when the loss of atoms is minimized and no thermal fraction is visible. Note that the condensate pictures displayed have been taken with the camera.

3.1.4 Lattice depth calibration method

In order to know and to adjust with precision the ratio U/J, or equivalently the lattice depth V_0, the calibration is a crucial step. In our setup, the lattice beams are power stabilized and one can control the power of each beam separately.

The calibration of the lattice beams consists in finding, for each of the three beams, the relation between the input setpoint of the feedback loop, here a voltage $U_{\text{i,setpoint}}$, and the effective lattice depth $V_{0,i}$ along the lattice direction i.

In the experiment, the lattice beam powers P_i are controlled with the help of Acousto Optical Modulators (AOM) with linear drivers. This implies that the relation between P_i and $U_{\text{i,setpoint}}$ and, equivalently, between $V_{0,i}$ and $U_{\text{i,setpoint}}$ is linear (this statement has been checked experimentally) The calibration thus consists in finding the coefficient κ_i such as:

$$V_{0,i} = \kappa_i \times U_{\text{i,setpoint}} \tag{3.4}$$

To do so, we use the amplitude modulation technique [42]. A schematic of it is given in Fig. 3.7.

After loading as usual the optical lattice, the power of the lattice beam i is modulated around P_i at a frequency f_{mod} for $t_{mod} = 20\,\text{ms}$. This creates two sidebands at the frequencies $f \pm f_{\text{mod}}$ on the lattice beam spectrum. If $2 \times f_{\text{mod}}$ is close to $f_{\text{res}} = \hbar(E_2(q=0) - E_0(q=0))$ where $(E_2(q=0) - E_0(q=0))$ represents the difference in energy between the second excited band and the lowest energy band, then the atoms can be transferred by a resonant two-photons process to the second excited band[1]. By monitoring the fraction of the atoms transferred to the second

[1]Because of the symmetry of the wavefunctions, it is not possible to transfer atoms from the ground state to the first excited band.

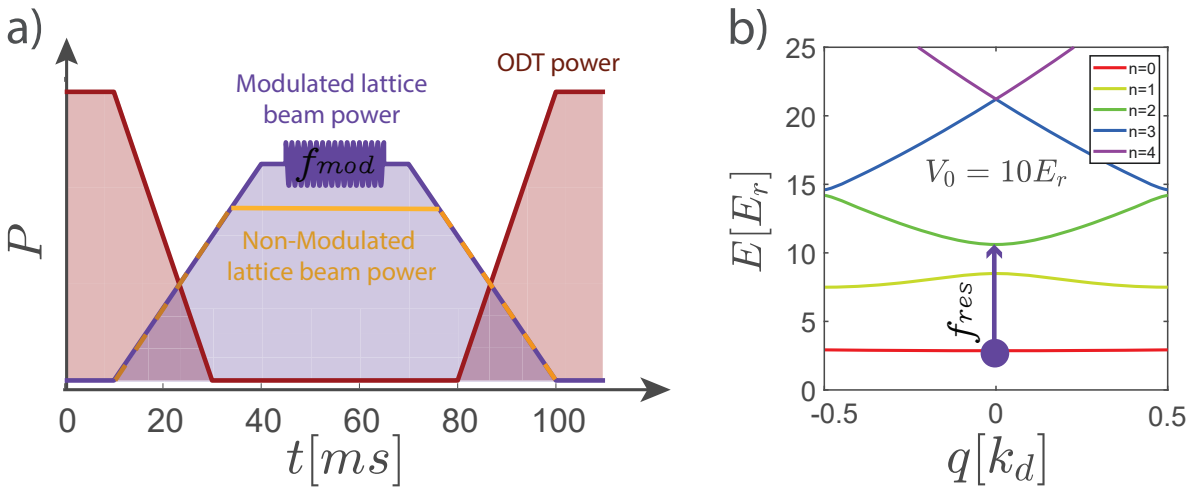

Figure 3.7: **Calibration of the optical lattice with the technique of amplitude modulation. a)** Experimental sequence used for the calibration. The power corresponding to the lattice direction we want to calibrate is represented in purple. The powers of the two other lattice beams are represented in yellow. Note that in order to be sure that we are not exciting the cloud in the two other lattice directions, their amplitude is set about 30% lower. **b)** Sketch of the transfer of an atom from the lowest energy band to the second excited band.

excited band, which is maximum when $2 \times f_{\mathrm{mod}} = f_{\mathrm{res}}(V_i)$, one deduces the value of $f_{\mathrm{res}}(V_i)$. In order to do that, there are different possibilities:

- The technique of band mapping that allows for the visualization of the population of the different bands (see §.3.1.5).
- For low lattice depths, the atoms in the excited bands are not trapped (see Fig. 1.2), resulting in a loss of atom that is possible to monitor with the camera.

The sequence used in the experiment consists in loading adiabatically the atoms back into the ODT (see Fig. 3.7). The atoms in the lowest energy band of the lattice are transferred to the lowest energy level of the ODT (to the condensate mode) while the ones in the excited bands go to other excited states. When the ODT trap depth is low, these atoms are either not trapped or are responsible for an increase of the gas temperature (because they carry high-momentum components). Monitoring either the size of the cloud or the atom number in the BEC after this sequence permits to find the maximum transfer to the second excited band, and thus $f_{\mathrm{res}}(V_i)$. One example of a calibration sequence is given in Fig. 3.8.a. The calibration is done for a power corresponding to a lattice depth $V_0 \sim 10\,E_r$.

From the calculation of the energy bands, we access the monotonic relation between f_{res} and V_i (Fig. 3.8.b), which can be inverted in order to get the measured value of V_i.

Remarks:

- The calibration is done for a lattice depth around $V_0 \approx 10\,E_r$ for two reasons. First, at this lattice depth, the atoms transferred to the second excited band are not trapped ($E_{n=2,min}(q = 0) > 10\,E_r$). Then, the sensibility of the measurement is higher for high lattice depths as df_{res}/dV_0 increases with V_0.
- The error on the measurement of f_{res} is about $\pm 2\,$kHz (see Fig. 3.8.a). Considering the sensitivity of the resonance frequency $df_{mod}/dV_0 \approx 12\,\mathrm{kHz}/E_r$, this translates in an uncertainty of about $\Delta V_0 = \pm 0.2\,E_r$ in the calibration of the lattice amplitude.

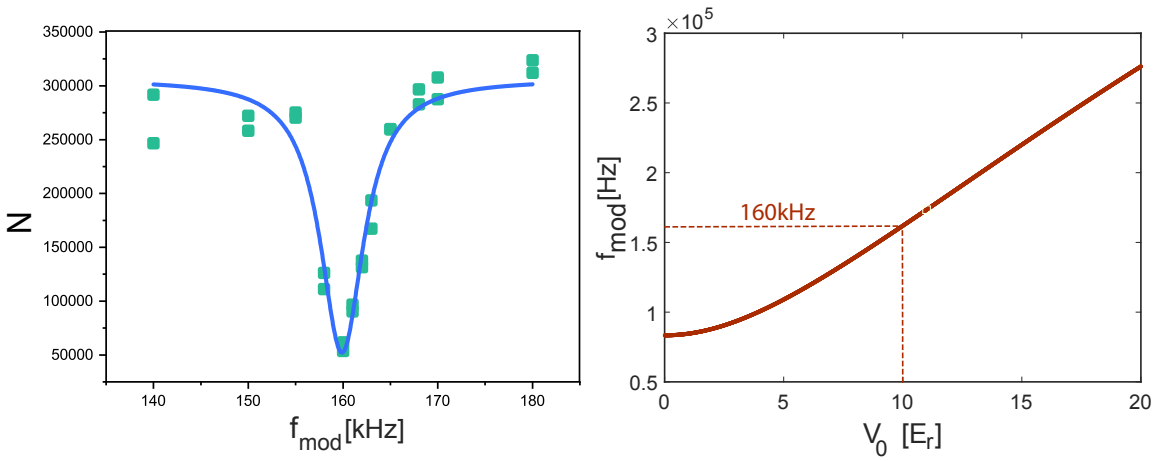

Figure 3.8: **Lattice calibration curves. a)** Number of atoms in the BEC measured after the amplitude modulation sequence as a function of f_{mod} . The experimental data are the green points, the blue line is a Lorentzian fit: the central frequency found is 160 kHz± 2 kHz. **b)** Calibration curve f_{mod} as a function of the lattice amplitude V_0. The sensitivity around $V_0 = 10\,E_r$ is $12\,\mathrm{kHz}/E_r$, resulting in a calibration of V_0 with an uncertainty inferior to $0.2\,E_r$.

3.1.5 Heating sequence

To investigate the superfluid to normal fluid transition, we have to heat up the lattice gases (see §.4.1.1). To do that, we perform a controlled heating sequence once the atoms are in the optical lattice (note that trying to load a heated gas into the lattice would result in the population of excited energy bands, a situation that must be avoided). After loading the BEC in the lattice, a series of non-adiabatic pulses of 0.5 ms duration each is performed with one of the lattice beams. The number of pulses (from 5 to 10) and their amplitude are varied to obtain different final temperatures in the lattice while keeping the number of atoms constant. After the pulse sequence, the cloud is left to thermalize for a certain time (during a few times h/J). One important thing to check is whether higher energy bands are filled during this process. In fact, the BH Hamiltonian neglects the existence of higher energy bands, as a result atoms must stay in the lowest one. By exploiting a band mapping technique [86] we can verify that no discernible fraction of atoms is transferred to higher lattice bands.

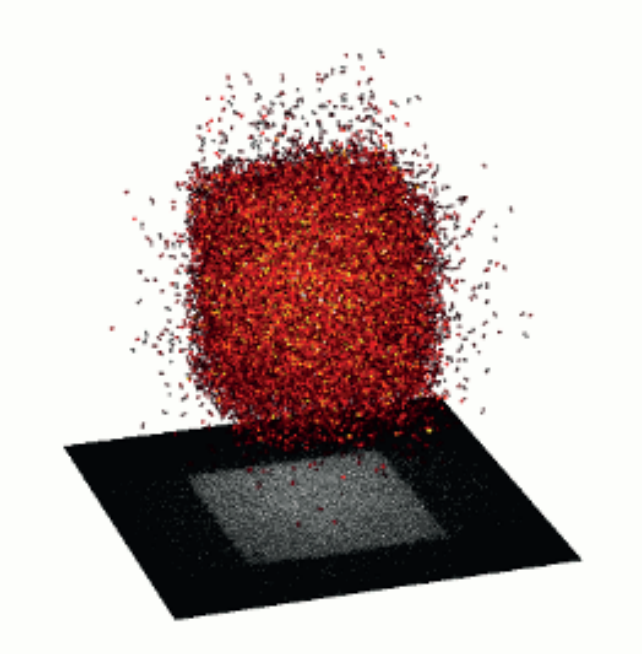

Figure 3.9: **Band mapping technique.** By ramping down to 0 slowly the optical lattice (instead of switching it off abruptly before the TOF), but not too slow so as the atoms to stay in their energy bands, the quasi-momentum of the atoms is adiabatically transferred to their momentum. If there are no atoms excited in the higher energy bands, the momentum distribution should be contained in the first Brillouin zone as it is the case here (the first BZ is a cube of total length k_d for a cubic lattice).

3.2 The electronic detection

He* atoms can be detected through the electronic detector described in this section. It can be divided in two parts: the Micro Channel Plates (MCP) and the Delay Lines (DL):

- *Micro-channel plates:* a MCP is a piece of metal in which billions of holes have been drilled. When an energetic atom (energy superior to the ionization threshold to remove one electron of a metal, usually about few eV) falls on the surface of the MCP, it can come back to the ground state extracting an electron from the metal. During this process, the electron has a certain probability to fall onto a hole. Because of a voltage difference applied between the top and bottom of the MCP, the electron is accelerated in the channel, inducing more and more extractions of secondary electrons from the surface of the channel. In other word, the MCP acts as an amplifier for the initial discharge. Monitoring the electronic showers generated at the output face of the MCP allows for the detection of incoming He* particles. Furthermore, because there are many channels, the electronic showers are spatially resolved on the MCP plane, which accounts for a spatially resolved He* detection. MCP are thus widely used for the detection of highly energetic particles in particle physics [87]. In these applications, the output face of the MCP is generally coupled to a phosphorus screen or to discrete photomultipliers to record the electronic showers. In our experiment, it is coupled to delay-line anodes in order to get the time resolution.
- *Delay line anodes:* they are made by wrapping with a thin mesh, metallic wires along two directions as represented in Fig. 3.11. When an electronic shower hits the DLs, a pulse is generated in the two wires. As explained later, the knowledge of the 4 arrival times at the two ends of the two wires allows for the identification of the in plane electronic shower location as well as the pulse creation time. With that, we can deduce the time and position at which an atom has fallen onto the surface of the MCP.

Besides high energy particles (kinetic), this detection technique can be used to detect atoms with a high internal energy. This can be applied to noble gases that have highly energetic metastable states. However, in order to be used in cold atoms experiments, the following requirements are needed:

- The metastable state has to be coupled to some higher energy states by an optical transition in order to be able to apply the basic cooling techniques.
- The lifetime of the metastable state has to be far longer than the running time of the experiment.
- The highest internal energy possible for the detection efficiency to be high.

A comparison of the different noble gases metastable states with values of lifetimes and energies is given in [88]. With its metastable state at 19.8 eV above the ground state, a lifetime τ_{He^*} of about 2 hours and the presence of an optical transition at $\lambda = 1083\,\text{nm}$ between the 2^3S_1 metastable state to the 2^3P_0 state[2] makes of the He atom the best candidate to be cooled down to quantum degeneracy and detected with the electronic detection. In addition, metastable Helium atoms are the only noble gas brought to quantum degeneracy.

3.2.1 The detection principle

In this paragraph, we will describe more in detail the different elements of the detector and the electronic chain that enables, from the signal obtained at the end of the delay lines, to access

[2]There is also an other transition at 389 nm.

the individual positions and times at which atoms are falling onto the detector. A more detailed description can be found in the amazing PhD manuscript of Hugo Cayla [78]. Schemes of the detection and pictures of the detection assembly are given in Fig. 3.10 and Fig. 3.11. Note that here, the MCP plane is oriented along the horizontal directions (the x and y directions). The atoms are falling on the detector along the gravity (the z direction).

The micro channel plates

In the experiment, we are using two inconel MCP in chevron configuration as depicted on the left of Fig. 3.10 and polarized with a voltage difference of 2.3 kV. The use of two plates is responsible for a higher amplification gain (defined as the number of electrons generated for each triggering event) and is of the order of 10^4. The geometry of the channels is also important for the performances of the detection:

- The open area ratio is the ratio between the area of the holes at the surface of the MCP and the total surface of the MCP. This ratio must be high in order to get a good detection efficiency as the electronic signal triggered by an atom that falls onto the MCP surface and not into a channel can not be amplified and thus detected. Currently, the MCP we are using have an open air ratio equal to 90% for the top plate and 70% for the bottom one.
- The channels are not drilled perpendicular to the surface but with an angle $\theta = 20°$. Without that, atoms could go through the channels without touching the walls, and as a consequence without triggering the electronic avalanche process required for the detection. However, as it will be explained later, this angle decreases the electronic detector resolution.

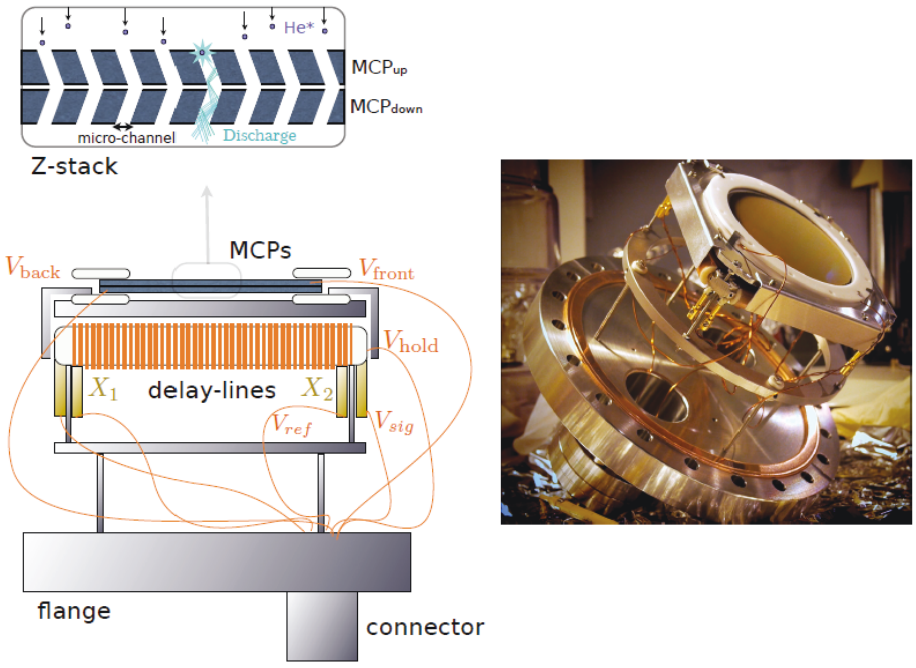

Figure 3.10: **Sketch of the electronic detector assembly.**

The delay lines

The delay lines are situated just below the MCP. Two metallic wires are wrapped regularly one hundred times around a holding board, one along x and the other one along y. When an electronic shower hits the delay lines, an electronic pulse is created onto the delay lines and

propagates along the two directions of each line at a speed $v_g = 1 \times 10^6$ m/s as represented in Fig. 3.11.

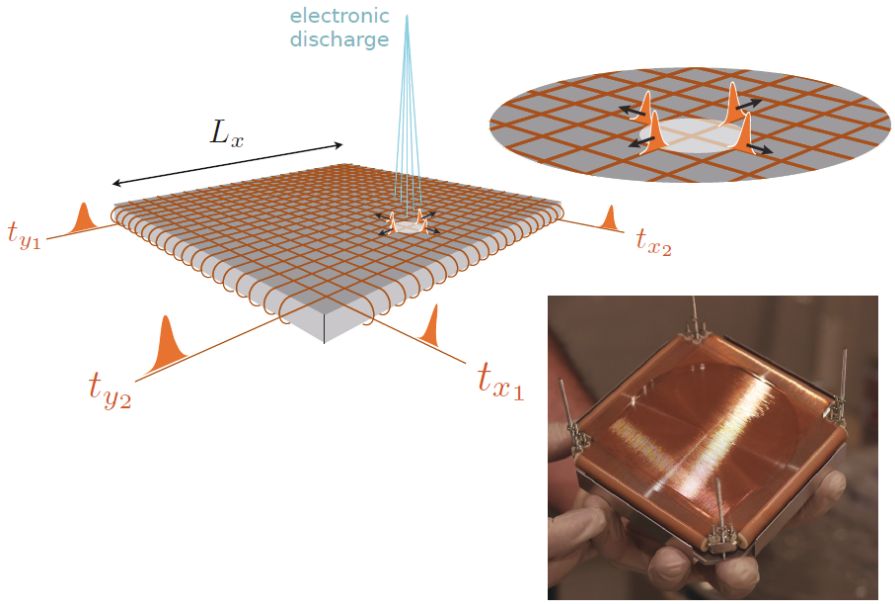

Figure 3.11: **Sketch of the delay lines.**

The time arrivals (t_{x1}, t_{x2}, t_{y1}, t_{y2}) of the 4 pulses at the end of the delay lines are then recorded. From the knowledge of these times, the time and location where the pulse have been generated can be inferred through:

$$x_{imp} = \frac{1}{2}\left(t_{x_1} - t_{x_2}\right) v_g \tag{3.5}$$

$$y_{imp} = \frac{1}{2}\left(t_{y_1} - t_{y_2}\right) v_g \tag{3.6}$$

$$t_{imp} = t_{x_1} + t_{x_2} - \frac{L_{DL}}{v_g} = t_{y_1} + t_{y_2} - \frac{L_{DL}}{v_g} \tag{3.7}$$

with $L_{DL} = 20$ m the total length of the DL wires. Provided the speed v_{COM} at which the atoms fall onto the detector is known, the vertical dimension can be retrieved using $z = v_{COM} \times t_{imp}$. In the experiment, the detector is situated at 43 cm below the center of the science chamber that corresponds to the in-trap cloud position. After switching off the trapping potentials, the atoms are falling under the gravity on the MCP in $t_{tof} = 297$ ms and the center of mass of the cloud hits the detector at a speed $v_{COM} = 2.9$ m/s. As a result, by recording all the 4-uplets (t_{x_1}, t_{x_2}, t_{y_1}, t_{y_2}), the 3D distribution of the atoms reaching the MCP can be reconstructed.

The measurement of the arrival times (t_{x_1}, t_{x_2}, t_{y_1}, t_{y_2}) must be done very precisely in order to get a good spatial resolution. For instance, using the Eq. 3.5, we see that the ability to distinguish two points separated by 1 mm requires to measure the arrival times with a precision better than $2 \times 1\,\text{mm}/10^6\,\text{m.s}^{-1} \approx 10^{-9}$ s. The electronics used to analyze the time signals must therefore be fast. Furthermore, since the pulses are a few ns wide and their amplitude varies (all the electronic showers are not coupled the same way to the DL and do not have the same amplitude because of the fluctuations of the MCP gain). Because of that, one needs to pay attention to the criteria used to attribute to each pulse an arrival time. This is the role of the constant fraction discriminator.

Electronic chain

Because the pulses have different amplitude, one can not use an amplitude sensitive criteria to set a time for each pulse (such as in the case of the leading edge discriminators). For this

reason, we choose to use a constant fraction descriminator (CFD), which sets the time from a fixed fraction $f_c \in [0\ 1]$ of the raising edge of the pulses. More precisely, from the analog signal $V_{pulse}(t)$, the CFD generates:

$$V_{CFD}(t) = V_{pulse}(t) - f_c \times V_{pulse}(t)(t - t_{delay}) \tag{3.8}$$

with t_{delay} a fixed time delay. The zero crossing point of $V_{CFD}(t)$ is then used as a reference for the triggering of a NIM signal (logical 0-1 volt signal with a sharp raising edge).

Finally, the logical NIM signal is converted to a digital time by a FPGA-based Time-to-Digital Convertor (TDC) developed by R. Sellem and D. Heurteau [89]. The elementary coding step is $t_0 = 120\,\text{ps}$.

3.2.2 Experimental sequence used for the detection

The clouds (lattice gases, BECs...) we investigate are polarized into the $m_J = 1$ state, that is to say a state which is sensitive to magnetic fields. Because we are probing the atoms after a long time of flight, one needs to pay attention to the presence of residual magnetic fields that could modify the distribution of atoms during the TOF. We choose to transfer the atoms from the $m_J = 1$ state to the $m_J = 0$ state at the beginning of the time-of-flight in order not to have to worry about the effect of the possible residual magnetic fields. In the trap, the atoms are kept polarized into the $m_J = 1$ state using a strong and uniform magnetic field. Because of it, the degeneracy of the sublevel $m_J = -1, 0, 1$ is lifted and they are separated by 12 MHz in energy. In order to transfer the atoms from the $m_J = 1$ to the $m_J = 0$ state, we are applying at the beginning of the TOF a resonant radio frequency (RF) pulse. The fraction of the atoms η_{RF} transferred depends on the RF pulse duration τ_{RF} and on the RF power P_{RF}. It can be calibrated by monitoring the Rabi oscillations between the 3 hyperfine levels in a Stern-Gerlach scheme were the atoms in the different states are separated during the time-of-flight by a strong magnetic gradient and imaged with the camera. Because the Rabi oscillations are occurring in a three level system, the maximum ratio of atoms that can be transferred from the $m_J = 1$ to the $m_J = 0$ state is $\eta_{RF,max} = 50\%$. Note that one could use a Raman transition in order to transfer all the atoms ($\eta_{RF,max} = 100\%$) from the $m_J = 1$ to the $m_J = 0$ state as done in [90].

Once the $\eta_{RF}N$ atoms have been transferred into the $m_J = 0$ state, the atoms in the magnetic states are kicked out using a strong magnetic gradient, such that they are not falling onto the MCP. A sketch of the experimental detection sequence is given in Fig. 3.12.

3.2.3 Performances and limitations

Detection range

As it will be discussed in details in §3.3, under certain conditions, the spatial distribution of the atoms after the time-of-flight $t_{\text{tof}} = 297\,\text{ms}$ (that is to say the distribution recorded by the detector) is directly proportional to the momentum distribution by the ballistic formula:

$$\tilde{\rho}(\vec{k}) = \rho(\vec{k}) \times |w(\vec{k})|^2 \propto \tilde{\rho}_{\text{tof}}(\vec{r} = \frac{\hbar t_{\text{tof}} \vec{k}}{m}) \tag{3.9}$$

where $\tilde{\rho}_{\text{tof}}(\vec{r})$ is the spatial atomic density measured by the MCP after the 297 ms of time-of-flight. The finite size of the MCP is responsible for the detection of the momentum distribution over a limited range of momenta. More precisely, the radius of the MCP is $R_{MCP} = 4\,\text{cm}$, the measurement of the momentum distribution along x and y is limited to $\sqrt{k_x^2 + k_y^2} \leq k_{max}$ with $k_{max} \approx 8.45 \times 10^6\,\text{m}^{-1}$ while it is only limited by the duration of the acquisition in the direction perpendicular to the plates (gravity). When working with lattice gases, this value has to be

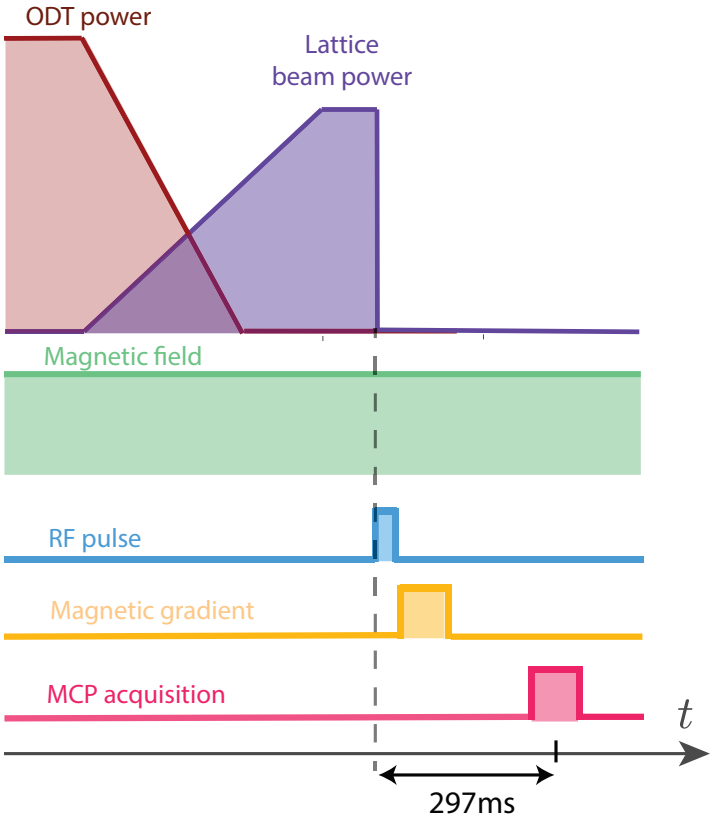

Figure 3.12: **Transfer of the atoms from the $m_J = 1$ to the $m_J = 0$ state.**

compared with the typical momentum components. For instance, we saw that the momentum distribution of a superfluid trapped into an optical lattice is characterized by periodic peaks reproducing along the lattice directions with a periodicity k_d where $k_d = 8.1 \times 10^6\,\mathrm{m}^{-1}$. As a result, we are able to measure the momentum distribution up to at least $k \approx \pm 1.1\,k_d$, including the first order diffraction peaks[3]. In fact, this range is a bit larger due to the geometry of the optical lattice: two of the lattice beams are oriented at 45° from the gravity, as a result, a factor $\sqrt{2}$ is won on the detection range (the same factor being necessarily lost in resolution) along these two directions.

Detection efficiency

The low detection efficiency is one of the main drawbacks of the electronic detector, especially for the measurement of the high-order correlation functions. It is defined as the percentage of the atoms detected by the electronic detector with respect to the number of atoms falling onto the MCP surface. It mainly depends on the fact that only a fraction of the atoms falling onto the MCP are triggering an electronic shower able to couple to the DL. With an open air ratio of about 90%, almost all the atoms that are arriving on the MCPs are falling in a micro-channel, so the detection efficiency is not limited by that. On the contrary, once in a micro-channel, an atom ionize a first electron, that has roughly a 1/2 probability of being ejected out of the channel and thus not available anymore to trigger the secondary electron necessary for the amplification process. Because of that, about one half of the atoms are lost for the detection.

If we consider an atom that has triggered a first electron going through the channel, the quality of the amplification can limit the detection. For instance, if the amplification of a pulse is low,

[3]Because the cloud is not falling exactly of the center of the MCP, one peak of the horizontal lattice beam is lost for the detection.

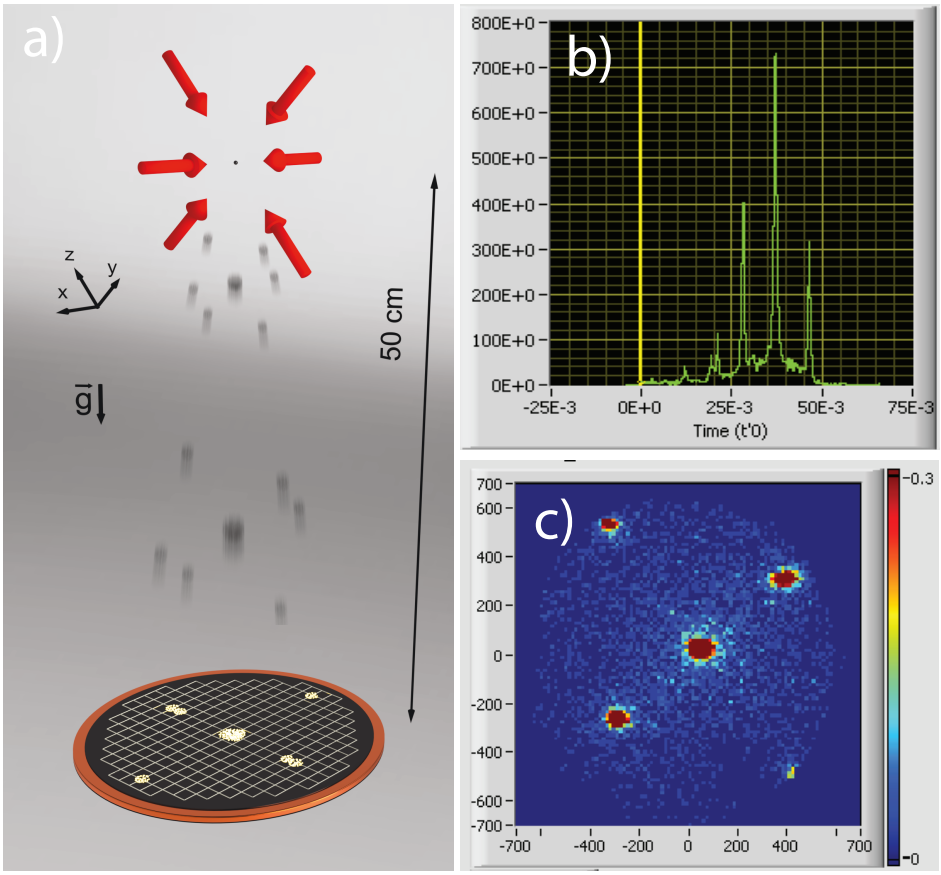

Figure 3.13: **Electronic detection of lattice superfluid. a)** Superfuid lattice gas falling onto the MCP. Because of the projection, the two peaks along the lattice direction at 45° from the gravity are falling onto the same location of the detector (peaks on the first diagonal of image c). **b)** Number of detected atoms as a function of time. **c)** Spatially resolved time integrated 2D count histogram of atoms detected on the MCP. The peaks on the bottom right is partly cut due to a bad centering of the lattice gas when falling onto the MCP.

the electronic shower will couple badly to the DLs, resulting in pulses of low amplitude that can be hard to separate from the electronic noise. Finally, noises on the electronic chain can be responsible for the missing of some atoms.

In order to calibrate the detection efficiency of the MCP, one has to count, for one given experimental realization, the number of atoms N_{MCP} detected divided by the number of atoms that felt on the MCP N_{MCP}^{hit}. If the first number is straightforward to get, knowing N_{MCP}^{hit} is not easy as it can be different from the total number of atoms N of the in-trap cloud probed for several reasons:

- In the experiment, only a fraction $\eta_{RF} < 50\%$ of the atoms are falling on the MCP surface (the atoms transferred to $m_J = 0$).
- All the atoms in the $m_J = 0$ state are not necessarily falling onto the MCP surface due its finite size. In particular, the clouds produced before the optical trap evaporation are too warm for their momentum distribution to be contained on the MCP surface. One needs also to pay attention to the saturation of the detector when trying to detect the distribution related to a Bose Einstein Condensate or a lattice superfluid. The best cloud that can be entirely detected on the MCP without any saturation problem is a Mott insulator.

When all the $m_J = 0$ atoms are falling on the MCP, the relation between the total number

of atoms N measured by using the optical imaging and the atoms detected with the electronic detector N_{MCP} writes:

$$N_{MCP} = N \times \eta \tag{3.10}$$

with $\eta = \eta_{RF} \times \eta_{MCP}$.
In the experiment, the detection efficiency has been estimated to $\eta_{MCP} = 30 \pm 10\%$ looking at the number of atoms detected on the MCP while performing Rabi oscillations of the BEC (with a large detuning of the RF frequency in order to avoid the detector saturation).

In the daily basis, the ratio $\eta = N_{MCP}/N$ is directly measured by imaging a Mott insulator at $s = 18$ with the camera (from which we access N) and measuring the number of counts detected onto the MCP. In this way, we are not sensitive to the possible fluctuations in η_{MCP} or η_{RF} (which can for instance happen if the resonance frequency of the RF has shifted).

Note that the maximum fraction of atoms that can be detected onto the MCP, taking into account the MCP detection efficiency and η_{RF}, is about $\eta_{max} \approx 15\%$.

Resolution in position

Here, we want to estimate the resolution in the measurement of the position of the particles detected by the electronic detector. For that, one needs to distinguish two different resolutions :

– *The in-plane resolution* that quantifies the error in position along x and y (horizontal plane). Reminding Eq. 3.5, the in-plane resolution is directly linked to the temporal resolution. Since the time is discretized with an elementary step of duration $t_0 = 120\,\text{ps}$, the in-plane position is also discretized with a pixel size that sets a lower bound for the in-plane resolution:

$$\delta x = \frac{1}{2} t_0 v_x \tag{3.11}$$

and is about $\delta x = \delta y = 60\,\mu\text{m}$.

The electronic chain and the way the analog pulses are converted into a list of times can be submitted to noise. The effect of the noise can add to the effect of the discrete time coding leading to the decrease of the resolution. Supposing that the noises in the measurements of the four times t_{x_1}, t_{x_2}, t_{y_1}, t_{y_2} are the same, then:

$$\sigma_x = \frac{1}{2}\sqrt{\sigma_{t_{x_1}} + \sigma_{t_{x_2}}} \times v_x = \frac{\sigma_t}{\sqrt{2}} v_x \tag{3.12}$$

One way to evaluate σ_t consists in looking at the fluctuations of the quantity D defined as:

$$D = t_{x_1} + t_{x_2} - (t_{y_1} + t_{y_2}) \tag{3.13}$$

If there is no noise, D is constant (and equal to zero if the DLs along x and y are exactly the same). In the presence of noise:

$$\sigma_D = 2\sigma_t \qquad \Rightarrow \qquad \sigma_x = \frac{\sigma_D}{2\sqrt{2}} v_x \tag{3.14}$$

In the experiment, we measured $\frac{\sigma_D}{2} \approx \sqrt{2} t_0$, resulting in an in-plane error of $\sigma_x \approx 2\delta x \approx 120\,\mu\text{m}$. A more detailed investigation of the in-plane resolution, in particular concerning the influence of the incoming particle flux can be found in [89].

– *The vertical resolution*, that is to say the resolution on the measurement of the positions along the gravity. Like in the former case, the discretization of the time is responsible for a discretization in the position measurement. Furthermore, the noise on the time measurement also translates into a noise in position.

$$\delta z = v_{COM} t_0 \approx 4 \times 10^{-10}\,\mathrm{m} \tag{3.15}$$

$$\sigma_z = v_{COM} \sigma_t \approx \sqrt{2} v_{COM} t_0 = \sqrt{2}\delta z \tag{3.16}$$

that are both about two orders of magnitude smaller than the in-plate pixel size and in-plane resolution. However, one needs here to consider an additional source of uncertainty. As it is depicted in Fig. 3.14, because of the inclination of the micro-channels of the MCP plates, two atoms separated by a certain distance Δz along the vertical direction can be detected at the same time. This results in an uncertainty on the measurement of the vertical position of:

$$\sigma_z \approx \Delta z_{max} = d_c / tan(\theta) \tag{3.17}$$

With $d_c = 12\,\mu$m and $\theta = 20°$, we get $\sigma_z \approx 32\,\mu$m, that is to say σ_z is equal to about a quarter of the in-plane resolution. Note that, as depicted by the blue points in Fig. 3.14, the angle has also an influence on the in-plane resolution: two points can excite the same microchannel, although separated in the x/y plane. However, the resulting in-plane position uncertainty is about $d_c \approx 12\,\mu$m, thus lower than $\sigma_{x/y}$ calculated before.

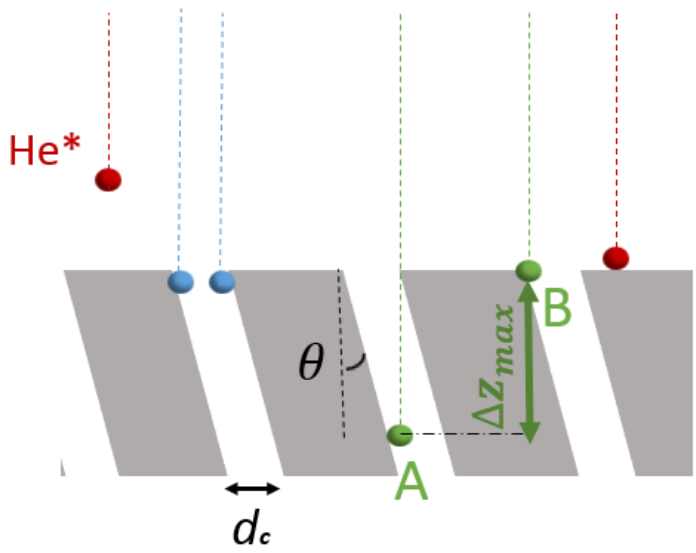

Figure 3.14: **Effect of the MCP channel angle on the detector resolution.** In order to avoid that the atoms go through the microchannel plate without hitting the walls, the microchannels are drilled with an angle $\theta = 20°$ from the vertical direction. As a result, the atoms A and B will be detected at the same time, although they did not arrived at the same time on the top surface of the MCP. The angle has also an effect on the in-plane resolution as demonstrated by the blue points: even if they arrive separated along the horizontal direction, they will excite the same microchannel and, as result, they will be detected on the same position of the detector. However, this position error is lower that the one originating from the time measurement uncertainty.

To summarize, we found:

$$\sigma_{x/y} \approx 120\,\mu\mathrm{m} \qquad \sigma_z \approx 32\,\mu\mathrm{m} \tag{3.18}$$

Using Eq. 3.9, this position resolution can be translated into a momentum-space resolution :

$$\sigma_{kx/ky} = \frac{m\sigma_{x/y} t_{tof}}{\hbar} \approx 2.0 \times 10^{-3}\, k_d \qquad \sigma_{kz} = \frac{m\sigma_z t_{tof}}{\hbar} \approx 5 \times 10^{-4}\, k_d \tag{3.19}$$

As it will be discussed later, this resolution is so good that it is not easy to measure it as it requires using a very narrow momentum distribution source (of the order of the resolution estimated). The only source currently available is the distribution given by the bunching peaks of a Mott insulator. By decreasing the size of these peaks down to a RMS size of about $0.012\,k_d$, we did not notice any saturation effect in the measurement of the sizes as it would happen when the resolution becomes of the order of the peaks size (see §.6.1). This confirms that $\sigma_{kx/ky} \ll 0.012\,k_d$ and $\sigma_{kz} \ll 0.012\,k_d$ and that the effect of the finite resolution can be neglected for the investigations carried out in this thesis.

Saturation

Besides the low detection efficiency, an other drawback of the electronic detection is the saturation, meaning that the detection efficiency can drop dramatically when the flux of particle to be detected is high. This is for instance the case when trying to measure the distribution of a BEC or a superfluid lattice gas.

One can distinguish different types of saturation:

- *The local saturation* happening at the surface of the MCP when it is submitted to a high particle flux. If two atoms arrive at the same location of the MCP within a time inferior to the characteristic time needed for the electronic charges to reload the depleted channel, the electronic amplification of the second pulse will be far lower than the amplification of the first one, decreasing the probability to be detected by the electronics. In the lab room, a very strong saturation manifests for instance when looking at the number of counts detected as a function of the time. Instead of measuring a number of counts that is symmetric with respect to the arrival time of the center of mass, the number of counts is asymmetric, and characterized by a number of detected atoms lower at longer times (see magenta curve in Fig. 3.15). However, one need to be careful since it can reveal difficult to detect a low saturation effects with this criteria.

  The problem of saturation has been widely investigated [91], although it is difficult to characterize it properly since it depends on many parameters (the type of MCPs, the incoming particle type, the polarization, the flux of particles). Previous He* experiments reported saturation effects for flux higher than $\phi_{atoms} = 125 \times 10^3$ particles/cm^2/s [11]. In our experiment, we evaluated the saturation threshold using a BEC. More precisely, by varying the RF pulse duration which sets the proportion of atoms transferred to the $m_J = 0$ state, one can go from a regime where there is no saturation, to a strongly saturating regime. Furthermore, as the saturation is local, some parts of the detected distribution can be saturated while the low density regions are not. The results displayed in Fig. 3.15 demonstrate a saturation effect for an incoming particle flux higher than $\phi_{max} \approx 250 \times 10^3$ atoms/cm^2/s, that is to say of the same order of magnitude than the one measured by other teams.

  In terms of momentum density, a saturation occurs for the distributions presenting a peaked momentum density higher than $n(k)_{max} \approx 30 \times 10^3\, k_d^{-3}$, which is easy to reach when working with lattice superfluids. In fact, if we consider a superfluid with $L = 20d$. Then the peak density is about $\alpha_0 \times N/(2\pi/L)^3 \approx 0.03 \times \alpha_0 N\, k_d^{-3}$ where α_0 represents the proportion of atoms in the central diffraction peak. This means that when working with lattice superfluid clouds, a saturation is happening as soon we reach a detection of about 10 atoms per peaks. This implies to work with a very low RF transfer.

- *The global saturation of the TDC* is due to the presence of a multiplexor working at 16.4 MHz which limits the detection of events at 16.4/4 MHz per channel. For flux higher than this value, the reconstruction efficiency drops. This effect has been investigated using UV-photon sources and is described more in details in [89]. In our experiment, we are usually working far from this limit.

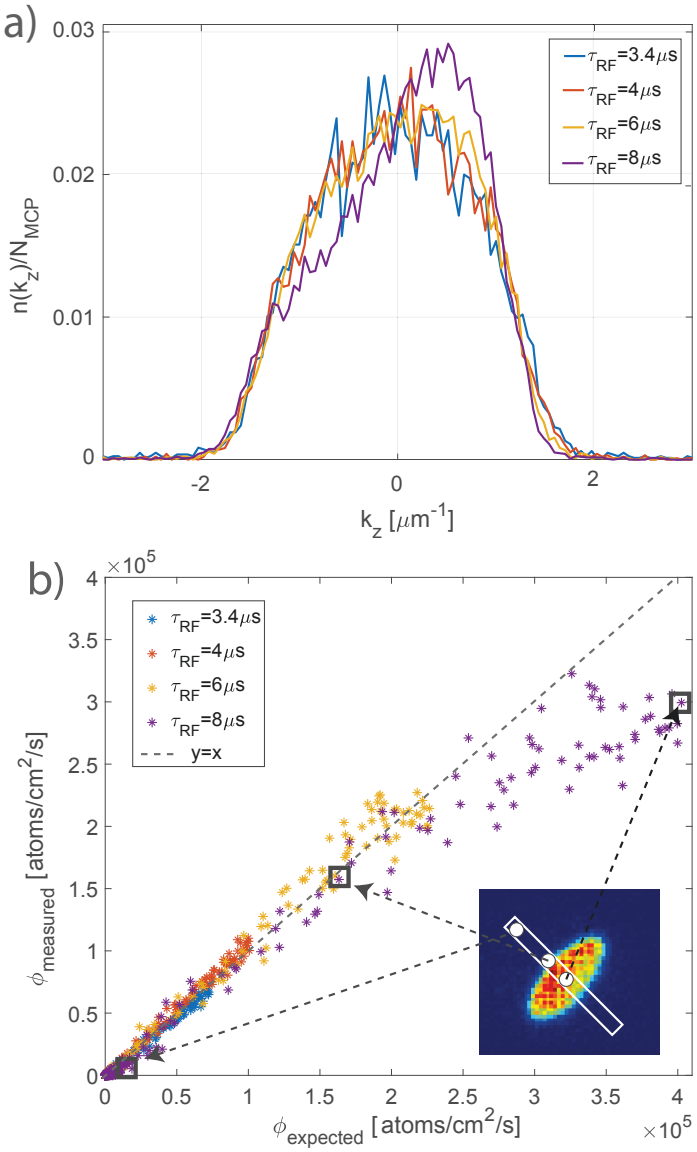

Figure 3.15: **Local saturation of the electronic detector. a)** Cuts along the gravity axis of the BEC distribution measured by the detector for increasing proportions of atoms hitting the MCP (the atom number is fixed) performed by increasing the RF transfer to the $m_J = 0$ state (by increasing the RF pulse duration). The density has been renormalized by the detected number of atoms. If there is not saturation, the curves are supposed to overlap. This is the case up to $\tau_{RF} = 6\,\mu$s. However, the saturation is present for the data with the maximum RF transfer which displays the characteristic asymmetry. **b)** For each bin of the cut and each RF pulse duration, is calculated the flux $\phi_{measured}$ as a function of the expected flux $\phi_{expected}$. $\phi_{expected}$ has been calculated considering that when there is no saturation, and provided we are in the linear regime of the Rabi oscillations (which was checked), $\phi_{measured} = \phi_{expected} \propto \tau_{RF}^2$. The results plotted in the figure show a saturation from particle flux higher than $\phi \approx 250 \times 10^3$ atoms/cm^2/s.

– *The "software" saturation* meaning that for high flux of data, it becomes hard for the program that converts the sequence of times in real atomic positions to find the 4-uplets corresponding to one atom, resulting in a lower reconstruction efficiency or in mistakes in the attribution of the coordinates. Here again, we are usually working far from this type of saturation.

3.3 Condition to access the in-trap momentum distribution

3.3.1 The far field regime of expansion

In this section, we calculate the evolution of the system after switching off abruptly the 3D optical lattice. We suppose that the atoms evolve freely during the propagation, that is to say that we neglect the interaction between the atoms during this phase. The validity of this hypothesis will be discussed in §.3.3.2. Under this condition, the evolution of the wavefunction is completely comparable to the propagation of waves in optics. For simplicity, and because the Hamiltonian of ideal particles is separable, we will consider the 1D case [77].

In the lattice, before the lattice potential is switched off at $t = 0$, the expression of the field operator is according to Eq. 1.13:

$$\hat{\Psi}(x, t = 0) = \sum_j w\left(x - x_j\right) \hat{b}_j \tag{3.20}$$

where x_j refers to the position in space of the lattice site j and w is the Wannier function centered on a lattice site. The Wannier functions can be approximated by the harmonic oscillator ground state[4] as depicted in Fig. 3.16.

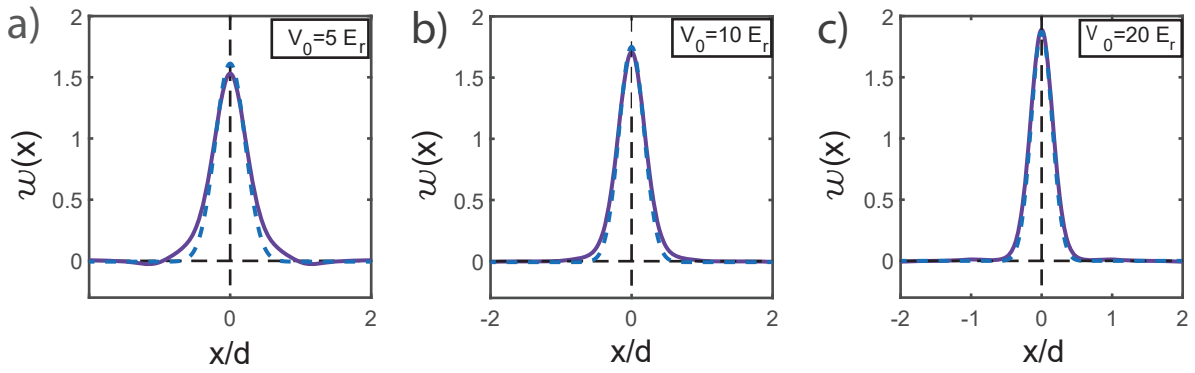

Figure 3.16: **Comparison between the Wannier functions and the harmonic oscillator ground state wave functions.** *In purple*, the Wannier functions. *In blue*: the Wannier functions under the harmonic approximation. **a)** $V_0 = 5\,E_r$, **b)** $V_0 = 10\,E_r$, **c)** $V_0 = 20\,E_r$.

$$w(x) \approx \frac{1}{\pi^{1/4}\sqrt{x_0}} \exp\left\{\frac{-x^2}{2x_0^2}\right\} \tag{3.21}$$

with $x_0 = \sqrt{\hbar/m\omega_{latt}} \approx 250 \times s^{-1/4}$ mm the oscillator length and ω_{latt} the oscillation frequency in each lattice site $\omega_{latt} = 2\sqrt{s} \times \omega_r$.

Time evolution of the wave function centered around the lattice site j.

At $t = 0$, the lattice potential is switched off. The wavefunction centered around the lattice site j evolves freely and writes under the harmonic oscillator approximation:

$$w\left(x - x_j, t\right) = \underbrace{\frac{1}{\pi^{1/4}\sqrt{W(t)}} \exp\left\{-\frac{(x - x_j)^2}{2W(t)^2}\right\}}_{amplitude} \times \underbrace{\exp\left\{-i\frac{(x - x_j)^2}{2W(t)^2}\frac{\hbar t}{m x_0^2}\right\}}_{phase} \tag{3.22}$$

[4] At least qualitatively for $s > 5$.

with $W(t) = x_0\sqrt{1+(\hbar t/mx_0^2)^2}$ the time-dependent width of the gaussian envelope.
This envelope expends rapidly and for $t \gtrsim 10\,\mu$s, $W(t > 10\,\mu s) \sim \hbar t/mx_0$ and $W(t > 10\,\mu s) > d$.

Let's now consider the amplitude and the phase terms separately:

1. *Amplitude factor:* For $|x| \ll W(t)$ and $t > 1$ ms (to ensure that $W(t) > L$ where L refers to the in-situ cloud size), one can show that $\exp\left\{-\frac{(x-x_j)^2}{2W(t)^2}\right\} \approx \exp\left\{-\frac{x^2}{2W(t)^2}\right\}$. This hypothesis means that if we restrict the observation of the wavefunction to the typical width $W(t)$, one can forget the dependence on the initial site for the amplitude term.

2. *Phase factor:* Provided that $t \gg \frac{mL^2}{2\hbar}$, the phase factor is equal to $\exp\left\{-i\frac{m}{2\hbar t}\left(x^2 - 2xx_j\right)\right\}$, that is to say one can neglect the quadratic factor in the initial site position in the phase term.

Consequently, under the two conditions:

$$|x| \ll W(t) \quad \text{(Condition.1)} \qquad\qquad t \gg t_{\mathrm{FF}} = \frac{mL^2}{2\hbar} \quad \text{(Condition.2)} \tag{3.23}$$

Equation. 3.22 simplifies:

$$w\left(x - x_i, t\right) = \sqrt{\frac{m}{\hbar t}} \times e^{i\frac{\hbar Q(x)^2 t}{2m}} \tilde{w}\left[Q(x)\right] \times e^{-iQ(x)x_i} \tag{3.24}$$

with $Q(x) = \frac{mx}{\hbar t}$

Adding the contribution to the different lattice sites.

Injecting the former equation into Eq. 3.20 and generalizing to the 3D case, one obtains the expression of the wave function:

$$\hat{\Psi}(\vec{r}, t) = \sum_j w\left(\vec{r} - \vec{r}_j, t\right)\hat{b}_j = \left(\frac{m}{\hbar t}\right)^{3/2} \times \tilde{w}\left[\vec{Q}\right] e^{i\frac{\hbar \vec{Q}^2 t}{2m}} \times \sum_j e^{-i\vec{Q}.\vec{r}_j}\hat{b}_j \tag{3.25}$$

The atomic density after a long time-of-flight $\rho_{\mathrm{tof}}(\vec{r}, t) = \left\langle \hat{\Psi}^\dagger(\vec{r}, t)\hat{\Psi}(\vec{r}, t)\right\rangle$ can be written:

$$\rho_{\mathrm{tof}}(\vec{r}, t) = \mathcal{F}(\vec{Q} = \frac{m\vec{r}}{\hbar t}) \times \mathcal{S}(\vec{Q} = \frac{m\vec{r}}{\hbar t}) \tag{3.26}$$

with:

– *the form factor* $\mathcal{F}$

$$\mathcal{F}(\vec{Q}) = \left(\frac{m}{\hbar t}\right)^3 \times \left|\tilde{w}(\vec{Q})\right|^2 \tag{3.27}$$

It plays the role of a smooth envelope.

– *the structure factor* $\mathcal{S}$

$$\mathcal{S}(\vec{Q}) = \sum_{j,i} e^{-i\vec{Q}.(\vec{r}_j - \vec{r}_i)}\left\langle \hat{b}_i^\dagger \hat{b}_j\right\rangle \tag{3.28}$$

It contains the information about the coherence of the source.

Remark:

- *Analogy with the optics.* There is a strong analogy between the free propagation of the matter-wave from the optical lattice and the propagation of a light-wave in free space through the Huygens-Fresnel decomposition. Condition 1 is the analog of the paraxial approximation in optics and Condition 2 is the analog of the far-field (FF) limit defining the regime where the Fraunhofer diffraction applies.

- *Intuitive determination of t_{FF}.* As done in [92], the far-field condition ($t_{\text{tof}} \gg t_{\text{FF}}$) can be guessed intuitively. In the far field regime, the quadratic term in the phase factor has to be negligible, *i.e*, $\frac{m}{2\hbar t}\left(\vec{r}_j^{\,2} - \vec{r}_i^{\,2}\right) = \frac{m}{2\hbar t}\left(\vec{r}_j + \vec{r}_i\right).\left(\vec{r}_j - \vec{r}_i\right) \ll 1$. The maximum value of $\left(\vec{r}_j + \vec{r}_i\right).\left(\vec{r}_j - \vec{r}_i\right)$ is equal to L^2, and the former condition is satisfied whatever i and j if: $\frac{L^2 m}{2\hbar t} \ll 1$, which corresponds to the far field condition found before.

Mapping between the momentum distribution and the atomic distribution after a long time-of-flight

Here, we introduce the in-trap momentum space operator:

$$\hat{a}(\vec{k}) = \frac{1}{\sqrt{V}} \sum_j e^{-i\vec{k}.\vec{r}_j} \hat{b}_j \tag{3.29}$$

The momentum density writes:

$$\rho(\vec{k}) = \left\langle \hat{a}^\dagger(\vec{k})\hat{a}(\vec{k}) \right\rangle = \frac{1}{V} \sum_{j,i} e^{-i\vec{k}.(\vec{r}_j - \vec{r}_i)} \left\langle \hat{b}_i^\dagger \hat{b}_j \right\rangle = \text{FT}[C^{(1)}](\vec{k}) \tag{3.30}$$

with $C^{(1)}(i,j) = \left\langle \hat{b}_i^\dagger \hat{b}_j \right\rangle$ the first order correlation function. The comparison between Eq. 3.26 and Eq. 3.30 gives:

$$\boxed{\rho(\vec{k}) = \frac{\rho_{\text{tof}}(\vec{r} = \frac{\hbar t}{m}\vec{k}, t)}{\left(\frac{m}{\hbar t}\right)^3 \times \left|\tilde{w}(\vec{k})\right|^2}} \tag{3.31}$$

Provided there is no interaction effect during the time-of-flight and the conditions 1 and 2 are satisfied, that is to say when the time of flight exceed t_{FF} and we are investigating the atomic distribution close to the center, the time-of-flight atomic distribution maps the in-trap momentum distribution.

Effect of the finite time-of-flight

Without considering the far-field approximation, the atomic density during the time of flight writes in the 1D case:

$$\rho_{\text{tof}}(x,t) = \left(\frac{m}{\hbar t}\right) \times \left|\tilde{w}(\frac{mx}{\hbar t})\right|^2 \frac{1}{V} \times \sum_{j,i} e^{i\frac{mx}{\hbar t}(x_j - x_i) - i\frac{m}{2\hbar t}\left(x_j^2 - x_i^2\right)} \left\langle \hat{b}_i^\dagger \hat{b}_j \right\rangle \tag{3.32}$$

Using for the first-order correlation function and the in-situ density profiles the expressions introduced in §.2.2.2 to treat the limits $U/J \to 0$ and $U/J \to \infty$, and considering a Thomas-Fermi profile for the superfluid extending over $M = 2M'$ lattice sites and a unique Mott plateau for the Mott insulator, we can derive the analytic solution for the evolution of the atomic density as a function of the time-of-flight:

SF ($U/J \to 0$)	MI ($U/J \to \infty$)
$\left\langle \hat{b}_i^\dagger \hat{b}_j \right\rangle = \sqrt{\bar{n}_i}\sqrt{\bar{n}_j}$	$\left\langle \hat{b}_i^\dagger \hat{b}_j \right\rangle = \delta_{i,j}\bar{n}_j$
$n_j = \bar{n} \times \left(1 - (j/M')^2\right)$	$\bar{n}_j = n_0$ for $j \in [-M'; M']$
$\rho_{\text{tof}}(x,t) = \left(\frac{m}{\hbar t}\right)\left\lvert\tilde{w}(\frac{mx}{\hbar t})\right\rvert^2 \times \left\lvert \sum_{j=-M'}^{j=M'} \bar{n} e^{i\frac{mx}{\hbar t}x_j - i\frac{m}{2\hbar t}x_j^2} \right\rvert^2$	$\rho_{\text{tof}}(x,t) = \left(\frac{m}{\hbar t}\right)\left\lvert\tilde{w}(\frac{mx}{\hbar t})\right\rvert^2 \times N$

– *Propagation of a perfect MI*
Because of the absence of coherence between the lattice sites, the wave packets centered on the different lattice sites do not interfere between each other during the expansion and the quadratic term is canceling when replacing the double sum in Eq. 3.32 by a simple sum. There is no far-field condition in this case. Of course, this approximation does not hold anymore when getting close to the transition where some coherence can be restored (see §.5).

– *Propagation of a SF*
In Fig. 3.17 is represented the calculated 1D profiles during the expansion of the lattice superfluid. For $t < t_{\text{FF}} \approx 50\,\text{ms}$, the diffraction is near-field. The peaks are large since they are not fully developed. Once the FF regime is reached, the distribution is scale invariant with the scaling factor $k_x = \frac{mx}{\hbar t}$ which makes the link between the position-space and the momentum-space. The size of the diffraction peaks σ reaches the Fourier limit $\sigma = 2\pi/L$ (see §.2.2.4), which is confirmed by the formula:

$$\rho_{\text{tof}}(x, t \to \infty) \propto \left(\frac{\sin\left(\frac{Mmxd}{2\hbar t}\right)}{\sin\left(\frac{mxd}{2\hbar t}\right)}\right)^2 \propto \left(\frac{\sin\left(\frac{k_x dM}{2}\right)}{\sin\left(\frac{k_x d}{2}\right)}\right)^2 \tag{3.33}$$

3.3.2 Effect of the interactions

To be sure to measure the momentum distribution of the lattice gases after a time-of-flight, interactions between the atoms should be cut at the beginning of the time-of-flight in order for the expansion to be ballistic. In the He experiment, this is not possible due to the absence of a Feshbach resonance that could be used in order to set a_s to 0. One can understand that interactions affect the TOF distribution from energetic arguments. Because of the conservation of the energy (close system), the energy of the trapped gas must be found in the asymptotic TOF distribution. As the latter is only of kinetic kind (because the density is extremely diluted), the asymptotic TOF distribution must comprise both the in-trap kinetic and the average interaction energy. During the first stage of the expansion, the atoms located on the same lattice site expend with the influence of the mean-field energy generated by other atoms initially present in the same lattice site. At a later time, the different wave-functions expending from different lattice sites begin to overlap and an additional mean-field effect between atoms located initially on different lattice sites occurs (this effect is expected to be far less dramatic since by the time the wavefunctions of different sites begin to overlap, the atomic density has decreased by a lot). As a result, the atomic density measured at a long time-of-flight might not map the in-trap momentum distribution anymore.

Furthermore, beyond mean-field effects can also play a role during the time-of-flight. In fact, the momentum distribution of a superfluid lattice gas is characterized by the presence of high-momentum components that can induce two-body collisions at the beginning of the time-of-flight.

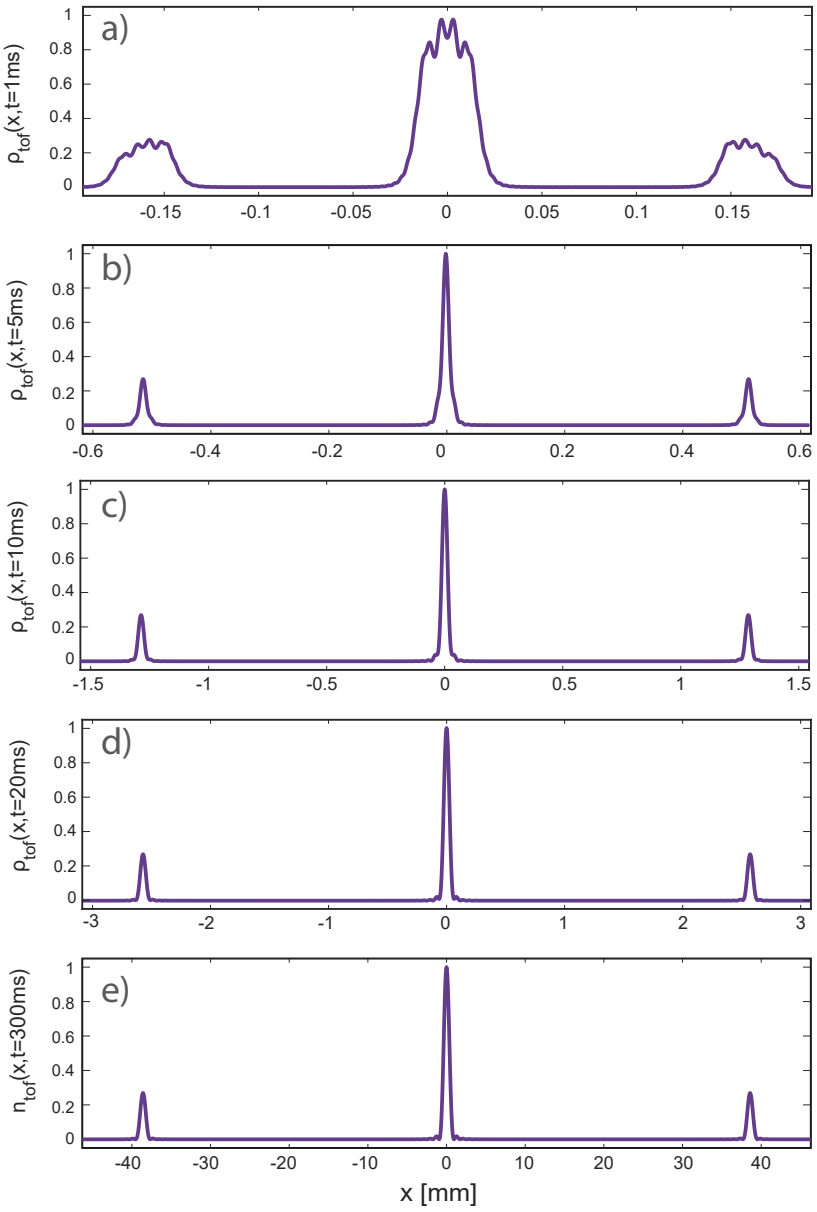

Figure 3.17: **Atomic density as a function of the time of flight**. Calculated ρ_{tof} as a function of x for different time-of-flights in the case of a 1D lattice with $M = 2M' = 60$ and $s = 10$. **a)** $t = 5\,\text{ms}$. **b)** $t = 10\,\text{ms}$. **c)** $t = 20\,\text{ms}$. **d)** $t = 300\,\text{ms}$.

Effect of the interactions treated at the mean-field level

- *Phase contribution.* First, let us consider a lattice site with only one atom. At very short time (when the different wavefunctions localized on the different lattice sites have not overlapped yet), the expansion is ballistic and driven by the zero point energy of the lattice site, $\omega_{\text{latt}}/2\pi \geq 100\,\text{kHz}$. If a lattice site is filled with two atoms, the difference with the former case is that now, there is an interaction energy U_{int} entering the problem. Since $U_{\text{int}}/h \approx$ kHz $\ll \omega_{\text{latt}}/2\pi$, the expansion is still driven by the zero point energy of the lattice site local harmonic oscillator. However, Kupferschmidt and colleagues demonstrated in [93] that a phase is added during the expansion as compared to the single particle case. The origin of this phase comes from the fact that the time evolution of the phase of the wave-function of a lattice site depends on its initial energy: when filled with more than one atom, the energy E_2 associated to the lattice site is larger (typically by U_{int}) with respect to that of a unity-filled site E_1. As a consequence, a phase difference $(E_1 - E_2) \times t/\hbar$ appears between the two wave-functions over a time duration t. As a result, if we consider now many lattice sites with different fillings (as it is the case in

the superfluid regime due to the on-site number fluctuations), the different wavepackets interfere during the time of flight with a phase that depends on the lattice site filling at the beginning of the TOF (this interaction dependent phase factor was not taken into account in the former section). The interaction are consequently at the origin of a dephasing between the different wavepackets. By analogy with the optics, one finds that this dephasing will result in the decrease of the interference pattern contrast. If this can be dramatic in lower dimensions as reported in [94], in 3D, provided $a_s \ll x_0$ ($U_{\text{int}} \ll \hbar\omega_{\text{latt}}$) and the lattice filling is not too high, the contrast should not be decreased by more than 5%, which generally sits on the experimental error bars for the density distribution measurements.

- *Mean-field energy during the overlap of single-site wavefunctions.* While the wavepackets coming from the different lattice sites overlap at the beginning of the TOF, a mean-field energy term proportional to the atomic density may enter the problem. However, by the time the wavepackets begin to overlap, the atomic density has decreased by a factor $(x_0/d)^3 \approx (150\,\text{nm}/750\,\text{nm})^3 \approx 10^2$ (for $s = 10$). This effect is consequently negligible. But if it was not, it would manifest as a broadening of the diffraction peaks (as it is the case in expending BEC's).

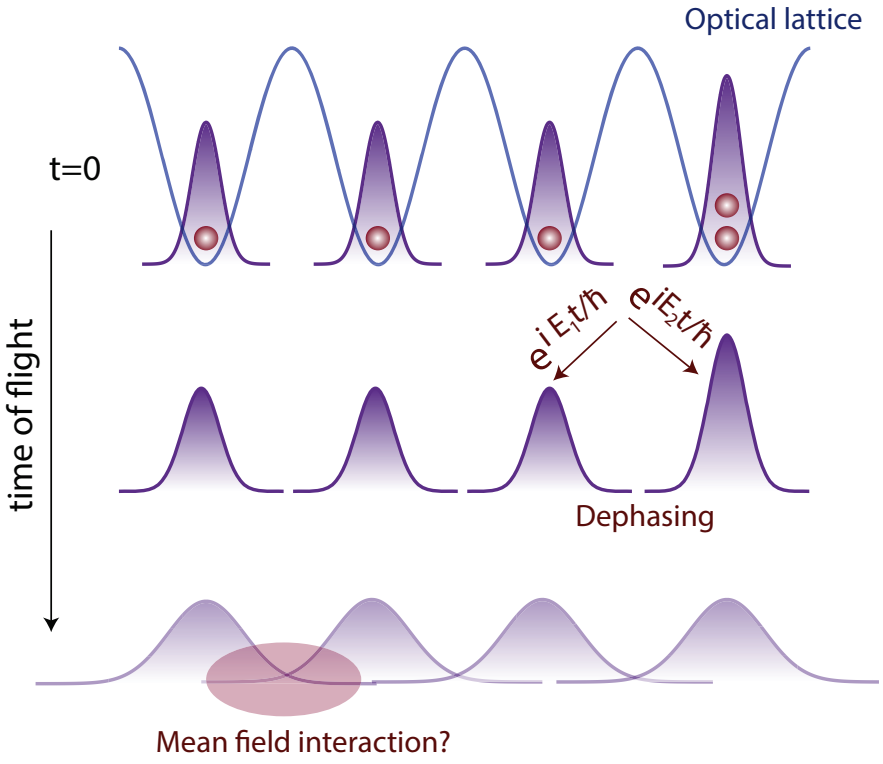

Figure 3.18: **Effect of the interactions during the time of flight**. Interactions can be responsible for the breakdown of the mapping between the far-field atomic distribution and the in-trap momentum distribution given in Eq. 3.31.

Two-body collisions

If interactions at the mean-field level during the time-of-flight have been widely investigated, mainly in order to understand whether the time-of-flight distribution is directly mapping the in-trap momentum distribution, beyond mean-field studies remains elusive. One effect, easily observable in 1D lattice gases or 2D in lattice gases with elongated geometries is the presence of scattering halos surrounding the diffraction peaks [86]. This is due to the fact that while they separate, atoms with different velocity classes (the diffraction peaks for instance) can undergo s-wave scattering collisions. For the same reasons, halos have also been observed during the collision of two condensates [95, 96]. In a 3D optical

lattices with a spherical symmetry, this effect is less important because the atomic density is decreasing rapidly during the time-of-flight and the 3D scattering spheres are more difficult to resolve with a 2D optical imaging. Previous works evaluated numerically the order of magnitude of the percentage of the atoms in the collision spheres [97], although no quantitative investigation has been carried out so far. The collisions have been neglected in most of the experiments. For most of the data taken during this thesis,we were unable to detect the presence of collision spheres in the momentum distribution. This was attributed to the fact that the number of collisions is proportional to the atomic density and only low atom number clouds were probed (the lattice filling at the center of the cloud was at maximum equal to 2).

With the possibility to create 3D optical lattice gases and to measure the full momentum distribution with a large dynamic range, the He* experiment has everything required to investigate this effect. To confirm our hypothesis and to demonstrate that collisions are actually negligible, we have investigated this effect. The results are given in §.3.4.3.

3.3.3 Summary of the conditions required to access the momentum distribution in TOF measurements

Far field regime:
For a finite size cloud of length $L = Md$, t_{FF} depends on M, on the mass m and on the lattice spacing d. In Tab. 3.1, we compare the far-field condition in the He experiment and in Rb experiments.

Atom	He	Rb
Atomic mass m [u]	4	87
Lattice spacing d [nm]	775	400
t_{FF} [ms]	50	250

Table 3.1: **Comparison of the far-field regime in He and Rb experiments.** The light mass of the Helium atom enables to compensate the fact that for a system of M lattice sites, the Rubidium cloud is almost 2 times smaller than the Helium one. For $M = 50$, the far-field regime is reached after 250 ms for Rb clouds, and after 50 ms for the He one.

In most of the experiments using imaging techniques to probe the clouds after a time-of-flight, t_{tof} is generally limited to 30 ms (the longer is the TOF, the more dilute is the cloud, and the noisier is the image obtained with usual imaging techniques), which means that these experiments are generally not probing the clouds in the far-field regime of expansion since $t_{\mathrm{tof}} \gtrsim t_{\mathrm{FF}}$. In our experiment, although t_{FF} is long, the atoms can be probed after 297 ms time of flight, that is to say $t_{\mathrm{tof}} \gg t_{\mathrm{FF}}$. The far-field condition is consequently fulfilled.

The effects of interactions during the expansion:
Most of the experiments in the thesis are performed with a filling close to 1 and the scattering length is small. As a results, the effect of the interactions during the time-of-flight is expected to be negligible.

From a theoretical point of view, these two aspects guaranty that the measured atomic distribution after the 297 ms time-of-flight maps directly the in-trap momentum distribution of the lattice gases. However, since the He* experiment relies on the measurement of the momentum distribution, we did check experimentally all these criteria.

3.4 Experimental verification

3.4.1 Far-field regime

In the far field regime, the atomic density scales perfectly with the in-trap momentum distribution using the ballistic relation $\vec{k} = \frac{m\vec{r}}{\hbar t}$ (the distribution is just dilating linearly with time). The near- and the far-field regimes can consequently be identified by looking at the ratio $r = \sigma/d_{pp}$ where d_{pp} refers to the distance between two diffraction peaks and σ their size (here the rms size). In the near-field regime, the ratio is expected to vary as $r \approx 1/t$ while it is approaching a constant in the far-field regime.

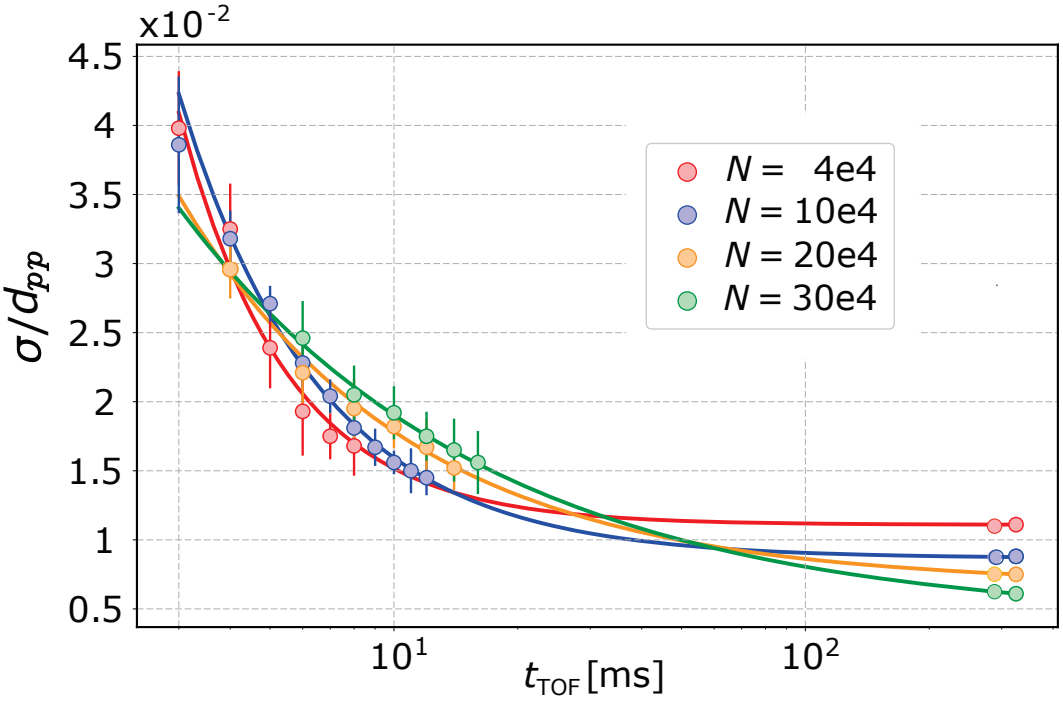

Figure 3.19: **Far-field regime in the He experiment.** Time evolution of the width σ of the diffracted peaks normalized to the peak distance d_{pp}. The data have been taken at $s = 10$ and for different atom numbers N. The solid lines are a guide to the eye.

The measurement of the ratio $r_\sigma = \sigma/d_{pp}$ for different time-of-flights and different cloud sizes is presented in Fig. 3.19. Except for the data corresponding to $t_{tof} = 325\,\text{ms}$ and $t_{tof} = 297\,\text{ms}$ that have been taken with the help of the electronic detector, the ratio has been extracted from the 2D images of the clouds after different time-of-flights. The data in red ($N = 4 \times 10^4$ atoms) corresponds to the case of clouds with $M = 50$ for which we previously calculated $t_{\text{FF}} \approx 50\,\text{ms}$, and which represents the wider cloud used for all the data referred to in this manuscript (consequently for which the far-field condition is the most difficult to fulfill). Looking at the graph, the ratio r_σ saturates around $t \approx 100\,\text{ms}$, in agreement with t_{FF}. The far-field regime takes as expected more time to set when the number of atoms increases (so as the cloud size). However, for all the data presented here, the far-field regime is reached before 300 ms.

This demonstrates that the measurements done with the electronic detector are performed deep in the far-field regime for all the range of parameters used in the Helium experiment.

3.4.2 QMC comparisons

We identified previously two possible effects of the interactions at the mean-field level on the distributions obtained after the time-of-flight. The on-site interaction energy initially present in the system can be at the origin of a lower contrast of the diffraction peaks in the superfluid phase whereas a

mean-field interaction that may appear during the time-of-flight would result in an increase of the peak width. Since the interaction energies to consider here are very small as compared to $\hbar\omega_r$, interaction effects should result in small modifications of the measured distribution as compared to the momentum distribution, and thus requires a precise knowledge of the momentum distribution. As a results, we choose to compare the measured profiles with QMC calculations. More precisely, we compared the momentum distribution computed with the QMC method and the experimental distribution of lattice superfluid gases at $U/J = 9.6$, that is too say in an intermediate regime between a non correlated superfluid ($U = 0$) and a regime driven by interactions. It is crucial to stress here that the QMC calculations we refer to are calculations of the in-trap momentum distributions. In particular, this means that these QMC distributions DO NOT take into account the experimental configuration where a TOF dynamics occurs (like it is the case for instance in [98]). This original approach, that has never been performed before our work, thus does not rely on any assumptions about the experiment. The advantage of this method also relies on the fact that the finite temperature of the clouds can be taken into account in the problem. These QMC calculations have been performed by Giuseppe Carleo using the worm algorithm as discussed briefly in §.1.2.3.

Experimental parameters

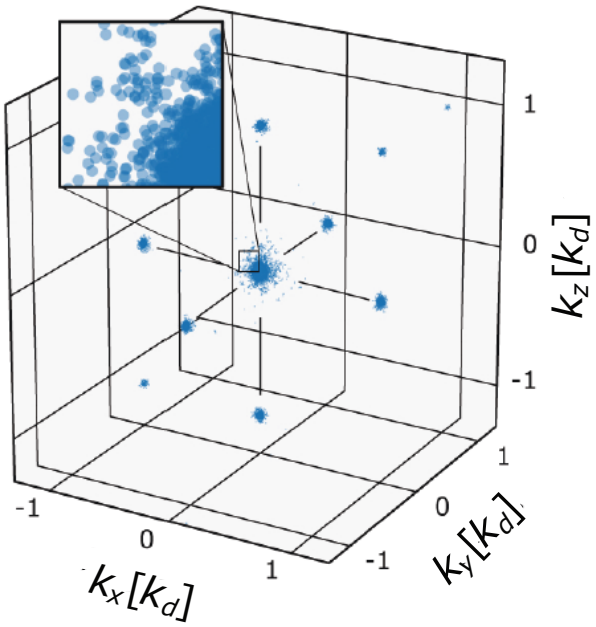

Figure 3.20: **Three-dimensional atom distribution of a lattice gas measured with the electronic detector.** Atom-by-atom reconstruction of the 3D momentum distribution for a ratio $U/J = 9.6\,(3)$ of the Bose-Hubbard parameters and obtained from about 500 experimental runs (here only $t_{tof} = 297\,\text{ms}$). Each blue dot is a single atom. The inset is a magnified view of the central region.

The experimental data have been taken with a pure BEC of $N = 40\,(8) \times 10^3$ atoms loaded into the 3D optical lattice at $U/J = 9.6\,(3)$ (with $w_{ext} = 2\pi \times 140\sqrt{V_0}\,\text{s}^{-1}$). This number of atom has been chosen in order to have a filling inferior to 2 at the center of the cloud (Fig. 3.22). The atom number is calibrated using the absorption imaging: the number of atoms in the Bose Einstein Condensate before the transfer to the optical lattice trap is measured and compensated from the imperfect transfer efficiency (about 10% loss during the transfer).

The atomic distribution is measured after 325 ms time-of-flight using the electronic detection. Because of the high atomic density present in the diffraction peaks, one needs to pay attention to the saturation of the detector. We measured that an effect of saturation of the detector is appearing when the fraction of the atoms detected η onto the MCP is more than 0.3% (corresponding to a detection of

100 atoms/shot). Because of the Wannier envelope, the side peaks are less dense and the saturation is appearing for higher values of transfer efficiency, about 1.5%. In order to optimize the time required to measure the full time-of-flight distribution with a good statistics and a good dynamic range, we choose to divide the data into two sets:

- One set of about 500 shots with $\eta \approx 1.5\%$ to be able to measure the low density parts of the time-of-flight distribution.

- One set of about 1000 files with $\eta \approx 0.3\%$ in order to access the central peak with no saturation effect.

We then used the first order diffraction peaks, not saturated in the both case (see Fig. 3.21), to patch together the two sets of data.

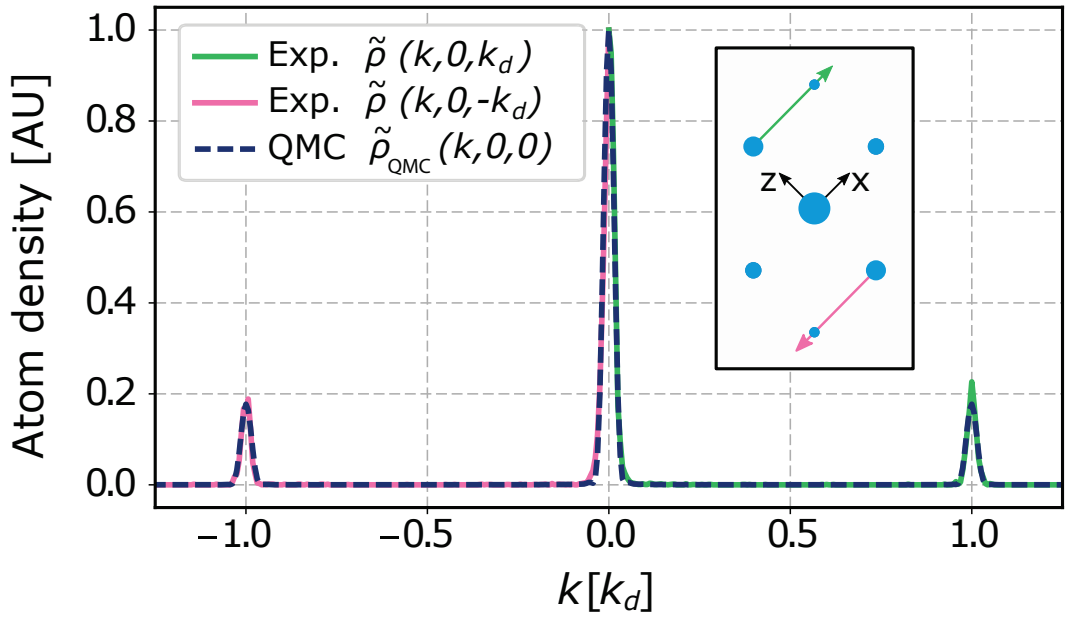

Figure 3.21: **Saturation effect of the electronic detection.** 1D cuts $\tilde{\rho}(k, 0, \pm k_d)$ compared to the QMC profile $\tilde{\rho}_{QMC}(k, 0, 0)$. The height of the central peak of these distributions has been normalized to one. Saturation effects are not present on the first- and second-order peaks of diffraction.

For the comparison with the QMC data, 1D cuts along the lattice directions are calculated. As we are detecting the atoms one by one, the cut along the x-direction $\tilde{\rho}(k_x, 0, 0)$ is calculated by making the histogram of the k_x values for all the atoms with $k_y = k_z = 0$. To get a good signal to noise ratio, some weak transverse integration $\Delta k_\perp$ is allowed, however paying attention no to decrease the amplitude of the peaks. The longitudinal discretization step Δk of the histogram requires also to be far smaller that the finest structure in the diffraction pattern (typically the peak size). The final values chosen are $\Delta k = k_d/160$ and $\Delta k_\perp = 3 \times k_d/160$.

QMC parameteres

The QMC simulation have been performed with the parameters corresponding to the experiment: N, ω_{ext}, U, J, ω_r and taking into account the Wannier envelop ($\tilde{\rho}_{QMC} = |\tilde{w}|^2 \times \rho$). The QMC profiles are also calculated using the same transverse and longitudinal integration for a direct comparison. The only free experimental parameter that is not possible to measure a priori in the experiment is the temperature. The QMC simulations have consequently been performed for a set of temperatures ranging from $T = J$ to $T = 10\,J$.

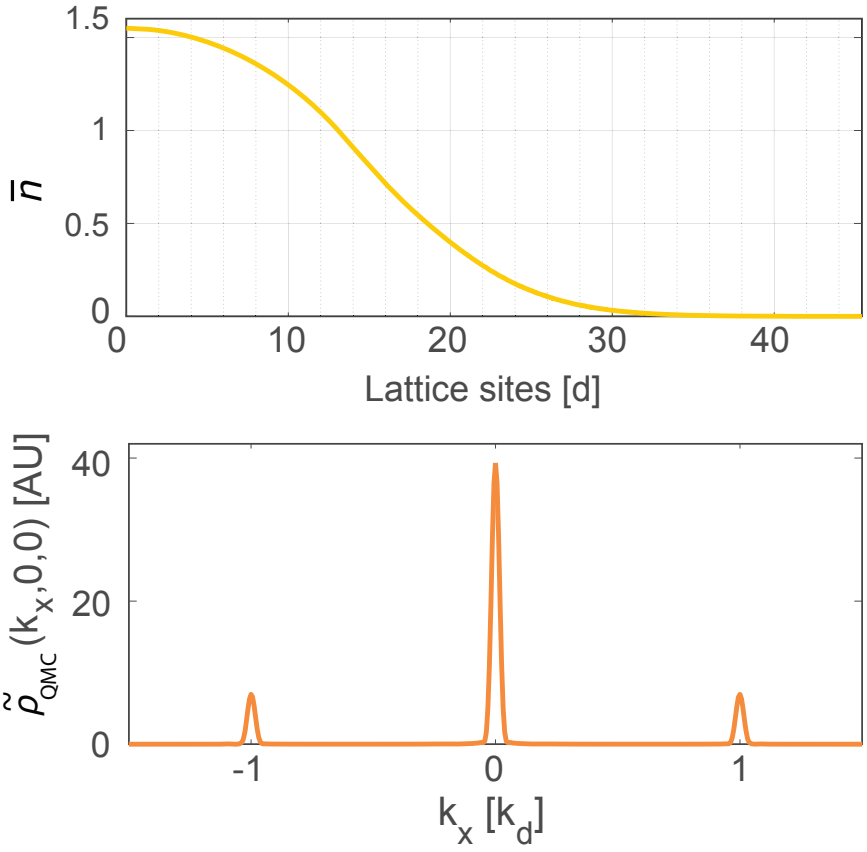

Figure 3.22: **In-situ density distribution and the momentum distribution calculated with the QMC method for T = 3.9 J.** *Top graph:* In-situ density expressed in terms of the average lattice filling $\bar{n}$. The cloud extends over 25 lattice sites radius and the average filling at the center is lower than 2 ($\bar{n} \sim 1.5$). *Bottom graph:* Corresponding momentum distribution in an arbitrary unit.

Comparison between the two distributions

In Fig. 3.23 are plotted a 1D cut along one lattice direction along with the cut calculated with the QMC method for $T = 3.9\,J$. The temperature has been chosen carefully with a method explained in §.4. The two distributions have been overlapped using the first order diffraction peaks. By doing so, the two distributions match very well over 3 orders of magnitude in density. The only two regions where there are some discrepancies are:

- The central region due to the saturation of the central peak.
- The very low densities at the border of the first Brillouin zone ($k = \pm k_d/2$) and due to a poor statistics.

Besides that, the diffraction peaks are Fourier limited and not broadened by interactions. The contrast of diffraction pattern corresponds within a few percents to the one of the QMC data. Finally, the good overlap between the distributions eliminates the existence of other experimental problems (the presence of a high density background, an oscillation of the cloud, a low resolution in the momentum space etc...).

As a conclusion, this is an experimental validation of our experiment as a good quantum simulator for the investigation of the Mott transition in the momentum space.

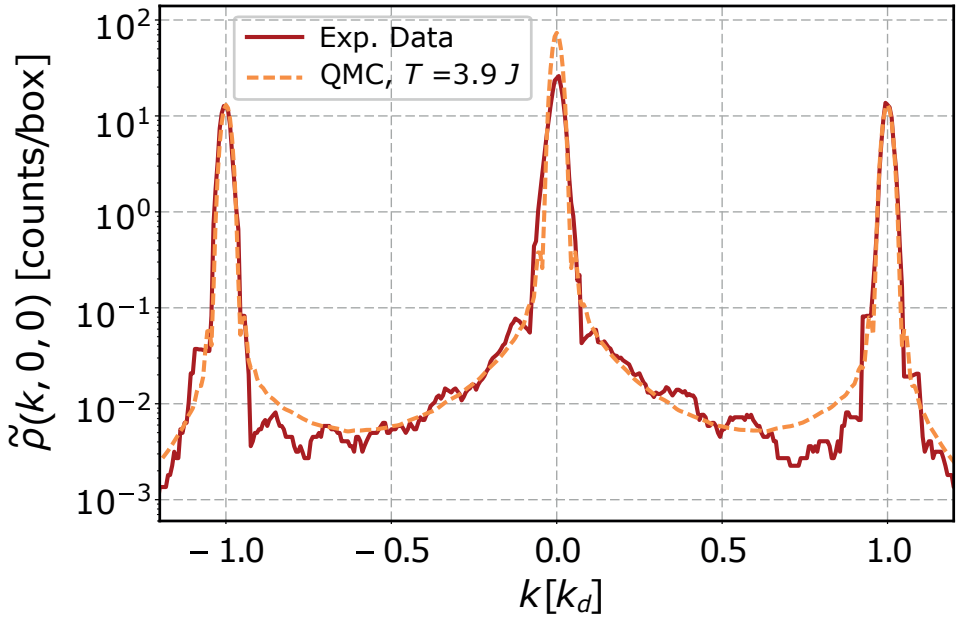

Figure 3.23: **Comparison of the measured atom distribution $\tilde{\rho}$ with ab-initio Quantum Monte-Carlo calculation of the in-trap momentum distribution $\tilde{\rho}_{\mathbf{QMC}}$.** Log-plot of 1D high flux cuts through the measured 3D distribution $\tilde{\rho}$ (red), and $\tilde{\rho}_{QMC}(k,0,0)$ through the QMC momentum distribution (dashed orange line) obtained for our experimental parameters and $T = 3.9\,J$. The temperature T is the only adjustable parameter.

3.4.3 Collisions during the expansion of a lattice gas

When the lattice potential is switched off, the quasi-momenta map into momenta and different copies of the initial state are created along the lattice axis, with an average momentum equal to $j \times k_d$. Due to their high relative velocities, two copies with an average momentum $j \times k_d\vec{u}_1$ and $j' \times k_d\vec{u}_2$ ($j \neq j'$, $\vec{u}_2$ and $\vec{u}_1$ are two directions of the lattice basis), can collide efficiently. If we consider two atoms from different copies that are colliding (elastic scattering), then:

$$\vec{k}_1 + \vec{k}_2 = \vec{k'}_1 + \vec{k'}_2 \tag{3.34}$$

with:

$$\vec{k}_1 = j \times k_d\vec{u}_1 \qquad \vec{k}_2 = j' \times k_d\vec{u}_2 \tag{3.35}$$

$$\vec{k'}_1 = \frac{\vec{k}_1 + \vec{k}_2}{2} + \frac{|\,\vec{k}_2 - \vec{k}_1\,|}{2}\vec{u}_{sc} \qquad \vec{k'}_2 = \frac{\vec{k}_1 + \vec{k}_2}{2} - \frac{|\,\vec{k}_2 - \vec{k}_1\,|}{2}\vec{u}_{sc} \tag{3.36}$$

where $\vec{k}_1$ and $\vec{k}_2$ represent the momentum of the two particles before the collisions, $\vec{k'}_1$ and $\vec{k'}_2$ their momentum after the collision and $\vec{u}_{sc}$ is a random direction (s-wave scattering) in which the particles are scattered. When imaging the momentum distribution, this is responsible for the appearance of spheres in between two diffraction peaks, centered in $\frac{\vec{k}_1+\vec{k}_2}{2}$ and with a diameter equal to the distance between the peaks. An image of the collision spheres measured in the He experiment is given in Fig. 3.24.

Measurement of the collisions in the 3D lattice gases expansion

In order to estimate the number of collisions happening during the time-of-flight propagation, we measured the distribution of the lattice gases with the electronic detector at different values of U/J ($U/J \ll (U/J)_c$) and for different atom numbers N. In order to get a chance to see these spheres, whose density is usually low, one needs to load the optical lattice with a large number of atoms, contrary to what is done in the experiments carried out in this thesis. This enables to increase the density of the different copies, and thus increases the probability for two atoms to collide. Fig. 3.24.b

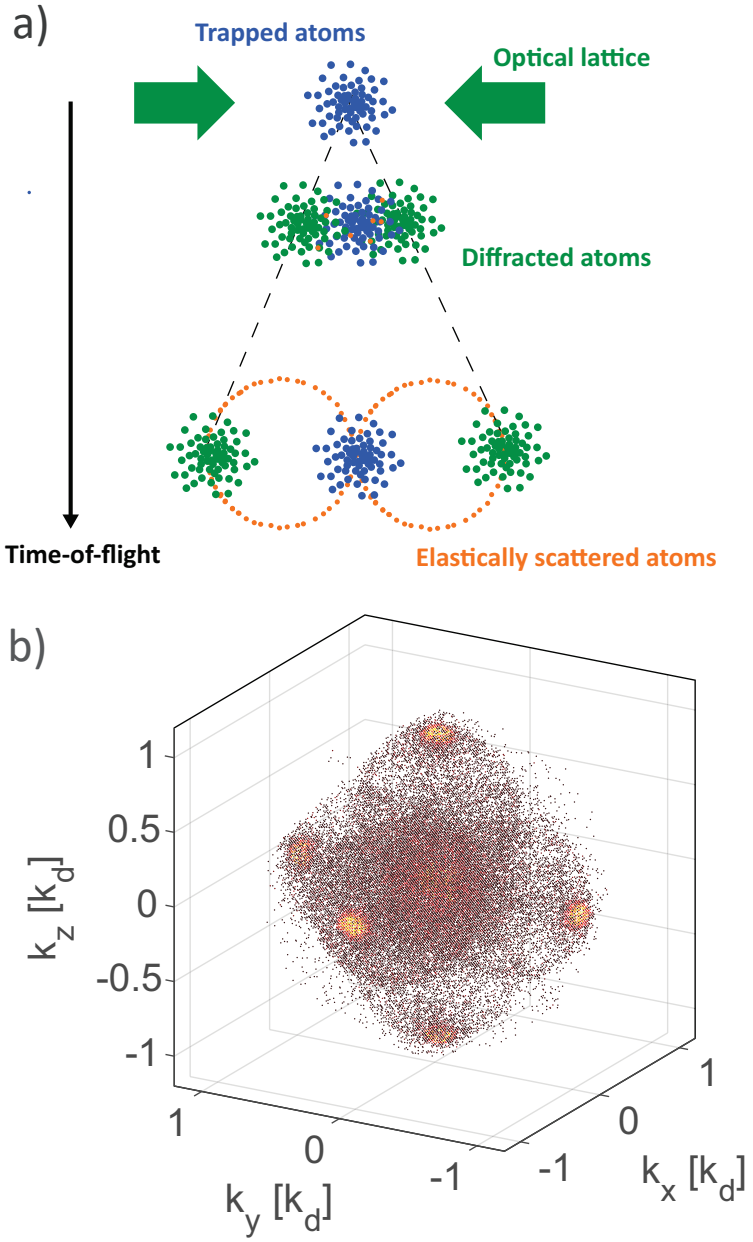

Figure 3.24: **3D collisions happening during the time-of-flight of a lattice gas. a)** 1D Sketch of the collision spheres production during the time-of-flight. **b)** Atomic distribution of a 3D lattice gas with $N = 594\,(100) \times 0^3$ atoms and $s = 5$ detected using the electronic detection. The momentum distribution has been modified by the collisions happening at the beginning of the time-of-flight. The associated collision spheres are clearly visible in between the central peak and the first-order diffraction peaks.

represents the distribution measured by the electronic detector for $N = 594\,(100) \times 10^3$ atoms and $s = 5$. One can identify clearly the scattering spheres in between the central peak and 5 over 6 first-order peaks (the sixth one is a bit cut by the MCP). From these images, we have calculated the number of atoms in the collision spheres in between the central diffraction peak (copy $j = 0$) and the six first order diffraction peaks (copies $j = 1$) situated at $\vec{k} = \pm k_d\,\vec{u}_i$ with $i = x, y, z$.

Collision as a function of N:

In Fig. 3.25, are plotted the number of collisions N_{coll}^{meas} (figure a) and the probability η_{01} (figure b) of collisions between the central diffraction peak and the first order ones as a function of the number

of atoms N at $s = 5$. We see that the number of collisions measured N_{coll}^{meas} increases as expected

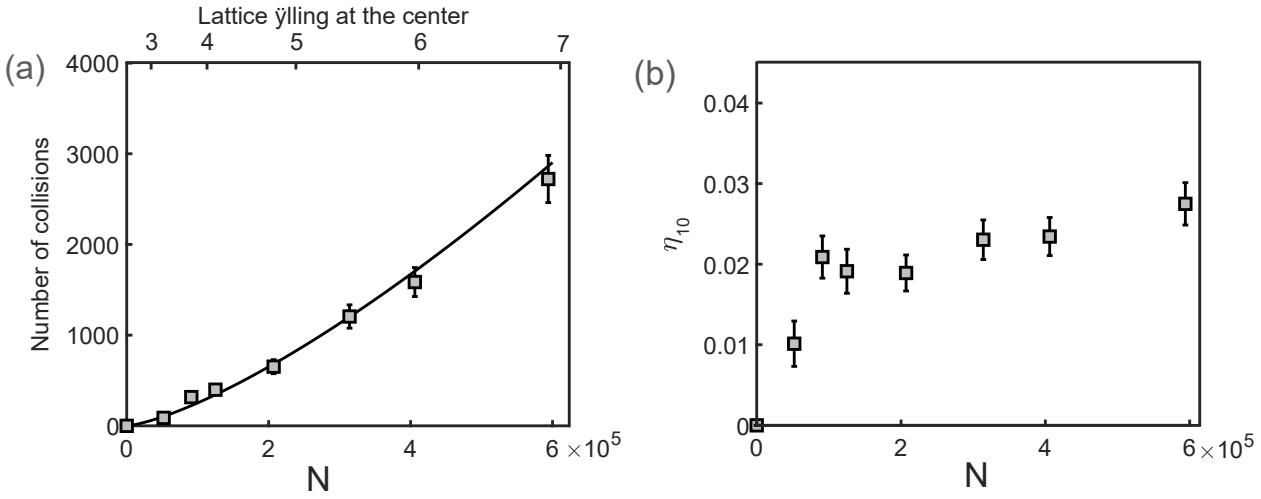

Figure 3.25: **Number of collisions as a function of N**. The data have been taken at $s = 5$ **a)** Measured number of collisions N_{coll}^{meas}. The error bars on the number of collisions correspond to the average standard deviation calculated from the different halos. The line is a guide to the eyes. **b)** Probability of collisions η_{01}.

with N. From the number of atoms in the collision spheres, we derived the probability η_{01} that two atoms, from the copy $j = 0$ and the copies $j = 1$ to collide. The results are plotted in Fig. 3.25.b. Even for high numbers of atom, the probability stays very low ($\leq 5\%$), which confirms the fact that the collisions are negligible in usual experiments.

Collision as a function of s:

We then repeated the same measurement varying the amplitude of the lattice while keeping $N = 3.9 \times 10^5$ atoms. The results are displayed in Fig. 3.26.

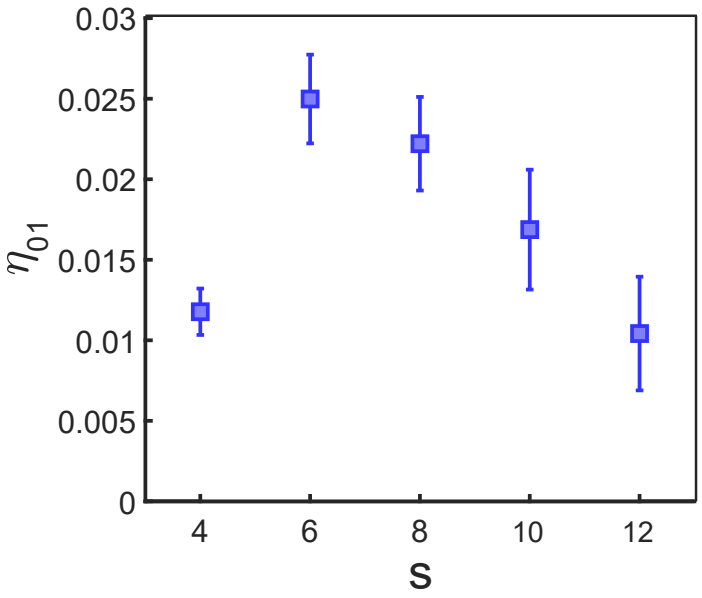

Figure 3.26: **Probability of collision as a function of s**. Measured probability of collision η_{01} between atoms in the copy $j = 1$ and $j = 0$ with $N = 3.9 \times 10^5$ atoms.

The behavior of η_{01} as a function of s is non monotonic with a maximum probability around $s = 6$. This is due to the fact that only the collisions 1-0 are considered: at low values of s, η_{01}

increases because atoms begin to populate the first order diffraction peaks. When s increases even more, however, higher diffraction peaks get populated, resulting in the decrease of η_{01}. However, from the knowledge of the amplitude of the diffraction peaks (set by the Wannier coefficient), one can compute the probabilities of collisions for the different combinations of copies. By doing so, we find that the probability that an atom undergoes a collision during the time-of-flight stays inferior to 5%, and for the experimental parameters used in all the experiments carried out in this manuscript ($N_{BEC} < 40 \times 10^3$ atoms, $s \geq 8$), the probability stays below 10^{-4}.

As a result, the modification of the momentum distribution due to collisions during the TOF can be neglected.

Note that this investigation is still an on-going work. Antoine Ténard, a first year PhD student working on the experiment, has developed a classical model of collisions which is in very good agreement with the experimental data shown in this paragraph.

We have thus demonstrated in this chapter that the He experiment is measuring the momentum distribution of the lattice gases in 3D, with a single-sensitivity, a good precision and a high dynamic range. This will be used in the last three chapters in order to investigate the Bose-Hubbard phase diagram.

4. Characterization of the Bose-Hubbard Hamiltonian phase diagram

One important goal of the quantum simulation is a better understanding of complex condensed matter materials from the investigation of simple models, *i.e*, hamiltonians that are supposed to capture the essential physics of these systems. In particular, one would like to reconstruct the phase diagram of the bulk homogeneous systems, and investigate the properties (macroscopic and microscopic) of the different phases. As illustrated in §.1, with the possibility to engineer a large zoology of quantum systems and with the existence of efficient probes, cold atoms experiments are an excellent testbed.

In the case of the bosonic Mott transition (and its extension to $T \neq 0$), three dimensionless parameters are entering the problem: U/J, T/J and μ/U. In the experiment, we will only investigate the phase diagram (T/J, U/J) with a chemical potential corresponding to a unity lattice filling.
In the experiment, U/J can be set at wish and known precisely. On the contrary, because cold atoms clouds are isolated from any reservoir, they form a closed system. As a result, the macroscopic properties are hard to control. For instance, the temperature is difficult to set at wish and can only be increased from a lower bound. A lot of work is dedicated to lower the temperature in experiments. This is one requirement for the investigation of low temperature phases (for instance the AFM phase in the Fermi lattice systems [99]). Furthermore, its measurement remains challenging, especially in lattice systems. In the first part of this chapter, we explains the thermometry method we developed and used to measure the temperature of the clouds produced. This thermometry is based on the comparison between the momentum distribution of the lattice gases probed in the experiment and QMC data performed at finite temperature.

The impossibility to produce quantum gases at $T = 0$[1] thus raises an important doubt about the ability to probe the quantum phase transition using cold atoms. For instance, some properties at $T = 0$ might disappear once a finite temperature is introduced [57]. The same concern also appears when considering the finite size of the cold atomic clouds and, in most of the experiments, their inhomogeneity. However, we saw in §.1.3.3 that it is possible to retrieve from the behavior of trapped and finite temperature systems information about the Mott transition (defined for homogeneous systems). This constitute thus a motivation for the investigation of the Mott transition with cold atoms.

In the first section, we provide a description of the thermometry method used to measure the temperature of the lattice gases probed in the experiment. This will be used in order to relate the properties of the clouds probed to their position in the Bose-Hubbard phase diagram, that is to say the coordinates $(T/J, U/J)$. Then, we will concentrate on the investigation of the SF-MI and SF-NF phase transitions through observables such as the condensate fraction.

[1] For the sake of brevity, we say $T = 0$ but what is important is that the temperature is lower than the different energy scales in the system for all the degrees of freedom to be frozen.

4.1 Thermometry of the lattice gases

Thermometry methods used in other systems than lattice gases are quite efficient. For weakly interacting systems, the theory usually provides analytic functions that relate some features of the momentum distribution of gases to their temperature [100, 101]. As a result, the temperature can usually be inferred from time-of-flight images.

In strongly interacting systems, things become more complicated since the relation between measurable observables such as the position-space or the momentum-space densities with the temperature is generally not known analytically. However, the temperature can be inferred in most of the cases using the equation of state of the gas [102] (when known) or monitoring the low density high-momentum tails of the time-of-flight distributions (of course this technique does not apply to very low temperatures for which the tails are very dilute). When dealing with lattice gases, experiments usually explore regimes for which the analytic resolutions are scarce. Furthermore, the high-momentum tails are hidden by the periodicity of the distribution.

One method used to estimate roughly the temperature in the lattice gases relies on the hypothesis that the loading of the optical lattice from the BEC trap is adiabatic, meaning the entropy stays constant: $S = S_0$ with S_0 the entropy of the BEC. From the measurement of the initial entropy S_0 and provided one knows the function $S(T, U/J)$ in the optical lattice, the final temperature in the optical lattice can be estimated using $S(T, U/J) = S_0$ [98]. Of course, this method relies:

- On the assumption that the entropy is constant during the loading, which can be only roughly checked experimentally. In our experiment, we checked that S was constant when increasing V_0 by loading a superfluid at $U/J = 5$, going to $U/J = 100$ (Mott phase) and then going back, with the same ramp, to $U/J = 5$. A breakdown in the adiabaticity during the sequence should result, when comparing the two momentum distributions at $U/J = 5$, in a decrease of the peak contrast (heating) and/or a loss of atoms. In our experiment, the comparison confirmed that the adiabaticity criteria is good in a first approximation, but not perfect (see Fig. 4.1). Note that by transferring the atoms from the crossed optical trap to the optical lattice and then back to the crossed optical trap enables identically to check the adiabaticity of the transfer from the crossed dipole trap to the lattice trap.

- On the knowledge of $S(T, U/J)$, which is mostly available only in the weakly interacting regime (for a very low lattice amplitude) or for a perfect Mott insulator.

The second thermometry method that have been used is based on the comparison between the momentum distribution of the clouds probed in the experiment with the numerical profiles provided by the QMC algorithm and ran for different temperatures [98, 48]. This is the method chosen here. Its has been found to provide an estimation of the temperature with a relatively good precision, at least in the superfluid phase, however at the expense of heavy and time consuming calculations (for each lattice amplitude, one needs to compute with the QMC algorithm the momentum distributions associated to a panel of temperatures). Furthermore, since the QMC profiles depend on the experimental parameters such as the external trapping frequency ω_{ext} or the number of atoms N, it constrains a lot the applicability of this method since the numeric must be performed for each experimental configuration.

4.1.1 Thermometry across the SF-NF transition

In this section, we are measuring the temperature of a lattice superfluid at $U/J = 9.5$ ($s = 9.6$), that is to say in an intermediate regime between weak interacting gases where the mean-field theories provide a good estimation of the distribution and the strongly interacting limit. The data have been taken with $N = 40 \times 10^3$ atoms and $\omega_{ext} = 2\pi \times 95 \times \sqrt{s}\,\mathrm{s}^{-1}$, ensuring a filling at the center of the trap of $\bar{n}_0 \approx 1$.

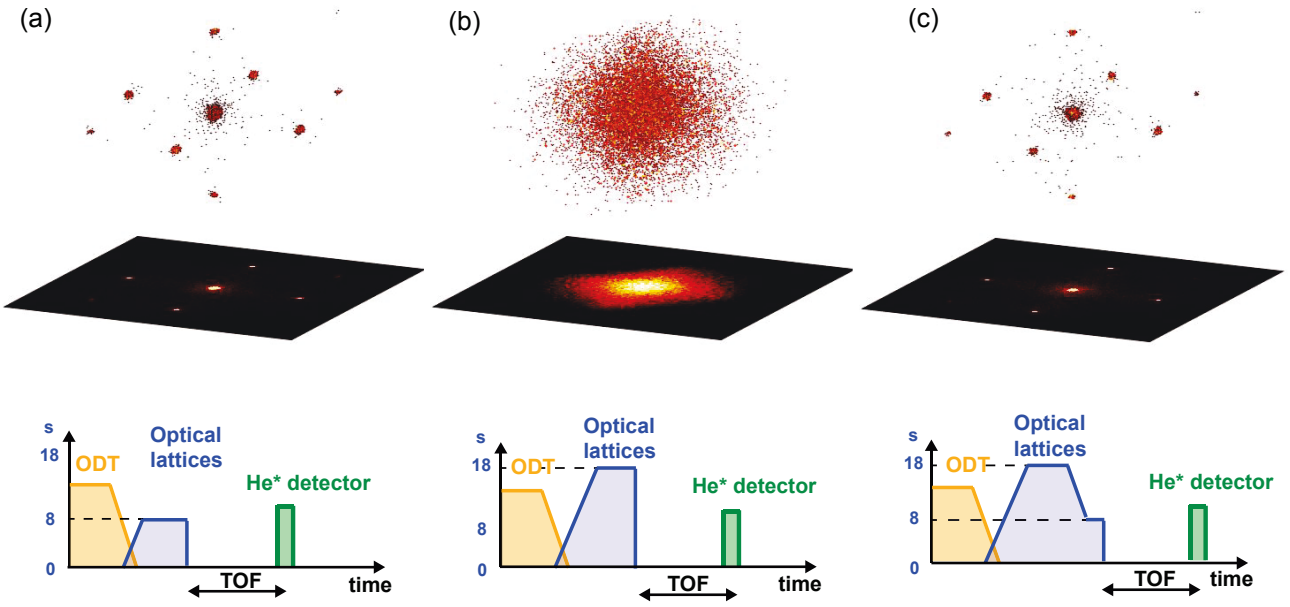

Figure 4.1: **Adiabatic ramping of the lattice potential.** Momentum distribution of a lattice gas at **a)** $s = 8\,(U/J = 5)$. **b)** $s = 18\,(U/J = 100)$. **c)** $s = 8\,(U/J = 5)$ and measured after ramping up to $s = 18$ the optical lattice before going down to $s = 8$. The ramping up and down sequence results in a loss of about 10% of the atoms and the visibility of the interference pattern is only decreased by 5%, meaning that the optical lattice depth is increased adiabatically.

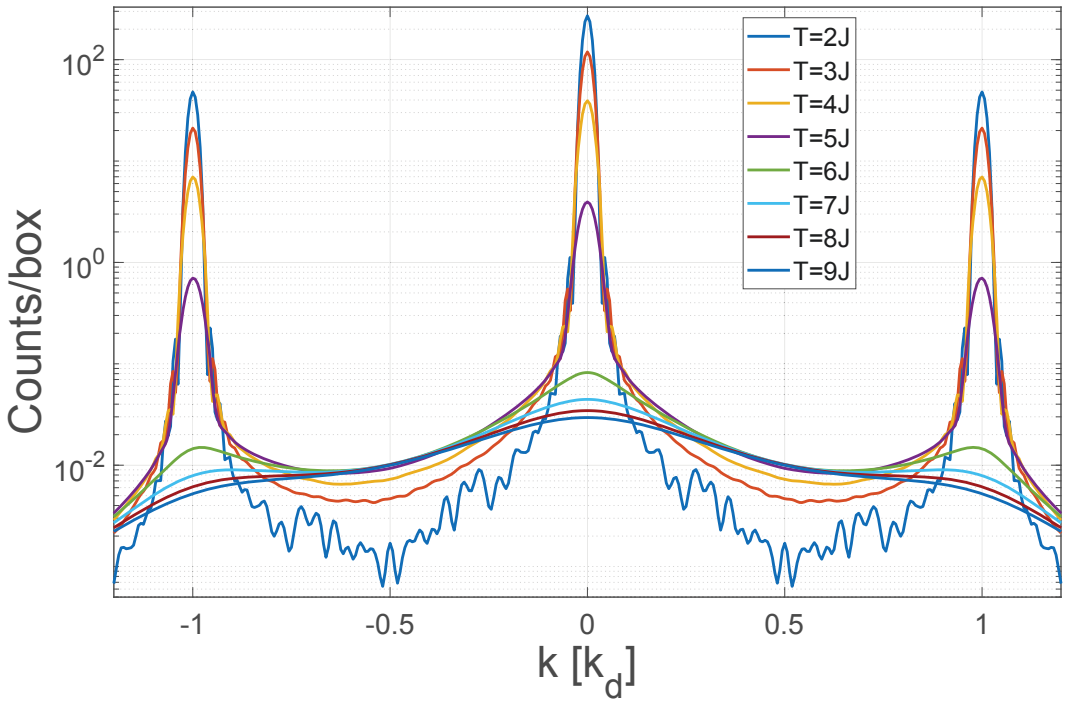

Figure 4.2: **QMC profiles at U/J = 9.5 and N = 40 × 10³ atoms**. The profiles are calculated for different temperatures and with a transverse integration $\Delta k_\perp = 1.5\,k_d/160$ and a longitudinal bin size $\Delta k = k_d/160$. The volume of the elementary cell in the momentum space is $V_{box} = (3 \times 3 \times 1) \times (k_d/160)^3$.

Momentum distributions computed with the QMC method

To estimate the temperature of the clouds, a set of QMC profiles with the same parameters as the one used in the experiment (number of atoms, external trapping frequencies and lattice amplitude) have

been computed by Giuseppe Carleo. They provide the momentum distribution $\tilde{\rho}_{QMC}$[2] along the lattice axis with a transverse integration (half of the transverse bin size) $\Delta k_\perp = 1.5\, k_d/160$ and a longitudinal bin size $\Delta k = k_d/160$. The momentum densities are consequently expressed in atoms/box with the box size being $k_d/160 \times (3, 3, 1)$. The different QMC profiles for temperatures ranging from $T = J$ to $T = 9\, J$ are plotted in Fig. 4.2. When the temperature increases, the contrast of the diffraction peaks decreases because more and more atoms leave the condensate to fill higher momentum modes. As a results, the background, especially at the border of the first BZ ($k = k_d/2$) increases. For these reasons, a parameter which is very sensitive to the temperature is the ratio of the momentum density at $k = k_d$ to the momentum density at $k = k_d/2$:

$$r_T = \frac{\tilde{\rho}(k_d, 0, 0)}{\tilde{\rho}(k_d/2, 0, 0)} \tag{4.1}$$

This ratio can be calculated for the QMC data as a function of the temperature. It is given in Fig. 4.3 (blue line). We see that from $T = 2\, J$ to $T = 6\, J$, r_T varies by four orders of magnitude, which makes it a very sensitive probe for the measurement of the temperature, at least in the superfluid phase. At high T, once the gas is thermal (for a homogeneous system, the condensation occurs within our experimental parameters around $T = 6\, J$), the variation of r_T with T is smoother. This is due to the fact that at this point, when the condensate mode is not macroscopically filled anymore, an increase in the temperature of the system results only in a small increase of the high energy state filling. As a result, the temperature only shows up as an increase in the density at the border of the first Brillouin zone.

Experimental data and temperature measurement

In order to measure the temperature corresponding to a set of data, 1D profiles (with the same box size) are extracted from the 3D momentum distribution. Then the ratio r_T^{exp} is computed and from the calibration curve $r_T = f(T)$ provided by the QMC data, one extracts the measured temperature $T = f^{(-1)}(r_T^{exp})$. The goodness in the estimation of the temperature can then be checked by plotting on the same curve the considered experimental profile along with the QMC profile at the temperature estimated. Three examples are plotted as insets in Fig. 4.3.

Measurement of the temperature for different heated clouds

To investigate the SF-NF transition, different sets of data with different temperatures have been taken. In order to increase the temperature of the superfluid clouds, we followed the method described in §.3.1.5. In total, we took seven sets of data with temperatures ranging from $T = 2.9\, J$ to $T = 8.8\, J$ as depicted in Fig. 4.3.

[2]Careful, in this case, the Wannier envelop is not removed contrary to the QMC data for the investigation of the Mott transition that are calculated in quasi-momentum space

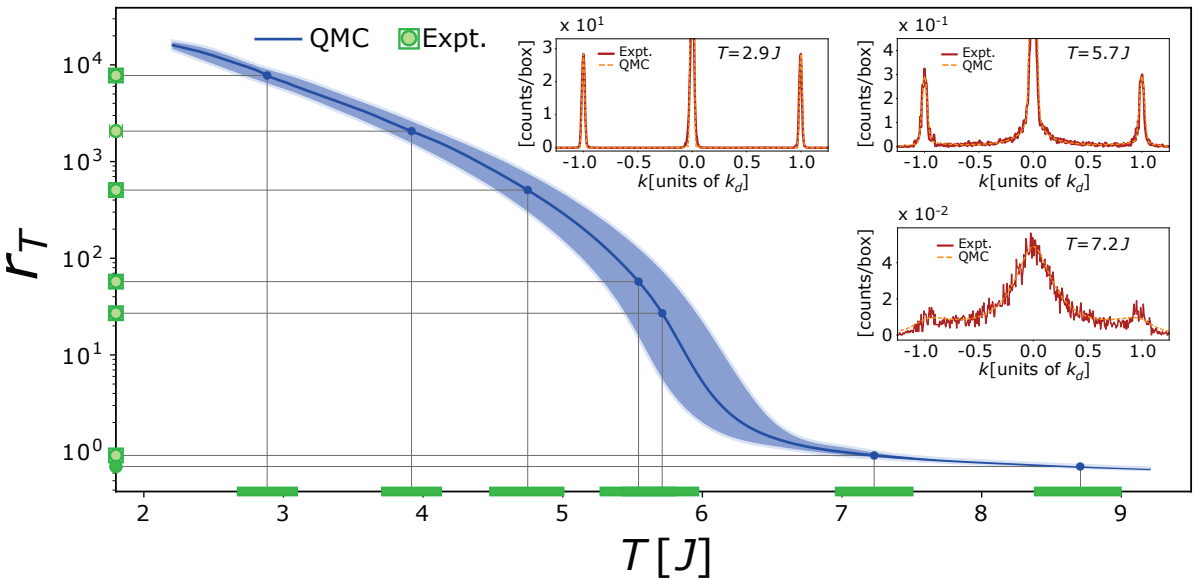

Figure 4.3: **Thermometry of lattice superfluids**. Plot of the ratio $r_T = \tilde{\rho}(k_d, 0, 0)/\tilde{\rho}(k_d/2, 0, 0)$ as a function of the temperature T and extracted from the QMC calculations (blue line). The different values of the ratio r_T and corresponding to the different sets of data are plotted in green along the y-axis. Using the calibration curve, the temperature of the different clouds is inferred (green rectangles on the temperature axis). The blue shaded area takes into account the uncertainty in the experimental atom numbers (20% uncertainty). The width of the rectangles depicts the corresponding error in determining the temperature. Three experimental 1D cuts $\tilde{\rho}(k, 0, 0)$ corresponding to $T = 2.9\,J$, $5.7\,J$ and $7.2\,J$ are also shown along with the QMC profiles.

4.1.2 Thermometry across the SF-MI transition

Investigating the Mott transition requires to produce lattice gases at high lattice amplitude $U/J \gg (U/J)_c \approx 30$. With the optical lattice setup used for the investigation of the SF-NF transition, the maximum value of U/J reachable was about $U/J \approx 40$, obtained at the maximum lattice laser power. In order to be able to reach higher lattice amplitudes without needing to buy a more powerful laser (that is actually not available), we decreased the lattice beam waists (to increase the intensity of the beams). In the new configuration, this ratio can be increased up to $U/J = 100$ ($s = 18$), however, resulting in higher external trapping frequencies, of the order of $\omega_{ext} = 2\pi \times 140\sqrt{s}$ s^{-1}. To keep the average filling close to unity at the center of the cloud, the data have been taken with $N = 3\,000$ atoms for $U/J = \{5,\ 10,\ 15,\ 20,\ 25,\ 30,\ 35,\ 45,\ 60,\ 92\}$ (this number of atoms has been determined using the Gutzwiller method). The QMC calculation have been performed by Tommaso Roscilde at ENS de Lyon.

The QMC distributions are computed in the quasi-momentum basis (meaning without taking care of the Wannier modulation), and one accesses directly $\rho(\vec{k})$. The whole 3D momentum distributions have been calculated on a cubic grid, with a pixel size $\Delta k = (0.5/72)\,k_d$ for the data at $U/J < 25$ and $\Delta k = (0.5/64)\,k_d$ otherwise. To be able to compare directly the QMC data and the experimental ones, the measured momentum distributions are binned over the same grid as the QMC data, and are thus represented as 3D histograms of counts. The advantage is that depending on the kind of measurement, one can choose to compare either the full distribution or only a part of it (for instance, one can only use the cuts along the lattice axis). For a given U/J, the QMC distributions $\rho_{QMC}(\vec{r}_i, U/J, T/J)$ are available by steps of $\Delta T = 0.2\,J$. In Fig. 4.4 are plotted the 1D cuts along a lattice axis for $U/J = \{10,\ 30,\ 92\}$ for different temperatures.

Furthermore, if the temperature is still inferred from the comparison between the momentum distributions measured in the experiment and a set of QMC distributions calculated for different

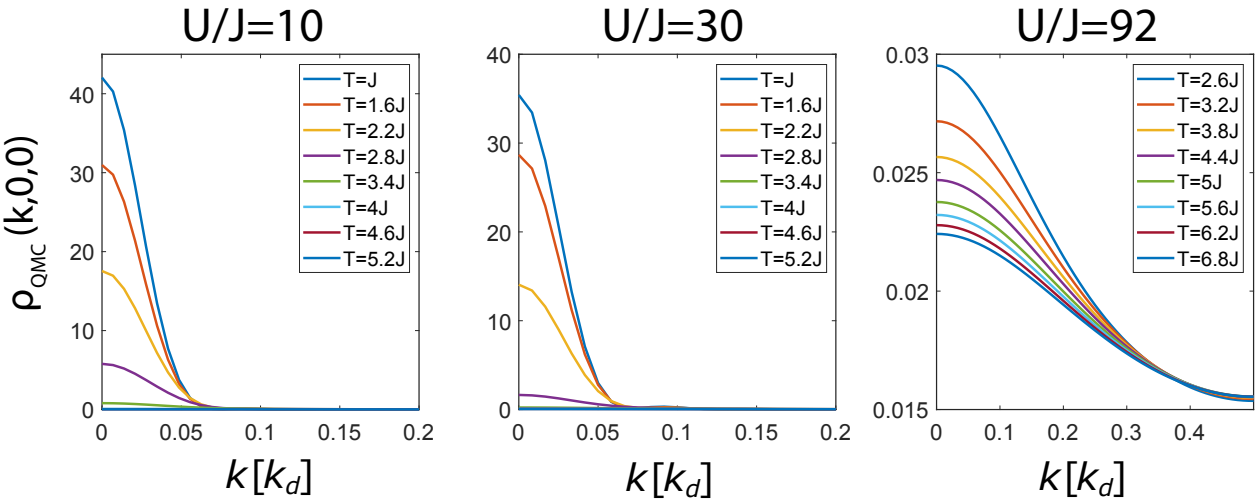

Figure 4.4: **1D momentum cuts calculated with the QMC algorithm for different temperatures.** The data are plotted for $U/J = \{10,\ 30,\ 92\}$ from the left to the right.

temperatures at the U/J considered, we choose other observables than r_T to set the connection. In fact, in the Mott insulator regime, r_T hardly changes with the temperature, which is also the case in the superfluid phase close to the transition. Furthermore, because these data have been taken with $N = 3\,000$ atoms (to compare with the $N = 40\,000$ atomic clouds probed for the investigation of the SF-NF transition), the low density regions of the cuts are noisier than ones corresponding to the investigation of the SF-NF transition, which makes difficult the measurement of r_T. We consequently looked at:

- The residual of the difference between the measured momentum distribution and the one corresponding to the QMC data at the different temperatures available and at fixed U/J:

$$Res(U/J, T/J) = \frac{1}{N_{pixel}} \sum_{\text{pixel } i} |\rho(\vec{r}_i, U/J) - \rho_{QMC}(\vec{r}_i, U/J, T/J)|^2 \tag{4.2}$$

  This quantity is expected to be minimal when $\rho \approx \rho_{QMC}$

- the RMS size of the distributions:

$$RMS_{QMC}(U/J, T/J) = \sqrt{\frac{\sum_{\text{pixel i}} r_i^2 \rho_{QMC}(\vec{r}_i, U/J, T/J)}{\sum_{\text{pixel i}} \rho_{QMC}(\vec{r}_i, U/J, T/J)}} \tag{4.3}$$

$$RMS_{meas}(U/J) = \sqrt{\frac{\sum_{\text{pixel i}} r_i^2 \rho(\vec{r}_i, U/J)}{\sum_{\text{pixel i}} \rho(\vec{r}_i, U/J)}} \tag{4.4}$$

  The size is increasing monotonically with the temperature. As a result, solving $RMS_{meas}(U/J) = RMS_{QMC}(U/J, T/J)$ should provide an estimation of the temperature.

Here $\rho(\vec{r}_i, U/J)$ is the momentum distribution measured at U/J and calculated over the same discretization grid as the one used to compute the QMC data. These rms size and the residuals can be calculated taking into account the entire distribution (Res_{3D} and RMS_{3D}) or limiting it to the lattice axis (Res_{1D} and RMS_{1D}). The variations of these four quantities as a function of the temperature and for $U/J = \{10,\ 30,\ 92\}$ are plotted in Fig. 4.6.

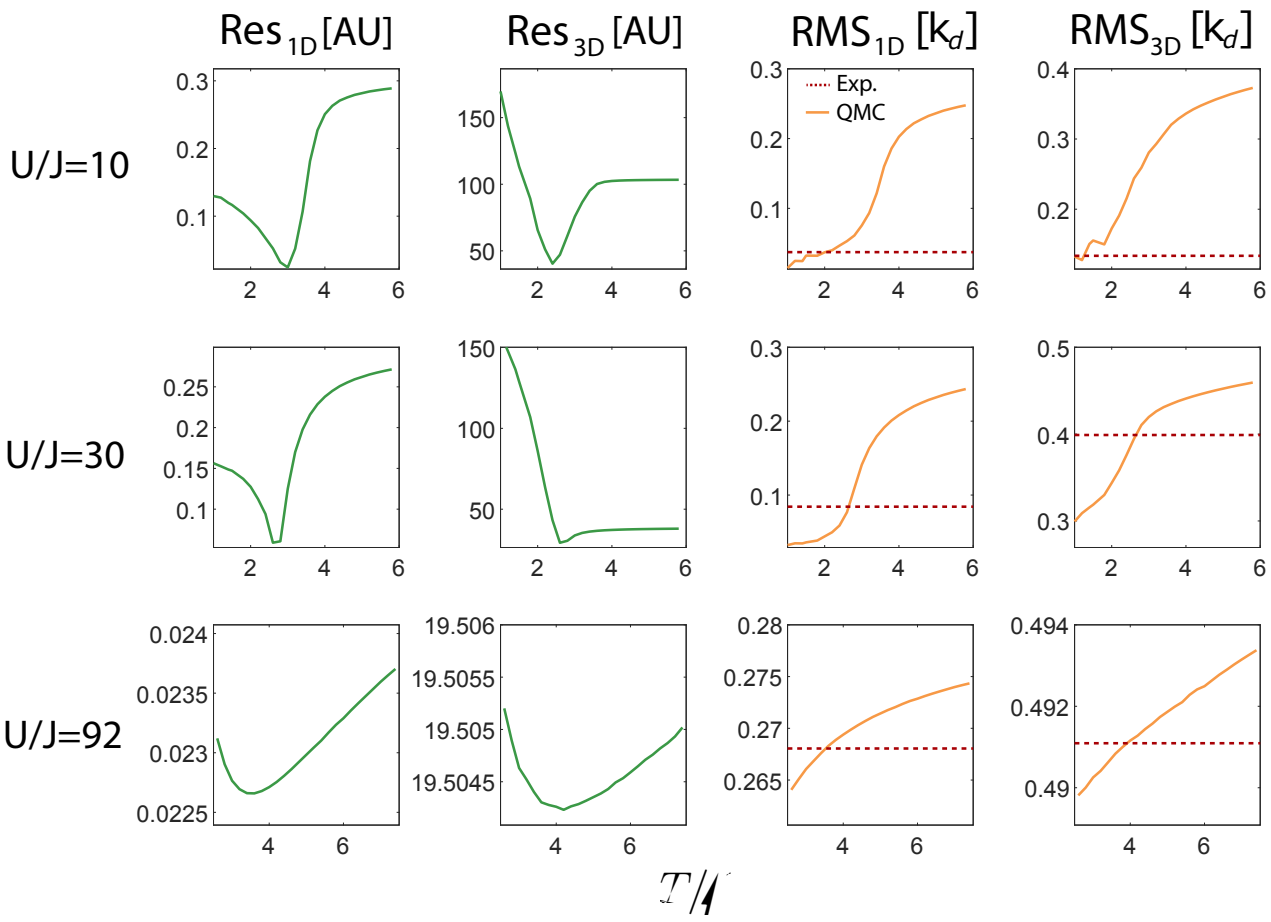

Figure 4.5: **Temperature measurement across the SF-MI transition**. The different lines represent data at $U/J = \{10,\ 30,\ 92\}$. *First and second column:* Values of Res_{1D} and Res_{3D} as a function of the temperature. We identify a more or less pronounced minimum, from which the temperature is extracted. *Third and fourth column:* Values of RMS_{1D} and RMS_{3D} as a function of the temperature for the QMC data (orange solid lines) and measured in the experiment (indicated by the red dashed lines). The temperature is extracted by solving the equation $RMS_{meas}(U/J) = RMS_{QMC}(U/J, T/J)$.

If at low U/J, the increase of the temperature results in a big change in the momentum distribution, it is not really the case in the Mott phase. Furthermore, in the Mott phase, due to the fact that the momentum distribution is extended, the data are quite noisy. As a result, the measurement of the temperature in the Mott phase is clearly less precise than in the superfluid phase.

In Fig. 4.6, are plotted the different temperatures extracted using the different methods. We choose, for each set of data taken at the same U/J, to define the temperature as the mean of the different temperatures found with the four methods. The uncertainty on the measurement is defined as the standard deviation of the four temperatures found (main plot of Fig. 4.8).

One can also check a posteriori, as done for the investigation of the temperature across the SF-NF transition, that the experimental profiles map the QMC ones for the temperature attributed (see Fig. 4.7).

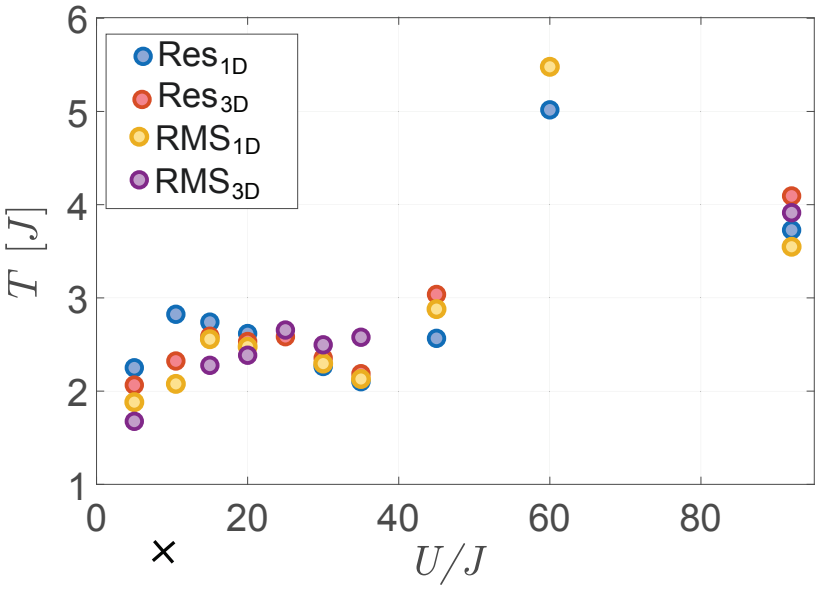

Figure 4.6: **Temperature of the lattice gases produced to explore the Mott transition.** The different colors represent the results obtained with the different methods. All the measurements match each other quite well.

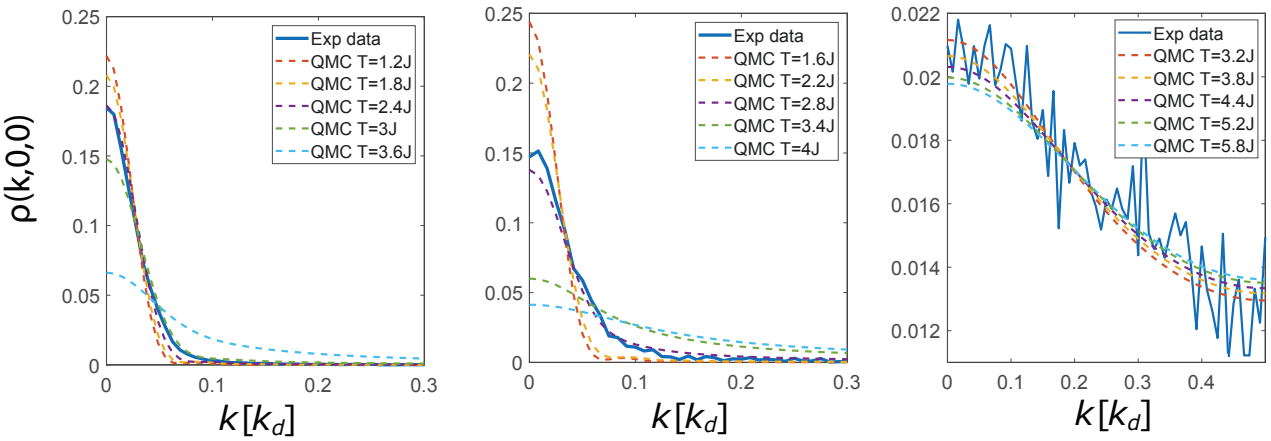

Figure 4.7: **Comparison between the experimental and the QMC momentum cuts for U/J = 10, 30 and 92**. The blue solid lines represent the experimental data. The dashed lines are the QMC cuts for temperatures around the ones measured in the experiment: $T(U/J = 10) = 2.4\,(3)\,J$, $T(U/J = 30) = 2.4\,(1)\,J$ and $T(U/J = 92) = 3.8\,(5)\,J$.

Comment on the evolution of the temperature in the experiment

In Fig. 4.8, are plotted the final temperatures measured for the different sets of data in units of kelvin, interaction parameters U and in units of the hopping energy J. Besides providing an estimate of the temperature of the clouds probed, which will be used in order to locate the different clouds in the Bose-Hubbard phase diagram, such a measurement provides an experimental evidence of the evolution of the temperature during the loading of an optical lattice. In fact, from a general point of view, this question is of major concern for the investigation of the low temperature phases with lattice potential geometries. However, because of the complexity to compute the entropy in strongly correlated systems, there are no analytic predictions for the evolution of the temperature.

For a non-interacting system, the relation between the entropy and the temperature can be derived, allowing the calculation of the temperature from the entropy conservation requirement. In this case, the only energy scale in the experiment is given by J, which decreases exponentially with the lattice

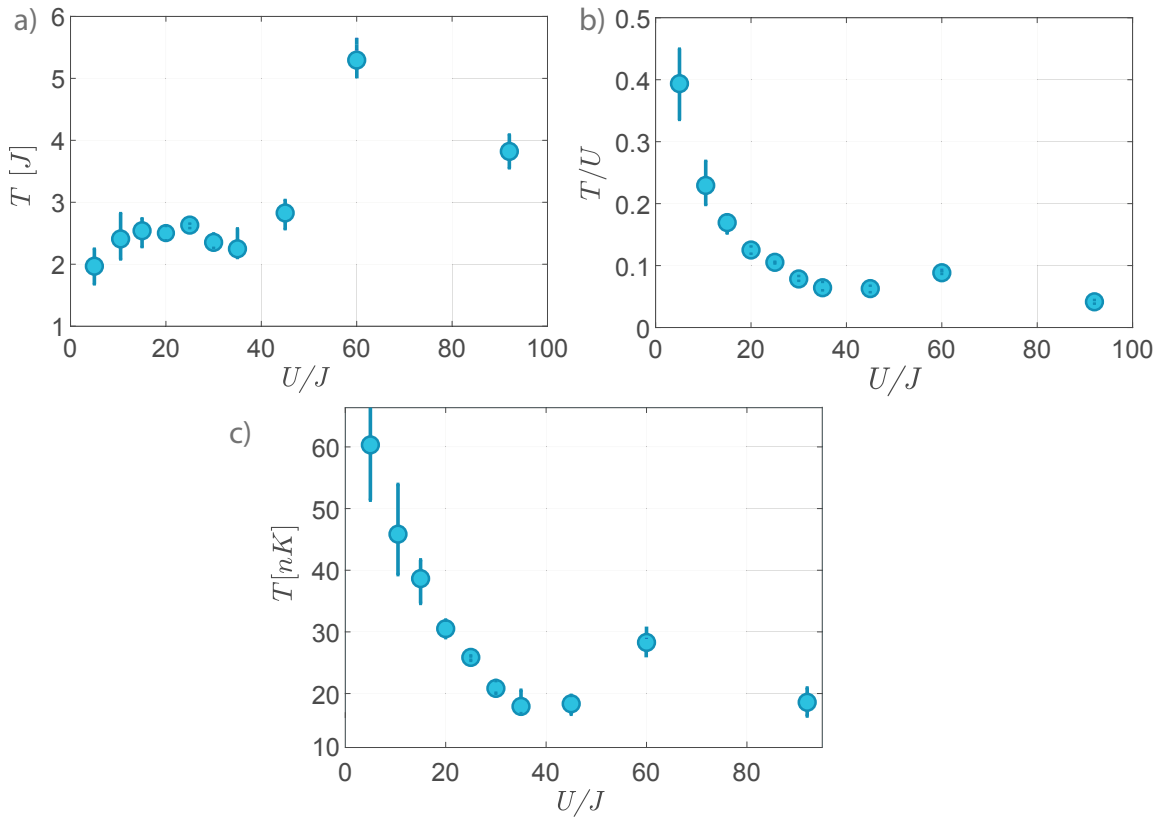

Figure 4.8: **Temperature of the different lattice gases produced in the experiment for different values of U/J across the Mott transition. a)** Temperatures in unit of J. **b)** Temperatures in unit of U. In particular, we see that the temperatures in the Mott phase are about $T \approx 0.1\,J \ll T_{melt}$. **c)** Temperatures in nK.

depth and one can show that the entropy of an infinite system depends only on T/J. As a result, to keep the entropy constant, one expects T/J to stay constant during the loading, resulting in a decrease of T with the lattice amplitude (since J decreases with increasing lattice amplitude V_0). This is thus expected to be true in the superfluid phase when interactions are very weak (at low lattice amplitude). When the interactions are not negligible, the entropy depends also on U/J and the ratio T/J can not be constant for high values of U/J [103]. That statement is confirmed in the experiment (see Fig. 4.8.a) as T/J seems to increase smoothly as a function of U/J in the superfluid phase.

When going deeper in the Mott insulating phase, the temperature is expected to increase because the increase of the energy gap $\Delta \approx U$ makes it more difficult for the excitations to be generated. As a consequence, to keep the entropy constant, the temperature of the cloud must increase. This reasoning holds for an infinite system but not in the present case. In presence of an harmonic trap, the Mott insulator has a wedding cake structure where MI regions are surrounded by superfluids or thermal shells where all the entropy of the system is concentrated. In this case, one can show that $\mathcal{S}_{MI} \propto T/U$ [57]. In the experiment, we find a similar behavior (see Fig. 4.8.b): T/U reaches a plateau from $U/J \geq 45$. Because of that, the temperature is expected to increase when going deeper in the Mott insulator phase, although it does not clearly appears to be true in our experiment (see Fig. 4.8.c).

These temperatures can also be compared with the ones measured in some other experiments:

- In [98], the authors investigated the 3D NF-SF transition and measured, using both QMC time-of-flight distributions and the isentropic analysis, $T_c \sim 3\,J$ close to the Mott transition.

- In [104], the authors measured in a 2D Mott from the in-situ atom number fluctuations, temperatures of the order of $T/U = 0.09\,(3)$ at $U/J = 300$.

- Monitoring also the atom number fluctuations in the Mott phase, $T/U = 0.16\,(3)$ has been measured in [105] at $U/J = 45$.

Our analysis yields values of temperatures in the Mott regime which are similar to those found from quantifying the on-site atom number fluctuations with the quantum gas microscopes. This measurement thus reinforce the identification of the phase diagram accessible for investigation in cold atom experiments.

4.1.3 Summary: Phase diagram probed in this manuscript

The estimated temperatures of the clouds used to investigate the SF-NF (red points) and the SF-MI transition (grey points) are represented in the phase diagram in Fig. 4.9. From this graph, we show that the He experiment is able to probe the different phases of the Bose Hubbard Hamiltonian.

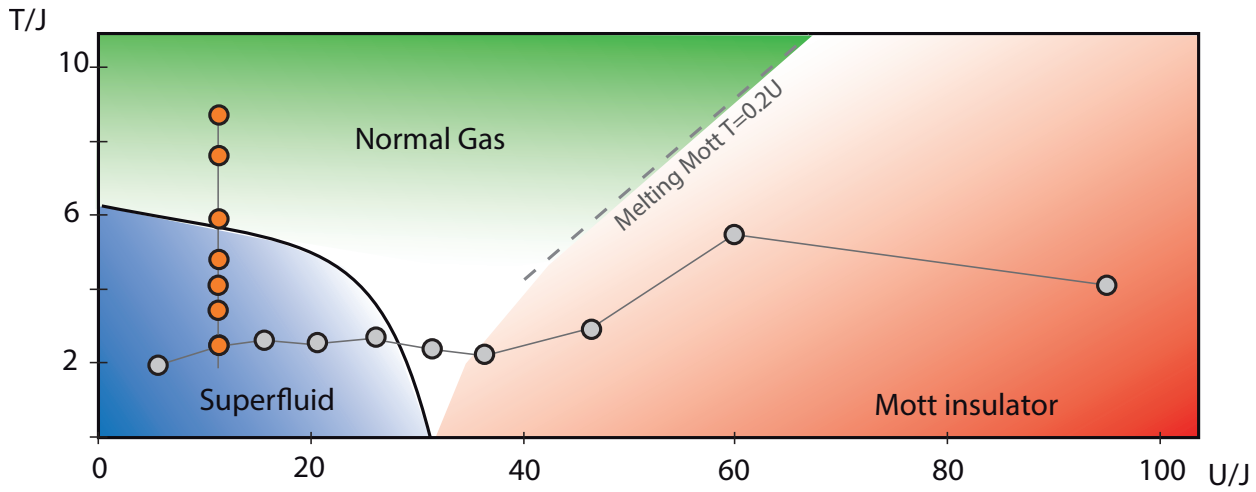

Figure 4.9: **Temperature of the lattice gas clouds used to investigate the SF-NF and the SF-MI transition.** *Red points:* Temperature of the clouds used for the investigation of the SF-NF transition. *Gray points:* Temperature of the clouds used for the investigation of the SF-MI transition.

Around the QCP, at $U/J \sim 30$ the temperature in the system is about $T = 2.5\,J$. For a homogeneous system, this finite temperature is driving the system out of the superfluid phase before reaching the critical value $(U/J)_c$ as represented on the graph displayed in Fig. 4.20 (downshift of about $\Delta(U/J) \approx 3$).

We can also ask if this temperature is low enough in order to probe the quantum critical regime mentioned in §.1.3.3. In [65], the authors provided the boundaries of the quantum critical regime in the particular cases of the Heisenberg antiferromagnet on a bilayer and of the 2D transverse field Ising model. However, no theoretical investigation of this region is available for the Bose-Hubbard Hamiltonian. From an experimental point of view, in 2D, the evolution of the shape of the in-situ density distribution around the QCP [106] has been investigated and showed a behavior compatible with the critical expected scaling laws, but did not provide any quantitative estimation of the critical exponents. One major difficulty lies in the precise determination of the temperature. In 3D, from my knowledge, no experimental investigation has been carried out to confirm these universal behaviors close to the QCP and to estimate the temperature range over which these features persist.

One prospect of our experiment is the investigation, as done for the SF-NF transition, of the evolution of the momentum distribution as a function of the temperature at the transition point to look for these universal features.

4.2 Investigation of the different crossovers between the SF, NF and MI phases

As a general case, the natural choice of observable to monitor a phase transition is the order parameter. For instance, in the case of the condensation transition, the order parameter is the condensate wave function that is equal to zero in the NF phase. The condensate fraction, defined as the ratio between the number of atoms in the BEC N_{BEC} (proportional to the the modulus squared of the condensate wavefunction) with the total number of atoms N:

$$f_c = N_{BEC}/N \tag{4.5}$$

is dropping to zero at $T/J = (T/J)_c$. Furthermore, since T_c tends to zero on approaching the SF to MI transition, the condensate fraction is also going to zero at the critical point $(U/J)_c$. In both cases, the measurement of the condensate fraction seems to be a good observable in order measure the boundaries of the Bose-Hubbard phase diagram.

However, as we already mentioned, because of the finite size and the inhomogeneity of the clouds probed in the experiment, the SF and NF phases as well as the SF and the MI phases are separated by smooth crossovers, and not phase transitions. One important aspect to stress is that the measurement of the condensate fraction is not providing the same information for the SF-NF crossover and for the SF-MI crossover:

- With a trapped gas, the crossing of the critical point $(T/J)_c$ from the NF to the SF phase translates into the appearance of a superfluid at the center of the trap. As the density at the center of an harmonically trapped gas is varying smoothly (the derivative of the in-trap density $n(\vec{r})$ is null at the center of the cloud), the cloud can be considered as locally homogeneous and the temperature at which the center of the cloud is becoming a superfluid should correspond to $(T/J)_c$, that is to say should be equal to the critical value corresponding to the SF-NF phase transition. As the onset of superfluidity can be easily detected, in our experiment, by looking at the momentum distribution and the fact that the condensate fraction acquires a non zero value, the measurement of $f_c(T/J)$ is expected to provide a good indication of the location of the condensate transition.

- On the contrary, the crossing of the Mott crossover from the SF phase to the MI phase in trapped gases translates into the appearance of a Mott plateau at the location of the cloud where $\bar{n}_i = 1$, which is possibly occurring in a limited region of the cloud. This makes difficult first the identification of the appearance of a Mott plateau through the measurement of the condensate fraction (the decrease of the condensate fraction induced by the appearance of a Mott plateau should be weak) and the comparison with homogeneous systems questionable.

In this section, we first investigate the evolution of the condensate fraction as a function of T/J and U/J. It is important here to precise that in usual experiments, measuring the condensate fraction f_c reveals difficult. In fact, it relies on the ability to separate the condensed atoms, from the other atoms, in order to measure their relative contribution, which turns out difficult in most 3D experiments conducted so far:

- With optical imaging, because of the line-of-sight integration and of the lack of cylindrical symmetry, the condensate fraction can only be estimated, but not measured precisely.

- The limited time-of-flight of some experiments, responsible for the measurement of a diffraction pattern that is not fully developed, renders the distinction between the condensate and the background intricate [107].

Bragg scattering enables to circumvent these difficulties thanks to possibility to couple to the light only the class of momentum $k = 0$, that is to say the condensed atoms [108]. In our experiment, the long time-of-flight, the very good momentum resolution, and the 3 dimensional detection allows us to

distinguish the condensate atoms from the rest of the cloud. If the measurement of the condensate fraction is easy in the case of the SF to NF transition, we will see that it is a bit more difficult across the Mott transition.

Due to the difficulty in measuring the condensate fraction, and because it may not be the most favorable observable for the investigation of the SF to MI transition, other teams have been investigating over the past years other observables such as the width or the height of the diffraction peaks [98, 92]. We will consequently also provide in a second time a comparison between these different observables.

4.2.1 Superfluid to Normal fluid transition

Here, we consider the data taken at $U/J = 9.5$. As we have already seen, the momentum distribution associated to atoms in the condensate mode is Fourier limited, meaning its size spreads over $\delta k \approx \pi/L \ll k_d$ (radius) with L the total size of the in-situ cloud (see Eq. 2.58) while the momenta of the other atoms (depletion) can be distributed over the whole BZ ($\delta k \approx k_d/2$). When the two coexist, the momentum distribution has a double structure made of a sharp (the condensate) and a broad distribution (the depletion) that can be separated out, for instance by looking closely at the shape of the distribution. In Fig. 4.10 is represented a 1D cut of the momentum distribution of a lattice superfluid along one lattice axis. The boundaries of the condensate, referred here by the vector k_0 can be inferred from the abrupt change of the slope visible in the momentum density profiles displayed in log scale. Note that:

- This precise identification relies on the fact that in the experiment, we can measure the momentum distribution with an excellent resolution and a large dynamic range. Such a precise measurement would be impossible using optical detection techniques.

- The value of the condensate size k_0 measured in the experiment can be compared with the expected size $k_0 \approx \pi/L$ (k_0 is a radius and L the diameter of the cloud) using the QMC data in order to access the size of the cloud L. More precisely, in the experiment, we measured $k_0 \approx 0.05\, k_d$. In the superfluid phase, one finds, using in-situ QMC profiles, $L = 2 \times 22\, d$ meaning that the expected value for k_0 is about $\pi/L = 0.045\, k_d$, in agreement with the experimental data.

The condensate fraction can be thus calculated through the formula:

$$f_c = \frac{N(|\vec{k}| < k_0)}{N_{BZ}} \tag{4.6}$$

where $N(|\vec{k}| < k_0) = N_{BEC}$ is the number of atoms in the condensate and N_{BZ} the number of atoms in the first BZ. Note that limiting the counting of the atoms to the first BZ is allowed by the periodicity of the lattice distribution.

When calculating the condensate fraction, one needs to pay attention to the saturation of the central peak. In §.3.2.3, we saw that it is possible to evaluate by how much a peak is saturated using the side diffraction peaks. If we note γ this saturation coefficient (ratio between the amplitude of the central peak and the expected one), the number of atom in the BEC N_{BEC} must be corrected by this factor. Moreover, for the identification of the BEC size given by k_0, we payed attention not to use saturated peaks (we used the side diffraction peaks or data taken with a very low transfer to the $m_J = 0$ state in order to avoid the saturation).

The results obtained for the different sets of data are plotted in Fig. 4.11 as a function of the temperature measured by the method explained in §.4.1.2.

Comment on the results

In the experimental data, the condensate fraction varies from $f_c = 65\%$ for $T = 2.8\, J$ to 0 for the three hotter clouds. In the absence of a theoretical model, we extract the critical temperature using

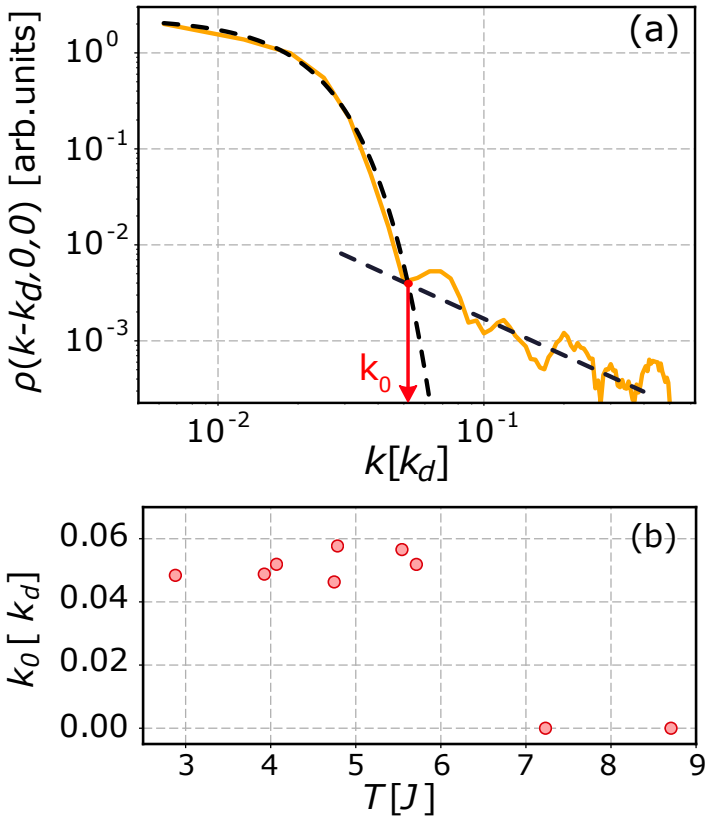

Figure 4.10: **Method to distinguish the condensate distribution from the depletion**. **a)** Momentum distribution centered around the first-order diffraction peak in log-log scale (in order to be sure there is not saturation). The size of the condensate k_0 is set as the location of the abrupt change in the momentum distribution. The dashed lines are respectively a gaussian fit to the diffraction peak for $k < k_0$ and a fit by an algebraic function for $k > k_0$. **b)** Values of k_0 found for the different sets of data. For $T > T_c$, $f_c = 0$ and the momentum distribution is only characterized by a broad distribution. In these cases, k_0 is set to 0.

an empirical function [107], obtaining $T_c = 5.9\,(2)\,J$. Our approach allows us to observe the onset of superfluidity with an unprecedented resolution. Furthermore, as mentioned in the introduction, we are expecting that the temperature of transition measured here compares well with the critical temperature of the condensation transition. We thus compare the measured T_c with the transition temperature T_{c0} of a homogeneous lattice gas whose chemical potential matches that at the trap center. T_{c0} is obtained from the QMC approach (monitoring the superfluid stiffness of the gas) and we find $T_{c0} = 6.3\,(3)\,J$, a value slightly shifted (by 6%) but compatible with the measured value of T_c.

As a conclusion, monitoring the evolution of the condensate fraction as a function of the temperature at fixed U/J (for $U/J < (U/J)_c$) transition seems to be a good observable in order to investigate the condensation transition.

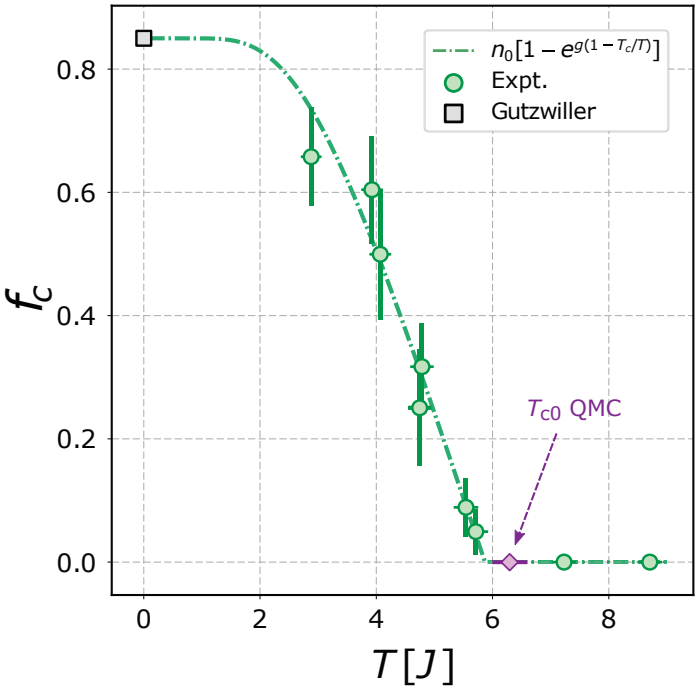

Figure 4.11: **Measured condensate fraction as a function of the temperature across the NF-SF transition**. The condensate fraction f_c (green dots) is plotted as a function of the temperature T. Each point is an average over more than 1000 experimental realizations and the error bars correspond to one standard deviation. The mean-field prediction calculated from the Gutzwiller ansatz is shown for $T = 0$ (grey square). Using an empirical fitting function (green dot-dashed line) we extract a critical temperature $T_c = 5.9\,(2)\,J$. For a homogeneous lattice gas with a chemical potential matching that at the trap center, $T_{c0} = 6.3\,(3)\,J$ (violet diamond).

4.2.2 Mott crossover

Review of previous measurements

Diverse experimental signatures of the appearance of Mott plateaus in trapped 3D lattice gases have been reported in experiments. It ranges from kinks in the visibility of the interference pattern [34] and in the width of the momentum distribution [109] to measuring the breakdown of superfluid currents [110]. So far, the reported measurements of the critical ratio $(U/J)_c$ for the Mott transition in 3D [110, 109] have fallen closer to the mean-field predictions than to the QMC calculations, underlying the difficulties to reach a good accuracy in the critical region of the crossover.

We propose in a first part to provide the experimental results obtained with the Helium experiment on the measurement of some observables already used to investigate the Mott crossover:

- The visibility of the interference pattern.

  The visibility we are calculating here is a direct extension for three-dimensional distributions of the visibility introduced for two-dimensional absorption images [34]. The visibility is defined as:

$$\mathcal{V}^{3D} = \frac{\tilde{\rho}_{max} - \tilde{\rho}_{min}}{\tilde{\rho}_{max} + \tilde{\rho}_{min}} = \frac{\tilde{\rho}(k_d, 0, 0) - \tilde{\rho}(k_d/\sqrt{3}, k_d/\sqrt{3}, k_d/\sqrt{3})}{\tilde{\rho}(k_d, 0, 0) + \tilde{\rho}(k_d/\sqrt{3}, k_d/\sqrt{3}, k_d/\sqrt{3})} \tag{4.7}$$

  The absence of a line-of-sight integration and the large dynamical range in density accessible with the He* detector yields values for the visibility that are much larger than previously reported with absorption images.

  For a homogeneous system, the visibility is expected to be equal to 1 in the SF phase and to drop at the transition. In fact, the visibility should decrease when $\tilde{\rho}(k_d, 0, 0) \approx \tilde{\rho}(k_d/\sqrt{3}, k_d/\sqrt{3}, k_d/\sqrt{3})$,

or similarly, when the density of the BEC in the momentum space $\sim N_{BEC}/V_{BEC}$ becomes of the same order of magnitude as the density related to the depletion $\sim N_{dep}/V_{dep}$ where $V_{BEC} \propto (k_d/16)^3$ ($L = 2 \times 16\,d$) and $V_{dep} \approx V_{BZ} \propto (k_d/2)^3$. This means that the visibility begins to decrease when $N_{BEC}/N_{dep} \approx 10^{-3} \Rightarrow f_c \approx 1\%$, that is to say for $U/J \approx (U/J)_c$. As a consequence, monitoring the evolution of the visibility $\mathcal{V}^{3D}$ as a function of U/J could be used to locate the critical point with a very good precision.

However, in inhomogeneous systems, the variation of the visibility is smoothen. The measurement of the visibility as defined in Eq. 4.7 is given in Fig. 4.12. The visibility is almost equal to one in the superfluid phase (note that such high values of visibility have never been reported before, highlighting the quality of the signals provided by the Helium detector), however, it begins to decrease before the transition and the variation remains smooth in the crossover region and in the Mott insulator phase.

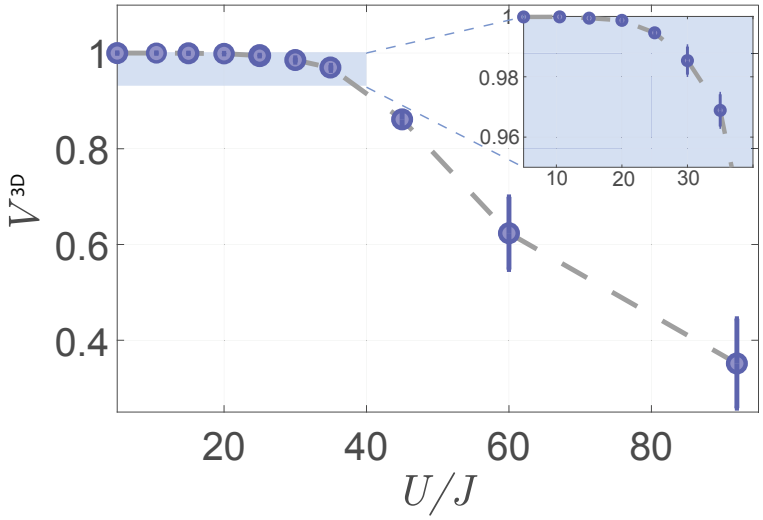

Figure 4.12: **Visibility across the Mott crossover**. The visibility $\mathcal{V}^{3D}$ (Eq. 4.7) as a function of U/J for $N = 3\,000$ atoms. In the superfluid phase, for $U/J \leq 20$, the visibility is higher than 99%. It begins to decrease before $(U/J)_c^{QMC} = 29.3$ which can be attributed to the increase of the depletion (and in particular of the thermal depletion and the effect of the finite temperature that drives the system out of the SF phase before (U/J) has reach the critical value). In the Mott phase, the visibility decreases faster but still slowly. This can be attributed to the role of the particle-hole excitations that restore some phase coherence (see §.5).

This can be attributed to different effects. The finite temperature is at the origin of a higher depletion background and thus a decrease of the visibility faster as compared to the $T = 0$ case. In the Mott phase, the decrease of the visibility is smoother than the expected one due to the existence of possible superfluid shells, or to the contribution of the particle-holes excitations, both of them responsible for the presence of thin features in the momentum density that are centered around the diffraction peaks.

- The width of the momentum distribution.
Here, we focus on the evolution of the diffraction peaks width by considering two quantities:

  1. The RMS size of the peaks, calculated from the 1D cuts in the interval $[-k_d/2; k_d/2]$.

  2. The half width at half maximum (HWHM) of the central diffraction peak. To increase the signal to noise ratio, the data are fitted by polylog functions, paying attention not to enlarge the peaks or to modify they amplitude. Note that to take into account the important background present in the momentum distribution of the lattice gases deep in

the MI phase, the peak height is defined as the difference between the maximal amplitude and the minimal one, basically $\rho_{max} - \rho_{min} = \rho(k = 0) - \rho(k = 0.5\, k_d)$. The HWHM is thus defined as the vector k' for which $\rho(k') = \rho_{min} + \frac{\rho_{max} - \rho_{min}}{2}$.

The results are displayed in Fig. 4.13. In both cases, the sizes increase slowly in the SF phase and in the Mott phase. For $U/J < (U/J)_c$ and in the crossover region, the increase of the visibility gets more pronounced, although it does not permit to identify the location of the apparition of the first Mott plateau contrary to what measured and stated in [109].

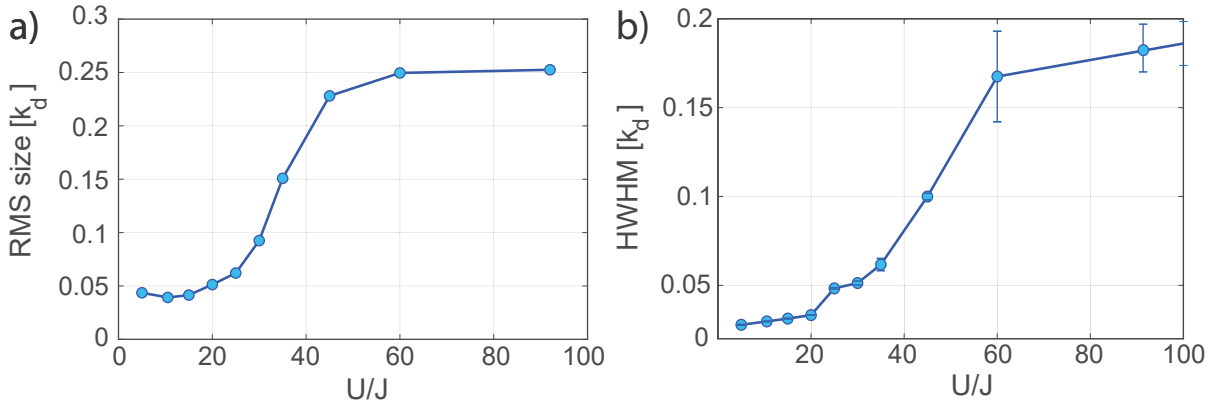

Figure 4.13: **RMS and HWHM sizes of the condensate across the Mott transition**. **a)** RMS size. **b)** HWHM sizes.

For comparison, these quantities have also been computed using the QCM data (see Fig. 4.14) for the different temperatures available.

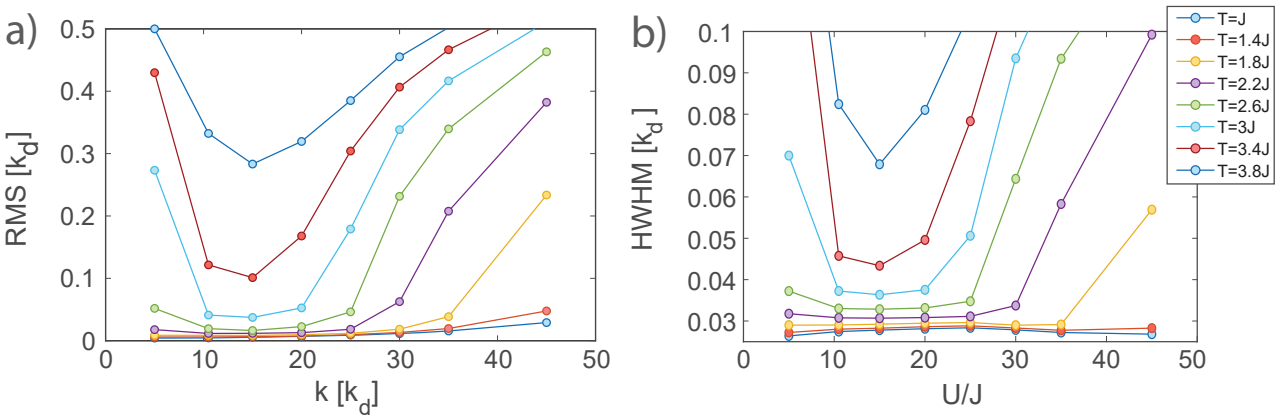

Figure 4.14: **RMS and HWHM size of the condensate across the Mott transition and calculated using the QMC data**. **a)** RMS sizes. **b)** HWHM sizes. The different curves are the values measured from the QMC momentum distributions at the different temperatures.

We find similar results as the ones obtained in the experiment for the usual cloud temperatures measured (about $T = 2\,J - 3\,J$). They correspond to the magenta, green and light-blue curves in Fig. 4.14.

Condensate fraction

The only investigation of the Mott crossover using the condensate fraction has been carried out in 2D by the group of I. Spielman [74]. Monitoring the evolution of the condensate fraction as a function

of U/J, they managed to identify the ratio U/J corresponding to the apparition of the first Mott plateau. This ratio revealed to be in good agreement with the QMC simulations performed taking into account the effect of the trap [111].

The idea of this paragraph is thus to extend the measurement of the condensate fraction across the Mott crossover in 3D. Note that the way we are computing the condensate fraction is however different from the method used in [74], especially regarding the method used in order to subtract the depletion background for the calculation of f_c in the crossover region.

In our experiment, we found that the measurement of the condensate fraction across the Mott transition is more intricate than the one across the SF-NF transition. In fact, the presence of a condensate in the system was previously determined from the presence of a double structure in the momentum distribution. This criterion is based on the fact that the depletion is extending over the whole BZ while the condensate was characterized by a peaked momentum distribution. In the crossover between the SF and the MI phases, the condensate and the non-condensed distributions can have similar sizes, rendering their distinction intricate. In fact, as we will see in §.5, particle-hole excitations in the Mott phase are restoring some coherence. When U/J decreases on approaching $(U/J)_c$, the particle-holes tend to delocalize over larger regions of the cloud, resulting in a phase coherence which extends over many lattice sites. In the momentum space, this translates into the appearance of peaks situated at the lattice nodes, that are very difficult to separate from the presence of a true condensate, characterized by a long-range coherence.

The first question we would like to address is whether it is possible to find a way to distinguish the lattice gases presenting some condensate parts from the other ones. In Fig. 4.15, are represented the 1D cuts along one lattice axis for the different sets of data taken at different values of U/J. These cuts can be divided into three categories:

- *When* $U/J = \{5,\ 10,\ 15,\ 20\}$, the momentum distributions present sharp interference peaks and the profiles look similar, except for the peak amplitudes that are decreasing with increasing U/J.

- *When* $U/J = \{60,\ 90\}$, the momentum distribution is varying smoothly. There is no feature associated to the presence of a condensate in the momentum space. As a result, for these sets of data, $f_c = 0$.

- *When* $U/J = \{25,\ 30,\ 35,\ 45\}$, it more difficult to state. The momentum distribution displays thin structures whose size increases with U/J. However, the origin of these features can be multiple. With the first apparition of a Mott plateau, the width over which the superfluid is extending is reduced, so one expects the associated peaks in the momentum space to increase. However, the superfluid shells are supposed to convert to a normal phase quite rapidly after the apparition of the first Mott plateau [57] due to the finite temperature. If so, they can not be responsible for the thin structures observed. On the other hand, one expects the distribution to sharpen on approaching the Mott transition in the Mott phase due to the particle-hole restored coherence.

We plotted in Fig. 4.16, the radial profiles $\rho(k_r = |\vec{k}|)$ in loglog scale. The idea is to see whether, as done for the investigation of the condensate fraction across the SF-NF transition, it is possible to distinguish the presence of a condensate from other possible contributions (thermal or quantum depletion, Mott insulator distribution with a short-range coherence). As the low density parts of the 1D cuts are noisy, we perform this analysis on the radial profiles. Since the condensate has a spherical symmetry, this averaging should not modify the condensate shape. In Fig. 4.16.a, we see that for low values of U/J ($U/J < 25$), one can distinguish easily the condensate from the depleted part and identified as previously by its linear decay in loglog scale (in agreement with the algebraic decay of the depletion density with k). When U/J increases, the depletion and the condensate become more and more difficult to separate. For $U/J \geq 45$, the double structure is not visible anymore. This fact

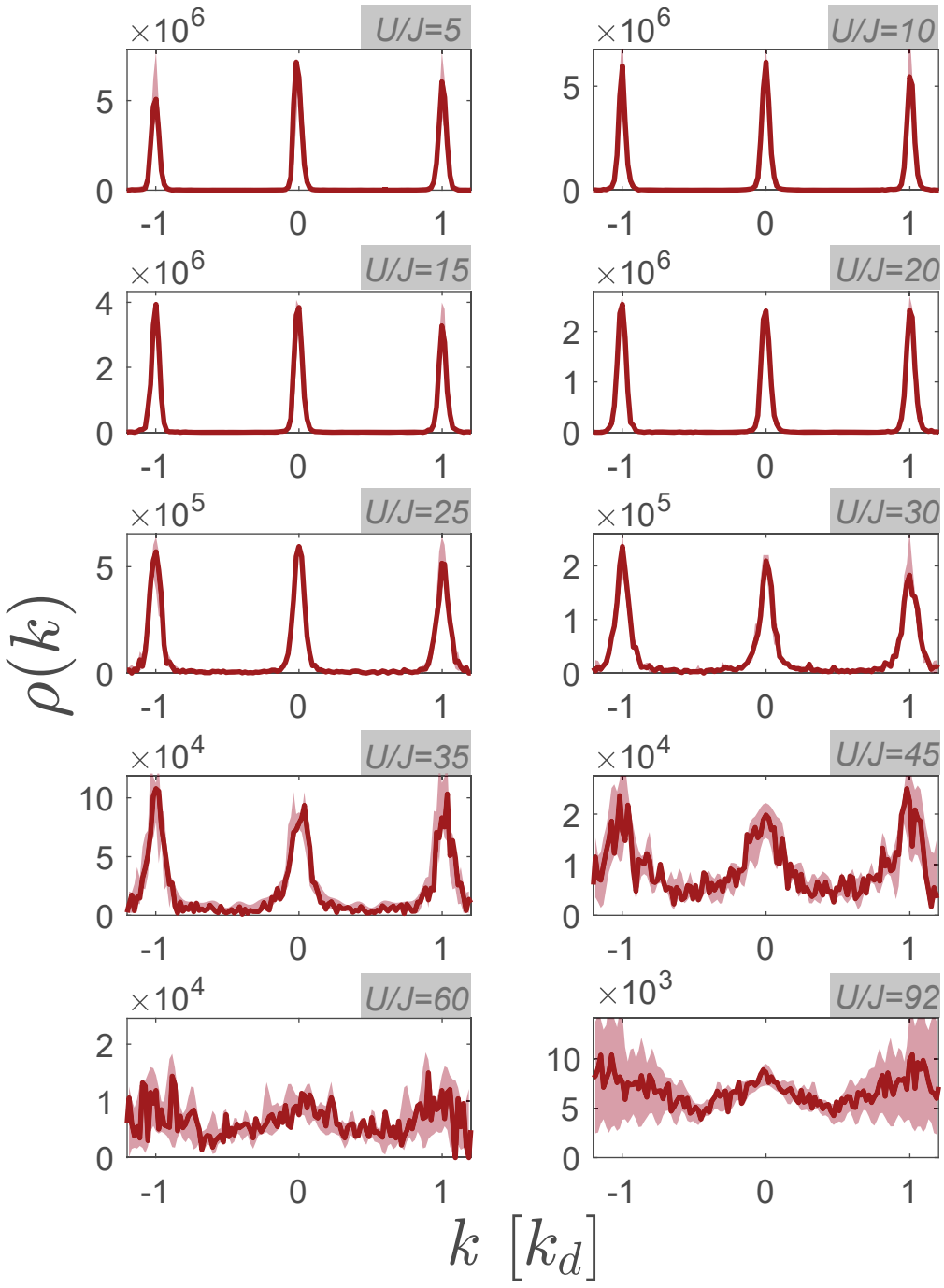

Figure 4.15: **Evolution of the momentum distribution across the Mott transition**. 1D cuts $\rho(k, 0, 0)$ for $U/J = \{5,\ 10,\ 15,\ 20,\ 25,\ 30,\ 35,\ 45,\ 60,\ 92\}$. The cuts have been computed allowing some transverse integration in order to increase the signal to noise ratio, however paying attention not to modify the shape of the profiles. The red filled areas represent the standard deviation for the momentum distribution calculated from many experimental realizations.

is confirmed when plotting the derivative of $\rho(k_r)$. If the momentum distribution is a sum of a broad structure and sharp one, $\rho(k_r)$ should present an inflection point corresponding to an extremum of $\rho'(k_r)$. It is indeed what is observed for $U/J < 45$, but not for higher values (Fig. 4.16.b). For these reasons, we choose to set $f_c(U/J = 45) = f_c(U/J = 60) = f_c(U/J = 92) = 0$.

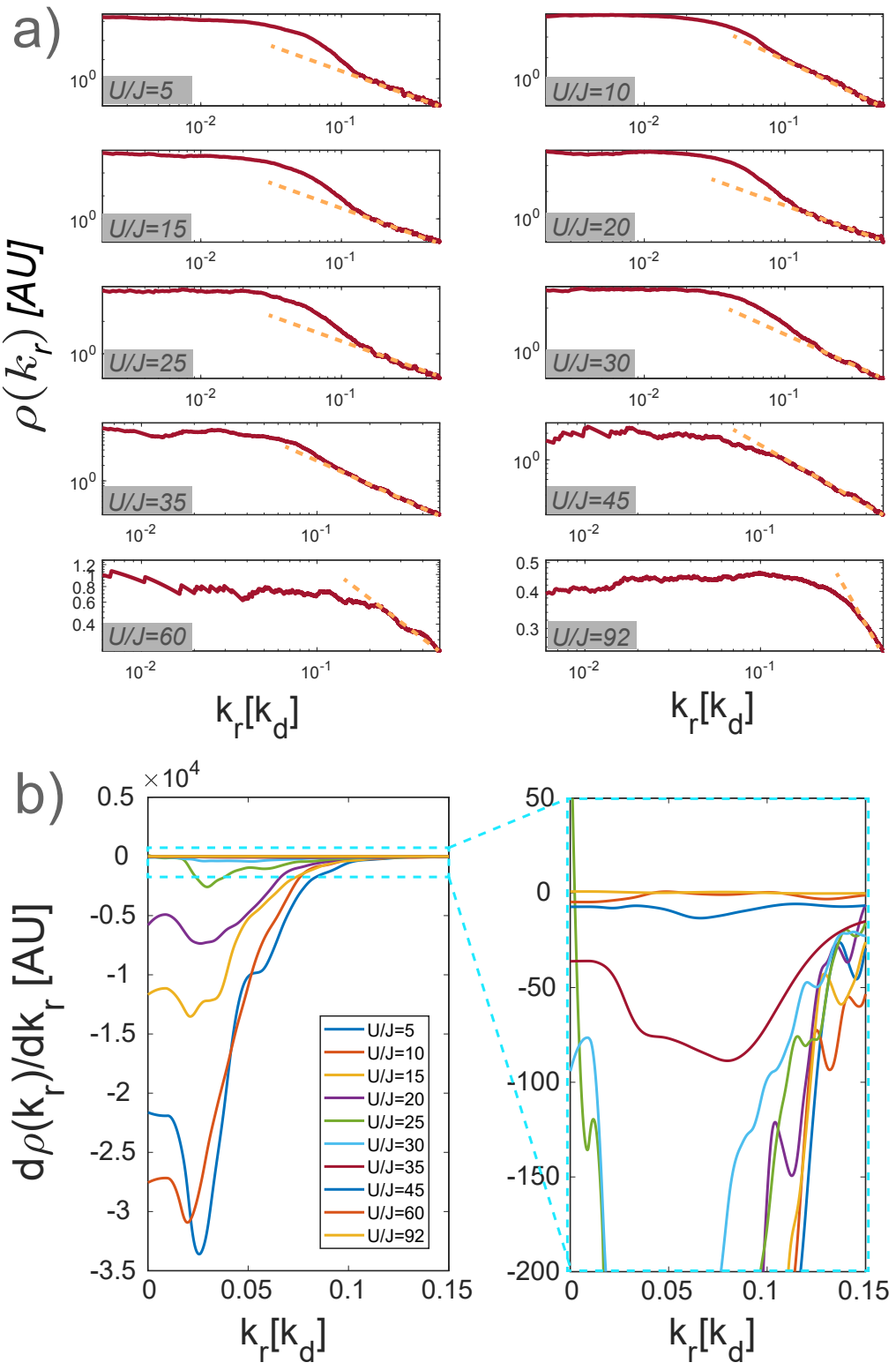

Figure 4.16: **Determination of the presence of a condensate. a)** Radial profiles $\rho(k_r)$ for different values of U/J. **b)** First derivative of the radial density $\rho'(k_r)$ for different values of U/J. The figure on the right is a zoom to the figure on the left.

Determination of the condensate fraction:

To determine the condensate fraction, we could have used the method employed for the calculation of f_c across the SF-NF transition and based on the determination of the condensate size k_0. As said before, for the SF-MI transition, the two contributions (depletion and condensate) become intricate to distinguish at increasing U/J, rendering the identification of k_0 approximate. Furthermore, close to

the transition, in the superfluid phase, the background becomes very important under the condensate peaks. When calculating the condensate fraction, one needs to remove its contribution to the atoms situated around the diffraction peaks. We have thus decided to proceed differently by calculating the fraction of atoms $P(k_r)$ detected with a momentum $|\vec{k}| < k_r$ as compared to the total number of atoms in the first BZ:

$$P(k_r) = \frac{N_{sphere}(k_r)}{N_{BZ}} = \frac{N(|\vec{k}| < k_r)}{N_{BZ}} \tag{4.8}$$

The results are given in Fig. 4.17. At low U/J, as long as k_r is smaller than the condensate size, $P(k_r)$ increases fast. The slow increase at larger k_r is attributed to the depleted atoms. For the data with $f_c = 0$ ($U/J \geq 45$), the momentum distribution is broad, and $P(k_r)$ varies almost as k_r^3 (which corresponds to the expected scaling for a momentum distribution that is uniform over the BZ, which is approximately the case for a MI deep in the Mott phase).

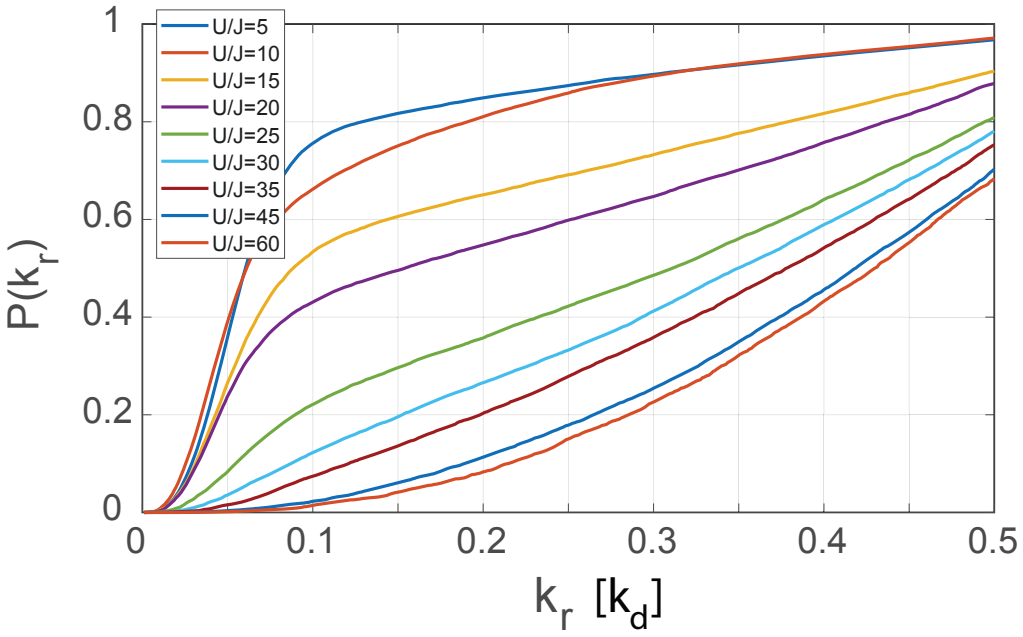

Figure 4.17: **Measured values of $\mathbf{P(k_r)}$.** Proportion of the atoms $P(k_r)$ detected with a momentum $|\vec{k}| < k_r$ with respect to the total number of atoms contained in the first BZ. The curves represent the value of $P(k_r)$ for the different values of U/J.

To set the value of the condensate fraction, we proceeded differently for the data with $U/J \leq 20$ and the data corresponding to $U/J > 20$:

- *Measurement of the condensate fraction for the data with $U/J \leq 20$.*
  For these data, the depletion background is low, the condensate fraction is then defined from the intersection of the linear curves obtained by fitting the low momentum and high momentum variations of $P(k_r)$ (see Fig. 4.18). One can check that, provided the condensate fraction is $\gtrsim 30\%$, this gives the value of the condensate fraction within a few percents uncertainty[3].

- *Measurement of the condensate fraction for the data with $U/J > 20$.*
  For the other data, the fraction of the depleted atoms below the condensate peak is not negligible

[3]In order to check this affirmation, we approximated the condensate and the depletion distributions by gaussian functions with sizes corresponding to their typical values in the experiment. We have then calculated for the whole simulated distribution $P(k_r)$. We found the same variation of $P(k_r)$ with k_r as the one observed in the experiment. We finally found that the condensate fraction was given, within a few percent uncertainty, by the ordinate of the crossing point as defined in the main text, provided $f_c \gtrsim 30\%$.

and has to be subtracted to compute the condensate fraction. In the absence of theory that could predict the shape and the width of this background, it is consequently impossible to do that carefully. This renders the measurement of the condensate fraction more approximate in this region. To evaluate the proportion of atoms under the condensate that belongs to the depletion, we fitted the spherical profiles by a double structure function made by the sum of two gaussians, the largest size being attributed to the depletion distribution. If we note $\rho(k_r) = \rho_{BEC}(k_r) + \rho_{dep}(k_r)$, then:

$$P(k_r) = \frac{N_{sphere}(k_r)}{N_{BZ}} = \frac{\int_{k=0}^{k_r} \rho(k_r) dk_r}{N_{BZ}} = \frac{\int_{k=0}^{k_r} \rho_{BEC}(k_r) dk_r}{N_{BZ}} + \frac{\int_{k=0}^{k_r} \rho_{dep}(k_r) dk_r}{N_{BZ}} = P_{BEC}(k_r) + P_{dep}(k_r) \tag{4.9}$$

where $\rho_{BEC}(k_r) = A_{BEC} e^{-0.5 \times (k_r/k_{BEC})^2}$ and $\rho_{dep}(k_r) = A_{dep} e^{-0.5 \times (k_r/k_{dep})^2}$ are the distributions used for the double gaussian fit.

The condensate fraction is equal to:

$$f_c = P(k_r = 0.5\, k_d) - P_{dep}(k_r = 0.5\, k_d) = \frac{\int_{k=0}^{k_d/2} \left[\rho(k_r) - \rho_{dep}(k_r)\right] dk_r}{N_{BZ}} \tag{4.10}$$

In order to check the consistency of this method, one can plot $P_{diff}(k_r) = P(k_r) - P_{dep}(k_r)$. If the background subtraction method we are using is efficient, $\rho(k_r) - \rho_{dep}(k_r)$ must be equal to the condensate distribution. As a result, considering the finite size of the condensate ($< 0.5 k_d$), $P_{diff}(k_r)$ must saturate at large k_r towards the value of the condensate fraction. This is what is observed with the experimental data (see Fig. 4.18). The condensate fraction is then defined as the average of $P_{diff}(k_r)$ performed on the interval $k_r \in [0.15; 0.4]\ k_d$.

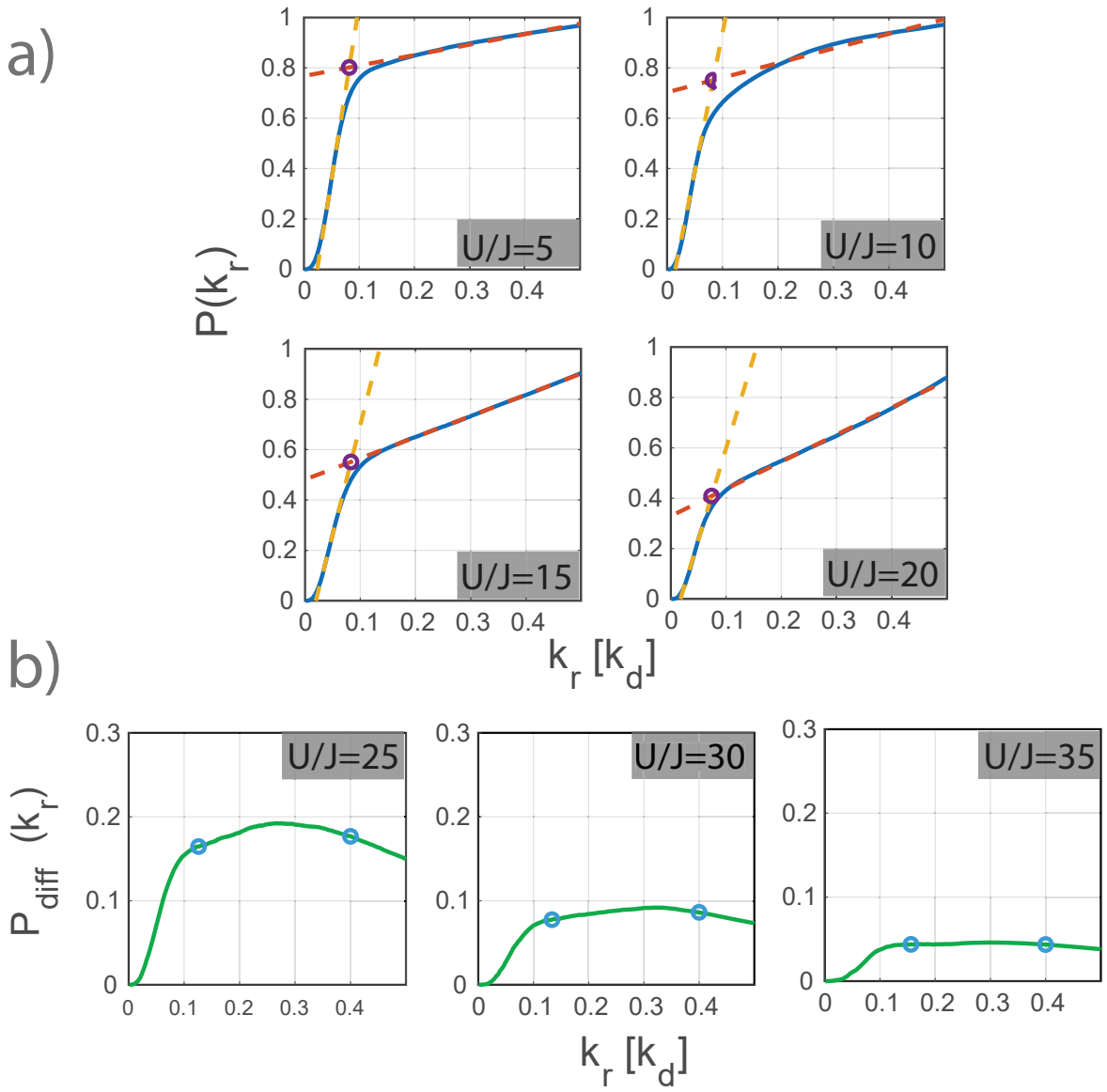

Figure 4.18: **Determination of the condensate fraction. a)** For the data at $U/J = \{10,\ 15,\ 20\}$. Proportion of atoms $P(k_r)$ with a momentum $|\vec{k}| < k_r$ with respect to the total number of atoms contained in the first BZ. The yellow dashed lines are the linear fits to the low and high momentum part of $P(k_r)$. The magenta point represents the crossing of the two yellow lines. The condensate fraction is set as the ordinate of the magenta point. **b)** For $U/J = \{25,\ 30,\ 35\}$. Proportion of atoms in the condensate $P_{diff}(k_r) = P(k_r) - P_{dep}(k_r)$ as a function of k_r obtained after removing the contribution of the depletion. When $k_r \gtrsim 0.1\, k_d$, this value reaches a plateau. f_c is set as the average value of $P_{diff}(k_r)$ in the interval $k_r \in [0.15; 0.4]\ k_d$ (interval represented with the blue points).

Condensate fraction across the Mott crossover:

The evolution of the condensate fraction as a function of U/J is plotted in Fig. 4.19. The condensate fraction reaches 80% for $U/J = 5$ and drops monotonically up to $U/J = 25$. A similar drop is expected for the homogeneous Bose-Hubbard Hamiltonian, suggesting that finite size and inhomogeneity effects are weak far from the Mott transition. On approaching the Mott transition, the decrease of f_c becomes much less pronounced, highlighting the crossover nature of the transition in our experimental realization. Furthermore, we measure a possible condensate fraction $f_c < 5\%$ for $U/J = 35$, *i.e*, above the critical value $(U/J)_c \approx 29.3$ for the Mott transition in a homogeneous system.

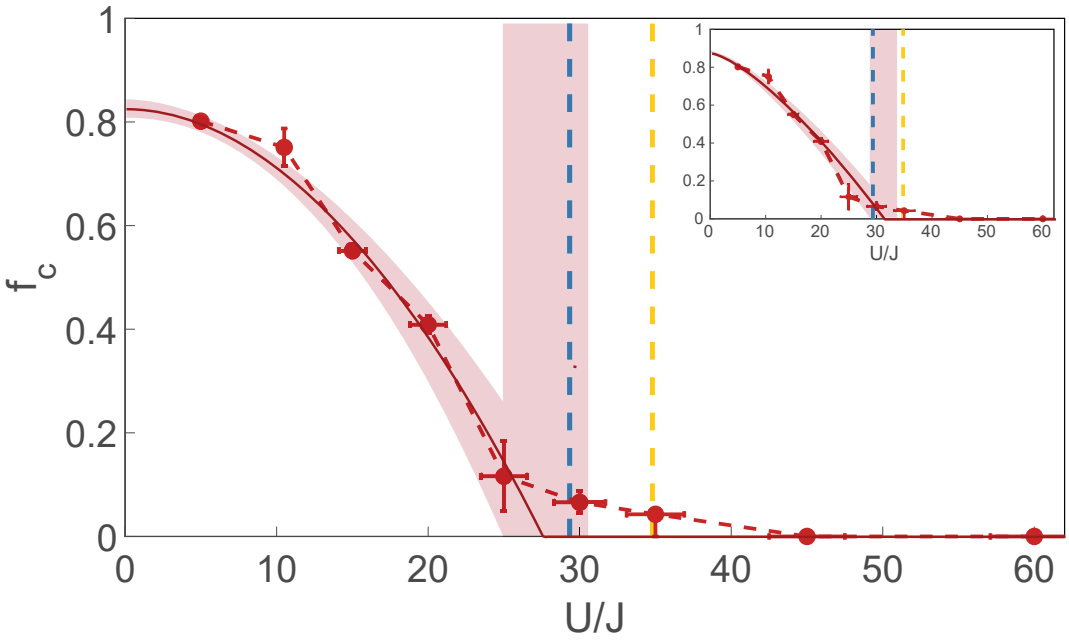

Figure 4.19: **Measured condensate fraction across the Mott transition**. The red points are the experimental data. The vertical error bars are computed differently for the different sets of data. For $U/J \leq 20$, they represent the error on the condensate fraction due to the uncertainty in the determination of the crossing point used to set f_c from the measurement of $P(k_r)$. For the rest of the data, the error bars are calculated considering the uncertainty in the results of the double structure fit. The horizontal error bars correspond to the uncertainty in the setting of the lattice amplitude $\Delta V_0 = \pm 0.2\, E_r$ (and converted in terms of an uncertainty in U/J). f_c is fitted by an empirical function $f(U/J) = f_0 \times [1 - ((U/J)/(U/J)_c^{meas})^{\alpha}]$. The red line is the result of the fit while the transparent red area is the uncertainty to the fit. The different points are attributed a weight that is inversely proportional to the vertical error bar length. For the main graph, only the points at $U/J < 30$ (data for which the effect of the trapping is less dramatic) have been taken into account for the fit. The parameters extracted are $f_0 = 0.83\,(2)$, $(U/J)_c^{meas} = 27.5\,(2.5)$, $\alpha = 1.9\,(2)$. The value of $(U/J)_c^{meas}$ can be compared with the critical values calculated by the mean-field theory (yellow dashed line) and the QMC method (blue dashed line) for a homogeneous system at $T = 0$, $(U/J)_c^{MF} = 34.8$ and $(U/J)_c^{QMC} = 29.3$. In inset, is represented the result of the fit if one considers all the points. In this case, $f_0 = 0.88\,(2)$, $(U/J)_c^{meas} = 31\,(2)$, $\alpha = 1.38\,(2)$.

To extract the critical value $(U/J)_c$ for the Mott transition with a unity lattice filling, we rely on fitting the measured condensate fraction. In the absence of an analytic prediction for the decrease of f_c in the inhomogeneous case (and also for the homogeneous case!), the experimental data are fitted by the function:

$$f(U/J) = f_0 \times [1 - ((U/J)/(U/J)_c^{meas})^{\alpha}] \tag{4.11}$$

where the free parameters are: f_0, α and $(U/J)_c^{meas}$. The result of the fit is plotted in red in Fig. 4.19. Since we would like to estimate the transition point for the homogeneous Mott transition, *i.e*, the appearance of a Mott plateau in the trap, we choose to only consider the points at $U/J < 30$, that is to say we eliminate the points situated in the smooth crossover region. Doing so, we find: $f_0 = 0.83\,(2)$, $(U/J)_c^{meas} = 27.5\,(25)$, $\alpha = 1.9\,(2)$. The critical value measured here is in agreement with the QMC results obtained for a homogeneous system although downshifted. This downshift can be attributed to finite temperature effects (see Fig. 4.20). For information, the inset displays the result of the fit if considering all the points. In this case: $f_0 = 0.88\,(2)$, $(U/J)_c^{meas} = 31\,(2)$, $\alpha = 1.38\,(2)$ and the critical parameter $(U/J)_c$ is upshifted as compared to the $(U/J)_c^{QMC}$. This can be attributed to the presence of condensate shells after the apparition of the first Mott plateau for trapped systems, underlying the difficulty in measuring the location of

the critical point using the condensate fraction as the observable to monitor the Mott transition with trapped systems.

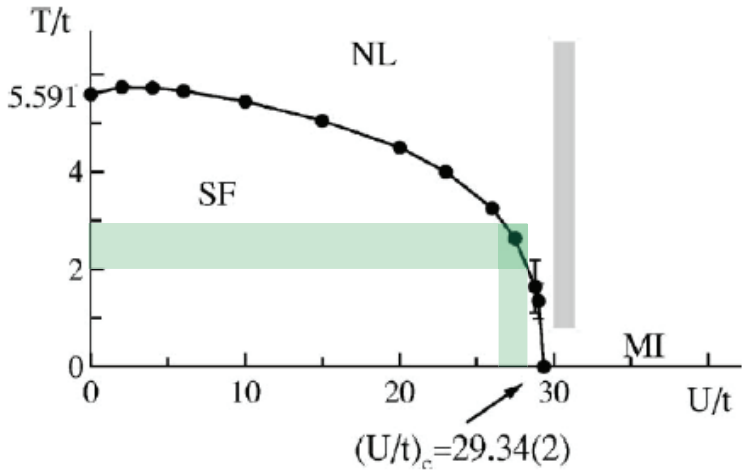

Figure 4.20: **Finite-temperature phase diagram for a homogeneous system at filling n = 1.** These results have been obtained in [24] using the QMC method. Close to $(U/J)_c^{QMC}$, the temperature of the lattice gases ranges from $T = 2\,J$ to $T = 3\,J$. Due to this finite temperature, the lattice gases are expected to be driven out of the SF phase through the condensation transition in between $U/J = 26$ and $U/J = 28$ (see green areas).

The height of the condensate peak

For an infinite homogeneous system, the height ρ_{peak} of the diffraction peaks is giving directly the condensate fraction. Here of course, we are not in this situation, but it still provides information about the average phase coherence in the system:

$$\rho_{peak} = \rho(\vec{k} = 0) = \frac{1}{V}\sum_{i,j} C(i,j) \tag{4.12}$$

We measured ρ_{peak} for the different sets of data and the results are displayed in Fig. 4.21.

The amplitude of the central peak decreases the same way as the condensate fraction, that is to say fast for $U/J < 30$, and slower after. However, the advantage of this method relies on the fact that no assumption on the depletion and its momentum distribution has been made. One can also fit the data by the same empirical function (and performed with the points at $U/J < 30$) as previously used for the identification of the critical point using the condensate fraction. We found: $(U/J)_c^{meas} = 26.3\,(2)$, in agreement with the previous value measured using the condensate fraction and with the value of the condensation transition at finite temperature predicted using the QMC algorithm and given in [24].

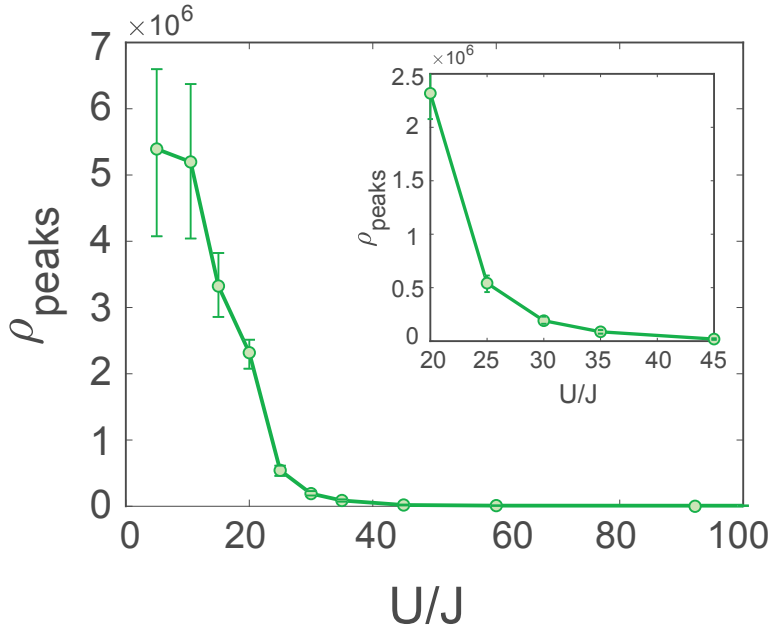

Figure 4.21: **Height of the central peak $\rho_{\mathbf{peaks}}$ across the Mott transition**. The inset is a zoom to the main figure between $U/J = 20$ and $U/J = 45$.

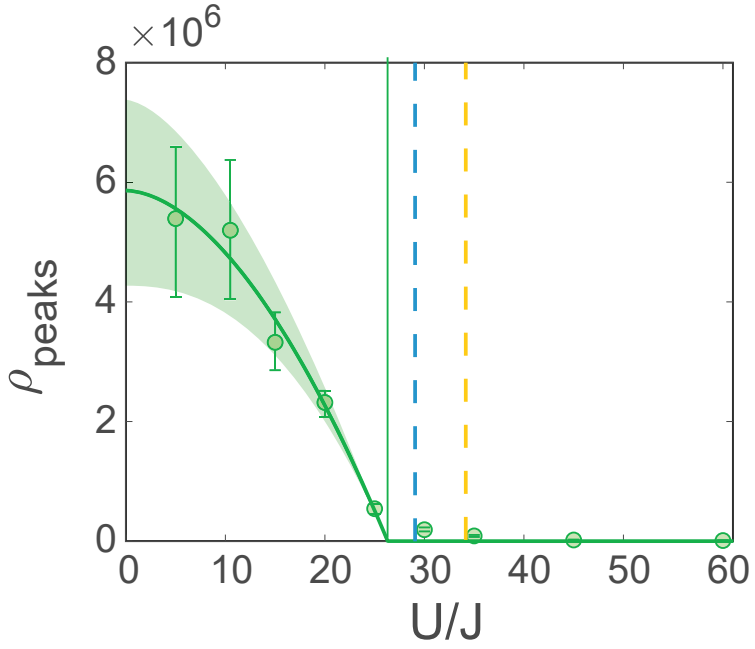

Figure 4.22: **Extracting $(\mathbf{U/J})_\mathbf{c}$ from the central peak height**. The data are fitted by the function $f(U/J) = f_0 \times [1 - ((U/J)/(U/J)_c^{meas})^\alpha]$. The critical parameter measured in this case is $(U/J)_c^{meas} = 26.2\,(2)$.

Conclusion

To summarize, we investigated the Mott crossover using different observables:

- The visibility of the interference pattern.
- The RMS and HWHM sizes of the central diffraction peak.
- The condensate fraction.
- The height of the central diffraction peak.

The visibility, the RMS and the HWHM sizes present a smooth variation across the Mott crossover. This was to expect since they are sensitive to the development of the depletion before the transition point (as a result, they begin to vary before $(U/J)_c$) and they are slightly modified by the appearance of a thin Mott plateau (located at the position where $\bar{n}_i = 1$) at the transition. As a results, we found that they are not good observables to monitor the Mott transition with trapped gases.

To remove the effect of the depletion that might hide some features associated to the appearance of the first Mott plateau, we calculated the condensate fraction trying to remove the contribution of the depletion. The method we used to remove the depletion seems to work quite well, however debatable in the absence of any theory providing the shape of the depletion close to the transition. Another method which hardly takes into account the depletion consists in measuring the peak height of the diffraction peaks and has the advantage of not being dependent on any supposition on the shape of the depletion. Furthermore, this quantity is expected to be sensitive to the decrease of the condensate fraction and, at the same time, of the increase of the peak width, both effects leading to the decrease of the peak height. We consequently found that these method is the most reliable one in order to infer the location of the appearance of a Mott plateau in the system. Taking into account the points for which the effect of the trap seems to be negligible, we found $(U/J)_c^{meas} = 26.3\,(2)$. It is important to stress that our measurement of the critical value U/J strongly differs from previously reported values: we measure a critical value well below the mean-field prediction previously identified [110], which happens to be even smaller than the QMC value, as expected at finite temperature. Our measurement thus seems compatible with the expectations from QMC predictions at finite temperature. However, the method used here remains still a bit debatable in the sense that we used, to fit the height of the central diffraction peak, an empirical function.

As a result, besides these basic observables, we also started looking at two other quantities, until now not investigated in lattice gases:

- The fluctuations in the condensate mode population. This is inspired by recent investigations carried out in the case of the condensation transition of an harmonically trapped cloud [112] and a discussion with T.Roscilde.

- A quantity that we will refer to as the susceptibility in reference of the linear response theory. This is inspired from a discussion with L.Pezze (Firenze).

The data given in the two paragraphs below are preliminary results and must be considered with a grain of salt.

4.2.3 Investigating fluctuations across the SF-MI crossover

Fluctuations are a key ingredient of classical as well as quantum phase transitions and can find their origin in the finite temperature (classical fluctuations) or in the Heisenberg inequality for non-commuting operators (quantum fluctuations). However, in experiments, fluctuations of quantities are also generally more difficult to measure than the mean values. First, we will review the case of the atom number fluctuation in BEC's across the condensation transition. This will illustrate the difficulty encountered in order to investigate the fluctuations from a theoretical and experimental point of view. Following a recent experiment that measured the increase of the condensate mode fluctuations on approaching the condensation transition from the SF phase [112], we attempted to provide such a measurement across the Mott transition.

Fluctuations in a harmonically trapped Bose Einstein Condensate

Fluctuations in the number of atoms in the lowest-energy single-particle state in cold atomic clouds across the condensation transition are easy to apprehend from a qualitative point of view. If we consider the case of a harmonically trapped gas of non-interacting particles at $T = 0$, all the particles occupy the single lowest energy state of the system, *i.e*, the condensate mode. If we call N_{BEC} the

number of atoms in this mode, then $N_{BEC} = N$, the total number of particles, and there are no fluctuations $\Delta N_{BEC} = 0$. If the temperature of the cloud increases, particles can fill higher energy states and the population of the different states can fluctuate. In particular, $\Delta N_{BEC} \neq 0$ and it increases with the temperature.

While the theory of the Bose Einstein condensation has been developed within the grand canonical ensemble, and appeared to provide a good quantitative analysis of the evolution of the condensate fraction across the condensation transition, it appeared clear that this description was not adequate to predict the physics of fluctuations below the condensation transition[4] [113]. In [114], Politzer was the first to derive, in the canonical ensemble, the expression of the fluctuations of the condensate mode occupation:

$$\Delta N_{BEC}^2 = \frac{\zeta(2)}{\zeta(3)} N \left(\frac{T}{T_{c0}} \right)^3 \tag{4.13}$$

with T_{c0} the ideal gas critical temperature. When adding interactions to the problem, no exact theory is currently available, although fluctuations are expected to be maximum at the transition point. In [112], the authors provided the first measurement of the condensate atom number fluctuations for a trapped interacting gas. They showed a scaling with temperature that resembles the one provided by the non-interacting formula (Eq. 4.13), with a downshift of the transition temperature in agreement with the results of the mean-field theory (see Fig. 4.23).

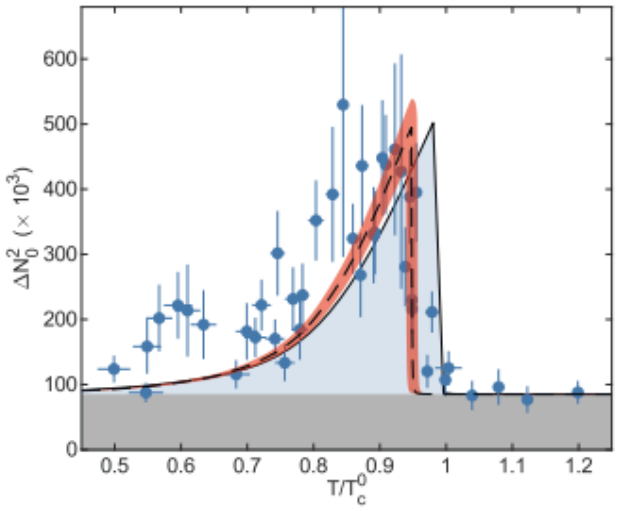

Figure 4.23: **Measurement of the condensate mode fluctuations**. The blue points are the experimental data. The light blue shading is the prediction for the non-interacting gas. The dashed line is a fit to the data using the non-interacting formula. Extracted from [112].

The absence of other investigations of fluctuations (in 3D) across a phase transition relies on the experimental challenge it represents. In fact, these fluctuations vary as $\sqrt{N}$, and are usually hidden below the technical fluctuations of the experiment. In [112], the authors put a lot of effort in order to remove the possible sources of fluctuation. In particular, one major difficulty for experiments using optical imaging detection relies on the quality of the detection (the background noise, *i.e*, the optical shot noise can for instance perturb the density measurement) and the ability to separate the condensate from the non-condensed atoms. Because we are detecting the atoms individually and the background noise is almost null, we will see that the He detector is, at first though, a good candidate to perform such a measurement.

Measurement of the atom number fluctuations in the He experiment and perspectives

We consequently decided to investigate the evolution of the fluctuations of the number of atoms in the lowest-energy single-particle state of lattice gases across the Mott transition. Like in the previous

[4] In particular, under this formalism, one finds very large total atom number fluctuations below the condensation transition that go against the particle conversation.

example, there is no analytic solution to the problem. However, some numerical QMC simulations performed by T.Roscilde (using the integral path method to solve the quantum rotor formulation of the BH Hamiltonian and applicable for systems with integer filling $n \gg 1$ [115]) provided us with an estimation of the fluctuations to observe at the transition. They are of the order of $\Delta N^2_{BEC} \approx 1.2N \approx N$, similarly to the observations in a harmonic trap [112].

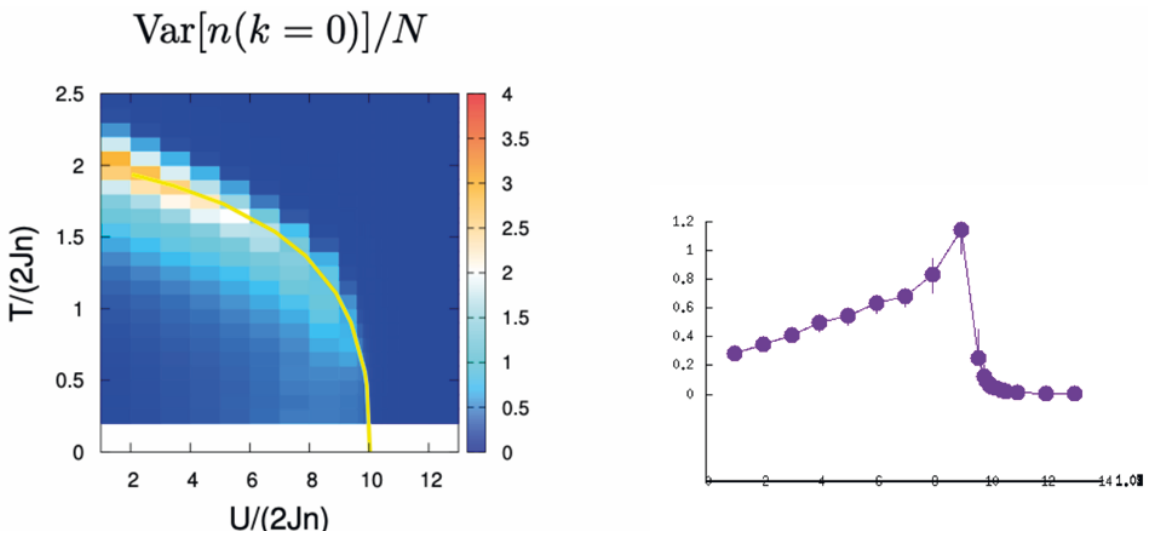

Figure 4.24: **Variance of the BEC atom number in the superfluid phase and across the Mott transition**. Calculated $(\Delta N_{BEC})^2/N$ for a homogeneous system (Careful, the abscissa and the ordinate values have to be multiplied by roughly a factor 3 in order to get the values of T/J and U/J in the good units. Provided and calculated by T. Roscilde.

However, in our experiment, we do not measure the total number of atoms, but a fraction η of it. As a results, $N^{MCP}_{BEC} = \eta N_{BEC}$ and $N^{MCP} = \eta N$, where the index MCP refers to the atom number counts measured with the electronic detector. Considering that, the order of magnitude of the fluctuations to be seen according to the QMC calculations is:

$$\left(\Delta N^{MCP}_{BEC}\right)^2 \approx \eta N^{MCP} \tag{4.14}$$

while the detection, limited to the atomic shot-noise (SN) level, is responsible for fluctuations:

$$\left(\Delta N^{MCP,SN}_{BEC}\right)^2 \approx N^{MCP}_{BEC} \approx f_c \times N^{MCP} \tag{4.15}$$

meaning:

$$\left(\Delta N^{MCP}_{BEC}\right)^2 = \frac{\eta}{f_c}\left(\Delta N^{MCP,SN}_{BEC}\right)^2 \tag{4.16}$$

In the set of data used to investigate the Mott transition , $\eta \approx 5\%$ (in order to avoid a saturation of the detection for the data taken in the superfluid phase), meaning the fluctuations we would like to measure, because of the low detection efficiency, are smaller than the one corresponding to the shot noise, except very close to the transition (for $f_c = 5\%$, the quantum fluctuations are of the order than the shot-noise detection fluctuations).

We computed the fluctuations of the number of atoms in the condensate mode and we found that the fluctuations measured in the experiment were dominated by the atomic shot-noise (see Fig. 4.25). However, reaching a detection efficiency of 15%, which is currently the upper limit in the experiment, would be enough to observe the true fluctuations in the number of atoms in the lowest-energy single-particle state, and which should provide a way to identify the location of the apparition of the first Mott plateau at the QCP. We are also planning to install on the experiment Raman beams in order to

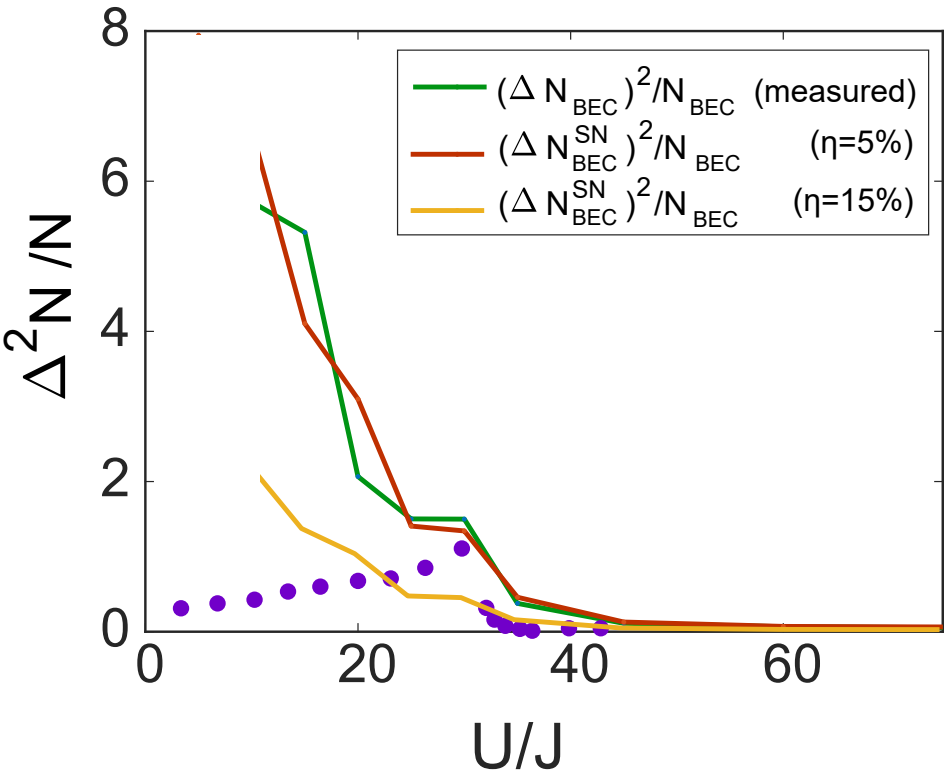

Figure 4.25: **Measurement of the lowest-energy single-particle state population fluctuations across the Mott transition**. *Green curve:* Experimental data (computed using $N_{BEC}^{MCP} = \eta N^{MCP}$). *Red curve:* Expected detection shot-noise fluctuations $\left(\Delta N_{SN}^{BEC}\right)^2 \approx N_{BEC}$ in the experiment. *Yellow curve:* Expected shot-noise fluctuation if we perform the measurement with a detectivity $\eta = 15\%$. *Magenta points:* Fluctuations predicted by the theory of quantum rotors and extracted from Fig. 4.24.

transfer the atoms to the $m_J = 0$ state with a Raman transition, which would allow to reach $\eta = 30\%$.

Note that Prośniak and colleagues recently demonstrated that the critical point of the Bose-Hubbard Hamiltonian could also be measured investigating the on-site fluctuations across the Mott transition [116]. They demonstrate in the paper that these fluctuations are maximum at the QCP, similarly to the condensate fluctuations.

4.2.4 Quantum fidelity approach

Quantum fidelity

The fidelity approach to the investigation of a quantum phase transition appeared a decade ago, following concepts borrowed from the quantum information theory [117, 118]. The advantage of this approach is that it relies only on the state of the system and does not require the knowledge of the Hamiltonian or of the symmetry breaking mechanisms at the origin of the QCP. The fidelity is a measurement of the overlap of two quantum states at nearby points in the parameter space. For instance, if we consider a Hamiltonian $\hat{\mathcal{H}}$ depending on a parameter θ and $|\psi(\theta)\rangle$ is the ground state wavefunction associated, the fidelity may be defined as:

$$\mathcal{F}(\theta, \delta\theta) = |\langle\, \psi(\theta + \delta\theta)|\psi(\theta)\rangle| \tag{4.17}$$

At a quantum phase transition, the ground state is supposed to change drastically for small changes in θ. As a result, for a given variation $\delta\theta$, the fidelity $\mathcal{F}(\theta, \delta\theta)$ is expected to drop in the vicinity of the QCP, that is to say when $\theta = \theta_c$. The position of the minimum of $d\mathcal{F}(\theta)/d\theta$ should thus indicate the location of critical point, as shown in [119] in the case of the XY spin chain model.

For a small change in θ, the fidelity can be expanded in the form:

$$\mathcal{F}(\theta, \delta\theta) = 1 - \frac{\chi\,[\theta]}{8}\delta\theta^2 + \mathcal{O}(\delta\theta^3) \tag{4.18}$$

where the constant coefficient 1 comes from the normalization of the wavefunction and the term in $\delta\theta$ is equal to zero due to symmetry. The term $\chi(\theta) = 4 \times \partial^2\mathcal{F}(\theta, \delta\theta)/\delta\theta^2$ is called the fidelity susceptibility and represents a quantity that is expected to be maximum at the transition point.

Link with the Fisher information theory

The interesting aspect of this method also comes from its link which the quantum Fisher information theory. The classical Fisher information is a way of measuring the amount of information that an observable X carries about an unknown parameter θ upon which the probability of X depends. If for instance the probability distribution of X is peaked around θ, then the measurement of X provides a good estimate of θ. What Fisher information theory provides is a bound to the precision on the estimation of a physical quantity.

Its quantum counterpart is defined for a unitarity transformation $e^{-i\theta\hat{O}}$ through:

$$\left\langle \psi|e^{-i\theta\hat{O}}|\psi \right\rangle = 1 - \frac{F(|\psi\rangle\,, \hat{O})}{8}\theta^2 + \mathcal{O}(\theta^3) \tag{4.19}$$

where $F(|\psi\rangle\,, \hat{O})$ is referred to as the Fisher information. That is to say, a definition and expression completely comparable to Eq. 4.17 and Eq. 4.18. In the case of a pure quantum state $|\psi\rangle$ as considered here, the Fisher information is equal to the variance of the operator $\hat{O}$, that is to say $F(|\psi\rangle\,, \hat{O}) = 4\Delta\hat{O}^2$. This definition can be generalized to the case of a system in a mixed state defined by a density matrix $\hat{\rho}$. The quantum Fisher information provides information about the degree of entanglement in the system. For instance, if we consider a system made of N-qubits [120]:

$$\begin{aligned} F(\rho, \hat{O}) &= N \qquad \text{if the state is separable} \\ &< Nk \qquad \text{if there are k-partite entanglement in the system} \end{aligned} \tag{4.20}$$

Entanglement is a unique property of quantum systems that takes the form of non-classical correlations. It has been demonstrated to play a major role at quantum phase transitions [121, 122, 123] and this motivated us to use the information theory in order to investigate the Mott transition, and more precisely, through the quantum fidelity approach.

In our experiment

Investigations of entanglement trough a fidelity measurement are scarce, due to the difficulty in measuring wavefunctions (or the full density matrix). On the contrary, experiments better provide the modulus square of the wavefunctions, that is to say probabilities.

For the investigation of the Mott transition, the parameter that controls the transition is $\theta = U/J$. Since the change in the ground state of the system across the Mott transition is better apprehended in the momentum space, it consequently appears to be a natural basis for the implementation of the quantum fidelity approach. Using classical statistics, and in analogy with the work done by H.Strobel and colleagues [120], we define the fidelity (in momentum space) by:

$$\mathcal{F}(U/J, \delta(U/J)) = \frac{\int_{\vec{k}} \sqrt{\rho(\vec{k}, U/J + \delta U/J)\rho(\vec{k}, U/J)}d\vec{k}}{\sqrt{\int_{\vec{k}} \rho(\vec{k}, U/J + \delta U/J)d\vec{k}} \times \sqrt{\int_{\vec{k}} \rho(\vec{k}, U/J)d\vec{k}}} = 1 - \frac{\chi\,[U/J]}{8}\delta(U/J)^2 + \mathcal{O}(\delta(U/J)^3) \tag{4.21}$$

Experimental results

To obtain the experimental value of the susceptibility $\chi\,[U/J]$ at a given U/J, the method consists in measuring the momentum distribution at different values of $U/J + \delta(U/J)$ and to apply Eq. 4.21. However, in the absence of theory that could provide any information about the amplitude of the variation of $\chi\,[U/J]$ or the range in $\delta(U/J)$ for which the variation of $\mathcal{F}(U/J, \delta(U/J))$ is quadratic, this measurement is not simple and needs to be the object of deep investigations.

To start with, we first checked whether the variation of $\mathcal{F}(U/J, \delta(U/J))$ with $\delta(U/J)$ at a fixed value of U/J is quadratic. As the susceptibility is supposed to be maximum at the transition, we choose to take some data around $U/J = 25$, by steps of about 0.4 in U/J. Note that such a measurement requires to be able to set precisely the lattice amplitude. In our experiment, this is provided by the good stabilization of the optical lattice power. However, steps of the order to $\delta(U/J) = 0.4$ correspond to variations in the setpoint voltage of about 5 mV. We thus checked that the analog output delivering the setpoint voltage was able to provide such an accuracy.

We measured, in a random way and during the same day, 6 sets of momentum distributions at $U/J = \{24.5,\ 26,\ 26.4,\ 26.8,\ 27.2,\ 27.6\}$. The corresponding 1D cuts are plotted in Fig. 4.26. We see by eyes that even for small variations in U/J, the momentum distribution varies, which is a good start for the susceptibility measurement!

In order to calculate $\mathcal{F}(U/J, \delta(U/J))$, we discretize the momentum distribution in a 3D histogram. Only the first BZ is considered (and the measured distribution is corrected from the Wannier distribution also calculated on the same grid). The number of atoms is rescaled by 3 000. If we note the pixel positions in momentum space $\vec{k}_i$ and the we define V_{pixel} as the pixel volume:

$$\mathcal{F}(U/J, \delta(U/J)) = \sum_i \sqrt{\rho(\vec{k}_i, U/J + \delta U/J)\rho(\vec{k}_i, U/J)}V_{pixel}/3000 \tag{4.22}$$

Of course, the size of the pixels used needs to be chosen with care: if the pixels are too large, the momentum distribution calculated is smoothen, with the consequence that the difference between the different momentum distributions corresponding to the different values of U/J vanishes. On the contrary, if the pixel size is too small, the momentum distribution is too noisy (there are a lot of pixels without counts, giving rise to false null momentum densities).

The results obtained for different pixel sizes (of cubic length Δk) are plotted in Fig. 4.27. $1 - \mathcal{F}(U/J, \delta(U/J))$ seems hardly to depend on the value of $\delta(U/J)^2$ while we are looking for a linear

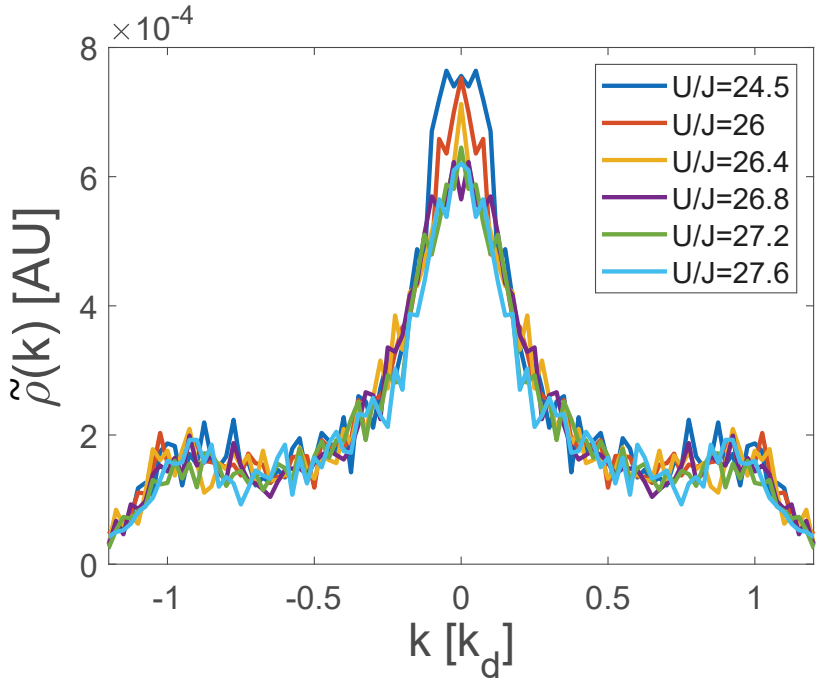

Figure 4.26: **1D cuts of the data used for the calculation of the fidelity susceptibility**.

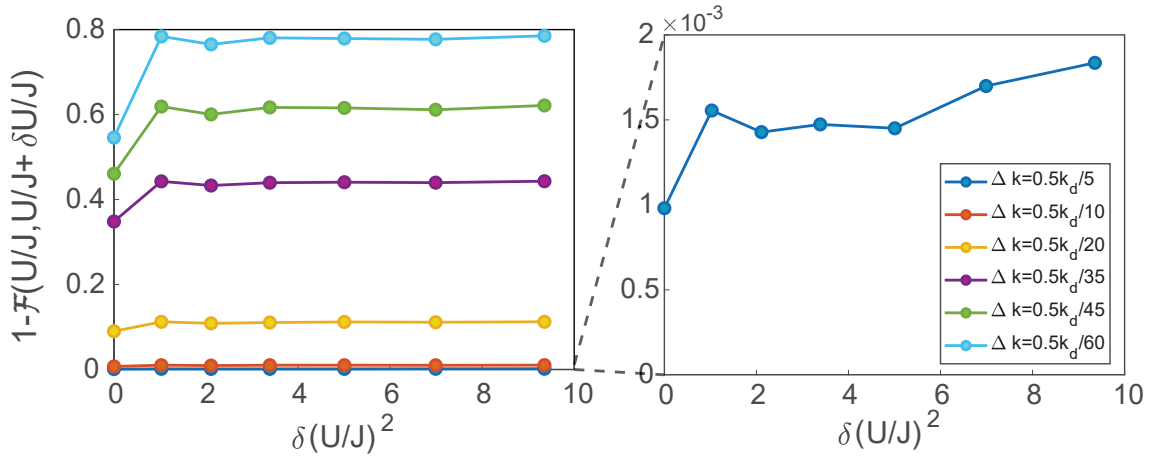

Figure 4.27: **Measurement of the susceptibility at U/J = 25**. Value of $1-\mathcal{F}(U/J,\delta(U/J))$ as a function of $\delta(U/J)^2$ for $U/J=25$ and for different pixel sizes. While we are expecting from the theory a linear variation of $1-\mathcal{F}(U/J,\delta(U/J))$ as a function of $\delta(U/J)^2$, on the experimental data (left graph), $1-\mathcal{F}(U/J,\delta(U/J))$ seems to be constant as a function of $\delta(U/J)^2$, except for the data with $\Delta k = 0.1\,k_d$ (right graph). Note that here, $1-\mathcal{F}(U/J,\delta(U/J))$ is not equal to zero for $\delta(U/J)^2=0$. This comes from the fact that to test the effect of the zeros in the momentum distribution computed or the effect of the statistics, the integral $\sum_i \sqrt{\rho(\vec{k}_i,U/J)\rho(\vec{k}_i,U/J)}V_{pixel}$ as been computed using two separate sets of data at $U/J=25$. Of course, we see that the smaller the pixel size, the larger is the value $1-\mathcal{F}(U/J,\delta(U/J)=0)$.

variation. Furthermore, the smaller is the pixel size, the higher the value of $1-\mathcal{F}(U/J,\delta(U/J))$. We attribute that to the presence of zeros in the measured distribution. Since the position of the zeros in the momentum distribution corresponding to the $\delta(U/J)=0$ and $\delta(U/J)>0$ are independent, the product $\rho(\vec{k}_i,U/J+\delta U/J)\rho(\vec{k}_i,U/J)$ has a lof of zeros, as a result:

$$\sum_i \sqrt{\rho_{meas}(\vec{k}_i,U/J+\delta U/J)\rho_{meas}(\vec{k}_i,U/J)}V_{pixel} \ll \sum_i \sqrt{\rho(\vec{k}_i,U/J+\delta U/J)\rho(\vec{k}_i,U/J)}V_{pixel} \quad (4.23)$$

In fact, to test the effect of the zeros in the measured 3D momentum distribution, we separated the set at $U/J = 25$ in two, and calculated the sum $S = \sum_i \sqrt{\rho_{\text{set1}}(\vec{k}_i, U/J)\rho_{\text{set2}}(\vec{k}_i, U/J)V_{pixel}}$. In theory, $S = \sum_i \sqrt{\rho_{\text{set1}}(\vec{k}_i, U/J)\rho_{\text{set1}}(\vec{k}_i, U/J)V_{pixel}} = \sum_i \sqrt{\rho_{\text{set2}}(\vec{k}_i, U/J)\rho_{\text{set2}}(\vec{k}_i, U/J)V_{pixel}} = 3\,000$. In the experiment, S goes from 2 970 for $\Delta k = 0.1\,k_d$ to 1 360 to $\Delta k = 0.5/60\,k_d$, while the proportion of zeros in the momentum distribution histograms goes from 0 to 85% (from $\Delta k \geq 0.5k_d/20$, the proportion of zeros is superior to 50%). Note that the point at $\delta U/J = 0$ represented in Fig. 4.27 is calculated from the two sets of data ρ_{set1} and ρ_{set2} (equal to S).

The only curve where a linear tendency seems to appear is the one for which $\Delta k = 0.1\,k_d$. However, this large binning implies smoothing a lot the distributions and we do not expect to be able to perform quantitative measurements of the susceptibility in this configuration. The conclusion is that we should take more data in order to be able perform the susceptibility measurement this way.

Since we do not have enough signal to resolve properly the full 3D momentum distribution, especially in the low density domains, we concentrated the calculation in the region of high densities, that is to say along the lattice axis. We consequently computed $\mathcal{F}_{1D}(U/J, \delta(U/J))$, defined similarly as $\mathcal{F}(U/J, \delta(U/J))$ but using the 1D cuts $\rho_{1D}(k_i) = \rho_{1D}(k_i, 0, 0)$ instead of the full momentum distribution in the integral:

$$\mathcal{F}_{1D}(U/J, \delta(U/J)) = \frac{\sum_i \sqrt{\rho_{1D}(k_i, U/J + \delta U/J)\rho_{1D}(k_i, U/J)V_{pixel}}}{\sqrt{\sum_i \rho_{1D}(k_i, U/J + \delta U/J)V_{pixel}} \times \sqrt{\sum_i \rho_{1D}(k_i, U/J)V_{pixel}}} \tag{4.24}$$

The 1D cuts are calculated with a transverse integration $\Delta k_\perp$. The results are plotted in Fig. 4.28. In this case, and for a transverse integration of $\Delta k_\perp = 0.25\,k_d$, we see a clear linear variation of $1 - \mathcal{F}_{1D}(U/J, \delta(U/J))$ as a function of $\delta(U/J)^2$. A linear adjustment provides the slope α that we use to compute the 1D susceptibility $\chi_{1D}(U/J, \Delta k_\perp) = 8 \times \alpha$. Of course, the wider the transverse integration, the lower is $\chi_{1D}(U/J, \Delta k_\perp)$ as represented in Fig. 4.28.b.

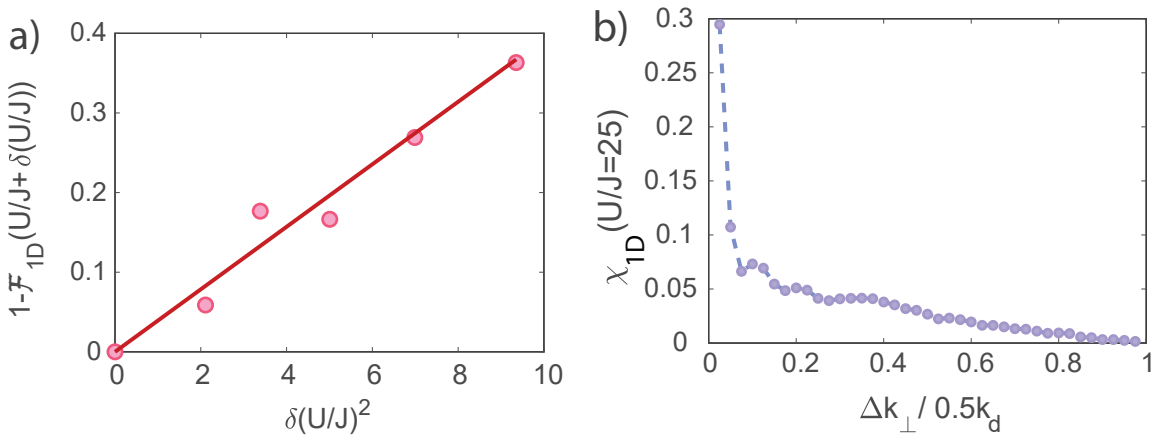

Figure 4.28: **Measurement of the 1D susceptbility $\chi_{1D}(U/J)$ for $U/J = 25$** . **a)** Value of $1 - \mathcal{F}_{1D}(U/J, \delta(U/J))$ for $\Delta k_\perp = 0.25\,k_d$ as a function of $\delta(U/J)^2$. **b)** Value of $\chi_{1D}(U/J = 25)$ as a function of $\Delta k_\perp$.

For very low transverse integrations, we expect the susceptibility to reach a plateau (when the transverse integration becomes lower than the thinest features in the momentum distribution, *i.e*, the diffraction peaks), that is not visible in the Fig. 4.28.b. We attribute the divergence of χ_{1D} at low $\Delta k_\perp$ to the fact that the data become too noisy when decreasing too much $\Delta k_\perp$. To monitor the evolution of $\chi_{1D}(U/J)$ across the transition, we would need to access the values of χ_{1D} in the plateau area for different values of U/J (if we use a large and constant transverse integration to measure χ_{1D} for the different values of U/J, the integration will result in a different smoothing of the distributions depending on the size of the diffraction peaks, especially close to the transition, which could interfere in the measurement of the susceptibility). To do that, a better statistics is necessary.

In both cases (1D or 3D method), the investigations needs to the continued in order to conclude on the do-ability of this measurement, notably by taking some data with a better statistics.

5. Revealing one-particle correlations in Mott insulators

We have seen in §.2.2.2 that the presence of particle-hole excitations in the Mott insulator phase was responsible for the presence of some short-range coherence. This coherence can be revealed by the presence of a small periodic modulation of the momentum distribution on top of the flat momentum distribution of the perfect Mott insulator.

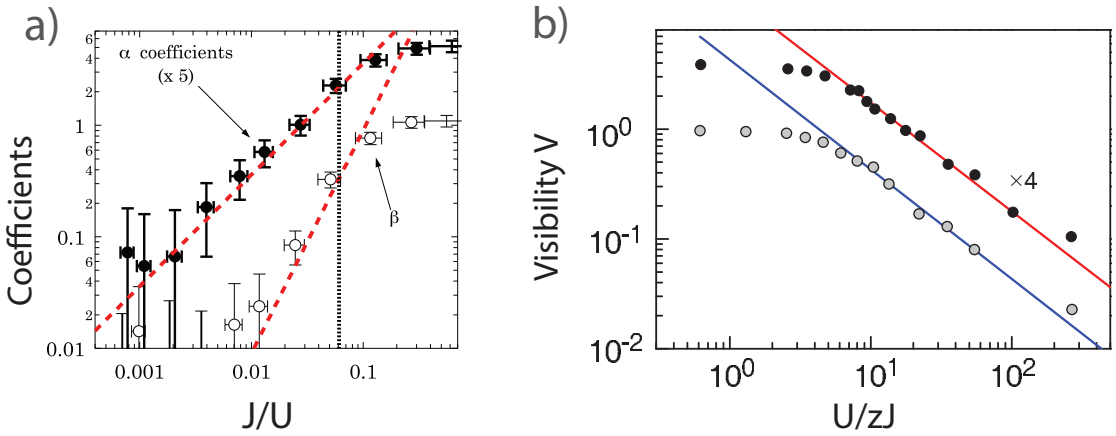

Figure 5.1: **Signatures of the particle-holes excitation revealed in other experiments**. **a)** In 2D through the measurement of the periodic momentum distribution modulation induced and analyzed up to the second order in the perturbation theory. The experimental data are fitted by cosine functions with a periodicity of k_d (first order expansion) and $k_d/2$ (second order expansion) from which the respective amplitudes α and β are extracted and reported on the graph. The lines represent the amplitude expected $\alpha_{theo} = 8\,J/U$ and $\beta_{theo} = 90\,(J/U)^2$. Extracted from [124]. **b)** In 3D through the evolution of the visibility. Because of the residual coherence restored by the particle-hole excitations, the visibility decreases slowly in the MI phase. The different data represent different atom numbers (the upper curve has been shifted for the two sets of data to be visible). The lines represent the fit by an algebraic function decaying in U/J as expected from the first order perturbation theory. Extracted from [75].

This effect has been investigated in 2D [124] (see Fig. 5.1.a), up to the second order perturbation theory in J/U. They demonstrated a periodic modulation with amplitudes in perfect quantitative agreement with the perturbation theory. In 3D, the effect of particle-hole excitations has been put into relief by measuring the decrease of the visibility as $J/U \to 0$ in the Mott phase. Defining the visibility $\mathcal{V}$ as:

$$\mathcal{V} = \frac{\tilde{\rho}_{2D}(k_d, 0) - \tilde{\rho}_{2D}(k_d/\sqrt{2}, k_d/\sqrt{2})}{\tilde{\rho}_{2D}(k_d, 0) + \tilde{\rho}_{2D}(k_d/\sqrt{2}, k_d/\sqrt{2})} \tag{5.1}$$

where $\tilde{\rho}_{2D}$ refers to the 1D integrated (line-of-sight integration) momentum distribution measured by the usual optical imaging techniques, and the definition of the momentum distribution given in Eq. 2.42 (also integrated along the line-of-sight), the variation of the the visibility due to the particle-hole excitations at the first order (and integrated along one direction to mimic the effect of the optical

detection integration used in [75]) writes:

$$\mathcal{V} = \frac{3z}{4} n_0(n_0+1)\frac{J}{U} \tag{5.2}$$

resulting in a linear decrease of the visibility with J/U in the limit $J/U \to 0$. Note that here, z refers to the number of nearest neighboring sites. Gerbier and colleagues [75] measured quantitatively such a decrease (see Fig. 5.1.b), although the visibility for high U/J was systematically higher than the one predicted by the first order perturbation theory.

In both cases, the investigation of the particle-hole coherence has been limited to the first and second orders in the perturbation theory. In 3D, it has only been done indirectly by measuring the visibility. Note that particle-hole excitation have also been investigated in-situ [125, 48] through the in-situ density-density correlations $\langle \hat{n}_i \hat{n}_j \rangle$.

To provide a quantitative investigation of the one-particle coherence in the MI phase (and in the momentum space), one needs to access the real shape of the momentum distribution (as it was the case in the 2D experiment mentioned before). In 3D, the line-of-sight integration inherent to the optical imaging techniques prevents to carry such a measurement. With the possibility to measure the momentum distribution in 3D and with a very good resolution, we consequently provide in this chapter a description of the one-particle coherence deep in the MI phase and on approaching the transition.

5.1 Particle-hole excitations: perturbative theoretical approaches

The quantitative understanding of the modification of the momentum distribution due to the particle-hole excitations requires going beyond the mean-field theories. Many calculations have been using the strong coupling methods in order to calculate the Green function of the Mott insulator [29, 126, 127]. Green functions are of particular importance for the investigation of N-body systems through their excitations. In this section, a brief reminder of the Green function formalism will be given. The idea is not to (re)demonstrate the results obtained in [29, 126, 127] as it is beyond reach of this manuscript, but to provide an intuition about the Green functions and their relations to the single-particle spectral function $\mathcal{A}(\vec{k},\omega)$ and the momentum distribution $\rho(\vec{k})$.

5.1.1 Green's functions and spectral functions

Example: the classical harmonic oscillator

In order to get a physical intuition of the Green's functions, one can study the case of a damped harmonic oscillator in 1D, and more precisely its response to an external excitation $f(t)$. This means solving the equation:

$$\ddot{x}(t) + \eta\dot{x}(t) + \omega_0^2 x(t) = f(t) \tag{5.3}$$

with $\eta\dot{x}(t)$ the dissipation term. The Green function $\mathcal{G}(t)$ of the system {fluid+harmonic oscillator} is given by the impulse response function, that is to say the solution of Eq. 5.3 for $f(t) = \delta(t)$. The knowledge of the Green function enables then to compute easily the response of the system to any drive $f(t)$ using: $x(t) = \mathcal{G} * f(t)$ or in the frequency domain: $\tilde{x}(\omega) = \tilde{G}(\omega)\tilde{f}(\omega)$. In the example developed here [128, 129]:

$$\tilde{\mathcal{G}}(\omega) = -\frac{1}{\omega^2 - \omega_0^2 + 2i\omega\omega_0\xi} = -\frac{1}{(\omega-\omega_+)(\omega-\omega_-)} \Rightarrow \mathcal{G}(t) = \frac{1}{\omega_R}\sin(\omega_R t)e^{-\omega_0\xi t}\Theta(t) \tag{5.4}$$

with $\omega_\pm = i\omega_0\xi \pm \omega_R$, $\omega_R = \omega_0\sqrt{1-\xi^2}$, $\xi = \eta/2\omega_0$ and $\Theta(t)$ the Heaviside function. In the temporal domain, the former equation thus provides the information about the resonant frequency ω_R of the system, that is to say, the frequency at which it can be excited as well as the lifetime of the oscillation $\tau = 1/\omega_0\xi$. The excitation spectrum of the harmonic oscillator is determined by the interaction

with the viscous fluid (through ξ) and the lifetime of the oscillation is finite due to the presence of a dissipation term.

Without the interaction, the system oscillate at $\omega = \omega_0$ without damping ($\tau = \infty$):

$$\tilde{\mathcal{G}}_0(\omega) = \frac{-1}{\omega^2 - \omega_0^2} \tag{5.5}$$

Comparing Eq. 5.4 and Eq. 5.5 leads to the Dyson equation:

$$\tilde{\mathcal{G}}(\omega) = \tilde{\mathcal{G}}_0(\omega) + \tilde{\mathcal{G}}_0(\omega)\Sigma(\omega)\tilde{\mathcal{G}}(\omega) \tag{5.6}$$

where $\Sigma(\omega) = 2i\xi\omega_0\omega$ is called the self-energy. The interest of the self-energy relies on the possibility to link the excitations of a complex system (in this case the system fluid+harmonic oscillator) to the excitations of only one particle (here the harmonic oscillator) without fluid (interaction) and with new properties given by the self energy: a finite lifetime τ and a new resonant frequency ω_R. When the system is complex and cannot be solved analytically, the difficulty thus relies on the calculation of the self-energy.

Furthermore, one can show that the energy absorbed by the system driven by a monochromatic excitation $\tilde{f}(\omega) = \delta(\omega - \omega_e)$ is equal to:

$$\mathcal{A}(\omega_e) = \frac{1}{\pi}\text{Im } \tilde{\mathcal{G}}(\omega_e) \tag{5.7}$$

which is the one-particle spectral function.

Quantum systems

All the developments done before can be translated to quantum mechanical problems and the solving of the Schrodinger equation:

$$\hat{\mathcal{H}}\Psi(\vec{r}, t) = i\hbar\frac{\partial}{\partial t}\Psi(\vec{r}, t) \tag{5.8}$$

where the Green function is the solution of the equation:

$$\left[i\hbar\frac{\partial}{\partial t} - \hat{\mathcal{H}}\right]\hat{\mathcal{G}}(t) = \delta(t) \tag{5.9}$$

In the rest of the paragraph, we will consider its Fourier transform developed on the momentum basis:

$$\mathcal{G}(\vec{k}, \omega) = \left\langle \vec{k}|FT\left[\hat{\mathcal{G}}(t)\right]|\vec{k}\right\rangle \tag{5.10}$$

To simplify the notations, we will also get rid of the tilde to refer to the Fourier transform.

In this chapter, we will treat the case of a quantum gas in the Mott insulating phase. We can first consider the simple case of a homogeneous and infinite cloud in the Mott insulating phase for which $J/U \approx 0$. Then the ground state of the system is a product of Fock states on each lattice sites with filling n_0. In the absence of tunneling between the lattice sites, that is to say without coupling, the adding or removing of a particle is characterized by a gain or a loss of an energy: $\hbar\omega_+ = Un_0 - \mu$ and $\hbar\omega_- = U(n_0 - 1) - \mu$. As a result [34]:

$$\mathcal{G}_0(\vec{k}, \omega) = \frac{n_0 + 1}{\hbar\omega + \mu - Un_0} + \frac{n_0}{\hbar\omega + \mu - U(n_0 - 1)} \tag{5.11}$$

meaning the Green function is independent on the momentum.

Like in the case of the presence of a fluid that couples to the harmonic oscillator, the presence of finite a tunnelling in the system will be at the origin of the modification of the excitation spectrum.

The Green function $\mathcal{G}(\vec{k},\omega)$ can be calculated using the Dyson equation linking $\mathcal{G}_0(\vec{k},\omega)$ and the self-energy $\Sigma(\vec{k},\omega)$ like in the case of the harmonic oscillation:

$$\mathcal{G}(\vec{k},\omega) = \frac{\mathcal{G}_0(\vec{k},\omega)}{1-\Sigma(\vec{k},\omega)\mathcal{G}_0(\vec{k},\omega)} \tag{5.12}$$

Of course, the difficulty relies on the calculation of the self-energy $\Sigma(\vec{k},\omega)$. Since there is no method to find the self-energy of a quantum correlated system, diagramatic perturbation methods have been developed to provide an estimation of it. From a general point of view, the self-energy can be developed as a series:

$$\Sigma(\vec{k},\omega) = \sum_{n=0}^{+\infty} \left\langle \vec{k}|\hat{V}\left(FT\left[\hat{\mathcal{G}}(t)\right]\hat{V}\right)^n|\vec{k}\right\rangle \tag{5.13}$$

where $\hat{V} = -J\sum_{\langle i,j\rangle}\hat{b}_i^\dagger\hat{b}_j$ the kinetic part of the BH Hamiltonian (and treated perturbatively in the strong-coupling methods). This calculation will not be developed in this manuscript and we will just review in the next section the main results obtained in [126, 29].

Before that, we want to give, for quantum systems, the physical interpretation of the spectral function previously defined:

$$\mathcal{A}(\vec{k},\omega) = -\frac{1}{\pi}\mathrm{Im}\mathcal{G}(\vec{k},\omega) \tag{5.14}$$

Using Eq. 5.10, one can show that [130, 131]:

$$\mathcal{A}(\vec{k},\omega) = \sum_\alpha \delta(\hbar\omega - E_\alpha)\left|\left\langle E_\alpha|\vec{k}\right\rangle\right|^2 \tag{5.15}$$

where E_α refers to the eigenenergies of $\hat{\mathcal{H}}$. As a result, the spectral function can be understood as the conditional probability for a particle to occupy a state with an energy $E=\hbar\omega$ provided it has a momentum $\vec{k}$. It is consequently linked to the momentum distribution through:

$$\rho(\vec{k}) = -\int_{-\infty}^{0} A(\vec{k},\omega)d\omega \tag{5.16}$$

5.1.2 Strong-coupling methods for the investigation of the Mott phase

The strong-coupling method developed in [29] by K. Sengupta and N. Dupuis goes beyond the standard mean-field theories. They introduced, similarly to the Bogoliubov treatment of weak interactions, quadratic quantum fluctuations on top of the classical Gutzwiller solution for the perfect Mott insulator. They found:

$$\mathcal{G}(\vec{k},i\omega) = \frac{1-Z(\vec{k})}{i\omega - E_{\vec{k}}^-} + \frac{Z(\vec{k})}{i\omega - E_{\vec{k}}^+} \tag{5.17}$$

Where the excitation energies $E_{\vec{k}}^\pm$ (corresponding to the particles and the holes) and the associated spectral weight $Z_{\vec{k}}$ are given by:

$$E_{\vec{k}}^\pm = -\delta\mu + \frac{E(\vec{k})}{2} \pm \frac{1}{2}\left[E(\vec{k})^2 + 4E(\vec{k})U\tilde{x} + U^2\right]^{1/2} \tag{5.18}$$

$$Z(\vec{k}) = \frac{E_{\vec{k}}^+ + \delta\mu + U\tilde{x}}{E_{\vec{k}}^+ - E_{\vec{k}}^-} \tag{5.19}$$

with $\tilde{x} = n_0 + 1/2$ and $\delta\mu = \mu - U(n_0 - 1/2)$.

Using the Eq. 5.17, Eq. 5.16 and Eq. 5.14, the momentum distribution writes:

$$\boxed{\rho(\vec{k}) = 1 - Z(\vec{k})} \tag{5.20}$$

which is equal, within the strong coupling method

$$\boxed{\rho_{sc1}(\vec{k}) = \frac{1}{2} - \frac{\frac{E_{\vec{k}}}{2} + \frac{3}{2}U}{\sqrt{E(\vec{k})^2 + 6E(\vec{k})U + U^2}}} \tag{5.21}$$

where we took $n_0 = 1$ ($\tilde{x} = 3/2$) and $E_{\vec{k}} = -2J\sum_{x,y,z}\cos(\pi k_i/k_d)$ for a Mott insulator in a 3D cubic lattice and with a unity filling. This function is plotted in Fig. 5.2 for different values of U/J and along one axis of the lattice. We see that the distribution becomes more and more peaked on approaching the Mott transition, and diverges for $U/J \approx 35$ which corresponds to the critical point calculated within the mean-field theories [27, 30]. As a result, one can guess that this function is not accurate close to the real transition predicted by the QMC method ($(U/J)_c^{QMC} = 29.3$).

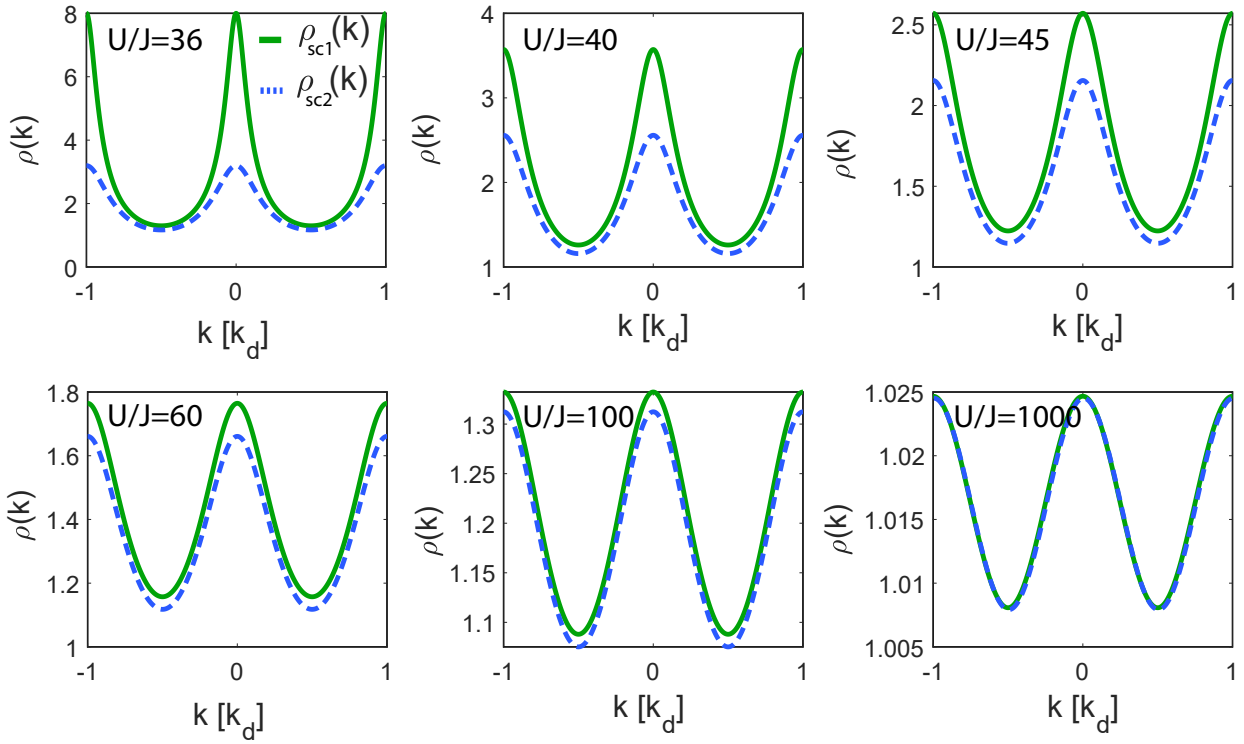

Figure 5.2: **Strong coupling momentum distributions.** Values of $\rho_{sc1}(\vec{k})$ (green lines) and $\rho_{sc2}(\vec{k})$ (blue dashed lines) as a function of $k = (k_x, 0, 0)$ for different values of U/J.

In order to improve this strong coupling method, Nandini Trivedi and colleagues started from this expression and created a scaling ansatz for the momentum distribution using some known properties of the system close to the transition [126]:

- the power-series expansion of the scaling ansatz, done with the small parameter $x = \frac{3J}{U}$, must reproduce the strong-coupling expansion through the given order.
- the critical point must correspond to the exact value $(U/J)_c = 29.3$ calculated by the QMC methods [24].
- $\int_{\vec{k}} \rho_{sc2}(\vec{k})d\vec{k} = n_0$

They obtained:

$$\boxed{\rho_{sc2}(\vec{k}) = -\frac{1}{2} + \frac{x + \xi_{\vec{k}}x + \frac{c'}{d^2}x^2 + 2\frac{e'}{d^2}\xi_{\vec{k}}x^3}{\left[1 + 2\bar{a}\xi_{\vec{k}}x + 4\bar{b}\xi_{\vec{k}}^2x^2 + \frac{\bar{c}}{d^2}x^2 + 8\bar{d}\xi_{\vec{k}}^3x^3 + 2\frac{\bar{e}}{d^2}\xi_{\vec{k}}x^3\right]^{\gamma_s}}} \tag{5.22}$$

with $\xi_{\vec{k}} = E_{\vec{k}}/(6J)$ and the expression of the coefficients can be found in [126]. We plotted $\rho_{sc2}(\vec{k})$ in Fig. 5.2 and compared it to $\rho_{sc1}(\vec{k})$. The scaling solution ρ_{sc2} has been compared to QMC distributions (by the authors of the paper) and showed a very good agreement even at the transition. As a result, we will use the momentum distribution expression given in Eq. 5.21 for comparison with the experimental data. Note that the scaling solution is performed for infinite and homogeneous systems.

5.2 Experimental results

In Fig. 5.3, are plotted the experimental 1D cuts $\rho(k,0,0)$ obtained for the set of data with $N = 3000$ atoms (filling inferior to 2), and $U/J = \{92, 60, 45, 35\}$. At $U/J = 92$, the momentum distribution is almost flat (we remind here that the momentum $\rho(k,0,0)$ distribution that we plot is obtained from the TOF density $\tilde{\rho}(k,0,0)$ and normalized by the Wannier function using Eq. 3.9). A small periodic modulation, attributed to the coherence restored by particle-holes is although visible. When going close to the transition, the momentum distribution gets more and more peaked, as the particle-holes can delocalize over longer distances, restoring a medium-range coherence. Because of the link between the momentum distribution and the spectral weight $\rho(\vec{k}) = \mathcal{N}\left(1 - Z(\vec{k})\right)$, this provides for the first time a direct measurement of the narrowing of the spectral weight on approaching the Mott crossover.

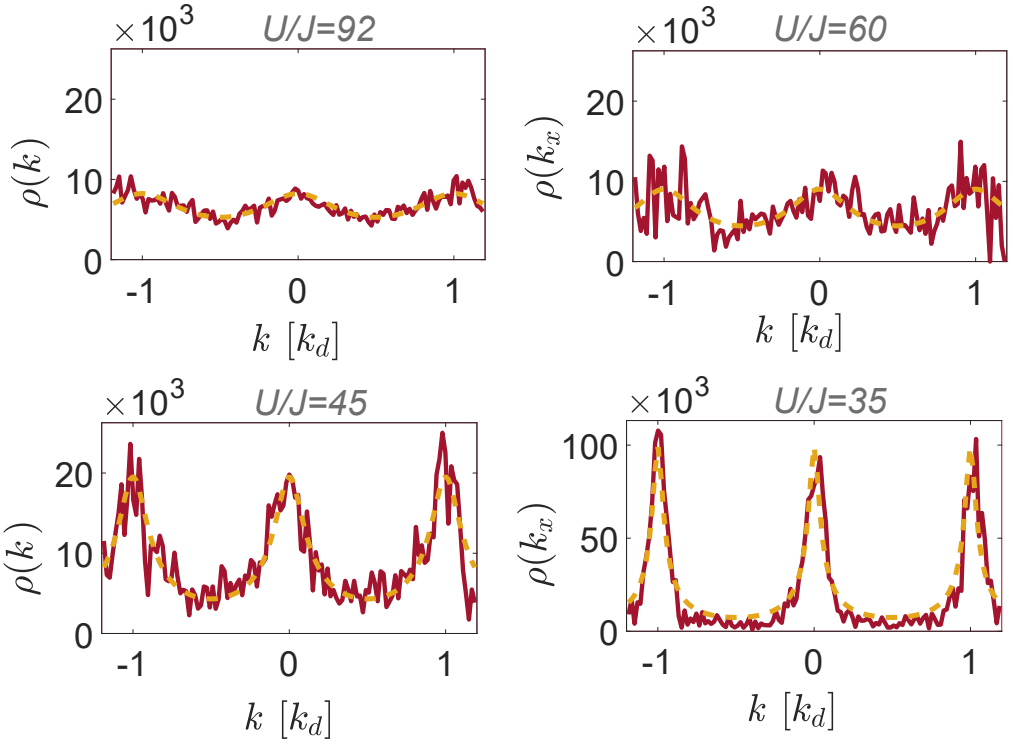

Figure 5.3: **Measured momentum distribution in the Mott insulating phase**. 1D profiles (red lines) $\rho(k,0,0)$ for the data taken with $N = 3\,000$ atoms, and for $U/J = \{92\ 60\ 45\ 35\}$. The dashed orange curves represent the result of the fit by the function $\mathcal{N} \times \rho_{sc2}(k,0,0)$ where U/J (or x) and $\mathcal{N}$ are the two free parameters.

In order to compare the experimental data with the scaling solution of the strong coupling theory, the profiles are adjusted by the function $\mathcal{N} \times \rho_{sc2}(k,0,0)$ where $\mathcal{N}$ is a normalizing coefficient (expected to tend towards the total number of atoms $\mathcal{N} = N = 3\,000$ when $U/J \to \infty$). $\mathcal{N}$ and $x = 3J/U$ are the only free parameters. The results of the fit are the dashed orange lines plotted in Fig. 5.3. We see that the agreement between the experimental data and the scaling solution is pretty good, at least for high values of U/J. For $U/J = 35$, we although notice that the low density regions of the momentum distribution are not well reproduced by the strong-coupling profile. In order to get a more quantitative comparison, the results of the fit are given in Tab. 5.1.

The values $(U/J)_{meas}$ extracted from the fits are always lower than the corresponding U/J. This can be understood looking at the contrast of the periodic modulation and defined here as:

$$\mathcal{C}^{1D} = \frac{\max(\rho(k,0,0)) - \min(\rho(k,0,0))}{\max(\rho(k,0,0)) + \min(\rho(k,0,0))} \tag{5.23}$$

U/J	92	60	45	35
$(U/J)_{meas}$	56 (10)	42 (1)	31.7 (6)	29.5 (2)
$\mathcal{N}$	4700 (1000)	3800 (1600)	3600 (1400)	6200 (2600)

Table 5.1: **Results of the fit of the Mott insulator profiles with the strong coupling solution plotted in Fig. 5.3.** The two free parameters are $U/J = 3x$ and $\mathcal{N}$. We see that if the agreement between the strong coupling solution and the experimental data is good, the quantitative analysis reveals major discrepancies.

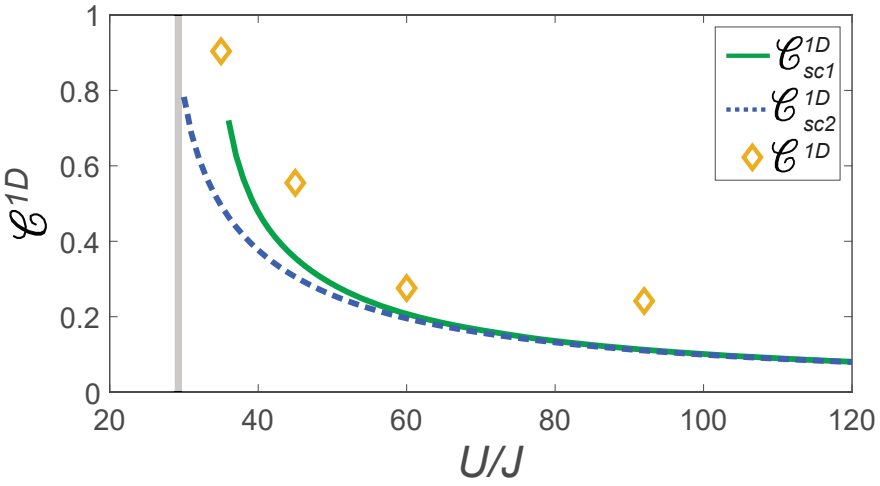

Figure 5.4: **Contrast of the momentum distribution modulation for the data at U/J $\geq$ 35.** The yellow points are the experimental data. The green and dashed blue curves are the contrast computed considering respectively the momentum distributions $\rho_{sc1}(k)$ and $\rho_{sc2}(k)$.

The experimental values are plotted in Fig. 5.4. On the same graph, are also plotted the contrast calculated according to the two numerical predictions of the strong coupling methods. In the experiment, the contrast of the modulation is far higher than the one expected from the strong coupling theories, in agreement with the quantitative discrepancies mentioned above. The interpretation to give to these results is that the phase coherence in the clouds extends over a longer distance than what predicted by the strong-perturbative treatments.

We consequently investigated different possible hypothesis for the observation of such discrepancies. Note that such an effect has already been seen in [34] deep in the Mott insulator regime.

- *Temperature effect.*
  The strong coupling methods are performed considering $T = 0$ while our data are taken with $T \approx 3 - 5\,J$. Using the QMC distributions, one can also compute the contrast $\mathcal{C}$ that should be observed in the experiment and characterize the effect of the temperature. The values are represented in Fig. 5.5. In this graph, we also represented with dashed lines the contrast measured in the experiment for the four values of U/J investigated here. Of course, we find that for a certain temperature, the contrast of the QMC profiles equals the measured one. This was actually expected since the temperature is inferred by comparison between the experiment profiles and the QMC data (and more precisely by looking at the width of the momentum distribution). However, the QMC data provide us with the knowledge that the contrast is expected to decrease when the temperature increases (which is actually not trivial [57]). As a result, the effect of the finite temperature is not expected to be at the origin of the strong contrast measured.

- *Inhomogeneity of the clouds.*
  When looking at the contrast provided by the QMC method, we see that at low temperature,

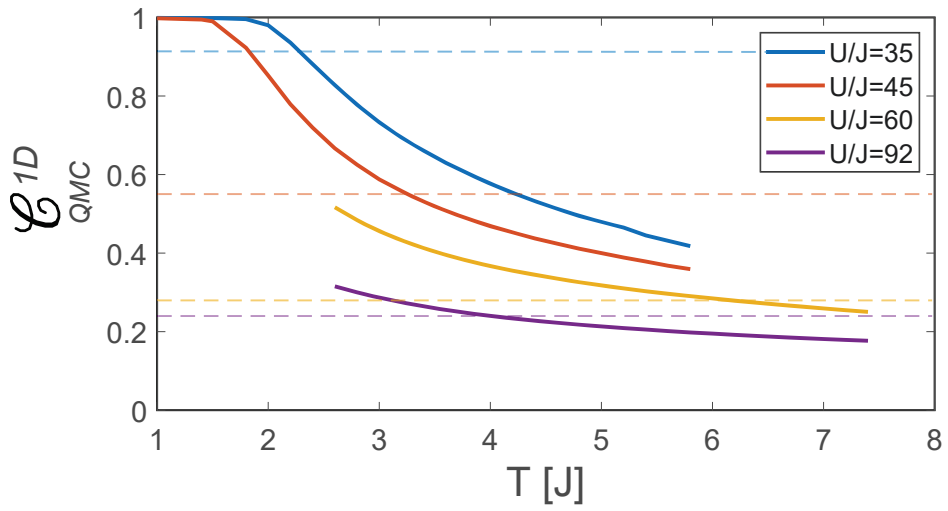

Figure 5.5: **Contrast of the momentum distribution computed with the QMC profiles as a function of the temperature**. The dashed lines are the values of the contrast measured in the experiment.

$\mathcal{C}$ corresponding to the data at $U/J = 35$ and $U/J = 45$ is going to 1. The QMC data are performed taking into account the presence of the external trapping, which means in particular, the inhomogeneity of the could. The inhomogeneity is responsible for the wedding cake structure which is characterized, at low temperature, by the presence of superfluid shells surrounding the Mott plateaus. In the momentum space, this is illustrated by the presence of sharp peaks, resulting in the very high contrast as represented in Fig. 5.5. In the experiment, we measured a residual condensate fraction at $U/J = 35$ (see §.4.2.2), so we attribute, close to the transition, the unexpected modulation contrast to the existence of superfluid shells. Far from the transition, these shells are driven thermally so we do not expect them to play a role.

- *Non adiabaticity of the ramping sequence.*
That is the argument the author in [34] gave to justify the discrepancy on the modulation contrast for high U/J . More precisely, when increasing the lattice potential in the Mott phase, the external trapping is increasing, and thus the cloud is compressing by forming Mott plateaus with increasing integer fillings. For the atoms to redistribute over the cloud, they need to tunnel, which is highly suppressed in the Mott phase as J is weak. In the experiment, the lattice potential is always ramped up with the same speed $dV_0/dt = 0.35\,E_r/\text{ms}$. It might happen that from a certain lattice amplitude (with $U/J > (U/J)_c$), the atoms do not have the time to redistribute anymore and the system freezes. This is in agreement with the data computed in Fig. 5.5. In order to evaluate the deviation of the experimental data with the scaling solution of the strong coupling theory, we have calculated the ratio:

$$d(u) = \frac{u - u_c}{u_{meas} - u_c} \tag{5.24}$$

where $u = U/J$. We find that the deviation is very important for the data at $U/J = 35$ and then, it seems to converge towards approximately 2. If the left part the graph can be attributed to the presence of the superfluid shells as mentioned earlier, the high U/J saturation of $d(u)$ is consistent with the freezing of the system while ramping up the lattice in the Mott phase. This could be checked by looking at the evolution of the momentum distribution as a function of the optical lattice amplitude ramping speed. However, slowing down the ramping may result in the increase of the cloud temperature due do the technical heating. And, as we saw on the QMC data, an increase of the temperature would also result in the decrease of the modulation contrast. To carefully perform this measurement, we should investigate first the heating effects in the experiment. This has not been been done so far.

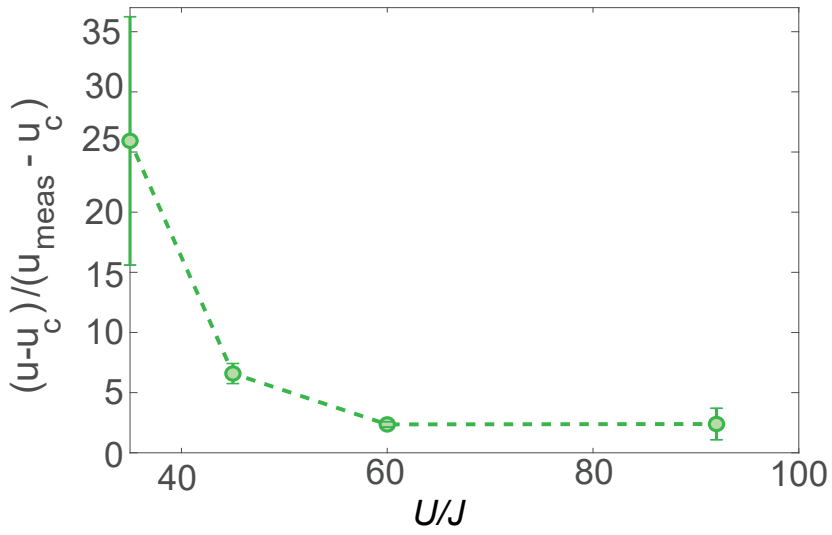

Figure 5.6: **Difference between the experimental data and the strong coupling theory**.

Phase coherence

To provide a physical insight into the narrowing of $Z(k_x)$, we expand $\rho(k_x) = \sum_p \alpha_p e^{i2_x/k_d}$ in Fourier components along the lattice axis, finding:

$$\alpha_p = \sum_j \left\langle \hat{b}_j^\dagger \hat{b}_{j+p} \right\rangle \tag{5.25}$$

The Fourier amplitudes α_p quantify the average phase coherence between lattice sites distant by p sites. The evolution of the amplitudes $|\alpha_p|$ as U/J decreases highlights the continuous change from a perfect Mott state (for which $\alpha_p = 0$ for $p \neq 0$) to a Mott state with a finite spatial coherence ($\alpha_p = 0$ for $p > 1$). Close to the Mott transition, the mobility of the quasi-particles extends over several lattice sites, say distant by p sites, and results in $\alpha_p \neq 0$. The narrowing of the spectral weight $Z(k_x)$ thus reflects the coherent tunneling of the quasi-particles over several lattice sites. In Fig. 5.7, we plot the Fourier amplitudes $|\alpha_p|$ extracted from the measured $\rho(k_x)$. A mobility of the quasi-particles over up to $p \approx 6$ lattice sites is observed at $U/J = 35$, a distance corresponding to about a quarter of the size of the trapped gas.

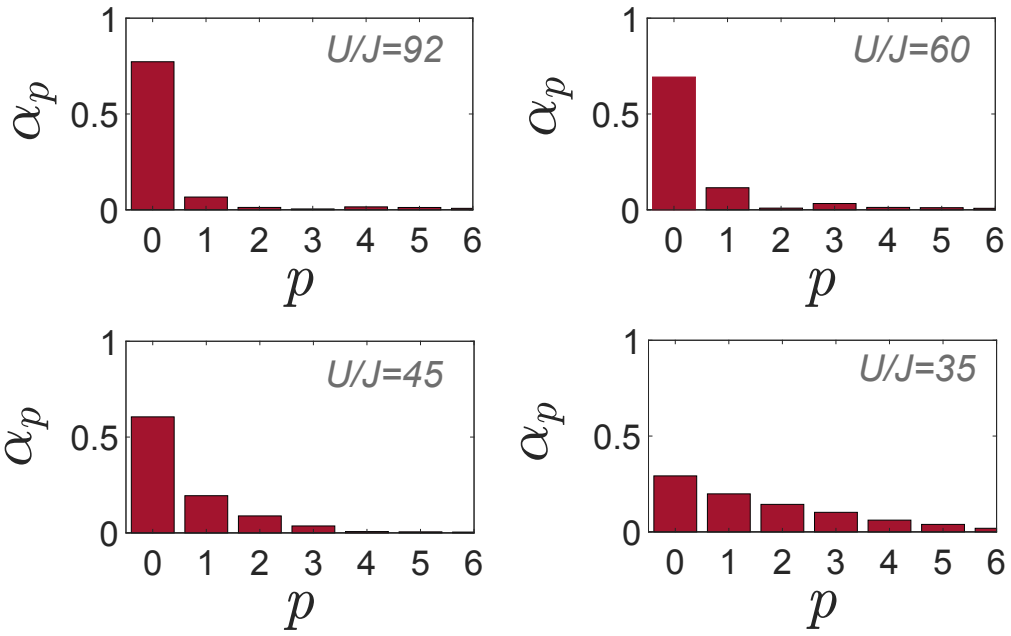

Figure 5.7: **Spectral weight of the quasi-particles in the Mott state**. Histograms of the amplitudes α_p corresponding to the momentum densities displayed in Fig. 5.3.

6. Investigation of higher order correlations

We already mentioned the importance of the knowledge of the correlation functions to characterize strongly correlated systems. For instance, the second-order correlation function of incoherent systems provides information about the spacial distribution of the source, while measuring $g^{(n)} = 1$ for all $n > 1$ is a characterization of a fully phase coherent system. At the critical point of a phase transition, the correlation functions may display universal algebraic feature with universal exponents that would be interesting to measure. The correlations also provide a deep insight on the microscopic mechanisms that drive (quantum) transitions. Among them, pairing mechanics of type $\vec{k}/-\vec{k}$ can be found in the BCS phase of fermionic systems or, in the present case, in the Bogoliubov excitations in the superfluid phase. The investigation of the strongly interacting gases through the correlation measurements thus provide a tool for the identification of complex phases as well a better understanding of the matter from a microscopic point of view.

However, up to now, correlation measurements (at order $n \geq 2$) in lattice systems remain elusive, since very difficult to measure. In principle, to measure the full correlation functions $g^{(n)}$, either in the position-space or in the momentum-space, the individual position of each atoms (Glauber theory of detection) must be inferred. The single-particle detection is accessible only in few experiments such as the quantum gas microscope experiments, the electron microscopy experiments and the He experiments (§.1.3.2). Note that it is however possible to infer the correlation functions from optical imaging density measurements [132] as it will be described more in details in §.6.2, however limited to the 2D and 1D geometries, or suffering from the optical line-of-sight integration. For these experiments, the question of the optical resolution also enters the problem.

In the Helium experiment, the detection at the single atom level in the momentum space and in 3D allows for the calculation of the momentum-space correlation functions. Note that other teams working with He* and using the same electronic detection have been measuring correlations in other systems than the lattice gases:

- At the Institut d'Optique, an other team leaded by D. Boiron and C. Westbrook has measured the second-order correlations in different systems. They demonstrated for instance the presence of $k/-k$ pairs created during the collision of two condensates [7] or investigated the HBT effect [3] in a harmonically trapped 3D thermal gas.

- A group in Australia led by A.G. Truscott investigated the high-order correlations up to the order 6 in a 1D non interacting thermal gas [133].

In our experiment, we concentrate on the investigation of the correlations in lattice gases in 3D. More particularly, we have measured the second-order correlation function in:

1. A Mott insulator at $U/J = 92$ (we measured also the third-order in that case).

2. In the depleted part of a superfluid across the NF-SF transition at $U/J = 9.5$.

In the first section, we will provide a description of the algorithm used in order to measure the correlation functions, taking as example the second-order correlation function (the measurement of the

higher-order correlation functions can be adapted easily). We will also review the different parameters one needs to pay attention when calculating the correlation functions (§.6.1). Then we will deal with the results obtained for a Mott insulator at $U/J = 92$, that is too say deep in the MI phase (§.6.2) and provide the first results of the computation of the third-order correlation function (§.6.3). Finally, we will provide the results obtained for the calculation of the second-order correlation function in the thermal part of a lattice gas across the superfluid transition at $U/J = 9.5$ (§.6.4).

6.1 Method to calculate the correlation functions

In this section, the detailed procedure used to compute the second-order momentum correlation function will be explained, with using, as an example, a Mott insulator. This procedure can be generalized to the calculation of higher-order correlation functions and for the investigation of different phases up to some details that will be explained in the corresponding sections. The different tests carried out in this part have been performed with a set of data corresponding to:

- A lattice gas with $N = 15\,(5) \times 10^3$ atoms $\Rightarrow L = Md \approx 32\,d$ computed with the Gutzwiller method
- In the MI phase at $U/J = 92$
- About 900 shots taken
- The percentage of the atoms detected on the MCP is $\eta \approx 5\%$

6.1.1 Second-order correlation functions of lattice gases

The measurement of the two-particle momentum correlations quantifies the conditional probability for an atom in a given experimental realization to have a momentum $\vec{k}_1$ provided one atom is detected with a momentum $\vec{k}_2$:

$$G^{(2)}(\vec{k}_1, \vec{k}_2) = \left\langle \hat{a}^\dagger(\vec{k}_1)\hat{a}^\dagger(\vec{k}_2)\hat{a}(\vec{k}_1)\hat{a}(\vec{k}_2) \right\rangle \tag{6.1}$$

The normalized second-order correlation function writes:

$$g^{(2)}(\vec{k}_1, \vec{k}_2) = \frac{\left\langle \hat{a}^\dagger(\vec{k}_1)\hat{a}^\dagger(\vec{k}_2)\hat{a}(\vec{k}_1)\hat{a}(\vec{k}_2) \right\rangle}{\rho(\vec{k}_1)\rho(\vec{k}_2)} = \frac{G^{(2)}(\vec{k}_1, \vec{k}_2)}{G^{(2)}_{NC}(\vec{k}_1, \vec{k}_2)} \tag{6.2}$$

where we define G_{NC} as the non-correlated second-order correlation function considering the fact that $G^{(2)}(\vec{k}_1, \vec{k}_2) = \rho(\vec{k}_1)\rho(\vec{k}_2)$ when the particles of momentum $\vec{k}_1$ and $\vec{k}_2$ are totally uncorrelated.

Because lattice systems display a translational invariance for displacements corresponding to the lattice vectors, the correlation functions depend only on the momentum separation $k_2 - k_1$, *i.e*:

$$G^{(2)}(\vec{k}_1, \vec{k}_2) = G^{(2)}(\delta k\, \vec{u}) \qquad g^{(2)}(\vec{k}_1, \vec{k}_2) = g^{(2)}(\delta k\, \vec{u}) \tag{6.3}$$

with $\vec{k}_1 - \vec{k}_2 = \delta k\, \vec{u}$ and $\vec{u}$ is oriented along a reciprocal lattice vector, *i.e*, $\vec{u} = \vec{K} / \parallel \vec{K} \parallel$. We remind the expression of the reciprocal lattice vectors $\vec{K} = k_d \times (n_x\vec{u}_x + n_y\vec{u}_y + n_z\vec{u}_z)$ with n_x,n_y and n_y integers and $\vec{u}_x$, $\vec{u}_y$ and $\vec{u}_z$ are the lattice axis directions. Furthermore, as the representation of the full distribution is intricate, we calculate the correlations along some specific directions. These directions can be chosen at will and, in the present work, they are oriented along the reciprocal lattice vectors $\delta\vec{k} \propto \vec{u}$.

Since the correlations only depend on $\delta\vec{k}$, one can integrate (average) over $\vec{k}_1$:

$$g^{(2)}(\delta k) = \int_{\vec{k}} \left[\frac{\left\langle \hat{a}^\dagger(\vec{k})\hat{a}^\dagger(\vec{k}+\delta\vec{k})\hat{a}(\vec{k})\hat{a}(\vec{k}+\delta\vec{k}) \right\rangle}{\rho(\vec{k})\rho(\vec{k}+\delta\vec{k})} \right] d\vec{k} = \frac{\int_{\vec{k}} \left\langle \hat{a}^\dagger(\vec{k})\hat{a}^\dagger(\vec{k}+\delta\vec{k})\hat{a}(\vec{k})\hat{a}(\vec{k}+\delta\vec{k}) \right\rangle d\vec{k}}{\int_{\vec{k}} \rho(\vec{k})\rho(\vec{k}+\delta\vec{k}) d\vec{k}} \tag{6.4}$$

Performing such an integration to increase the signal-to-noise ratio was suggested in the early paper by Glauber [134].

6.1.2 Algorithm

When working with atomic coordinates, integrating over $\vec{k}$ means summing over all the positions in momentum-space of all the atoms. Because it is more simple, we calculate the second-order correlation function using the second expression in Eq. 6.2, that is to say, we calculate separately $G^{(2)}(\delta\vec{k})$ and $G^{(2)}_{NC}(\delta\vec{k})$ to access $g^{(2)}(\delta\vec{k}) = G^{(2)}(\delta\vec{k})/G^{(2)}_{NC}(\delta\vec{k})$ as usually done in other experiments [3, 95].

Remarks:
In the experiment, we are not measuring directly $\rho(\vec{k})$ but $\tilde{\rho}(\vec{k}) = \rho(\vec{k})\left|\tilde{w}(\vec{k})\right|^2$. Then the second-order correlation function measured is:

$$g^{(2)}_{meas}(\delta k) = \frac{\int_{\vec{k}} \left|\tilde{w}(\vec{k})\right|^2 \left|\tilde{w}(\vec{k}+\delta\vec{k})\right|^2 \left\langle \hat{a}^\dagger(\vec{k})\hat{a}^\dagger(\vec{k}+\delta\vec{k})\hat{a}(\vec{k})\hat{a}(\vec{k}+\delta\vec{k})\right\rangle d\vec{k}}{\int_{\vec{k}} \left|\tilde{w}(\vec{k})\right|^2 \left|\tilde{\omega}(\vec{k}+\delta\vec{k})\right|^2 \rho(\vec{k})\rho(\vec{k}+\delta\vec{k}) d\vec{k}} \tag{6.5}$$

However, if we suppose that $\left\langle \hat{a}^\dagger(\vec{k})\hat{a}^\dagger(\vec{k}+\delta\vec{k})\hat{a}(\vec{k})\hat{a}(\vec{k}+\delta\vec{k})\right\rangle$ only depends on $\delta\vec{k}$, then it can go out the integral (the same for the product of the momentum densities on the denominator) and one retrieve Eq. 6.2. In other words, the Wannier coefficient has an effect on the non-normalized correlation functions but not on the normalized correlations.

The expression of $G^{(2)}(\delta\vec{k})$ calculated along the lattice directions is given by:

$$G^{(2)}(\delta\vec{k}) = \int_{\vec{k}} \left\langle \hat{a}^\dagger(\vec{k})\hat{a}^\dagger(\vec{k}+\delta\vec{k})\hat{a}(\vec{k})\hat{a}(\vec{k}+\delta\vec{k})\right\rangle d\vec{k} \tag{6.6}$$

To increase the signal-to-noise ratio, we also perform a transverse integration:

$$G^{(2)}(\delta k\vec{u}) = \int_{|\vec{k}_\perp|<\Delta k_\perp} G^{(2)}(\delta k\vec{u} + \vec{k}_\perp)\, d\vec{k}_\perp \tag{6.7}$$

The procedure to calculate $G^{(2)}(\delta k)$ is depicted in Fig. 6.1. For each atom detected in one shot, we define a tube of radius $\Delta k_\perp$ oriented along $\vec{u}$ from which the histogram of the distances from this atom to the ones contained in the tube is recorded. The histograms corresponding to the different atoms of the considered shot are then summed and $G^{(2)}$ is averaged over many realizations of the experiment. A plot of $G^{(2)}$ measured along the x-axis is given in Fig. 6.2.a. Three bunching peaks are visible at $\delta k = 0$ and $\delta k = \pm k_d$ on top of a broad background which can be identified as resulting from the density profile $\tilde{\rho}(\vec{k}) = |\tilde{w}(\vec{k})|^2 \times \rho(\vec{k})$. This background is equal to the auto-correlation of the momentum density of the Mott insulator. It corresponds to the value of the $G^{(2)}$ function in the absence of correlations between atoms and earlier referred as $G^{(2)}_{\mathrm{NC}}$. The ratio $G^{(2)}$ divided by $G^{(2)}_{\mathrm{NC}}$ yields the normalized two-body correlation function $g^{(2)}$:

$$g^{(2)}(\delta\vec{k}) = \frac{G^{(2)}(\delta\vec{k})}{G^{(2)}_{\mathrm{NC}}(\delta\vec{k})} \tag{6.8}$$

By definition, $g^{(2)}(\delta k) = 1$ if there is no correlation in the system and $g^{(2)}(\delta k) \neq 1$ otherwise (see Fig. 6.2.b). The presence and the characteristics of these peaks will be discussed in details in §.6.2.

To ensure a proper normalization, we calculate $G^{(2)}_{\mathrm{NC}}$ with a procedure that is similar to the one used for the calculation of $G^{(2)}$ but by getting rid of the correlations before performing the calculation of the histograms. To do that, for each atom in a given experimental realization, we calculate the histogram of the distances between the given atom and all the atoms in the other experimental realizations, that is too say removing the ones that belong to the same shot. The value of $G^{(2)}_{\mathrm{NC}}$ for the same set of data mentioned earlier is given in Fig. 6.2.a.

The result of dividing $G^{(2)}$ by $G^{(2)}_{\mathrm{NC}}$, *i.e.*, $g^{(2)}(\delta k) = G^{(2)}(\delta k)/G^{(2)}_{\mathrm{NC}}(\delta k)$ is plotted in Fig. 6.2.b for the same set of data used in Fig. 6.2.a.

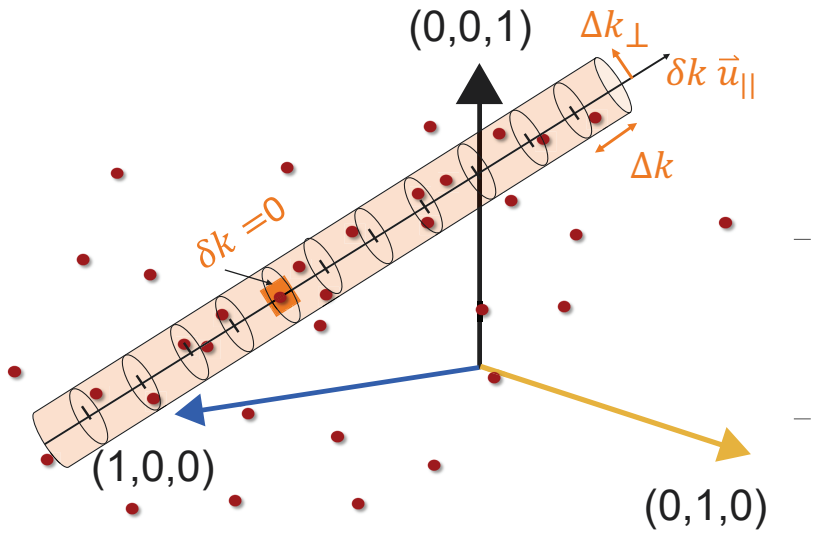

Figure 6.1: **Method to calculate $\mathbf{G^{(2)}}$.** One atom from a given shot is chosen (highlighted in orange). A tube of radius $\Delta k_\perp$ oriented along $\vec{u}$ and centered on the considered atom is defined. The distances (algebraic) δk between the atom and the other ones contained in the tube are extracted. The operation is repeated for all the atoms of the shot and the results are saved in a histogram with a longitudinal step Δk.

6.1.3 Resolution of the detector and binning of the data

When measuring a physical quantity with a detector, one needs to pay attention to different parameters in order to ensure the fidelity of the measurement. In fact, in a general way, the physical signal $X_M(x)$ measured by a detector is the convolution of the real signal $X(x)$ by the impulse response $f_{imp}(x)$ of the detector, that is to say by the signal measured when $X(x) = \delta(x)$:

$$X_M(x) = X * f_{imp} \tag{6.9}$$

If the detection is perfect, then $f_{imp} = \delta(x)$ and $X_M = X$. On the contrary, the detected quantity can be modified by the detection, leading to incorrect measurements.

In particular, one generally needs to pay attention to:

- The detector pixel size. In fact, detectors usually only measure discrete quantities, by steps that are multiple of the pixel size. The pixel size provides a lower bound for the resolution at which the measurement can be performed.
- The resolution of the detection system, that characterizes the intrinsic uncertainty of the measurement. A finite resolution can come from the detector itself or an element of the detection chain (in the case of the optical detection, one needs to pay attention to the Airy spot).
- The way the data are processed to infer the quantities of interest. For instance, in our case, we will see that the binning of the momentum distribution can distort the correlation signals.

If the effect of the detection discretization and of the finite resolution are inherent to the detector/experimental chain, a careful investigation of the parameters to be used in order to process the data can eliminate some sources of error.

Elementary pixel size and resolution of the momentum distribution measurement:

When measuring an atom distribution in the momentum-space with the He* detector, what we have at the end of the electronic chain is a list of times, discretized by steps of 120 ps. We provided

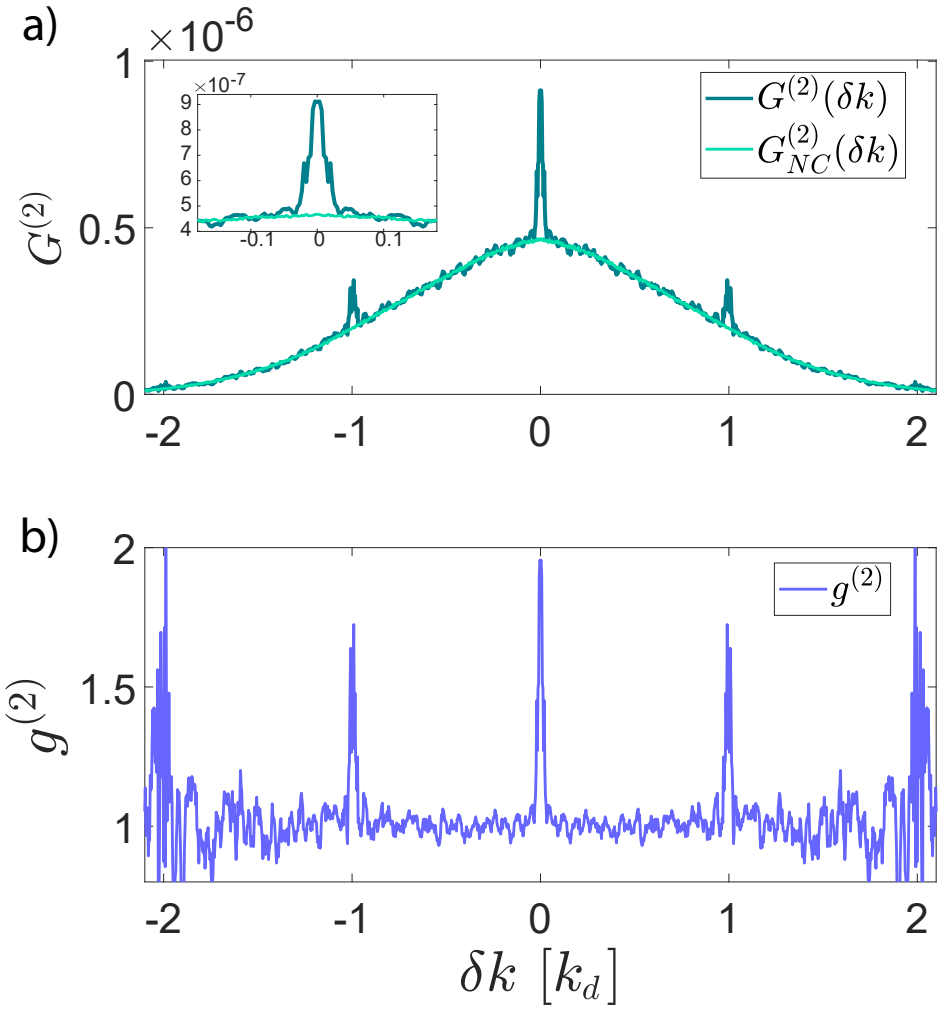

Figure 6.2: **Correlation functions.** Values of the different correlation functions along the x-axis obtained for a Mott insulator at $U/J = 92$. **a)** $G^{(2)}(\delta k)$ and $G^{(2)}_{\mathrm{NC}}(\delta k)$. **b)** $g^{(2)}(\delta k)$.

in §.3.2.3 the relation between these times and the momentum-space atomic coordinates (and whose numerical values depend on experimental parameters such as t_{tof}). The time discretization translates into a momentum coding step $\delta k_{\text{in-plane}} = 1.0 \times 10^{-3}\, k_d$ along the two directions defined by the detector and $\delta k_{\text{gravity}} = 6 \times 10^{-9}\, k_d$ along the gravity.

If the system has a perfect resolution, the measured signal is given by the convolution of the real signal with the pixel shape. In our case, the resolution is finite, and we estimated it to be of the same order of magnitude than the in-plane pixel size in all the directions. As a result, as long as the momentum distribution does not display any feature finer than $\sim 1.0 \times 10^{-3}\, k_d$, the effect of the discretization/finite resolution does not have to be taken into account. We will see a bit later that this is the case for the experiments carried out in this thesis. In fact the resolution of the Helium detector is so good that it has not been possible to identify in any distributions an effect of it, supporting the difficulty encountered to measure it properly.

Transverse integration and longitudinal binning of the data.

Computing the correlation functions along the lattice axis means calculating longitudinal cuts in the full correlation functions (3D function). The cuts are characterized by a transverse integration $\Delta k_\perp$ and a longitudinal binning Δk. We will see in the next paragraph that the correlation peaks can be approximated by the function $g^{(2)}(\delta \approx 0) = 1 + \eta \times e^{-2(\delta k/l_c)^2}$, where l_c is the correlation length which sets the typical size of the correlation peaks. As a result:

- When the transverse integration $\Delta k_\perp$ becomes of the order of the peak size, *i.e*, $\Delta k_\perp \approx l_c$, the measured cuts display correlation peaks with an amplitude that is decreasing when the transverse integration increases, while the shape of the peaks is not affected as represented in Fig. 6.3[1] (the slight differences in the coherence lengths measured along the different lattice axis will be discussed later). As a result, the measurement of the real peak amplitude requires using $\Delta k_\perp < l_c$, while it can be interesting to increase the transverse integration to investigate with a better signal to noise ratio the size of the peaks.

- The longitudinal integration is always set such as $\Delta k \ll l_c$. If it was not the case, the measured peak shape would be given by the convolution of the real peak shape with the bin, resulting in an increase of the peak width and a decrease of its amplitude. In all the measurement $\Delta k \approx 0.1\, l_c$.

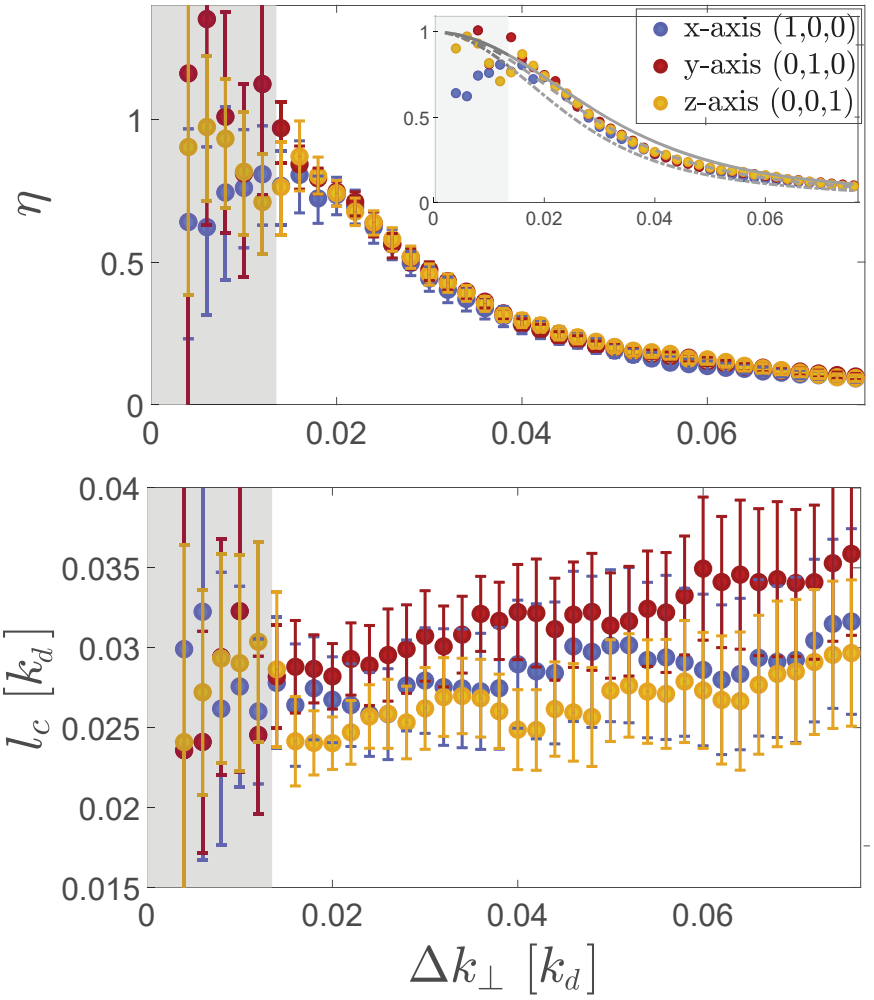

Figure 6.3: **Effect of the transverse integration on $\mathbf{g^{(2)}}(\delta\mathbf{k})$. a)** Amplitude of the bunching η as a function of $\Delta k_\perp$. In the inset, are represented the theoretical expectation for $\eta(\Delta k_\perp)$ considering $\eta(\Delta k_\perp = 0) = 1$ and $l_c = 0.028\, k_d$ (grey line), $l_c = 0.032\, k_d$ (grey dashed line) and $l_c = 0.035\, k_d$ (grey dotted-dashed line). **b)** Correlation length l_c as a function of $\Delta k_\perp$. Grey areas on both graphs correspond to the region where the signal is too noisy to provide quantitative information.

[1] This is a consequence of the fact that the peaks are approximately spherically symmetric, as demonstrated in §.6.2.3.

6.1.4 Influence of a misalignment on the the amplitude of the correlation peaks

Since we are only calculating the correlations along specific directions and the transverse integration is small, the directions must be chosen carefully. An error in the orientation along which the correlations are calculated with respect to the lattice directions would result in missing the peaks located at the reciprocal lattice nodes $\vec{K} \neq \vec{0}$, or at least would result in the decrease of their measured amplitude. Because Mott insulators do not show any clear feature in their momentum distribution to find the lattice axis directions, some momentum distributions of superfluids at $s = 8$ were taken before each set of correlation data. At this lattice amplitude, the peaks are very well contrasted, allowing to measure precisely the orientation of the lattice axis. In the second time, these directions were fine-tuned by maximizing the amplitude of the bunching peaks at $\delta k = \pm k_d$ while rotating a bit the axis along which the correlations were calculated. One example is given in Fig. 6.1.4. Here we see that a mismatch as small as two degrees 2° results in a decrease by a factor 2 of the peak amplitude.

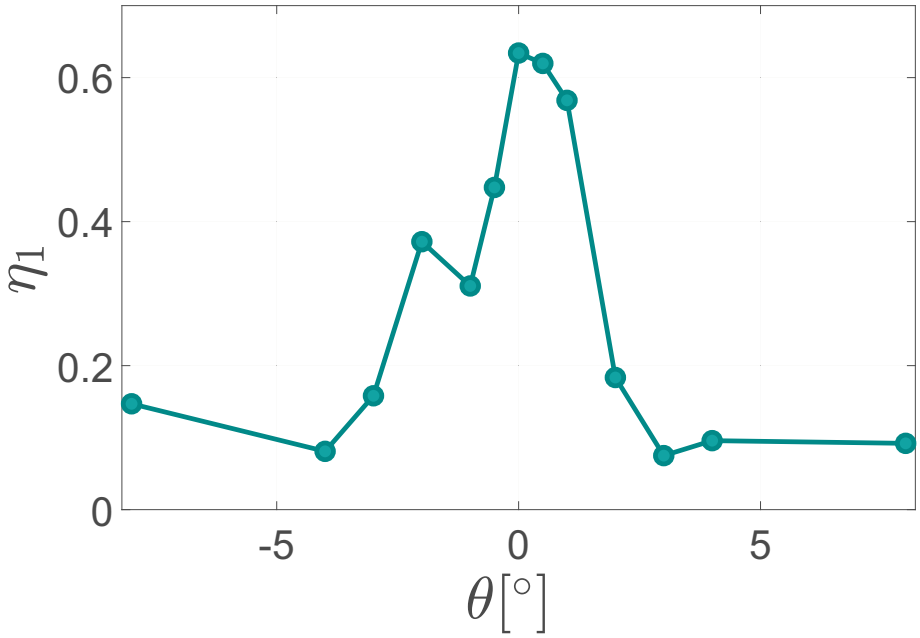

Figure 6.4: **Measured $\delta\mathbf{k} = \mathbf{k_d}$ correlation peak amplitude $\eta^{\delta\mathbf{k}=\mathbf{k_d}}$ as a function of the angle between the lattice axis and $\vec{u}$.**

6.2 Two-body correlation deep in the Mott phase

In this section, we will comment on the second-order correlation signal obtained for a Mott insulator at $s = 17.8$, $(U/J = 92)$. We saw in the last paragraph some of the results, however not commented from a physical point of view. In particular, we saw that the second-order correlation function along the lattice axis was characterized by periodic bunching peaks. A similar observation has been measured in 2005 in the team of I. Bloch [135]. A first paragraph will be dedicated to a short review of their findings. We will particularly show that the He* experiment allows to go beyond certain limitations of this pionnering experiment and that was preventing these authors to provide a quantitative analysis of the correlation signal (§.6.2.1). In a second time, we will thus provide a complete description of the results obtained with the He experiment .

6.2.1 Review of the Folling et al. experiment

As mentioned in §.2.2, in the experiments using usual imaging techniques (that only measures densities and do not possess the single atom detection), a direct measurement of $G^{(2)}(\vec{k}_1, \vec{k}_2) = \left\langle \hat{a}^\dagger(\vec{k}_1)\hat{a}^\dagger(\vec{k}_2)\hat{a}(\vec{k}_1)\hat{a}(\vec{k}_2) \right\rangle$ is not possible. However, one can access the density-density correlations:

$$G^{(2)}_{\text{dens-dens}}(\vec{k}_1, \vec{k}_2) = \left\langle \hat{a}^\dagger(\vec{k}_1)\hat{a}(\vec{k}_1)\hat{a}^\dagger(\vec{k}_2)\hat{a}(\vec{k}_2) \right\rangle = \left\langle \hat{\rho}(\vec{k}_1)\hat{\rho}(\vec{k}_2) \right\rangle \tag{6.10}$$

The two expressions only differ by the auto-correlation term $\langle\, \hat{\rho}(\vec{k}_1)\rangle\delta(\vec{k}_1 - \vec{k}_2)$. This means that $G^{(2)}_{\text{dens-dens}}$ and $G^{(2)}$ are equal except when $\vec{k_1} = \vec{k_2}$, *i.e*, $\delta\vec{k} = 0$. When working with lattice gases, one can use the periodicity of the correlation functions to retrieve the information hidden by the auto-correlation signal, by investigating the other correlation peaks.

Following this idea, the authors in [135] measured the density-density correlation in an expanding cloud of a Rb 3D lattice gas prepared at $s = 50$ (deep in the MI phase). After a time-of-flight of few tenths of ms, they were imaging the cloud by absorption, providing a 2D image as depicted in Fig. 6.5.a. Because of the line-of-sight integration, they were actually measuring the spatially averaged normalized density-density correlation function:

$$C(\delta\vec{k}) = \frac{\int_{\vec{k}} \left\langle \rho_{2D}(\vec{k})\rho_{2D}(\vec{k} + \delta\vec{k}) \right\rangle d\vec{k}}{\int_{\vec{k}} \left\langle \rho_{2D}(\vec{k}) \right\rangle \left\langle \rho_{2D}(\vec{k} + \delta\vec{k}) \right\rangle d\vec{k}} \tag{6.11}$$

where ρ_{2D} is the 1D integrated momentum distribution, and $\vec{k}$ and $\delta\vec{k}$ are limited to the imaging plane directions.

The result of this computation is represented in Fig. 6.5.c where we clearly identify the periodic bunching peaks (except for the central peaks that is irrelevant as dominated by the auto-correlation term). The authors interpreted these periodic correlation peaks as coming from the multiple HBT interference effects coming from the expansion of the periodic incoherent atomic clouds localized at the lattice sites, and serving as a proof for the ordering of the indistinguishable particles in the optical lattice. However, they were not able to provide quantitative information on the peak width and amplitude:

1. The finite resolution of the optical imaging set by the point spread function (PSF) of the imaging system (the CCD pixel size was smaller than the rms value of the PSF) has a rms size $\sigma \approx k_d/40$. For large clouds ($M \approx$ tenths of sites), the measured correlation peaks were affected by the convolution with the PSF of the imaging system.

2. The line-of-sight integration is averaging the correlation peaks along the imaging direction, and is responsible for the drop in the measured amplitudes.

The bunching peaks amplitude measured was of the order of 10^{-4}, as compared to the amplitude $\eta = 1$ that should be measured within the HBT theory (applicability of the Wick theorem). The

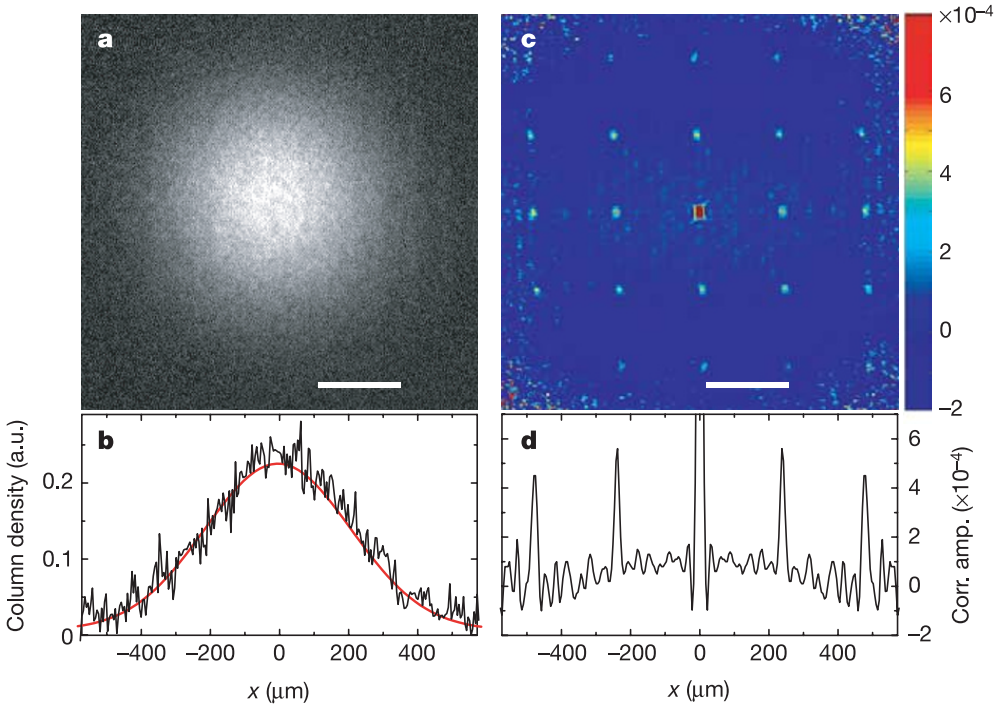

Figure 6.5: **Quantum noise interferometry to probe a Mott insulator** Density-density correlation measurement of a 3D Mott insulator. **a)** and **b)** Momentum distribution and 1D profile of the Mott insulator probed by imaging the cloud after a time-of-flight. **c)** and **d)** Corresponding density-density correlation computed from the 1D integrated momentum distribution and the profile along one of the lattice axis. If the periodic bunching peaks are clearly visible, the contrast of the bunching peaks $\eta \approx 10^{-4}$ is very low. Extracted from [135].

authors checked, by varying the number of atoms in the lattice gases and the expansion time that the bunching peak amplitude was in agreement with what should be measured considering a real bunching amplitude of 1 and taking into account the effect of the finite resolution and of the optical integration. However, because of the important drop of the bunching peak amplitude and of the finite resolution of the detector, it was not possible to infer, with a good precision, the amplitude and the width of the bunching peaks. Note that an investigation of the second-order correlations in a 1D Mott insulator (with a double wavelength lattice) has been performed in [136] using the same noise-correlation method.

With the He experiment, the absence of the line-of-sight integration and the better resolution, coupled to the fact that we can work with small clouds (giving rise to large bunching peaks), enables to encompass the difficulties mentioned above and to provide a quantitative investigation of the momentum correlations of a Mott insulator.

6.2.2 Periodicity of the correlation pattern

We measured the second-order correlation function $g^{(2)}(\delta k)$ of a Mott insulator with $N = 15\,000$ atoms at $U/J = 92$. Like in the Folling et al. experiment, $g^{(2)}$ displays a periodic structure with the period given by k_d. Because of the 3D detection, we access the 3D second-order correlation function and the presence of the bunching peak can be detected at the nodes of the 3D reciprocal lattice defined by: $\vec{K} = k_d \times (n_x\vec{u}_x + n_y\vec{u}_y + n_z\vec{u}_z)$. In Fig. 6.6 we plotted the profiles of $g^{(2)}$ measured along different axis corresponding to the orientation given by $\vec{K}$ for $\vec{K} = k_d \times n_x\vec{u}_x$, $\vec{K} = k_d/\sqrt{2} \times n(\vec{u}_x + \vec{u}_z)$ and $\vec{K} = k_d/\sqrt{3} \times n(\vec{u}_x + \vec{u}_y + \vec{u}_z)$ where $n \in \mathbb{Z}$. The 3 profiles display respectively, beside the bunching peak located at $\delta k = 0$, bunching peaks at $\delta k = \pm k_d$, at $\delta k = \pm\sqrt{2}k_d$ and peaks at $\delta k = \pm\sqrt{3}k_d$.

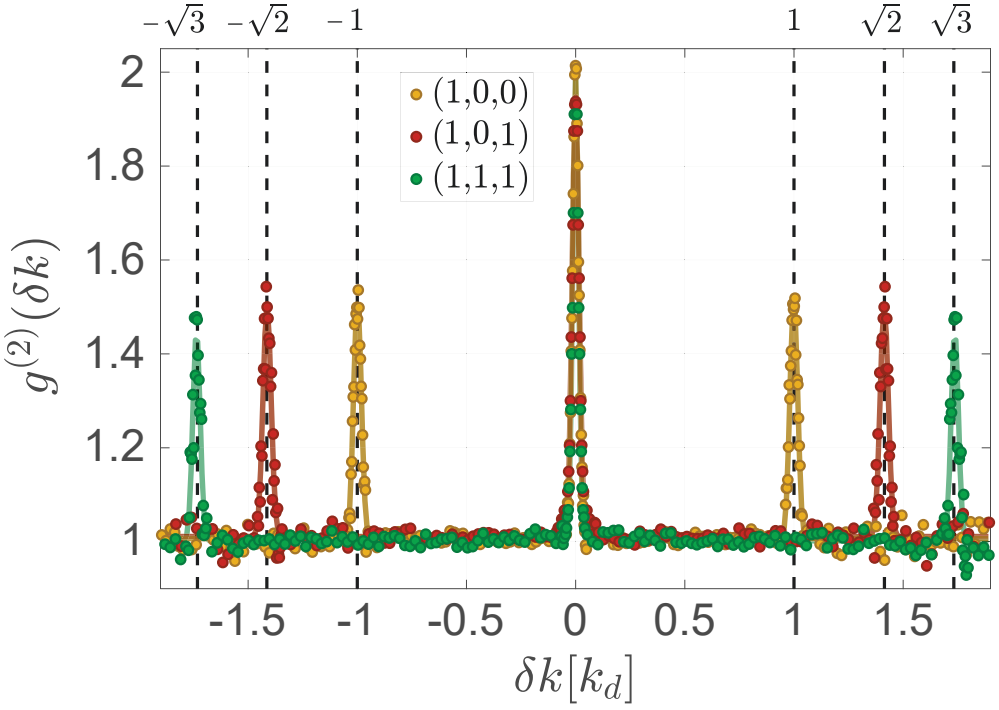

Figure 6.6: **Periodicity of the bunching.** 1D cuts $g^{(2)}$ along different axis of the reciprocal lattice for a Mott insulator at $s = 17.8$ and $N = 15\,000$ atoms. Here $\Delta k_\perp = 0.015\, k_d$ and $\Delta k = 0.003\, k_d$.

This constitutes the same signal as the ones put in evidence in the Folling et al. experiment, with the difference that the bunching amplitudes are far higher (of the order of 1 in the present measurement and of the order of 10^{-4} in the Folling experiment). We also notice that, contrary to what expected, the correlation peaks centered around $\delta k \neq 0$ have a lower amplitude than the central diffraction peak. We will provide in §.6.2.5 an explanation for it, but first, we will concentrate on the investigation of the shape and the amplitude of the central correlation peak.

6.2.3 Amplitude and shape of the central correlation peak

To investigate the amplitude and the shape of the central correlation peak, we zoom in the region $\delta k \approx 0$ of the correlation function $g^{(2)}(\delta k)$ calculated previously for a Mott insulator at $s = 17.8$ and $N = 15000$ atoms. The profiles along the 3 lattice directions and with $\Delta k_\perp = 0.015\, k_d$ and $\Delta k = 0.003\, k_d$ are represented in Fig. 6.7.

We see that the local bunching peak is isotropic and is characterized by a gaussian shape. The bunching peak is then fitted by:

$$g^{(2)}(\delta k) = c + \eta e^{-2(\delta k/l_c)^2} \tag{6.12}$$

along the 3 lattice directions. The results are represented by the lines in Fig. 6.9. From the fits, we extract for each direction the different parameters c, η and l_c. The results are displayed in Tab. 6.1.

Lattice axis direction	x	y	z
c	1.007 (5)	1.007 (3)	1.013 (5)
η	0.97 (3)	0.95 (2)	1.01 (1)
$l_c\,[k_d]$	0.029 (1)	0.032 (1)	0.026 (1)

Table 6.1: **Investigation of the central bunching peak.** The table provides the results of the fit by the function $g^{(2)}(\delta k) = c + \eta e^{-2(\delta k/l_c)^2}$ of the different correlation profiles displayed in Fig. 6.7.

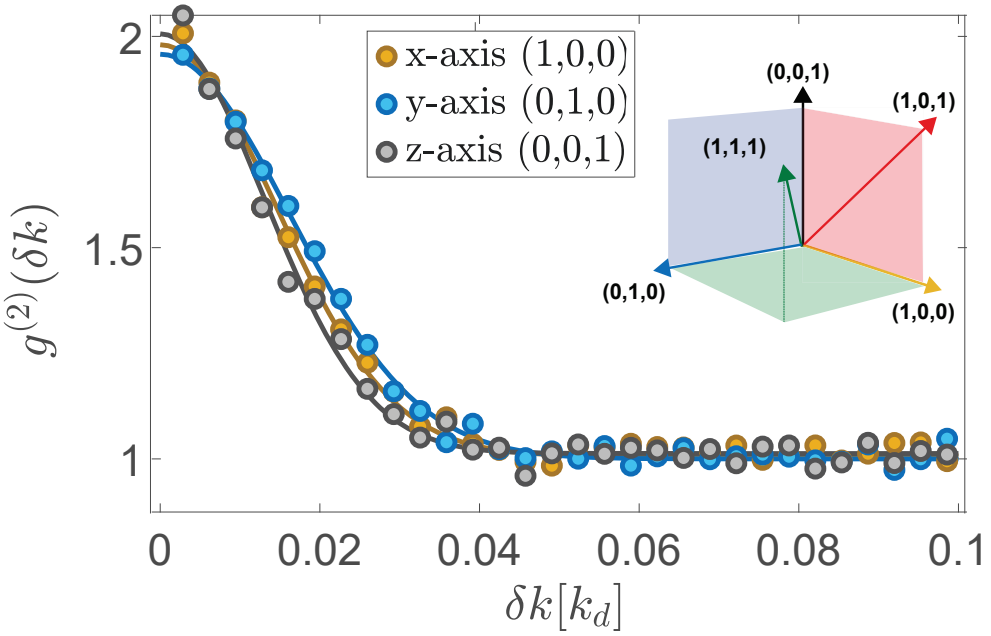

Figure 6.7: **Second-order correlation function $\mathbf{g^{(2)}(\delta k)}$ of a Mott insulator.**

- *Value of $g^{(2)}$ far from $\delta k = 0$.* From the fit, we find $g^{(2)}(|\delta k| > l_c) = c \sim 1$ along the different directions as expected. This is an evidence of the quality of the normalization procedure.

- *Amplitude η of the bunching peak.* We find a very well contrasted peak with $g^{(2)}(0) = 1.98\,(3)$, very close to the value ($g^{(2)}(0) = 2$) given by the Wick theorem for systems characterized by gaussian mode fluctuations, as it is expected for a perfect Mott insulator. As a result, even if there is some finite tunneling in the present case (as mentioned in §.5), the second-order correlation peak has an amplitude in agreement with the one found considering a perfect Mott insulator. Note that there has been only a few observations of $g^{(2)}(0) \approx 2$ with massive particles [137, 133, 90] and none of them was obtained in a 3D isotropic situation.

- *Correlation length l_c.* The correlation length measured along the different directions are a bit different, but compatible within few percent. The slight anisotropy is also confirmed by the evolution of $\eta(\Delta k_\perp)$ represented in Fig. 6.3. In fact, considering an isotropic bunching peak, one can compute analytically the effect of the transverse integration on the amplitude of the correlation peak (with $\eta(0) = 1$):

$$\eta(\Delta k_\perp) = 0.5 \times \left(\frac{l_c}{\Delta k_\perp}\right)^2 \times \left(1 - \exp\left\{-2\,(\Delta k_\perp / l_c)^2\right\}\right) \tag{6.13}$$

In the inset of Fig. 6.3, the expected theoretical variation of $\eta(\Delta k_\perp)$ for different values of l_c close to the coherence lengths measured along the different directions (and represented in the bottom graph of Fig. 6.3) are represented. None of these theoretical curves fit perfectly the experimental data, however surrounding them. This comforts in the idea of the presence of a slight asymmetry in the bunching peak shape that may come from a small difference in the external trapping frequencies along the lattice axis. In the rest of the manuscript, we refer to l_c as the average coherence length along the different lattice directions. We find for the set of data considered $l_c = 0.028\,(6)\,k_d$. In order to check if this value is in agreement, as it is the case for the amplitude, with what should be obtained within the applicability of the Wick theorem, we have performed some simulations that are given in the next paragraph.

Bunching peak shape of a fully incoherent Mott insulator

For a homogeneous Mott insulator with no coherence between the lattice sites (perfect Mott), we already saw in §2.2.4 that the first-order correlation function simplifies in the quasi-momentum space (Eq. 6.14):

$$g^{(1)}(\vec{k_1}, \vec{k_2}) = FT[n](\vec{k_2} - \vec{k_1})/\rho(\vec{k} = 0) \tag{6.14}$$

with $\delta\vec{k} = \vec{k}_2 - \vec{k}_1$. In this case, the Wick's theorem also applies and :

$$g^{(2)}(\vec{k}_1, \vec{k}_2) = g^{(2)}(\delta\vec{k}) = 1 + |g^{(1)}(\delta\vec{k})|^2 = 1 + |FT[n](\delta\vec{k})/\rho(\vec{k} = 0)|^2 \tag{6.15}$$

where $n(\vec{r})$ is the in-situ density.

Because of the isotropic external trapping, $n(\vec{r})$ only depends on the distance to the center of the cloud. In Fig. 6.9, are represented different radial profiles $n(r)$ along with the corresponding Fourier transform modulus squared $|\tilde{n}(k)|^2$. These profiles approximate the Guzwiller profile at $T = 0$ calculated for a Mott insulator with $N = 15\,000$ atoms and $s = 18$ (see Fig. 6.8).

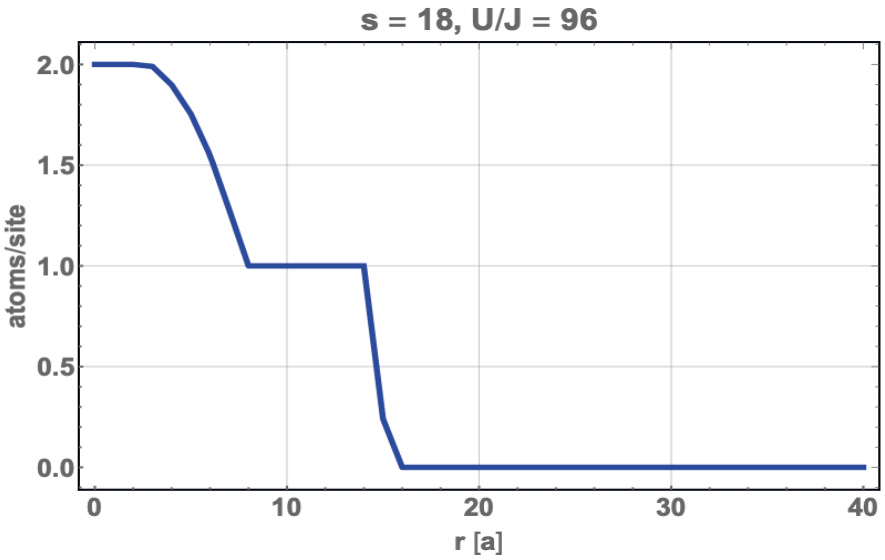

Figure 6.8: **In-situ density profile of a Mott insulator at s = 18 and N = 15 000 atoms calculated with the Gutzwiller method**. A plateau with a filling $n = 2$ is present at the center of the cloud. A superfluid, a Mott plateau with $n = 1$ and an other superfluid region are then present when going to the border of the cloud. The total size of the cloud is about $L = 2 \times 16\,d \approx 32\,d$.

We see in Fig. 6.9 that the shape of the bunching peak is quite insensitive to the exact in-situ profile of the Mott insulator such as the presence of a Mott plateau with a filling higher than 1 or superfluid rings separating different Mott plateau regions. This is due to the fact that in 3D, the outer Mott plateau occupies much more sites than the central plateau (this would not be the case in 1D). The bunching peaks have a gaussian shape whose RMS size only depends on the total in-situ cloud size (where the density drops to zero). Note that in the experiment, the superfluid regions surrounding Mott plateaus that appear in the Gutzwiller profile at $T = 0$ are driven with the finite temperature to thermal parts (all the entropy is concentrated in these regions), and might results in an increase of the in-situ cloud size. However, we saw in Fig. 6.9 that the presence of some non-superfluid areas at the border of the cloud results in a very small increase of the bunching peak width provided the fraction of the atoms in this area is low (which should be the case far from the Mott melting temperature, as we are in the experiment).

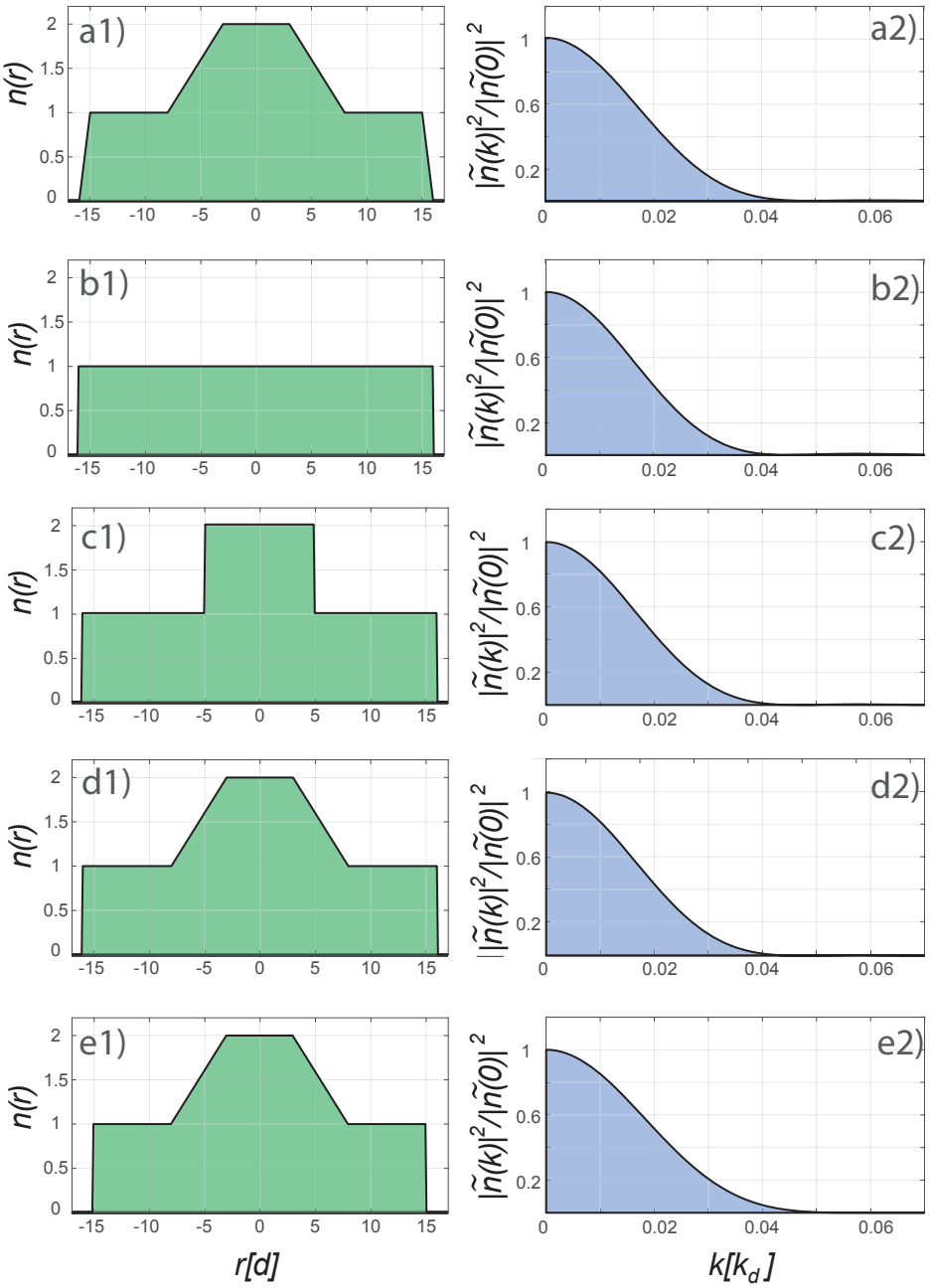

Figure 6.9: **Effect of the Mott in-situ profile on the bunching peak shape.** Panel of in-situ density profiles n (left column) along with the corresponding Fourier transform modulus squared $|\tilde{n}|^2$ (right column). The in-situ profiles tested are close to the $N = 15\,000$ atoms, $s = 18$ Gutzwiller profile plotted in Fig. 6.8 which is characterized by two Mott plateaus with filling $n = 2$ and $n = 1$ surrounded by two superfluid rings and a radius length $R = 16\,d$. **a1)** Guztwiller in-situ distribution with the thin superfluid density distribution in between two Mott plateaus modeled by a linear decrease of the density towards the edge of the cloud. **b1)** $n = 1$ Mott insulator with $R = 16\,d$. **c1)** Same profile as a1) with the superfluid rings replaced by Mott insulator phases. **d1)** Same profile as a1) where the superfluid region at the border of the edge of the cloud is replaced by a Mott insulator phase. **e1)** Same profile as a1) with the superfluid region at the border of the edge of the cloud removed. All the $|\tilde{n}|^2$ profiles are identical, except for e2) whose size is a bit larger. This is due to the fact that e2) corresponds to the only profile with $R = 15\,d < 16\,d$, resulting in a larger distribution in momentum space by 6%.

Fitting the theoretical correlation peaks displayed in Fig. 6.9 by the same function that is defined in Eq. 6.15, one finds $l_c \approx 0.027\,k_d$, that corresponds to the value obtained within the error bars from

the experimental data.

As a conclusion, the amplitude and the size of the central correlation peak measured in the experiment are in agreement with the fact that the Mott insulator investigated can be described by a Gaussian density operator.

Remark:
This was to expect since we saw in §.5, that even in the presence, at $s \sim 18$, of a residual first-order coherence induced by the particle-hole excitations, the correction on the bunching amplitude with respect to the correlations displayed by a Mott insulator with $J = 0$ at $s = 18$ is supposed to be of the order of the percentage.

6.2.4 Correlation length l_c as a function of N

An interesting property to investigate is the evolution of the coherence length l_c with the total number of atoms N. In the experiment, we have varied the atom number from $N = 3.0\,(6) \times 10^3$ to $N = 22\,(4) \times 10^3$ atoms and we have measured the correlation length l_c. Over this range of atom numbers, the lattice filling at the trap center varies from 1 to 2. The parameters used to calculate the bunching peak size for the different sets are given in Tab. 6.2. The measured values of l_c and η are also reported in the same table.

L	N	ΔN	$\Delta k_\perp$	$\Delta k_{\|\|}$	η	l_c
$[d]$	$[10^3]$	$[10^3]$	$[k_d]$	$[k_d]$	-	$[k_d]$
23	3	1	0.03	0.002	0.3	0.0388
25	5	1	0.03	0.002	0.32	0.035
30	12	2	0.03	0.001	0.51	0.03
34	16	3	0.03	0.001	0.43	0.027
36	20	4	0.03	0.001	0.42	0.025
38	22	4	0.03	0.001	0.40	0.023

Table 6.2: Parameters used to compute the data of Fig. 6.10 and Fig. 6.11. In order to measure the correlation length with a good precision, we use $\Delta k_\perp \approx l_c$, resulting in $\eta = g^{(2)}(\delta k = 0) - 1 < 1$. The measured value of of l_c and η are also reported.

In Fig. 6.10, we plot the measured values of l_c as a function of the total number of atom N. The two-body correlation length is found to decrease with the number of atoms. Using Eq. 6.15 with the in-situ density profile derived from the Gutzwiller anszat, we calculated, for each atom number N, the expected correlation length $l_c(N)$ in the case of a Mott insulator with the second-order correlation function given by the Wick's theorem. The results are represented by the grey dashed line in Fig. 6.10. We find that the measured values for l_c are in perfect agreement with the numerical calculations without adjustable parameters, *i.e.*, with the expectation for a Mott state with a Gaussian density operator, which confirms the statement made previously.

Another aspect of this result is that the measurement of $l_c(N)$ provides a very good tool in order to distinguish a Mott insulator from a thermal state, both trapped in an optical lattice. In fact, because both states are incoherent, their momentum distribution measured after a time-of-flight is large (modulated by the Wannier function), thus making the distinction between the two very difficult from the only knowledge of $\tilde{\rho}(\vec{k})$. They also display a periodic second-order correlation function with bunching peaks of the same amplitude and a size $l_c \propto 1/L$. However, the difference comes from the in-situ system size: for a Mott insulator, L depends strongly on N due to the incompressibility of the Mott state. On the contrary, for a thermal cloud, $L \approx \sqrt{\frac{k_B T}{m^* \omega_{ext}^2}}$ [3] is independent of N (see §.2.2.4)! This constitutes an additional proof that the gas investigated is not a thermal gas of ideal bosons but a strongly-interacting insulator, a Mott state.

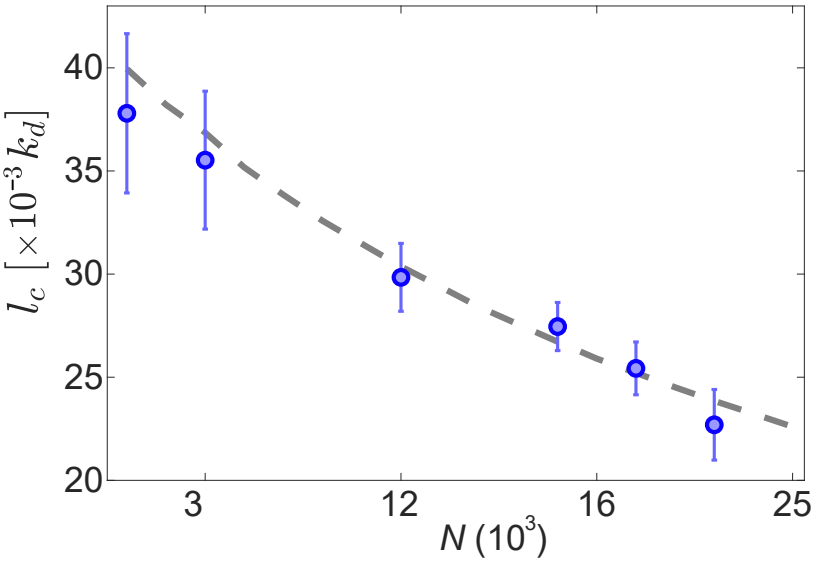

Figure 6.10: **Coherence length l_c as a function of N.** *Blue points*: experimental data. *Grey dashed lines*: Results of the numerical simulation.

Finally, in order to check the consistency with the theory, we plotted $l_c(L)$ with L extracted from the Gutzwiller profiles. The simulations gives $l_c \approx 1.1/L$, which is well reproduced by the experimental data (see Fig. 6.11).

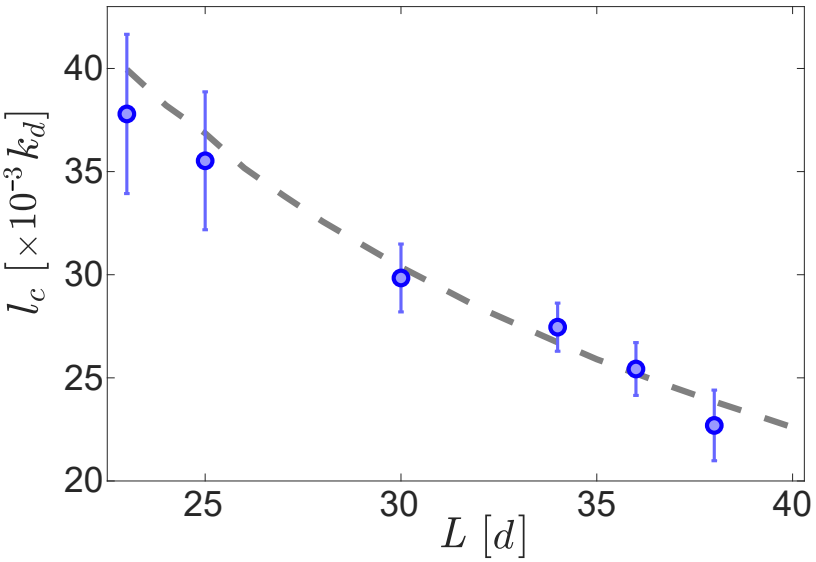

Figure 6.11: **Coherence length l_c as a function of the in-trap size L.** *Blue points*: Experimental data. *Grey dashed line*: Results of the numerical simulation $l_c \approx 1.1/L$.

6.2.5 Amplitude of the side correlation peaks

As it is visible in Fig. 6.6 and represented in Fig. 6.12, the amplitude of the bunching peaks located at the reciprocal lattice nodes $\vec{K} \neq 0$ is lower than the amplitude of the central bunching peak by roughly a factor 2. The expected periodicity of the correlation functions ensures that this should not be the case. We consequently tried to identify the origin of this discrepancy.

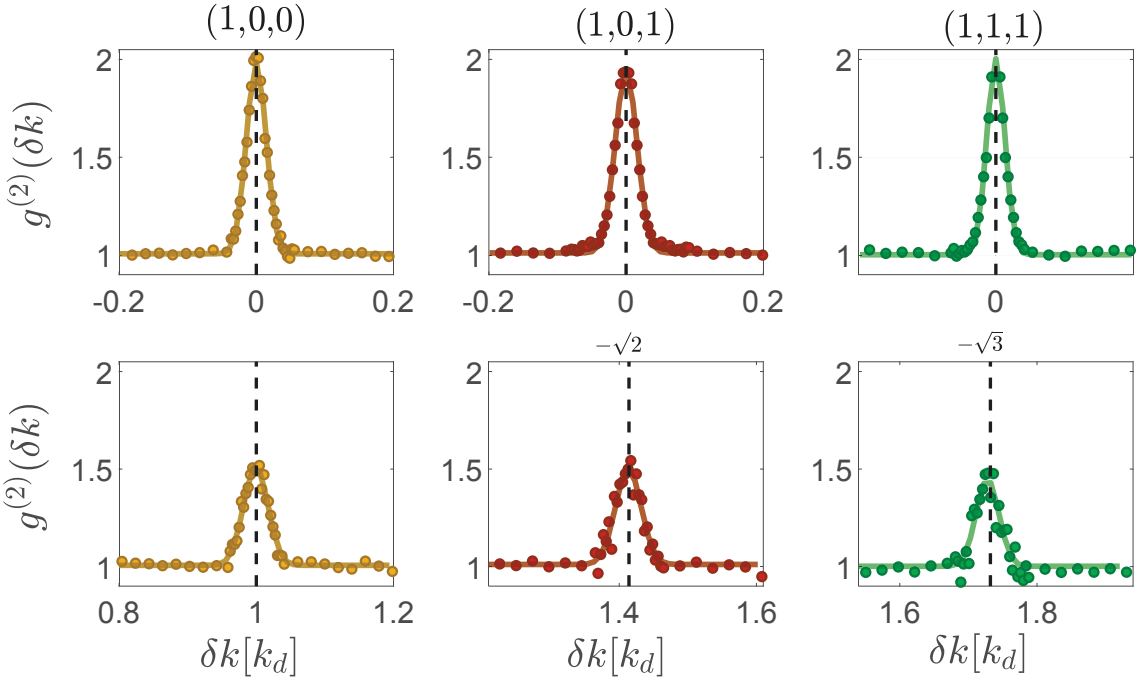

Figure 6.12: **Comparison between the central and the lateral bunching peaks** *Top graphs*: 1D cuts of the central bunching peak measured along the directions defined by (1,0,0), (1,0,1) and (1,1,1). *Bottom graphs*: Corresponding bunching peaks situated at $\delta k = k_d$, $\delta k = \sqrt{2}k_d$ and $\delta k = \sqrt{3}k_d$.

To get quantitative information about the amplitude and the size of the lateral bunching peaks, we fitted the different second-order correlation function profiles displayed in Fig. 6.6, and oriented respectively along the direction defined by (1,0,0), (1,0,1) and (1,1,1), with Gaussian functions:

$$g^{(2)}(\delta k) = c + \eta \times e^{-2(\delta k/l_c)^2} + \eta^{\delta k\neq 0} \times e^{-2((\delta k-\delta k_0)/l_c^{\delta k\neq 0})^2} + \eta^{\delta k\neq 0} \times e^{-2((\delta k+\delta k_0)/l_c^{\delta k\neq 0})^2} \quad (6.16)$$

The results are reported in Tab. 6.3.

Profile with the side peaks centered around $\delta k_0 =$	k_d	$\sqrt{2}k_d$	$\sqrt{3}k_d$
c	1.007 (2)	1.011 (3)	1.002 (1)
η	0.98 (2)	0.94 (3)	1.0 (2)
$l_c\,[k_d]$	0.029 (1)	0.031 (1)	0.026 (1)
$\eta^{\delta k\neq 0}$	0.51 (1)	0.49 (1)	0.45 (2)
$l_c^{\delta k\neq 0}\,[k_d]$	0.035 (1)	0.037 (2)	0.033 (1)
$\frac{\eta^{\delta k\neq 0}}{\eta}\left(\frac{l_c}{l_c^{\delta k\neq 0}}\right)^3$	1.04 (6)	1.15 (8)	1.12 (8)

Table 6.3: **Investigation of the shape of the lateral bunching peaks.** Results of the fit by the function given in Eq. 6.16 of the different correlation profiles displayed in Fig. 6.6.

The average two-body correlation length measured at $\delta\vec{k} \neq 0$, $l_c^{\delta k\neq 0} = 0.035\,(2)\,k_d$ is larger than the correlation length $l_c = 0.028\,k_d$ found from fitting the central correlation peak $\delta\vec{k} = 0$ by a few

times $k_d/1000$. On the other end, the amplitude $\eta^{\delta k\neq 0} = 0.49\,(3)$ of the peaks at $\delta\vec{k} \neq 0$ is in average lower than the central peak amplitude. However we find that the 3D integral of the bunching peaks, proportional to $\eta \times l_c^3$, is constant whatever the bunching peaks considered (see the last line in Tab. 6.3). This means that the probability for two atoms to bunch is independent on the separation $\vec{K}$ (where $\vec{K}$ is a vector of the reciprocal lattice), which is expected considering the periodicity of the bunching. It should be noted that the lower amplitude of the bunching associated with a larger correlation length is analog to a well-known phenomenon in spectroscopy. A measured resonance is that of the physical system convoluted with the response of the detector. When the latter has a resolution larger than the width of the resonance, the measured signal is enlarged but the integral of the resonance is that of the system. As a result, the amplitude of the measured resonance is lowered.

In the He* experiment, we attribute the larger correlation length $l_c^{\delta k\neq 0}$ of the bunching peaks centered around $\delta\vec{k} \neq 0$ to small imperfections of the He* detector in measuring particle distances comparable to its radius. This effect has been put in evidence in [138, 139]: the imaging of a regular pattern (a grid positioned just above the MCP) revealed some distortions on distances comparable with the MCP diameter. To our knowledge a full understanding of these distortions is missing but several origins for these imperfections have been identified. It includes the inhomogeneity of the electric field on the edges of the MCP and the presence of mechanical imperfections in the delay-line anode, *e.g.*, an imperfect winding of the cables. The correction of these distortions would require to calibrate the MCP position response as done in [138, 139] by imaging a periodic pattern. In our experiment, that would necessitate breaking the vacuum in order to install a grid on top of the MCP and we have not considered it yet for this reason.

As a result of the distortion, one atom with a momentum $\vec{k}$ is encoded by the detector as an atom with a momentum $\vec{k}_{meas} = \vec{k}+\delta_{dist}(\vec{k})$. Here the function $\delta_{dist}(\vec{k})$ reflects the deviation of the measured position with respect to $\vec{k}$ due to the above mentioned distortion effect of the He* detector. If one measures the momentum of two particles falling close-by, say $\vec{k}_1 \approx \vec{k}_2$, then $\delta_{dist}(\vec{k}_1) = \delta_{dist}(\vec{k}_2)$ because δ_{dist} smoothly varies over the surface of the MCP. As a result, $\vec{k}_{1,meas} - \vec{k}_{2,meas} = \vec{k}_1 - \vec{k}_2$. On the contrary, when considering $\vec{k}_2 = \vec{K}+\vec{k}_1$ with $\vec{K} \neq 0$, one has $\delta_{dist}(\vec{k}_2) \neq \delta_{dist}(\vec{k}_1)$ with the consequence that the measured difference $\vec{k}_{1,meas} - \vec{k}_{2,meas}$ is not equal to $\vec{k}_1 - \vec{k}_2$. Since $\delta_{dist}(\vec{k}_2) - \delta_{dist}(\vec{k}_1)$ is not a function of $\vec{k}_1 - \vec{k}_2$, the calculation of the average correlation function implies an average of $\delta_{dist}(\vec{k}_2) - \delta_{dist}(\vec{k}_1)$ which results in an effective broadening of the response of the He* detector at large separations between the particles, as shown in the experiment.

6.3 Three-body correlations deep in the Mott phase

From the same atom distributions as the ones used for the measurement of the second-order correlation, one can extract higher-order correlations. In this manuscript, we will limit ourselves to the investigation of the three-body correlation function, because the investigation of higher orders would require a higher statistics as it will be shown.

6.3.1 Measurement of the third-order correlation

Like for the second-order correlation, the periodicity of the third-order correlation function implies that $g^{(3)}(\vec{k}_1, \vec{k}_2, \vec{k}_3) = g^{(3)}(\vec{k}_1 - \vec{k}_3, \vec{k}_2 - \vec{k}_3, 0)$, meaning that $g^{(3)}$ only depends on the two coordinates $\delta\vec{k}_1 = \vec{k}_1 - \vec{k}_3$ and $\delta\vec{k}_2 = \vec{k}_2 - \vec{k}_3$ and can be written similarly to Eq. 6.2:

$$g^{(3)}(\delta\vec{k}_1, \delta\vec{k}_2) = \frac{\int_{\vec{k}_3} G^{(3)}(\vec{k}_1 - \vec{k}_3, \vec{k}_2 - \vec{k}_3)}{\int_{\vec{k}_3} G^{(3)}_{NC}(\vec{k}_1 - \vec{k}_3, \vec{k}_2 - \vec{k}_3)} \tag{6.17}$$

where the integral on $\vec{k}_3$ corresponds to a summation (an average) over the momenta of the atoms in the considered experimental realization. For one atom of momentum $\vec{k}_3$, we calculate the 2D histogram of the algebraic differences $\delta\vec{k}_1$ and $\delta\vec{k}_2$ for all the atoms in the same shot (removing the correlations of the atoms between themselves) which provides the value of $G^{(3)}(\vec{k}_1 - \vec{k}_3, \vec{k}_2 - \vec{k}_3)$. The histograms corresponding to the different atoms of momentum $\vec{k}_3$ are then averaged. Finally, the result is averaged over many shots. For the denominator $G^{(3)}_{NC}(\delta\vec{k}_1, \delta\vec{k}_2, 0)$, we are applying the same method, with the difference that now, the histogram is made by choosing the atoms 1 and 2 of momenta $\vec{k}_1$ and $\vec{k}_2$ in the different experimental shots, similarly to what was done for the normalization of the two-body correlation function.

Since it would be too long to calculate the whole distribution, we are limiting ourselves to the correlations along the lattice axis, meaning $\delta k_1 = \delta\vec{k}_1.\vec{u}_x$ and $\delta k_2 = \delta\vec{k}_2.\vec{u}_x$. Of course, to increase the signal to noise ratio, we are allowing some small transverse integration, that is to say we are also taking into account the atoms with $\left[(\delta\vec{k}.\vec{u}_y)^2 + (\delta\vec{k}.\vec{u}_z)^2\right] < \Delta k_\perp^2$. Finally the 2D histograms are calculated with a cubic pixel size equal to $\Delta k = 0.008\, k_d$.

6.3.2 Evidence of three-body bunching

The results, obtained for a Mott insulator at $s = 17.8$ and $N = 15\,000$ atoms (2 000 files used with a detection efficiency $\eta = 10\%$) are plotted in Fig. 6.13.

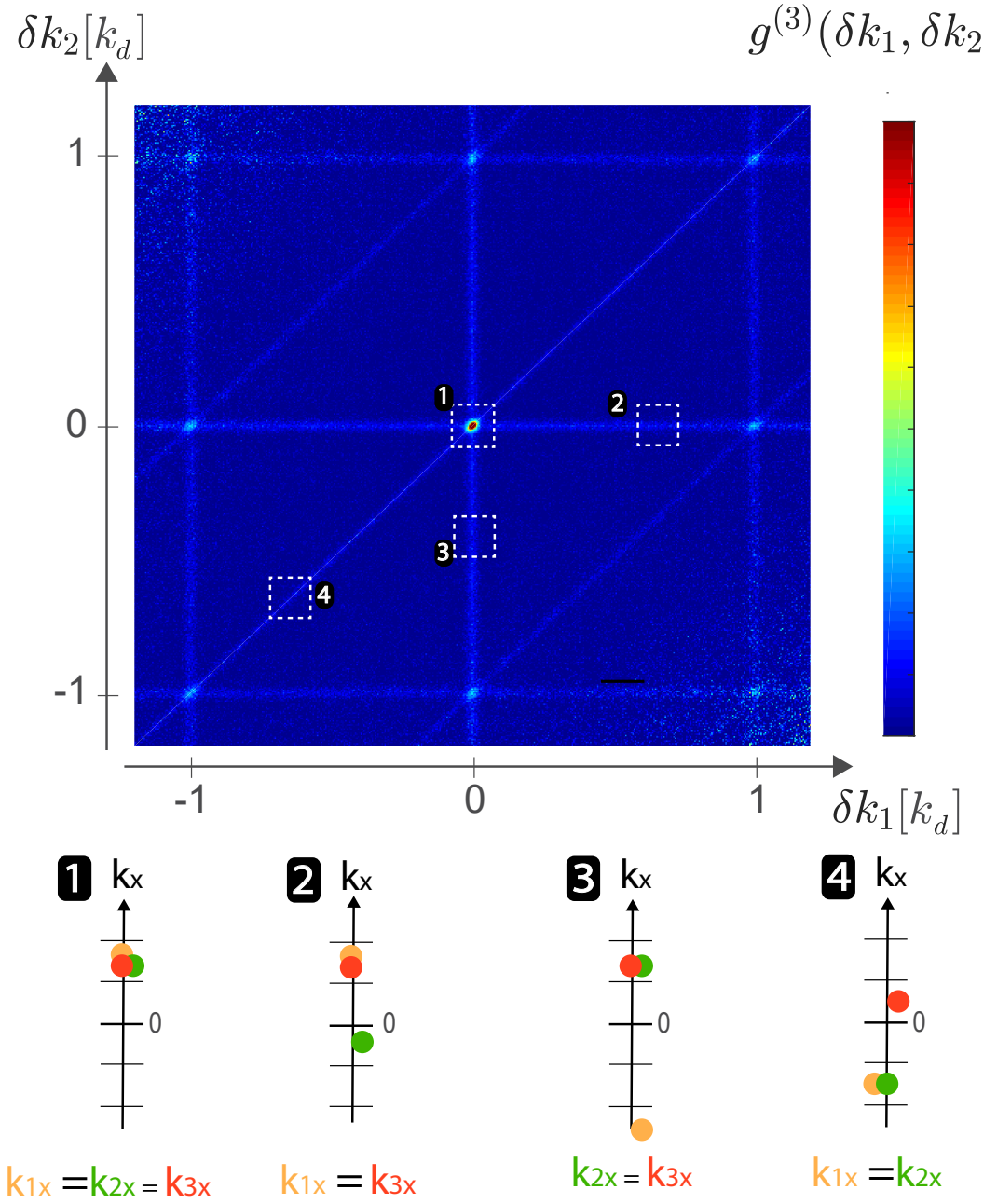

Figure 6.13: **3-particles momentum correlation $\mathbf{g^{(3)}(\delta k_1, \delta k_2)}$ computed along the x direction**. δk_1 and δk_2 represent the algebraic distances between atoms along the lattice axis. The background amplitude associated to un-correlated atoms has an amplitude ~ 1. The correlations along the lines defined by $\delta k_1 = 0$, $\delta k_2 = 0$ and $\delta k_2 = \delta k_1$ correspond to the two-body bunching $g^{(2)}(0)$ associated with finding two atoms close-by and illustrated in the cartoons 2,3 and 4. The intrinsic three-body correlation located at $\delta k_1 = 0\,[k_d]$ and $\delta k_2 = 0\,[k_d]$ has an even higher amplitude (see cartoon 1). Here we used $\Delta k = 0.008\,k_d$ and $\Delta k_\perp = 0.1\,k_d$.

The correlations that are intrinsically three-body are those for which three atoms are in the same coherence volume (sphere of radius l_c) and thus they are located at positions ($\delta k_1 = 0\,[k_d]$; $\delta k_2 = 0\,[k_d]$) where $[k_d]$ stands for modulo k_d (see cartoon 1). We also observe lines with a correlation above the background along the axis defined by $\delta k_1 = 0$, $\delta k_2 = 0$ and $\delta k_2 = \delta k_1$. Along each of these lines, two of the three atoms are close to each other and the correlation amplitude signals two-body bunching (see cartoons 2-4). No correlation is observed on the anti-diagonal defined by $\delta k_2 = -\delta k_1$. This is

expected since it corresponds to well separated, thus un-correlated momentum components.

6.3.3 Quantitative investigation of the three-body correlation signal

Third-order correlation of a perfect Mott insulator

Within the applicability of the Wick theorem, the third-order correlation function is expected to display a bunching with $g^{(3)}(0,0) = 3! = 6$, which means that the probability to find 3 particles close-by in the momentum space (modulus the lattice reciprocal vectors) is 6 times higher than the probability to find three particles with different momenta. The third-order correlation function can then be written as a function of the first-order correlation functions as discussed in §.2.2.3. We remind here its expression:

$$\begin{aligned} g^{(3)}_{MI}(\vec{k}_1,\vec{k}_2,\vec{k}_3) = 1 + \left|g^{(1)}_{th}(\vec{k}_1,\vec{k}_2)\right|^2 + \left|g^{(1)}_{th}(\vec{k}_1,\vec{k}_3)\right|^2 + \left|g^{(1)}_{th}(\vec{k}_2,\vec{k}_3)\right|^2 \\ + 2\mathcal{R}\left\{g^{(1)}_{th}(\vec{k}_1,\vec{k}_2)g^{(1)}_{th}(\vec{k}_1,\vec{k}_3)g^{(1)}_{th}(\vec{k}_2,\vec{k}_3)\right\} \end{aligned} \tag{6.18}$$

We plotted in Fig. 6.14 the theoretical value of $g^{(3)}_{MI}$ along the x-axis using the Wick theorem and with $l_c = 0.028\,k_d$ (value of the two-body coherence length measured in §.6.2.3) and we find a good qualitative agreement with the third-order correlation function measured in the experiment.

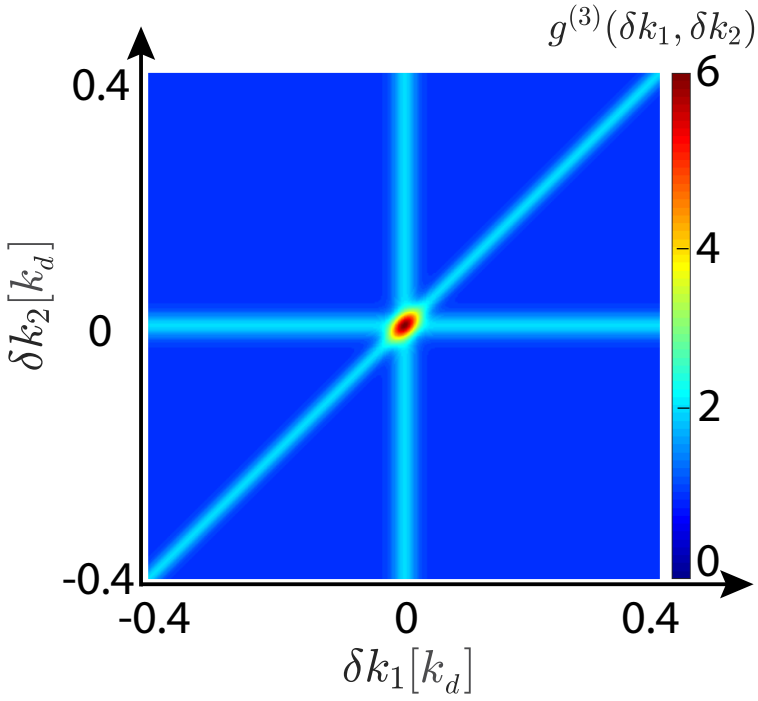

Figure 6.14: **Third-order correlation function $\mathbf{g^{(3)}(\delta k_1, \delta k_2)}$ for a perfect Mott insulator**. Plot of the function written in Eq. 6.18 with $l_c = 0.028\,k_d$ corresponding to the value of the two-body coherence length measured in §.6.2.3.

In the experiment

In order to increase the signal to noise ratio which is poor when using a transverse integration $\Delta k_\perp$ that is similar to the one used for the calculation of the two-body correlation functions ($\Delta k_\perp = 0.015\,k_d$), we used a large transverse integration $\Delta k_\perp = 0.1\,k_d$.

In Fig. 6.15 are represented two profiles, $g^{(3)}(\delta k_1, \delta k_2 = 0)$ (blue points) and $g^{(3)}(\delta k_1, \delta k_2 = 0.5\,k_d)$ (red points). The constant background of the $g^{(3)}(\delta k_1, \delta k_2 = 0)$ profile provides the value of $g^{(2)}(0)$

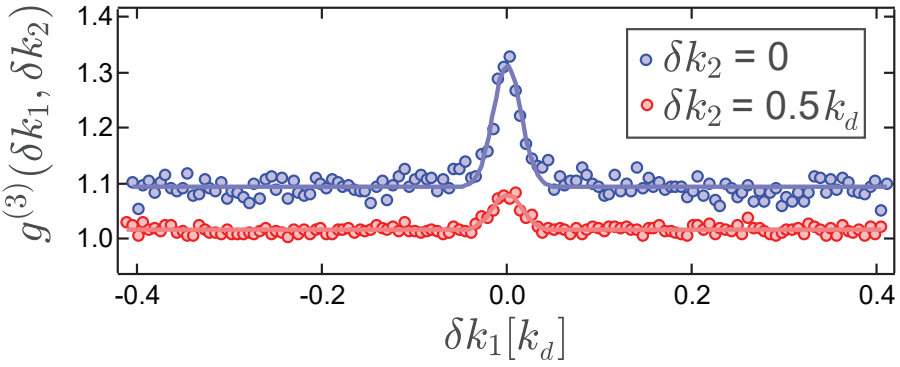

Figure 6.15: **Profiles extracted from the third-order correlation $\mathbf{g^{(3)}}(\delta\mathbf{k_1}, \delta\mathbf{k_2})$.** *In red.* For $\delta k_2 = 0$. *In blue.* For $\delta k_2 = 0.5\, k_d$.

($\vec{k}_2 = \vec{k}_3$) while the amplitude of the peak represents the value of $g^{(3)}(0,0)$. As for the second profile, the constant background (noted here bg) is supposed to be equal to 1 (amplitude of $g^{(3)}$ for un-correlated particles) while the amplitude of the peak represents the value of $g^{(2)}(0)$. To access the experimental values of the background and the amplitude of the peaks, we fitted the profiles by the function $f(x) = a + b \times e^{-2(x/\sigma)^2}$. We found $g^{(3)}(0,0) - bg = 0.31\,(1)$ and $g^{(2)}(0) - bg = 0.07\,(2)$ with $bg = 1.01\,(1)$. Because of the large integration used, the amplitudes of the two-particle and the three-particle bunching peaks are far lower than what predicted within the applicability of the Wick theorem, and respectively equal to $g^{(3)}(0,0) - 1 = 5$ and $g^{(2)}(0) - 1 = 1$.

The investigation of the amplitude of the bunching peak displayed in the profile $g^{(3)}(\delta k_1, \delta k_2 = 0.5\, k_d)$ as function of the transverse integration $\Delta k_\perp$ is given in Fig. 6.16 (green points). Since the profile $g^{(3)}(\delta k_1, \delta k_2 = 0.5\, k_d)$ is supposed to be equivalent to $g^{(2)}(\delta k_1)$, we plotted on the same graph (yellow, red and blue points) the results obtained for the second-order correlation bunching peaks investigated in §.6.1.3. We have found a good agreement between the two measurements, which confirms that the the calculation of $g^{(3)}$ is correct.

One can proceed similarly using the profile $g^{(3)}(\delta k_1, \delta k_2 = 0)$ to investigate the evolution of the third-order correlation peak $g^{(3)}(0,0)$. The measurement of the third-order bunching peak amplitude as a function of $\Delta k_\perp$ (by fitting the profile $g^{(3)}(\delta k_1, \delta k_2 = 0)$) reveals, at low transverse integration, an amplitude $g^{(3)}(0,0)$ that becomes very high (>10) while the theory of gaussian density operators predicts $g^{(3)}(0,0) = 6$ (see Fig. 6.17). We attribute the unexpected behavior at low transverse integration to a poor statistics that leads to unfaithful measurements. The saturation of the coherence length measured along the $\delta k_2 = 0$ axis for $\Delta k_\perp > 0.6\, k_d$ may set a limit on the range of transverse integrations to use to get a statistics that is good enough for the measurements to be quantitative. From a theoretical point of view, the effect of the integration on the amplitude of the third-order correlation peak is more intricate than the for the 2-body bunching peak and has not been investigated yet (to do that, one needs to simulate the effect of the integration on the function given by Eq. 6.18. Work in progress!).

To investigate the shape and the amplitude of $g^{(3)}(\delta k_1, \delta k_2)$ in a similar way as we proceeded with $g^{(2)}(\delta k)$, *i.e*, with a transverse integration that is smaller than l_c, it would be necessary to take a larger set of experimental data so as to enhance the statistics.

However, if there are still some work to carry in order to provide a complete description of the three-body correlations in a Mott insulator, the present measurement demonstrates the possibility to investigate high-order correlations in the He experiment.*

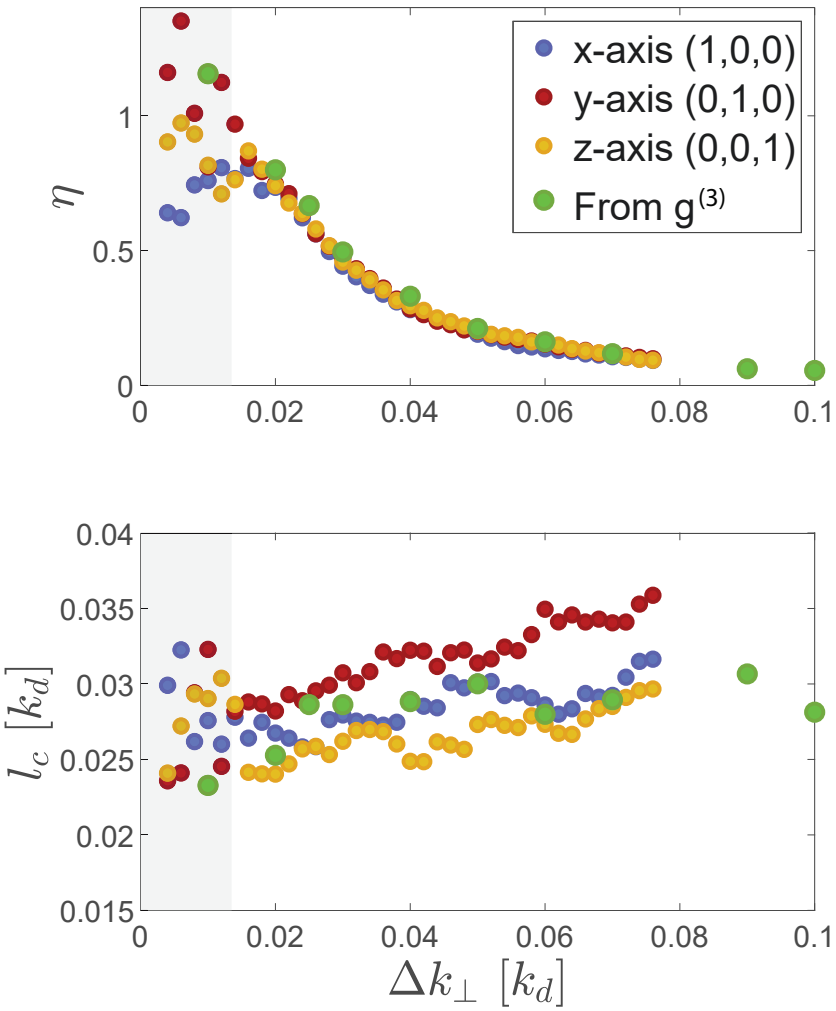

Figure 6.16: **Effect of the transverse integration on $\mathbf{g^{(3)}(\delta k_1, \delta k_2 = 0.5\, k_d)}$.** The profile $g^{(3)}(\delta k_1, \delta k_2 = 0.5\, k_d)$ is fitted by the function $f(\delta k_1) = c + \eta e^{-2(\delta k_1/l_c)^2}$ in order to extract the width and the amplitude of the second-order correlation peak as a function of the transverse integration. The results are displayed by the green points. The values of η and l_c obtained are similar to the ones found in §.6.1.3 and displayed in Fig. 6.3. These data are also displayed in the graph (yellow, red and blue points).

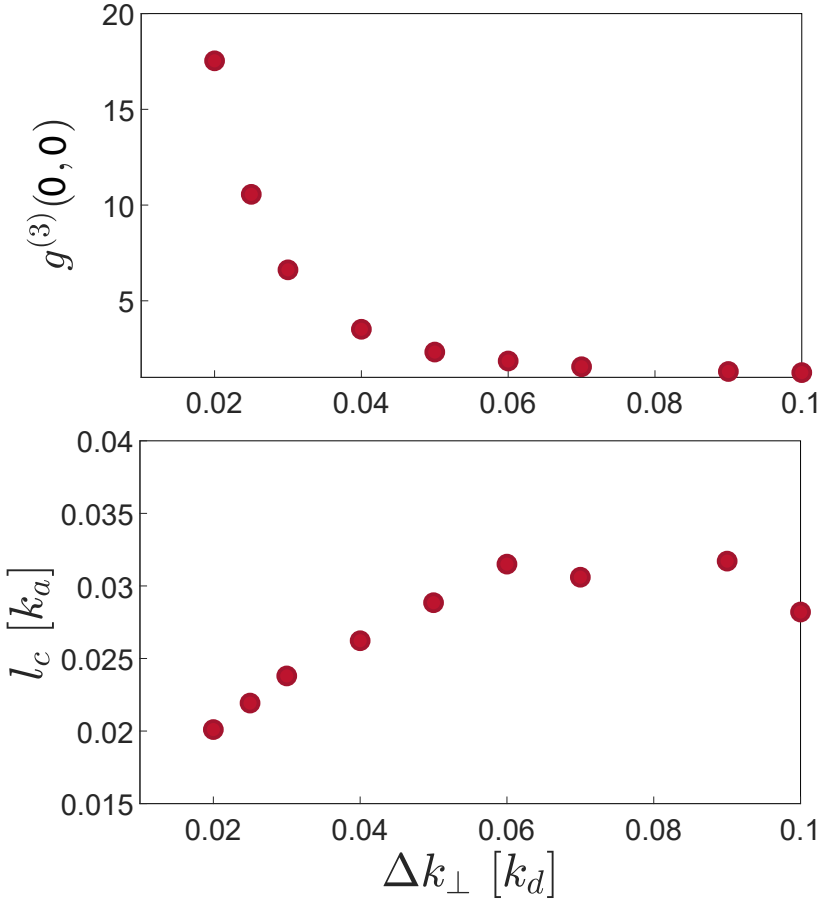

Figure 6.17: **Three-body bunching peak**. *Top graph.* Measured value of $g^{(3)}(0,0)$ as a function of $\Delta k_\perp$. *Bottom graph.* Coherence length measured along the $\delta k_2 = 0$ axis.

6.4 Two-particles correlations across the NF-SF transition

We have seen in the previous section that the correlations measured deep in the Mott insulator regime were the ones of a perfect Mott insulator for which the Wick theorem applies. We put in evidence the HBT-type momentum-space bunching and related it to the in-situ density distribution of the lattice gas. HBT-type correlations (or equivalently, systems that can be described by a gaussian density matrix) can be found in many systems: in the light emitted by a distant star [2] as well as in various systems ranging from nuclear collisions [140], to solid-state systems [141] and finally in the momentum distribution of massive thermal and non-interacting atomic clouds [3, 133, 137].

To go beyond these non-interacting systems, researchers began to investigate, in optics, how the presence of interactions during the propagation from the source to the detector modifies the two-body correlations measured [142]. Another question, this time not investigated so far to the best of our knowledge, is the effect of the presence of interaction between the particles in the source and detected after a ballistic expansion. Note that the correlations induced by the interactions have a different origin from the statistical correlations at the origin of the HBT effect. The idea is thus to investigate the modification of the HBT-correlations due to the interactions between particles in the source.

We have already investigated one extreme case in the strength of the interactions, *i.e*, a perfect Mott insulator. For this system, the interactions are so strong that this parameter "disappears of the problem". This explains why the correlations found for the Mott insulator are of statistical origin (bosonic bunching). In weakly interacting systems, one can encounter two different situations. Either the gas is thermal and the interaction energy is far lower than the energy scale given by the temperature so that the interaction between the particles can be neglected (this is for instance the case of usual gases at room temperature). At low temperature, weak interactions can be treated with usual mean-field theories, a description that provides a faithful description of one-body correlations but which is washing out all $n > 1$ correlations between the atoms resulting from their interaction. More advanced theories, such as the Bogoliubov theory (§.1.2.3), allow to account for correlations at the order $n \geq 2$. They usually lead to the description of the systems in terms of independent quasi-particles whose collective degrees of freedom can be factorized. The correlations on the degrees of freedom of the quasi-particles can then be computed using the Wick theorem (see §.2.2.3) and all the information about the system is contained in the second-order correlation functions. When interactions become stronger, *i.e*, when entering the regime of strongly interacting systems, the interpretation of the systems in terms of independent quasi-particles becomes increasingly false (the interaction between the quasi-particles needs to be taken into account), and for a system made of N particles, solving the system requires the knowledge of the correlation functions with $n > 2$ (and up to N depending on the complexity of the system). This situation is for instance encountered in lattice gases.

In the normal phase above the superfluid phase of the Bose-Hubbard phase diagram and at moderate temperature, the gas is thermal, yet the interaction energy U can be larger than the temperature. While at high temperature, the lattice gas is expected to display a HBT-type bunching of ideal bosons, the fact that the interaction energy becomes of the order of the temperature close to the transition has, most probably, an impact on the statistics, and thus on the correlations between particles.

In this part, we investigate the two-particle correlations in the thermal part of lattice gases at $U/J = 9.5$ (with the same data as the ones used for the investigation of the SF-NF transition performed in §.4.2.1) and across the SF-NF transition with the temperature varying from $T = 2.8\,J$ to $T = 8.8J$ ($T_c \approx 6\,J$, see §.4.1). In all the sets of data, $U \gtrsim T$. Note that such a measurement can be performed due to the ability, thanks to the 3D detection, to decompose the momentum distribution in the different momentum modes. More precisely, one can separate the condensate mode from the depletion as done in §.4.2.1 to measure the condensate fraction. This allows us for instance to investigate the correlations only in the depletion, *i.e*, without considering the contribution to the condensate (because of the macroscopic occupation of the condensate mode in the SF phase, the correlation signal

would be dominated by the correlations of the condensate if the correlations were calculated over the whole cloud).

6.4.1 Experimental parameters and results

Spatially-resolved $g^{(2)}$ measurement

In the superfluid part, two different contributions to the correlation signal can be distinguished:

- The condensate mode is supposed to be characterized by $g^{(2)}(\delta k) = 1$ whatever δk (see §.2.2).
- The depletion, whose correlation signal will be investigated here, should display a periodic bunching (see the discussions given in §.2.2).

In fact, if we run the correlation program for the data at $T = 2.8\,J$, each time considering only the atoms in the condensate or in the depletion, we find, around $\delta k = 0$ no bunching for the condensate and a bunching for the depleted part as illustrated in Fig. 6.18.

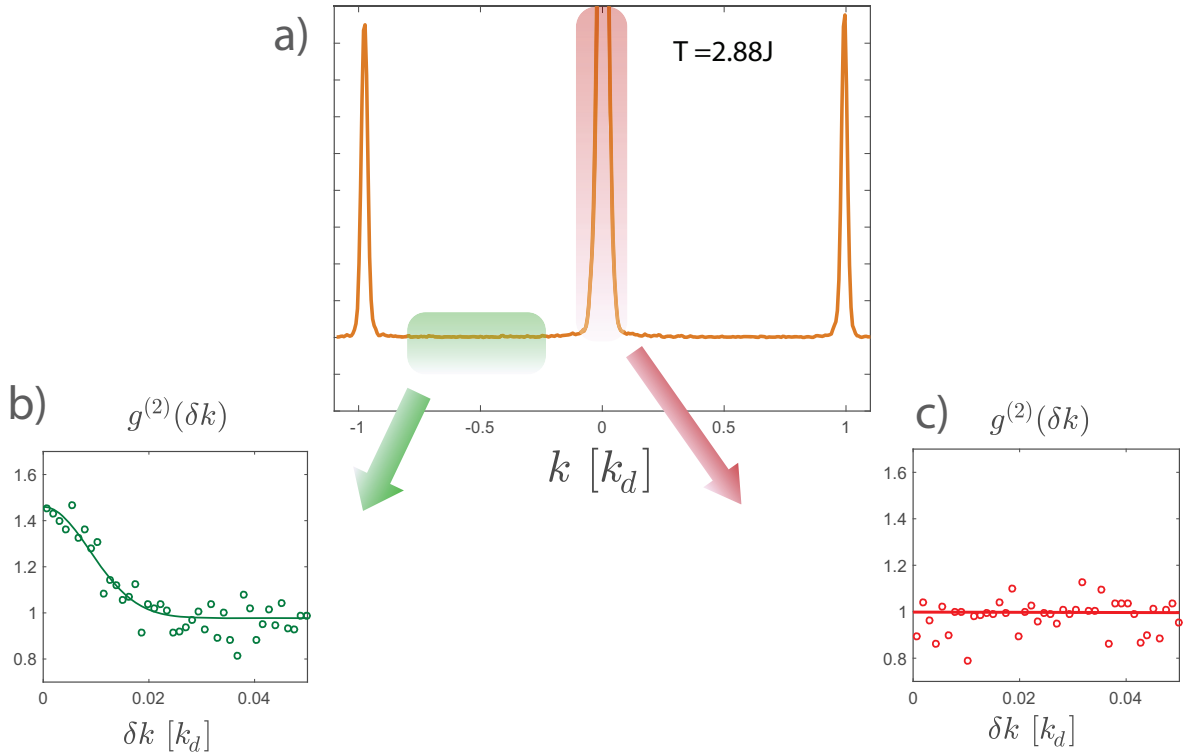

Figure 6.18: **Spatially-resolved measurement of the second-order correlation $\mathbf{g^{(2)}(\delta k)}$. a)** Momentum distribution $\tilde{\rho}(k)$ of a lattice gas at $U/J = 9.5$ and $T = 2.8\,J$. **b)** Measured $g^{(2)}(\delta k)$ obtained considering only the quantum and the thermal depletion modes. We observe a contrasted bunching. **c)** Measured $g^{(2)}(\delta k)$ obtained considering only the condensate. We find $g^{(2)}(\delta k) = 1\ \forall k$, as expected for a coherent source.

Investigation of the bunching in the depletion

First, we focus on the investigation of the width l_c of the correlation peak around $\delta k = 0$. In order to increase the signal to noise ratio, the correlations are calculated the same way as explained in §.6.1 with $\Delta k_\perp = 0.0072\, k_d$. To extract the peak width l_c, we proceed similarly as in §.6.2.3 by fitting the $g^{(2)}$ profiles calculated along the lattice axis by the fitting function $g^{(2)}(\delta k) = 1 + \eta\, e^{-2(\delta k/l_c)^2}$. The values of l_c measured across the transition are represented by the orange squares in Fig. 6.19.a.

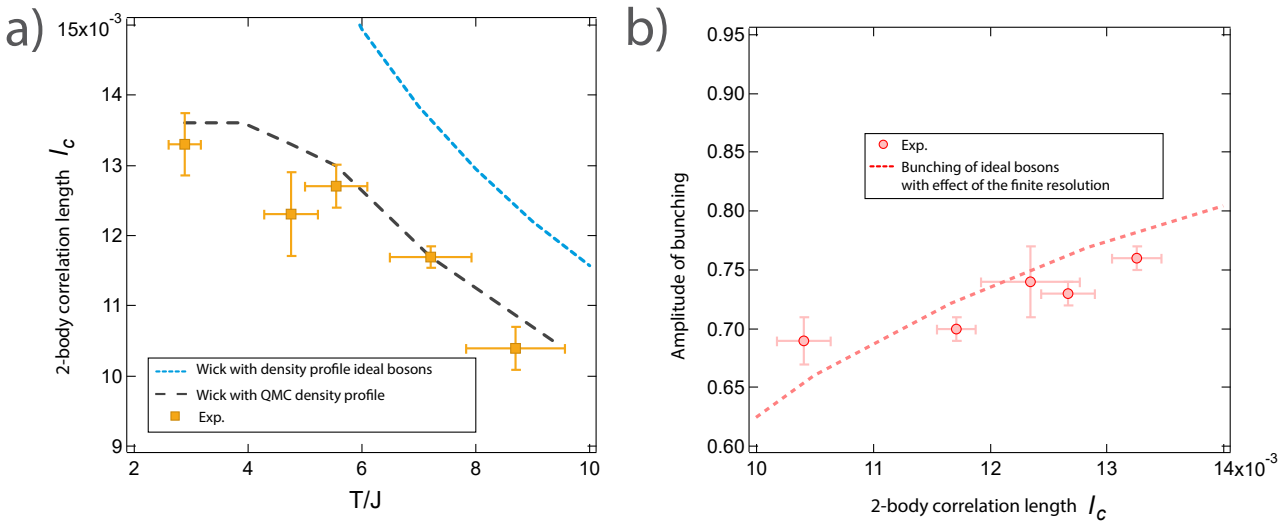

Figure 6.19: **Coherence length $\mathbf{l_c}$ and amplitude η of the bunching measured across the SF-NF transition**. **a)** The orange squares represent the value of $l_c/\sqrt{2}$ measured for the different sets at different temperatures. The blue dashed line is the theoretical prediction within the Wick theorem where the in-trap density is that of ideal bosons at T ($s = \sqrt{\frac{k_B T}{m\omega_{ext}^2}}$). The black dashed line is the prediction within the Wick theorem and with the in-trap density extracted from the in-trap QMC density distributions. **b)** The red points represent the value of η measured for the different sets at different temperatures. The red dash line is a prediction of the amplitude of the bunching within the Wick theorem ($\eta = 1$) and assuming a finite resolution of the system ($\sigma_k = 1.4 \times 10^{-3}\, k_d$).

Within the applicability of the Wick theorem, and for a bunching peak with a gaussian shape, the peak width is equal to $l_c = \sqrt{2}/s$ where s represents the rms size of the source as demonstrated in §.2.2.4.

We are first comparing in Fig. 6.19.a the experimental data with the peak width obtained in the case where $s = \sqrt{\frac{k_B T}{m\omega_{ext}^2}}$, which provides the expected bunching peak width corresponding to a non-interacting thermal gas. This is identical to what has been used so far with a thermal gas in a 3D harmonic trap [143, 133]. The data are represented by the blue dashed line. We see that the correlation length l_c measured sits always below the correlation length of a non-interacting gas[2]. This discrepancy suggests that the bunching phenomenon we observe can not be attributed to the expected bunching for ideal bosons (and a quadratic Hamiltonian).

Because of the repulsive interactions between the particles, the in-trap shape of the lattice gases is modified (in particular, it is enlarged) with respect to the case of non-interacting particles. The exact in-situ profile of the lattice gases can be found using the QMC algorithm. To know whether the Wick theorem applies to the momentum-space degrees of freedom (the density matrix is not gaussian in the momentum space), we plotted in Fig. 6.19 the value of $l_c = \sqrt{2}/s$ (value of the coherence length within the applicability of the Wick theorem) with s calculated from the in-trap QMC profiles. The data are represented by the dark dashed line. The correlation length measured sits this time close to

[2]This can not be explained by effects such as the finite resolution of the detector.

the theoretical curve.

To measure the amplitude of the bunching, we investigated the evolution of the measured amplitude as a function of the transverse integration, similarly to the investigation carried out in §.6.1.3. The different curves $\eta(\delta k_\perp)$ are then fitted by the function:

$$\eta(\Delta k_\perp) = \eta(\Delta k_\perp = 0) \times 0.5 \times \left(\frac{l_c}{\Delta k_\perp}\right)^2 \times \left\{1 - \exp\left(-2\left(\Delta k_\perp / l_c\right)^2\right)\right\} \tag{6.19}$$

which corresponds to the theoretical prediction of the effect of the transverse integration for a gaussian bunching peak (and already given in Eq. 6.13) from which is extracted the values of $\eta = \eta(\Delta k_\perp = 0)$. The results are represented in Fig. 6.19.b by the red points. We see that for all the lattice gases investigated, the bunching amplitude is of the order of $\eta \sim 0.7$, that is to say far lower than the amplitude expected within the applicability of the Wick theorem ($\eta = 1$). We identified two different possible origins of the bunching amplitude:

- *Resolution of the detector.* Here the correlation lengths measured are smaller than the correlation lengths of the Mott insulators investigated in the previous section and the resolution might start playing a role in the measurement of the bunching peaks. If we take into account the finite resolution of the detection, the measured amplitudes should be equal to:

$$\eta_{res}(\sigma_k) = \eta \times \left(\frac{l_c}{\sqrt{l_c^2 + 4\sigma_k^2}}\right)^3 \tag{6.20}$$

  In Fig. 6.19.b, we plot along with the experimental data, the theoretical values of the bunching amplitude that one should measure in the experiment assuming $\eta = 1$ and a resolution $\sigma_k = 2.6 \times 10^{-3}\, k_d$ as a function of the correlation length and find a good agreement with the experimental data. However, the correlation length measured is also supposed to be affected by the finite resolution: $l_{c,meas}(\sigma_k) = l_c \times \sqrt{1 + 4(\sigma_k/l_c)^2}$ and for $\sigma_k = 2.6 \times 10^{-3}\, k_d$, the measured correlation lengths are not consistent with the Wick theorem + the finite resolution . As a conclusion, this means that, contrary to the investigation carried out with the Mott insulators, the amplitude and/or the size of the bunching in the depletion part of a superfluid below and above the transition can not be explained by the theory of gaussian density operators.

- *Physical origin:* Because of the correlation between the particles, the bunching amplitude is inferior to 1.

In order to characterize more precisely this system, we plan to spend some time trying to measure the resolution of the detector with a good precision (using a big thermal cloud and measuring the bunching width). This would allow to state on the origin of the bunching peak amplitude measured here.

6.4.2 Conclusion and prospects

The presence of such a discrepancy may not be surprising. In fact, the Wick theorem is valid for quantum states whose density matrix operator is Gaussian in the degree of freedom which is investigated. In the momentum space, a Gaussian density operator is obtained for non-interacting particles for which the Hamiltonian is diagonal. In the presence of large interaction coupling single-particle states with different momenta, this hypothesis is obviously wrong. This is the situation in our experiment where U is always larger than T, even for $T > T_c$, providing a physical reason behind our observations of the discrepancy with the predictions relying on the Wick theorem.

As mentioned in the introduction of the paragraph, the two-body correlations induced by the interaction between the atoms can, at first order, be captured by the Bogoliubov theory and the Wick theorem applies on the degrees of freedom of the quasi-particles. In order to provide a faithful comparison between the correlation functions (and more precisely the shape and size of the correlation

function features) derived from a Bogoliubov treatment of the interaction and our experimental data, the Bogoliubov development must be done taking into account the inhomogeneity of the lattice gases. However, performing these calculations is beyond the reach of this manuscript. We should yet stress that it would constitute one of the first investigation of the effect of interactions in many-body correlations, beyond the mere effect of statistical correlations. Indeed, to our knowledge, there has been a single work reporting such kind of correlations in 1D bosons [144]. Pursuing these investigations is of clear interest in the future.

Conclusion

In this thesis, we demonstrated the possibility, with the He* detector, to investigate strongly interacting systems through the characterization of their correlations in the momentum-space. We limited ourselves to the study of a system made of an ensemble of indistinguishable bosonic particles trapped in a 3D optical lattice potential. This system is described by the Bose-Hubbard Hamiltonian and one of the main goal of this thesis has consisted in investigating its phase diagram, with a different approaches than what has been done previously in other experiments. The main result of this thesis is the characterization of different phases of the Bose-Hubbard phase diagram through the measurement of one, two or three-body momentum correlations.

We first investigated the phase coherence of a Mott insulator from deep in the Mott phase and getting close to the Mott transition measuring the 3D momentum distribution (one-particle correlation). For a trapped system at $T \neq 0$, there is no theory that predicts the evolution of the coherence when getting close to the Mott transition and due to the proliferation of the particle-hole excitations. We compared the experimental results with strong coupling theories available for $T = 0$ and homogeneous systems. Close to the transition, we found that the gases are much more coherent than predicted by the strong coupling theory. We attributed that to the possible presence of superfluid shells in the trapped clouds that increase the coherence and are not taken into account by the strong-coupling theories available.

Then we investigated the two-body momentum correlations deep in the Mott insulator phase. We measured HBT-type correlations that are quantitatively those of a many-body state whose density operator is Gaussian in the momentum-space, and illustrating the outstanding capability of our approach to identify Gaussian quantum states. We extended this investigation to the three-particle correlations, finding again results in agreement (here more qualitative) with the presence of a gaussian statistic to describe the Mott insulator state.

Finally, we began to investigate the influence of the particle interaction on the the statistical HBT-type correlations. We calculated the two-body correlation function in the thermal part of a lattice gas at moderate lattice amplitude and across the SF to NF transition. We showed that the correlations are not those of a system described by a gaussian density operator and we attributed that to the presence of the strong interactions. A theoretical work is now needed to investigate further this observation.

The second result of this thesis concerns the characterization of the Bose-Hubbard phase diagram and its boundaries. Because of the finite size and the inhomogeneity of the gases produced in most of the cold atom experiments, the phase transitions investigated in these experiments are in fact large crossovers between the different phases, and the investigation of the real phase transition thus become intricate. We particularly investigated different observables in order to infer, for the trapped systems, the boundaries of the SF-NF and the SF-MI transitions. This investigation also brought us to implement a thermometry method in order to measure the temperature of the lattice gases in the experiment. We found temperatures of the order of the ones measured in other cold atom experiments by different methods, thus confirming the order of magnitude of the temperatures currently reached in usual experiments.

Outlook

To complete the investigation of the Bose-Hubbard phase diagram, it would be interesting to probe the correlations close to the Mott transition, a region that is expected to exhibit large quantum fluctuations which should reflect in strong particles correlations. The first beyond mean-field effect originating from the interaction between the particles consists in the presence of momentum pair correlations $\vec{k}/-\vec{k}$ (Bogoliubov excitations) in the depletion of a superfluid. The measurement of this type of correlation would thus constitute the starting point for the investigation of the particle correlations around the QCP. This measurement would require to take a lot of data close to the transition, in the region where the depletion is important (we tried to measure these correlations with the sets of data taken for the investigation of the Mott transition but it was too noisy, partly due to the fact that to avoid any saturation effect of the diffraction peaks, these data have been taken with a low detection efficiency). Note that the measurement of $\vec{k}/-\vec{k}$ correlations is more difficult than the measurement of the local bunching since it is very sensitive to fluctuations of the center of mass velocity (sloshing) of the clouds from shot to shot.

Thanks to the capabilities provided by the He* detector, one can investigate other strongly interacting systems in different geometries. We are currently investigating 1D gases. An ensemble of 1D gases can be obtained by using only two of the three lattice beams installed in the experiment, with the consequence to create an array of 1D tubes. In this way, the tunnelling between the different tubes is frozen and each of the 1D tubes behaves as an independent 1D gas. Measuring the momentum distribution of these 1D gases would permit to measure a parameter called the Tan's Contact $\mathcal{C}$, a quantity that appears in systems where the interactions are of contact type [145]. This parameter is very important because it is a universal parameter that links the macroscopic properties (the thermodynamics functions) of the gases to their microscopic properties (the correlation functions). Its signature can be detected through the measurement of the high-k momentum tails of the gases since $n(k) \propto \mathcal{C}/k^4$. Because of the large dynamic range in the measurement of the momentum density accessible thanks to the electronic detection, $\mathcal{C}$ may in principle be measured in the He* experiment. This would constitute the first observation of the k^{-4} tails in a 1D gas. A recently published article from the group of L. Sanchez-Palencia (CPHT, Ecole Polytechique), with whom we are collaborating, demonstrated that the evolution of the contact with the temperature exhibits a maximum that could be used in order to probe the crossover to fermionization [146].

The knowledge of the contact parameter $\mathcal{C}$ is also very interesting to characterize fermionic systems. Before the beginning of this PhD thesis, I joined the C. Vale team in Melbourne and we measured the evolution of the contact parameter in a Fermi mixture (Lithium) at the unitary limit across the superfluid transition using the technique of Bragg spectroscopy [147]. Such a measurement could also be done in the Helium experiment using the fermionic isotope He-3. With the ability to measure correlation functions directly, one could also investigate the BEC-BCS transition, through the pair correlation signal $\vec{k}/-\vec{k}$ (Cooper pairs in the BCS phase). In the year to come, He-3 atoms will be installed and cooled in the experiment. The do-ability of the measurements mentioned above relies on the presence of a Feshbach resonance between He-3 atoms, which will be the first aspect to investigate in the experiment (this information is currently lacking for ^{3}He*).

Appendix: the cooling sequence

Here is described the sequence used to produce a BEC of ^{4}He* atoms. As mentioned in the introduction, the condensate appears when the inter-particle distance becomes of the order of the De.Broglie wavelength, or equivalently when the phase space density defined as the product $n\lambda_{dB}^3 \approx 1$ with $\lambda_{dB} = h/\sqrt{2\pi m k_B T}$ and n is the particle density. In Fig. 1 the different orders of magnitude of the phase-space density for the different cooling steps are plotted.

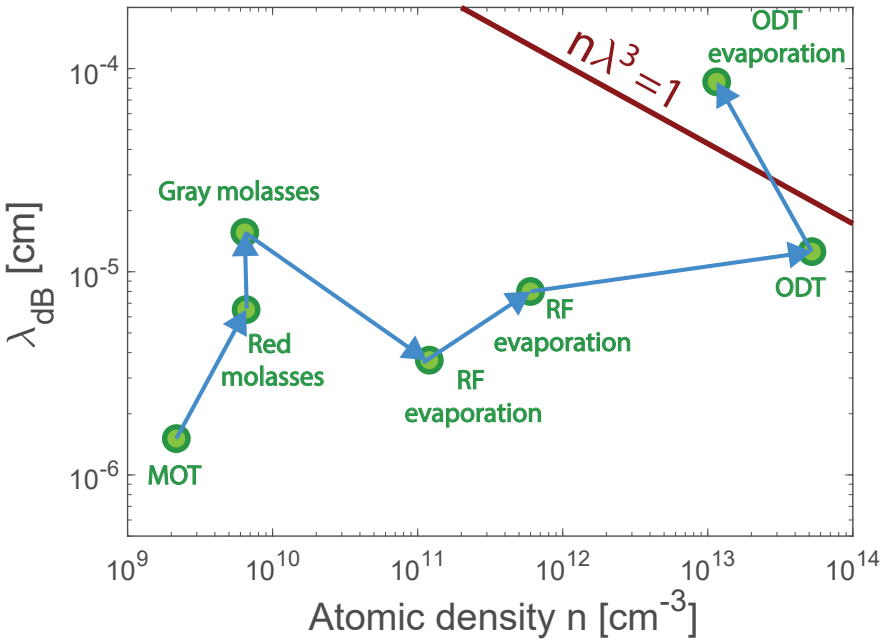

Figure 1: **Phase-space density for the different cooling steps**.

To cool the ^{4}He* down to the quantum degeneracy, two optical transitions are used. The $2^3S_1 \rightarrow 2^3P_2$, also referred to as the 1-2 transition is used for the Doppler cooling. The $2^3S_1 \rightarrow 2^3P_1$, referred to as the 1-1 transition is used for the sub-Doppler cooling and for the optical pumping. The energy levels and their associated fine sublevels are represented in Fig. 2. From a technical point of view, these two transitions are addressed using two independent laser sources emitting around $\lambda = 1083\,\text{nm}$ and locked using the technique of saturated absorption spectroscopy done from an Helium plasma cell [148].

Production of He* atoms

Initially, He atoms are coming from a basic pressurized gaseous He-4 industrial bottle. The atoms are in their ground state 1^1S_0. The first step consists in transferring them to the 2^3S_1 metastable state. Since the two levels are separated by about 20eV, it is not possible to do it optically. We do it using a plasma discharge. The source is composed of an anode and a needle playing the role of a cathode, between which is applied about 2.8kV. When Helium atoms are present, a plasma is generated and a small fraction of atoms (10^{-4}) are transferred to the 2^3S_1 state. Note that to reduce the speed of the metastable atoms produced, the source is cooled to cryogenic temperature using liquid Nitrogen.

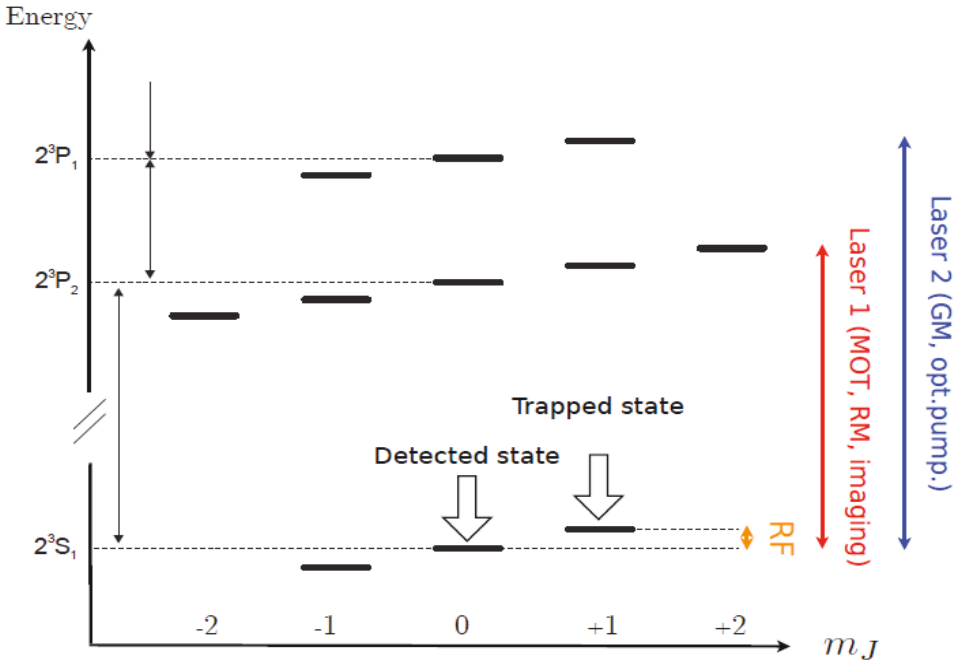

Figure 2: **He energy level used for the cooling**.

Doppler cooling

After the source, the metastable atoms are separated from the rest of the atoms and collimated using a transverse collimation along 2 directions. They are then entering a Zeeman slower that enables to further cool longitudinally the atoms. In both cases, the idea consists in using the dissipative part of the light in order to slow down the atoms (radiation pressure). In the case of the Zeeman slower, a gradient of magnetic field from the source towards the science chamber is applied is order for the atoms to stay in resonance with the light while they are slowing down (it compensates the change in the Doppler shift). At the end of this step, the velocity of the atoms is reduced to about $50\,\mathrm{m.s^{-1}}$, which is enough for them to be captured in a Magneto Optical Trap (MOT).

The MOT is composed of 6 red detuned laser beams from the 1-2 transition and intersecting at the center of the science chamber (SC) and a magnetic quadrupole, generated from two coils in an anti-Helmoltz configuration, also centered with the SC. Because of the detuning, the atoms with a zero velocity at the center of the SC are almost transparent for the light. On the contrary, if an atom is moving away from the center of the SC, the magnetic local gradient is putting the atom on resonance with the light resulting in a restoring force by the the radiation pressure. The combination of the light and of the magnetic gradient allows for the trapping and the cooling at the same time. The loading of the MOT lasts about 1 s and the temperature reached at the end of this step is about 1 mK with $N = 2 \times 10^9$ atoms.

The magnetic field is then turned off and the detuning is reduced to further decrease the temperature of the gas. This is the red molasses phase. Here, the main cooling mechanism is the Doppler cooling. Theoretically, the lowest temperature reachable is $T_D = \hbar\Gamma/2k_B$ where Γ refers to the width of the atomic transition. It is reached for a detuning equal to $\delta = -\Gamma/2$ and a low laser intensity (lowest than the saturation intensity). In the experimental apparatus, temperatures of the order of the Doppler temperature $T_D = 38\,\mu$K have been measured [149], but at the price of an important loss of atom. In order to optimize the phase space density, different parameters have been optimized and the cloud is at the end of this stage composed of about the same number of atoms as in the MOT phase, at a temperature of $80\,\mu$K.

Sub-Doppler cooling

To cool the cloud below the Doppler limit, we use a sub-Doppler technique called the Gray Molasses (GM). This technique can be implemented as soon as an experiment accesses an optical transition with a lambda configuration [150, 151], that is too say a transition characterized by two degenerate ground states $|\, g_1\rangle$ and $|\, g_2\rangle$ and an excited state $|\, e\rangle$.
More precisely, in our experiment, the levels $2^3S_1, m_J = \pm 1$ that play the role of the two ground states are coupled to the excited state $2^3SP_1, m_J = 0$ by respectively contra-propagative σ_+ and σ_- polarization light beams detuned by 16 MHz from the resonance and that creates a periodic dipolar potential. Since the transition $m_J = 0 - m_J = 0$ is not possible, we are indeed in a lambda configuration.

The principle of this technique relies (see Fig. 3) on the fact that because of the coupling with the light, one of the new ground state $|DC>$ is dark, meaning not coupled to the light, the other one $|BC>$ is coupled to the light with a periodic light-shift due to the interference of the beams. As a result, an atom in $|DC>$ stays in $|DC>$. Actually, this is true only if the velocity of the atom is zero. On the contrary, if an atom has a velocity v, then $|DC>$ is not an eigenstate of the system anymore and there is a coupling between $|DC>$ and the orthogonal state $|BC>$. The good thing is that the probability for one atom in $|BC>$ to go in $|DC>$ is higher when the atom is in a maximum of the periodic potential, and conversely, the probability for one atom in $|DC>$ to go in $|BC>$ is higher in the minimum of the potential. Because of the conservation of the energy which implies that the velocity of the atom at the maximum of the potential is lower than in the minimum, the transfer forth and back of the atoms between $|DC>$ and $|BC>$ results in the decrease of their velocity.

At the end of the GM sequence, $N \approx 2 \times 10^9$ atoms and $T \approx 20\,\mu$K.

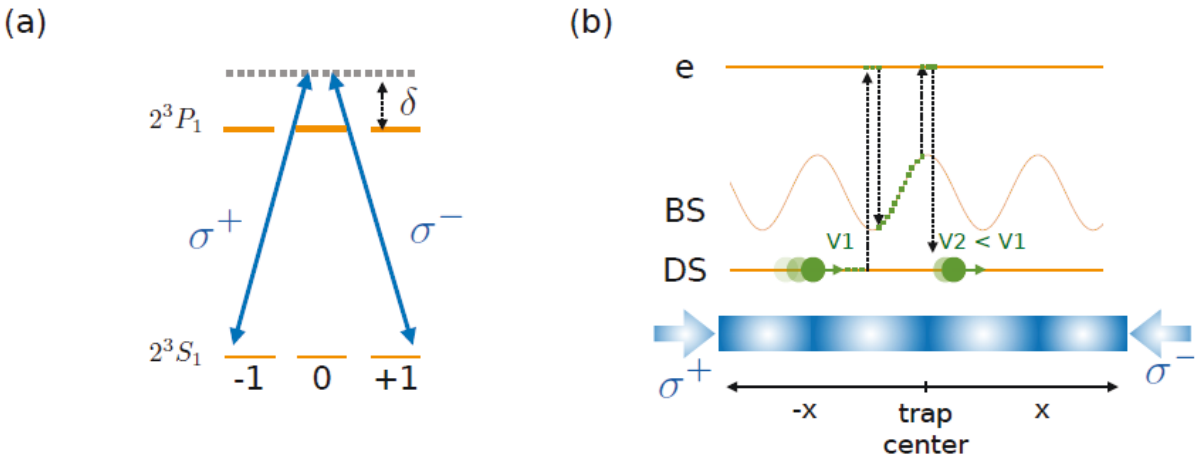

Figure 3: **Principle of the gray molasses**. **a)** 1-1 atomic transition. When the ground state is coupled to the excited state through σ_+ and σ_- polarized lights, the state $2^3S_1, m_J = 0$ does not play any role and we are left with the two ground states $m_J = \pm 1$. **b)** Illustration of the gray molasses cooling. Extracted from [78].

Radio-frequency evaporation

After the GM phase, the cloud is not dense enough to be transferred efficiently to an optical dipole trap (the density is kept low in the presence of close-to-resonance light to avoid the effect of Penning collisions). It is consequently transferred to a magnetic trap in which is performed a radio-frequency cooling.
More precisely, at the end of the GM phase, the atoms are pumped to the $m_J = 1$ state by optical pumping through the 1-1 transition and with a quantization axis given by a strong biais field oriented along the gravity. Then, a quadrupole trap, done with two anti-Helmoltz coils, is loaded. Because

of the Zeeman effect, the atoms in $m_J = 1$ are trapped at the center of the science chamber. To decrease the temperature, the idea is then to eliminate the hottest atoms. Because of their high kinetic energy, these atoms can go to the borders of the trap, which corresponds also to the location of stronger magnetic field and as a result, the area where the Zeeman shift is the more important. We then transfer the hottest atoms from the $m_J = 1$ state to the non-trapped $m_J = 0$ state applying a RF pulse resonant with the Zeeman shift of the hottest atoms. To reduce more and more the temperature, the RF frequency is then lowered in order to address colder and colder atoms. Because of rethermalization processes, the atoms left in the trap get colder. At the end of this cooling step, $N \approx 100 \times 10^6$ atoms and $T \approx 70\,\mu$K. Even if this temperature is higher than in the GM phase, the RF cooling has enabled to increase the density by almost two orders of magnitude (see Fig. 1).

Evaporative cooling

Finally, the cloud is transferred from the quadrupole trap to the optical trap by first loading the optical trap, ramping down slowly the quadrupole trap and using biais fields to optimize the transfer. The optical trap is a crossed optical trap made of two $\lambda = 1550\,$nm beams intersecting with an angle of 20° and oriented is a plane which is at 20° from the horizontal direction. The second beam is made by refocusing the first beam after going through the science chamber and they are detuned by a few tenths of MHz to avoid interferences. The maximum power is 18 W and the two respective waists are 130 and 66 μm.
Once loaded in the optical trap at maximum power, the power in the two beams is decreased over 700ms in order to remove the hottest atoms and to reach the condensation limit. At the end of this sequence, one can get up to $N = 1 \times 10^6$ atoms with no thermal fraction.

List of Figures

List of Tables

Bibliography

[1] C. J. Davisson and L. H. Germer, "Reflection of electrons by a crystal of nickel," *Proceedings of the National Academy of Sciences*, vol. 14, no. 4, pp. 317–322, 1928.

[2] R. H. Brown and R. Q. Twiss, "A test of a new type of stellar interferometer on Sirius," *Nature*, vol. 178, p. 1046–1048, 1956.

[3] J. V. Gomes, A. Perrin, M. Schellekens, D. Boiron, C. I. Westbrook, and M. Belsley, "Theory for a Hanbury Brown Twiss experiment with a ballistically expanding cloud of cold atoms," *Phys. Rev. A*, vol. 74, p. 053607, Nov 2006.

[4] C. K. Hong, Z. Y. Ou, and L. Mandel, "Measurement of subpicosecond time intervals between two photons by interference," *Phys. Rev. Lett.*, vol. 59, pp. 2044–2046, Nov 1987.

[5] R. Lopes, A. Imanaliev, M. C. A. Aspect, D. Boiron, and C. I. Westbrook, "Atomic Hong–Ou–Mandel experiment," *Nature*, vol. 520, p. 66–68, 2015.

[6] C. J. Pethick and H. Smith, *Bose–Einstein Condensation in Dilute Gases*. Cambridge University Press, 2 ed., 2008.

[7] P. Ziń, J. Chwedeńczuk, A. Veitia, K. Rzążewski, and M. Trippenbach, "Quantum multimode model of elastic scattering from Bose-Einstein condensates," *Phys. Rev. Lett.*, vol. 94, p. 200401, May 2005.

[8] M. H. Anderson, J. R. Ensher, M. R. Matthews, C. E. Wieman, and E. A. Cornell, "Observation of Bose-Einstein condensation in a dilute atomic vapor," *Science*, vol. 269, no. 5221, pp. 198–201, 1995.

[9] K. B. Davis, M.-O. Mewes, M. A. Joffe, M. R. Andrews, and W. Ketterle, "Evaporative cooling of Sodium atoms," *Phys. Rev. Lett.*, vol. 74, pp. 5202–5205, Jun 1995.

[10] M. Greiner, O. Mandel, T. Esslinger, T. W. Hänsch, and I. Bloch, "Quantum phase transition from a superfluid to a Mott insulator in a gas of ultracold atoms," *Nature*, vol. 415, p. 39–44, 2002.

[11] M. Schellekens, *L'effet Hanbury-Brown et Twiss pour les atomes froids*. PhD thesis, Université Paris Sud, 2007.

[12] J. H. de Boer and E. J. W. Verwey, "Semi-conductors with partially and with completely filled 3d-lattice bands," *Proceedings of the Physical Society*, vol. 49, pp. 59–71, aug 1937.

[13] N. F. Mott and R. Peierls, "Discussion of the paper by de Boer and Verwey," *Proceedings of the Physical Society*, vol. 49, pp. 72–73, aug 1937.

[14] M. P. A. Fisher, P. B. Weichman, G. Grinstein, and D. S. Fisher, "Boson localization and the superfluid-insulator transition," *Phys. Rev. B*, vol. 40, pp. 546–570, Jul 1989.

[15] J. Dalibard, "Cours du collège de France." https://www.college-de-france.fr/site/jean-dalibard/course-2012-2013.htm, 2013.

[16] N. W. Ashcroft and N. D. Mermin, *Solid State Physics*. Cengage Learning, 1976.

[17] C. Cohen-Tannoudji, B. Diu, and F. Laloé, *Mécanique Quantique*. EDP Sciences.

[18] S. Zhu and B. Wu, "Interaction effects on Wannier functions for bosons in an optical lattice," *Phys. Rev. A*, vol. 92, p. 063637, Dec 2015.

[19] H. A. Gersch and G. C. Knollman, "Quantum cell model for Bosons," *Phys. Rev.*, vol. 129, pp. 959–967, Jan 1963.

[20] O. Penrose and L. Onsager, "Bose-Einstein condensation and liquid Helium," *Phys. Rev.*, vol. 104, pp. 576–584, Nov 1956.

[21] L. Fallani and A. Kastberg, "Cold atoms: A field enabled by light," *EPL (Europhysics Letters)*, vol. 110, p. 53001, jun 2015.

[22] D. van Oosten, P. van der Straten, and H. T. C. Stoof, "Quantum phases in an optical lattice," *Phys. Rev. A*, vol. 63, p. 053601, Apr 2001.

[23] J. K. Freericks and H. Monien, "Phase diagram of the Bose-Hubbard model," *Europhysics Letters (EPL)*, vol. 26, pp. 545–550, jun 1994.

[24] B. Capogrosso-Sansone, N. V. Prokof'ev, and B. V. Svistunov, "Phase diagram and thermodynamics of the three-dimensional Bose-Hubbard model," *Phys. Rev. B*, vol. 75, p. 134302, Apr 2007.

[25] S. Sachdev, *Quantum Phase Transitions*. Cambridge University Press, 2 ed., 2011.

[26] E. Burovski, J. Machta, N. Prokof'ev, and B. Svistunov, "High-precision measurement of the thermal exponent for the three-dimensional XY universality class," *Phys. Rev. B*, vol. 74, p. 132502, Oct 2006.

[27] K. Sheshadri, H. R. Krishnamurthy, R. Pandit, and T. V. Ramakrishnan, "Superfluid and insulating phases in an interacting-Boson model: Mean-Field theory and the RPA," *Europhysics Letters (EPL)*, vol. 22, pp. 257–263, may 1993.

[28] N. Elstner and H. Monien, "Dynamics and thermodynamics of the Bose-Hubbard model," *Phys. Rev. B*, vol. 59, pp. 12184–12187, May 1999.

[29] K. Sengupta and N. Dupuis, "Mott-insulator–to–superfluid transition in the Bose-Hubbard model: A strong-coupling approach," *Phys. Rev. A*, vol. 71, p. 033629, Mar 2005.

[30] D. S. Rokhsar and B. G. Kotliar, "Gutzwiller projection for bosons," *Phys. Rev. B*, vol. 44, pp. 10328–10332, Nov 1991.

[31] N. Metropolis and S. Ulam, "The Monte Carlo method," *Journal of the American Statistical Association*, vol. 44, no. 247, pp. 335–341, 1949. PMID: 18139350.

[32] L. Pollet, K. V. Houcke, and S. M. A. Rombouts *Journal of Computational Physics*, vol. 225, p. 2249–2266, Sep 2017.

[33] L. Mathey, A. Vishwanath, and E. Altman, "Noise correlations in low-dimensional systems of ultracold atoms," *Phys. Rev. A*, vol. 79, p. 013609, Jan 2009.

[34] G. Fabrice, W. Artur, F. Simon, M. Olaf, G. Tatjana, and I. Bloch, "Interference pattern and visibility of a Mott insulator," *Phys. Rev. A*, vol. 72, p. 053606, Nov 2005.

[35] R. P. Feynman, "Simulating physics with computers," *International Journal of Theoretical Physics*, vol. 21, pp. 467–488, Jun 1982.

[36] P. L. Gould, G. A. Ruff, and D. E. Pritchard, "Diffraction of atoms by light: The near-resonant Kapitza-Dirac effect," *Phys. Rev. Lett.*, vol. 56, pp. 827–830, Feb 1986.

[37] P. L. Kapitza and P. A. M. Dirac, "The reflection of electrons from standing light waves," *Mathematical Proceedings of the Cambridge Philosophical Society*, vol. 29, no. 2, p. 297–300, 1933.

[38] P. J. Martin, B. G. Oldaker, A. H. Miklich, and D. E. Pritchard, "Bragg scattering of atoms from a standing light wave," *Phys. Rev. Lett.*, vol. 60, pp. 515–518, Feb 1988.

[39] T. Stöferle, H. Moritz, C. Schori, M. Köhl, and T. Esslinger, "Transition from a strongly interacting 1D Superfluid to a Mott Insulator," *Phys. Rev. Lett.*, vol. 92, p. 130403, Mar 2004.

[40] M. Ben Dahan, E. Peik, J. Reichel, Y. Castin, and C. Salomon, "Bloch oscillations of atoms in an optical potential," *Phys. Rev. Lett.*, vol. 76, pp. 4508–4511, Jun 1996.

[41] D. Jaksch, C. Bruder, J. I. Cirac, C. W. Gardiner, and P. Zoller, "Cold bosonic atoms in optical lattices," *Phys. Rev. Lett.*, vol. 81, pp. 3108–3111, Oct 1998.

[42] S. Friebel, C. D'Andrea, J. Walz, M. Weitz, and T. W. Hänsch, "CO_2-laser optical lattice with cold Rubidium atoms," *Phys. Rev. A*, vol. 57, pp. R20–R23, Jan 1998.

[43] K. Jiménez-García, R. L. Compton, Y.-J. Lin, W. D. Phillips, J. V. Porto, and I. B. Spielman, "Phases of a two-dimensional Bose gas in an optical lattice," *Phys. Rev. Lett.*, vol. 105, p. 110401, Sep 2010.

[44] C. Becker, P. Soltan-Panahi, J. Kronjäger, S. Dörscher, K. Bongs, and K. Sengstock, "Ultracold quantum gases in triangular optical lattices," *New Journal of Physics*, vol. 12, p. 065025, jun 2010.

[45] C. K. Thomas, T. H. Barter, T.-H. Leung, M. Okano, G.-B. Jo, J. Guzman, I. Kimchi, A. Vishwanath, and D. M. Stamper-Kurn, "Mean-field scaling of the Superfluid to Mott insulator transition in a 2D optical superlattice," *Phys. Rev. Lett.*, vol. 119, p. 100402, Sep 2017.

[46] R. Jordens, N. Strohmaier, K. Günter, H. Moritz, and T. Esslinger, "A Mott insulator of fermionic atoms in an optical lattice," *Nature*, vol. 455, p. 204–207, 2008.

[47] R. Grimm, M. Weidemüller, and Y. B. Ovchinnikov, "Optical dipole traps for neutral atoms," vol. 42 of *Advances In Atomic, Molecular, and Optical Physics*, pp. 95 – 170, Academic Press, 2000.

[48] M. Schellekens, R. Hoppeler, A. Perrin, J.Gomes, D. Boiron, A. Aspect, and C. Westbrook, "Probing the superfluid–to–Mott insulator transition at the single-atom level," *Science*, vol. 329, no. 5991, pp. 547–550, 2010.

[49] E. Haller, J. Hudson, A. Kelly, D. A. Cotta, B. Peaudecerf, G. D. Bruce, and S. Kuhr, "Single-atom imaging of fermions in a quantum-gas microscope," *Nat. Phys.*, vol. 11, pp. 738–741, 2015.

[50] T. Gericke, P. Würtz, D. Reitz, T. Langen, and H. Ott, "High-resolution scanning electron microscopy of an ultracold quantum gas," *Nature Physics*, vol. 4, p. 949–953, 2008.

[51] R. Bucker, A.Perrin, S.Manz, T.Betz, Ch.Koller, T.Plisson, J.Rottmann, T. Schumm, and J.Schmiedmayer, "Single-particle-sensitive imaging of freely propagating ultracold atoms," *New Journal of Physics*, vol. 11, 2009.

[52] S. R. Clark and D. Jaksch, "Signatures of the superfluid to Mott-insulator transition in the excitation spectrum of ultracold atoms," *New Journal of Physics*, vol. 8, pp. 160–160, aug 2006.

[53] M. Endres, T. Fukuhara, D. Pekker, M. Cheneau, P. Schau, C. Gross, E. Demler, S. Kuhr, and I. Bloch, "The Higgs amplitude mode at the two-dimensional superfluid/Mott insulator transition," *Nature*, vol. 487, p. 454–458, 2012.

[54] N. Fabbri, M. Panfil, D. Clément, L. Fallani, M. Inguscio, C. Fort, and J.-S. Caux, "Dynamical structure factor of one-dimensional bose gases: Experimental signatures of beyond-Luttinger-liquid physics," *Phys. Rev. A*, vol. 91, p. 043617, Apr 2015.

[55] H. Cayla, C. Carcy, Q. Bouton, R. Chang, G. Carleo, M. Mancini, and D. Clément, "Single-atom-resolved probing of lattice gases in momentum space," *Phys. Rev. A*, vol. 97, p. 061609, Jun 2018.

[56] D. Barredo, S. de Léséleuc, V. Lienhard, T. Lahaye, and A. Browaeys, "An atom-by-atom assembler of defect-free arbitrary two-dimensional atomic arrays," *Science*, vol. 354, no. 6315, pp. 1021–1023, 2016.

[57] F. Gerbier, "Boson Mott insulators at finite temperatures," *Phys. Rev. Lett.*, vol. 99, p. 120405, Sep 2007.

[58] S. Bergkvist, P. Henelius, and A. Rosengren, "Local-density approximation for confined bosons in an optical lattice," *Phys. Rev. A*, vol. 70, p. 053601, Nov 2004.

[59] L. Pollet, "Recent developments in quantum Monte Carlo simulations with applications for cold gases," *Rep. Prog. Phys.*, vol. 75, p. 094501, 2012.

[60] F. Delfino and E. Vicari, "Critical behavior at the spatial boundary of a trapped inhomogeneous Bose-Einstein condensate," *Phys. Rev. A*, vol. 95, p. 053606, May 2017.

[61] T. Donner, S. Ritter, T. Bourdel, A. Öttl, M. Köhl, and T. Esslinger, "Critical behavior of a trapped interacting Bose gas," *Science*, vol. 315, no. 5818, pp. 1556–1558, 2007.

[62] P. N. Ma, K. Y. Yang, L. Pollet, J. V. Porto, M. Troyer, and F. C. Zhang, "Influence of the trap shape on the detection of the superfluid—Mott-insulator transition," *Phys. Rev. A*, vol. 78, p. 023605, Aug 2008.

[63] M. Campostrini and E. Vicari, "Critical behavior and scaling in trapped systems," *Phys. Rev. Lett.*, vol. 102, p. 240601, Jun 2009.

[64] L. Pollet, N. V. Prokof'ev, and B. V. Svistunov, "Criticality in trapped atomic systems," *Phys. Rev. Lett.*, vol. 104, p. 245705, Jun 2010.

[65] I. Frérot and T. Roscilde, "Reconstructing the quantum critical fan of strongly correlated systems using quantum correlations," *Nature Communications*, vol. 10, 2019.

[66] R. J. Glauber, "The quantum theory of optical coherence," *Phys. Rev.*, vol. 130, pp. 2529–2539, Jun 1963.

[67] F. S. Rotondo, "Imaging with amplitude and intensity interferometers," 2004.

[68] G. Grynberg, A. Aspect, and C. Fabre, *Quantum Optics*. Cambridge University press, 2010.

[69] L. Mandel, "Fluctuations of photon beams: The distribution of the photo-electrons," *Proceedings of the Physical Society*, vol. 74, pp. 233–243, sep 1959.

[70] J. Goodman, *Statistical Optics*. A Wiley-Interscience publication, Wiley, 1985.

[71] C.W.Gardiner and P.Zoller, *Quantum noise*. Springer, 2000.

[72] G. C. Wick, "The evaluation of the collision matrix," *Phys. Rev.*, vol. 80, pp. 268–272, Oct 1950.

[73] M. Gaudin, "Une démonstration simplifiée du théorème de Wick en mécanique statistique," *Nuclear Physics*, vol. 15, 1960.

[74] I. B. Spielman, W. D. Phillips, and J. V. Porto, "Condensate fraction in a 2D Bose gas measured across the Mott-Insulator transition," *Phys. Rev. Lett.*, vol. 100, p. 120402, Mar 2008.

[75] F. Gerbier, A. Widera, S. Folling, O. Mandel, T. Gericke, and I. Bloch, "Phase coherence of an atomic Mott Insulator," *Phys. Rev. Lett.*, vol. 95, p. 050404, Jul 2005.

[76] S. S. Hodgman, R. I. Khakimov, R. J. Lewis-Swan, A. G. Truscott, and K. V. Kheruntsyan, "Solving the quantum many-body problem via correlations measured with a momentum microscope," *Phys. Rev. Lett.*, vol. 118, p. 240402, Jun 2017.

[77] E. Toth, A. M. Rey, and P. B. Blakie, "Theory of correlations between ultracold bosons released from an optical lattice," *Phys. Rev. A*, vol. 78, p. 013627, Jul 2008.

[78] H. Cayla, *Measuring the momentum distribution of a lattice gas at the single-atom level.* PhD thesis, Laboratoire Charles Fabry, Université Paris-Saclay, 2018.

[79] Q. Bouton, *Etude miscroscopique de la distibution en impulsion de condensats de Bose-Eintein d'Hélium métastable.* PhD thesis, Laboratoire Charles Fabry, Université Paris-Saclay, 2018.

[80] L. Hoendervanger, *A New Metastable Helium Machine : An Investigation into the Attributes of Trapping, Cooling and Detecting Metastable Helium.* PhD thesis, Laboratoire Charles Fabry, Université Paris-Saclay, 2015.

[81] A. Robert, O. Sirjean, A. Browaeys, J. Poupard, S. Nowak, D. Boiron, C. I. Westbrook, and A. Aspect, "A Bose-Einstein condensate of metastable atoms," vol. 292, no. 5516, pp. 461–464, 2001.

[82] F. Pereira Dos Santos, J. Léonard, J. Wang, C. J. Barrelet, F. Perales, E. Rasel, C. S. Unnikrishnan, M. Leduc, and C. Cohen-Tannoudji, "Bose-Einstein condensation of metastable Helium," *Phys. Rev. Lett.*, vol. 86, pp. 3459–3462, Apr 2001.

[83] F. Pereira Dos Santos, F. Perales, J. Léonard, A. Sinatra, J. Wang, F. Saverio Pavone, E. Rasel, C. Unnikrishnan, and M. Leduc, "Penning collisions of laser-cooled metastable helium atoms," *The European Physical Journal D - Atomic, Molecular, Optical and Plasma Physics*, vol. 14, pp. 15–22, Apr 2001.

[84] A.Messiah, *Quantum Mechanics.* Dunod, 2003.

[85] T. Gericke, F. Gerbier, A. Widera, S. Fölling, O. Mandel, and I. Bloch, "Adiabatic loading of a Bose–Einstein condensate in a 3D optical lattice," *Journal of Modern Optics*, vol. 54, no. 5, pp. 735–743, 2007.

[86] M. Greiner, I. Bloch, O. Mandel, T. W. Hänsch, and T. Esslinger, "Exploring phase coherence in a 2D lattice of Bose-Einstein condensates," *Phys. Rev. Lett.*, vol. 87, p. 160405, Oct 2001.

[87] G. Fraser and J. Pearson, "The direct detection of thermal neutrons by imaging microchannel-plate detectors," *Nuclear Instruments and Methods in Physics Research Section A: Accelerators, Spectrometers, Detectors and Associated Equipment*, vol. 293, no. 3, pp. 569 – 574, 1990.

[88] A. V. Phelps and J. P. Molnar, "Lifetimes of metastable states of noble gases," *Phys. Rev.*, vol. 89, pp. 1202–1208, Mar 1953.

[89] F. Nogrette, D. Heurteau, R. Chang, Q. Bouton, C. I. Westbrook, R. Sellem, and D. Clément, "Characterization of a detector chain using a FPGA-based time-to-digital converter to reconstruct the three-dimensional coordinates of single particles at high flux," *Review of Scientific Instruments*, vol. 86, no. 11, p. 113105, 2015.

[90] R. Lopes, A. Imanaliev, M. Bonneau, J. Ruaudel, M. Cheneau, D. Boiron, , and C. I. Westbrook, "Second-order coherence of superradiance from a Bose-Einstein condensate," *Phys. Rev. A*, vol. 90, p. 013615, 2014.

[91] M. L. Edgar, J. S. Lapington, and A. Smith, "The spatial extent of gain depression for MCP-based photon detectors," *Review of Scientific Instruments*, vol. 63, no. 1, pp. 816–819, 1992.

[92] F. Gerbier, S. Trotzky, S. Foelling, U. Schnorrberger, J. D. Thompson, A. Widera, I. Bloch, L. Pollet, M. Troyer, B. Capogrosso-Sansone, N. Prokofev, and B. V. Svistunov, "Expansion of a quantum gas released from an optical lattice," *Phys. Rev. Lett.*, vol. 101, p. 155303, 2008.

[93] J. N. Kupferschmidt and E. J. Mueller, "Role of interactions in time-of-flight expansion of atomic clouds from optical lattices," *Phys. Rev. A*, vol. 82, p. 023618, Aug 2010.

[94] S. Fang, R.-K. Lee, and D.-W. Wang, "Quantum fluctuations and condensate fraction during time-of-flight expansion," *Phys. Rev. A*, vol. 82, p. 031601, Sep 2010.

[95] R. I. Khakimov, B. M. Henson, D. K. Shin, S. S. Hodgman, R. G. Dall, K. G. H. Baldwin, and A. G. Truscott, "Ghost imaging with atoms," *Nature*, vol. 540, pp. 100–13, 2016.

[96] P. Ziń, J. Chwedeńczuk, and M. Trippenbach, "Elastic scattering losses from colliding Bose-Einstein condensates," *Phys. Rev. A*, vol. 73, p. 033602, Mar 2006.

[97] P. A. Murthy, D. Kedar, T. Lompe, M. Neidig, M. G. Ries, A. N. Wenz, G. Zürn, and S. Jochim, "Matter-wave Fourier optics with a strongly interacting two-dimensional Fermi gas," *Phys. Rev. A*, vol. 90, p. 043611, Oct 2014.

[98] S. Trotzky, L. Pollet, F. Gerbier, U. Schnorrberger, I. Bloch, N. V. Prokof'ev, B. Svistunov, and M. Troyer, "Suppression of the critical temperature for superfluidity near the Mott transition," *Nature Physics*, vol. 6, p. 998–1004, 2010.

[99] R. A. Hart, P. M. Duarte, T.-L. Yang, X. Liu, T. Paiva, E. Khatami, R. T. Scalettar, N. Trivedi, D. A. Huse, and R. G. Hulet, "Observation of antiferromagnetic correlations in the Hubbard model with ultracold atoms," *Nature*, vol. 519, p. 211–214, March 2015.

[100] M. A. Cazalilla, "Bosonizing one-dimensional cold atomic gases," *Journal of Physics B: Atomic, Molecular and Optical Physics*, vol. 37, pp. S1–S47, mar 2004.

[101] F. Dalfovo, S. Giorgini, L. P. Pitaevskii, and S. Stringari, "Theory of Bose-Einstein condensation in trapped gases," *Rev. Mod. Phys.*, vol. 71, pp. 463–512, Apr 1999.

[102] S. Nascimbène, N. Navon, K. J. Jiang, F. Chevy, and C. Salomon, "Exploring the thermodynamics of a universal Fermi gas," *Nature*, vol. 463, p. 1057–1060, February 2010.

[103] T.-L. Ho and Q. Zhou, "Intrinsic heating and cooling in adiabatic processes for Bosons in optical lattices," *Phys. Rev. Lett.*, vol. 99, p. 120404, Sep 2007.

[104] J. F. Sherson, C. Weitenberg, M. Endres, M. Cheneau, I. Bloch, and S. Kuhr, "Single-atom-resolved fluorescence imaging of an atomic Mott insulator," *Nature*, vol. 467, pp. 68–72, 2010.

[105] W. S. Bakr, I. G. Jonathon, A. Peng, S. Fölling, and M. Greiner, "A quantum gas microscope for detecting single atoms in a Hubbard-regime optical lattice," *Nature*, vol. 462, pp. 74–77, 2009.

[106] X. Zhang, C.-L. Hung, S.-K. Tung, and C. Chin, "Observation of quantum criticality with ultracold atoms in optical lattices," *Science*, vol. 335, no. 6072, pp. 1070–1072, 2012.

[107] U. Ray and D. M. Ceperley, "Revealing the condensate and noncondensate distributions in the inhomogeneous Bose-Hubbard model," *Phys. Rev. A*, vol. 87, p. 051603, May 2013.

[108] R. Lopes, C. Eigen, N. Navon, D. Clément, R. P. Smith, and Z. Hadzibabic, "Quantum depletion of a homogeneous Bose-Einstein condensate," *Phys. Rev. Lett.*, vol. 119, p. 190404, Nov 2017.

[109] M. J. Mark, E. Haller, K. Lauber, J. G. Danzl, A. J. Daley, and H.-C. Nagerl, "Precision measurements on a tunable Mott insulator of ultracold atoms," *Phys. Rev. Lett.*, vol. 107, p. 175301, Oct 2011.

[110] J. Mun, P. Medley, G. K. Campbell, L. G. Marcassa, D. E. Pritchard, and W. Ketterle, "Phase diagram for a Bose-Einstein condensate moving in an optical lattice," *Phys. Rev. Lett.*, vol. 99, p. 150604, Oct 2007.

[111] M. Rigol, G. G. Batrouni, V. G. Rousseau, and R. T. Scalettar, "State diagrams for harmonically trapped bosons in optical lattices," *Phys. Rev. A*, vol. 79, p. 053605, May 2009.

[112] M. A. Kristensen, M. B. Christensen, M. Gajdacz, M. Iglicki, K. Pawlowski, C. Klempt, J. F. Sherson, K. Rzażewski, A. J. Hilliard, and J. J. Arlt, "Observation of atom number fluctuations in a Bose-Einstein condensate," *Phys. Rev. Lett.*, vol. 122, p. 163601, Apr 2019.

[113] S. Grossmann and M. Holthaus, "Microcanonical fluctuations of a Bose system's ground state occupation number," *Phys. Rev. E*, vol. 54, pp. 3495–3498, Oct 1996.

[114] H. D. Politzer, "Condensate fluctuations of a trapped, ideal Bose gas," *Phys. Rev. A*, vol. 54, pp. 5048–5054, Dec 1996.

[115] R. Fazio and H. van der Zant, "Quantum phase transitions and vortex dynamics in superconducting networks," *Physics Reports*, vol. 355, no. 4, pp. 235 – 334, 2001.

[116] O. A. Prośniak, M. Łacki, and B. Damski, "Critical points of the three-dimensional Bose-Hubbard model from on-site atom number fluctuations," *Scientific Reports, Nature*, vol. 9, 2019.

[117] C. H. Bennett and D. P. DiVincenzo, "Quantum information and computation," *Nature*, vol. 404, p. 247–255, 2000.

[118] L. Pezzè, A. Smerzi, M. K. Oberthaler, R. Schmied, and P. Treutlein, "Quantum metrology with nonclassical states of atomic ensembles," *Rev. Mod. Phys.*, vol. 90, p. 035005, Sep 2018.

[119] P. Zanardi and N. Paunković, "Ground state overlap and quantum phase transitions," *Phys. Rev. E*, vol. 74, p. 031123, Sep 2006.

[120] H. Strobel, W. Muessel, D. Linnemann, T. Zibold, D. B. Hume, L. Pezzè, A. Smerzi, and M. K. Oberthaler, "Fisher information and entanglement of non-Gaussian spin states," *Science*, vol. 345, no. 6195, pp. 424–427, 2014.

[121] L.-A. Wu, M. S. Sarandy, and D. A. Lidar, "Quantum phase transitions and bipartite entanglement," *Phys. Rev. Lett.*, vol. 93, p. 250404, Dec 2004.

[122] T. J. Osborne and M. A. Nielsen, "Entanglement, quantum phase transitions, and density matrix renormalization," *Quantum Information Processing*, vol. 1, pp. 45–53, Apr 2002.

[123] I.Frérot and T.Roscilde, "Entanglement entropy across the superfluid-insulator transition: A signature of Bosonic criticality," *Phys. Rev. Lett.*, vol. 116, p. 190401, May 2016.

[124] I. B. Spielman, W. D. Phillips, and J. V. Porto, "Mott-Insulator transition in a two-dimensional atomic bose gas," *Phys. Rev. Lett.*, vol. 98, p. 080404, Feb 2007.

[125] M. Endres, M. Cheneau, T. Fukuhara, C. Weitenberg, P. Schauß, C. Gross, L. Mazza, M. C. Bañuls, L. Pollet, I. Bloch, and S. Kuhr, "Observation of correlated particle-hole pairs and string order in low-dimensional Mott insulators," *Science*, vol. 334, no. 6053, pp. 200–203, 2011.

[126] J. K. Freericks, H. R. Krishnamurthy, Y. Kato, N. Kawashima, and N. Trivedi, "Strong-coupling expansion for the momentum distribution of the Bose-Hubbard model with benchmarking against exact numerical results," *Phys. Rev. A*, vol. 79, p. 053631, May 2009.

[127] A. P. Matthias Ohliger, "Green's function approach to the Bose-Hubbard model," *Arxiv*, p. arXiv:0810.4399, 2009.

[128] Y. D. Chong, "Complex methods for the sciences." http://www1.spms.ntu.edu.sg/~ydchong/teaching/10_greens_function.pdf.

[129] V. Denechaud, *Vers une étude spectroscopique de la transition d'Anderson*. PhD thesis, Universite Paris Saclay, 2018.

[130] E. Akkermans and G. Montambaux, *Mesoscopic Physics of Electrons and Photons*. Cambridge University Press, 2007.

[131] A.-M. Tremblay, "Quantum Material's Theory, from perturbation theory to dynamical-mean Öeld theory."

[132] E. Altman, E. Demler, and M. D. Lukin, "Probing many-body states of ultracold atoms via noise correlations," *Phys. Rev. A*, vol. 70, p. 013603, Jul 2004.

[133] R. G. Dall, A. G. Manning, S. S. Hodgman, W. Rugway, K. V. Kheruntsyan, and A. G. Truscott, "Ideal n-body correlations with massive particles," *Nature Physics*, vol. 9, pp. 341–344, 2013.

[134] M. Naraschewski and R. J. Glauber, "Spatial coherence and density correlations of trapped Bose gases," *Phys. Rev. A*, vol. 59, pp. 4595–4607, Jun 1999.

[135] S. Fölling, F. Gerbier, A. Widera, O. Mandel, T. Gericke, and I. Bloch, "Spatial quantum noise interferometry in expanding ultracold atom clouds," *Nature Physics*, vol. 434, pp. 481–484, 2005.

[136] V. Guarrera, N. Fabbri, L. Fallani, C. Fort, K. M. R. van der Stam, and M. Inguscio, "Noise correlation spectroscopy of the broken order of a Mott Insulating phase," *Phys. Rev. Lett.*, vol. 100, p. 250403, Jun 2008.

[137] A. Öttl, S. Ritter, M. Köhl, and T. Esslinger, "Correlations and counting statistics of an atom laser," *Phys. Rev. Lett.*, vol. 95, p. 090404, Aug 2005.

[138] O. Jagutzki, J. Lapington, L. Worth, U. Spillman, V. Mergel, and H. Schmidt-Böcking, "Position sensitive anodes for MCP read-out using induced charge measurement," *Nuclear Instruments and Methods in Physics Research Section A: Accelerators, Spectrometers, Detectors and Associated Equipment*, vol. 477, no. 1, pp. 256 – 261, 2002. 5th Int. Conf. on Position-Sensitive Detectors.

[139] R. Hong, A. Leredde, Y. Bagdasarova, X. Fléchard, A. García, P. Müller, A. Knecht, E. Liénard, M. Kossin, M. Sternberg, H. Swanson, and D. Zumwalt, "High accuracy position response calibration method for a micro-channel plate ion detector," *Nuclear Instruments and Methods in Physics Research Section A: Accelerators, Spectrometers, Detectors and Associated Equipment*, vol. 835, pp. 42 – 50, 2016.

[140] G. Baym, "The physic of Hanbury-Brown and Twiss intensity interferometry: from stars to nuclear collisions," *Acta. Phys. Pol. B*, vol. 29, pp. 1839–1884, 1998.

[141] W. D. Oliver, J. Kim, R. C. Liu, and Y. Yamamoto, "Hanbury Brown and Twiss-type experiment with electrons," *Science*, vol. 284, no. 5412, pp. 299–301, 1999.

[142] E. S. Y. Bromberg, Y. Lahini and Y. Silberberg, "Hanbury Brown and Twiss interferometry with interacting photons," *Nature Photonics*, vol. 4, p. 721–726, 2010.

[143] M. Schellekens, R. Hoppeler, A. Perrin, J. V. Gomes, D. Boiron, A. Aspect, and C. I. Westbrook, "Hanbury Brown Twiss effect for ultracold quantum gases," *Science*, vol. 310, pp. 648–651, 2005.

[144] T. Schweigler et al, "Experimental characterization of a quantum many-body system via higher-order correlations," *Nature*, vol. 545, pp. 323–326, 2017.

[145] S. Tan, "Energetics of a strongly correlated Fermi gas," *Annals of Physics*, vol. 323, no. 12, pp. 2952 – 2970, 2008.

[146] H. Yao, D. Clément, A. Minguzzi, P. Vignolo, and L. Sanchez-Palencia, "Tan's contact for trapped Lieb-Liniger Bosons at finite temperature," *Phys. Rev. Lett.*, vol. 121, p. 220402, Nov 2018.

[147] C. Carcy, S. Hoinka, M. G. Lingham, P. Dyke, C. C. N. Kuhn, H. Hu, and C. J. Vale, "Contact and sum rules in a near-uniform Fermi gas at unitarity," *Phys. Rev. Lett.*, vol. 122, p. 203401, May 2019.

[148] F. Moron, A. L. Hoendervanger, M. Bonneau, Q. Bouton, A. Aspect, D. Boiron, D. Clément, and C. I. Westbrook, "An oscillator circuit to produce a radio-frequency discharge and application to metastable helium saturated absorption spectroscopy," *Review of Scientific Instruments*, vol. 83, no. 4, p. 044705, 2012.

[149] R. Chang, A. L. Hoendervanger, Q. Bouton, Y. Fang, T. Klafka, K. Audo, A. Aspect, C. I. Westbrook, and D. Clément, "Three-dimensional laser cooling at the Doppler limit," *Phys. Rev. A*, vol. 90, p. 063407, Dec 2014.

[150] A. Burchianti, G. Valtolina, J. A. Seman, E. Pace, M. De Pas, M. Inguscio, M. Zaccanti, and G. Roati, "Efficient all-optical production of large ^{6}Li quantum gases using D_1 gray-molasses cooling," *Phys. Rev. A*, vol. 90, p. 043408, Oct 2014.

[151] D. R. Fernandes, F. Sievers, N. Kretzschmar, S. Wu, C. Salomon, and F. Chevy, "Sub-Doppler laser cooling of fermionic 40K atoms in three-dimensional gray optical molasses," *EPL*, vol. 100, 2012.

Etude de la transition de Mott avec des atomes ultrafroids d'Hélium métastable

Quand un système physique est composé d'un ensemble de particules, les intéractions entre les différentes particules peuvent être à l'origine de propriétés physiques particulières. Un exemple canonique réside dans les propriétes supraconductrices de certains matériaux. En physique, les intéractions entre particules peuvent souvent être décrites par des méthodes de champ moyen. La force d'intéraction qu'exerce les autres particules sur une particule donnée est alors décrite comme un potentiel moyen indépendant des degrées de liberté des autres particules. Cette méthode revient à considérer les particules indépendantes avec un potentiel effectif due à la présence des autres particules. Cependant, cette approximation ne perment pas de rendre compte des propriétés de certains systèmes. Ces systèmes sont appelés systèmes à N-corps. Pour les étudier, il est nécessaire de prendre en compte les corrélations entre au moins deux particules.

Dans cette thèse, le système étudié est composé d'un ensemble de particules bosoniques en interaction (interaction répulsive de contact) et soumises à un potentiel 3D périodique.

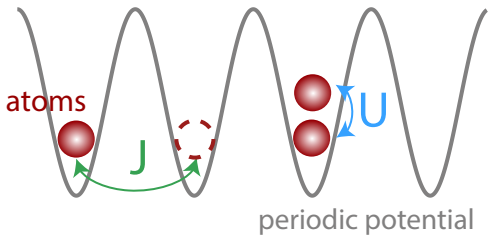

Figure 1: **Particules bosoniques piégées dans un potentiel périodique**

Ce système est décrit par l'Hamiltonien de Bose-Hubbard (BHH):

$$\hat{\mathcal{H}}_{\mathrm{BH}} = \underbrace{-J\sum_{i\neq j}\hat{b}_i^\dagger \hat{b}_j}_{\text{Terme d'énergie cinétique}} + \underbrace{\frac{1}{2}U\sum_i \hat{n}_i(\hat{n}_i-1)}_{\text{Terme d'interaction}} \tag{1}$$

Ou J caractérise l'énergie nécessaire afin qu'une particule passe d'un site à un autre par effect tunnel, U caractérise l'énergie d'interaction entre deux particules. Lorsque le ratio U/J est faible, les particules peuvent se délocaliser sur l'ensemble du réseau et le système est dans un état conducteur appelé phase superfluide (SF). Au contraire, lorsque U/J est grand, l'énergie du système est minimisée lorsque les particules localisent sur des sites différents (afin de minimiser l'énergie d'interaction répulsive) et on obtient un état isolant appelé isolant de Mott (MI). Ces deux phases sont séparárées par une transition de phase appelée transition du Mott et qui apparait pour une valeur critque du ratio U/J et notée $(U/J)_c$. Contrairement aux transitions de phase classiques où la compétition entre la température et un autre paramètre du système conduit à la possibilité de changement de phase, ici la transition de phase est dite quantique dans le sens où la température n'intervient pas. C'est la compétition entre l'énergie d'intéraction et l'énergie cinétique qui permet au systeme d'être dans une phase isolante ou superfluide.

Lorsque l'amplitude V du potentiel pérodique augmente, J diminue car il devient moins facile pour une particule de se déplacer sur un site adjacent par effet tunnel tandis que U augmente puisque les particules sont de plus en plus confinées au niveau des sites du réseau. Ainsi, lorsque V augmente, U/J augmente et il est donc possible, en contrôlant l'amplitude du potentiel V, d'obtenir soit une phase superfluide, soit une phase isolante.

Le but de cette thèse est donc d'étudier cette transition de phase. En 1998, Zoller et ses collègues [1] démontrèrent qu'un moyen simple de reproduire l'Hamiltonien de BH expérimentalement consiste à piéger des atomes froids dans la bande fondamentale d'un réseau optique. Grâce aux nombreux outils de mesure à disposition dans les expériences d'atomes froids, il est ainsi possible de mesurer des grandeurs telles que les positions atomiques dans l'espace réel ou en impulsion. Certaines expériences, grâce à des techniques d'imageries complexes, peuvent mesurer la position des atomes dans l'espace réel avec une résolution à l'atome unique. Cette possibilité de détection rend donc possible une mesure directe des fonctions de correlation à plusieurs particules. Dans l'expérience gaz sur réseau de l'Institut d'Optique, des atomes d'He* sont produits dans un état métastable très énergetique (20 eV au dessus du fondamental) et chargés dans la bande fondamentale d'un réseau optique 3D. Grâce à leur grande énergie interne, ces atomes peuvent être détectés après temps de vol de manière électronique, donnant accès à la distribution 3D en implusion du gaz sur réseau et résolue à l'atome unique [2]. Ces distributions peuvent ensuite être utilisées pour caractériser la transition de Mott grâce aux fonctions de corrélation en impulsion.

Chapitre 1 : La transition de Mott

Le premier chapitre consiste en une description théorique de la transition de Mott et des différentes phases. Loin de la transition, des théories perturbatives et/ou de champ moyen permettent de rendre compte des propriétés des différentes phases. Au contraire, près de la transition, ces methodes ne peuvent être appliquées et l'état du système reste mal compris, même s'il est possible d'obtenir des informations comme des fonctions de corrélation du premier ordre via des méthodes numeriques de type Quantum Monte Carlo (QMC). Une seconde partie traite donc de l'étude de cette transition avec des atomes froids piégés dans des réseaux optiques, de ses avantages et limitations, en particulier concernant les effects de taille et temperature finies ainsi que l'inhomogénéité des nuages d'atomes froids.

Chapitre 2 : Corrélations dans les systèmes quantiques macroscopiques

Après un rappel des notions de corrélation en optique classique et le lien avec la notion de cohérence, le formalisme des fonctions de corrélations en mécanique quantique est introduit. Une attention particulière est portée sur la compréhension des signaux de corrélation et la relation entre les corrélations de différents ordres via le théorème de Wick. Pour des systemes décrits par une statistique gaussienne (par example des états thermiques), le théoreme de Wick stipule que les fonctions de corrélation d'ordre N peuvent s'écrire uniquement comme des sommes de fonctions de corrélations du premier ordre.

Chapitre 3 : Mesure de la distribution en implusion résolue à l'atome unique

Dans ce chapitre, sont détaillés le dispositif et la séquence expérimentale qui permet de charger des atomes d'He* dans la bande fondamentale d'un réseau optique 3D et de détecter ces atomes individuellement après 300 ms de temps de vol. Notamment, le fonctionnement du détecteur electronique d'atomes est detaillé et ses principales caractéristiques sont données. Une seconde partie permet de démontrer que la distribution mesurée après temps de vol correspond

à la distribution en impulsion du gaz in-situ. Ceci est du notamment au fait que l'expension est longue (régime de Fraunoffer) et que les effets d'intéraction durant le temps de vol sont négligeables [2,3].

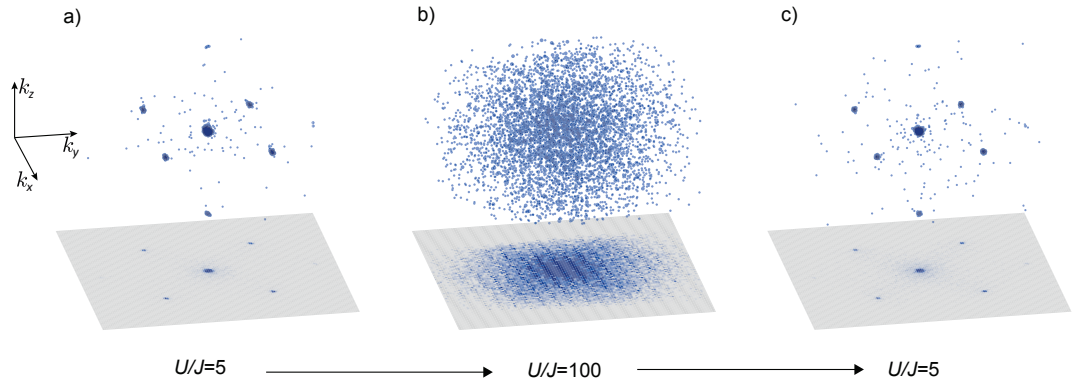

Figure 2: **Réalisation de la transition de Mott.** Distribution en impulsion d'un isolant de Mott ($U/J = 100$) et d'un superfluide ($U/J = 5$).

Chapitre 4 : Caractérisation du diagramme de phase

Les nuages crées dans les expériences d'atomes froids n'étant pas à $T = 0$, une méthode a été développée afin d'évaluer la temperature des nuages étudiés. Cette technique repose sur la comparaison entre des distributions en implusion des nuages produits et des distributions calculées, en tenant compte des paramètres expérimentaux, par l'algorithme QMC fournie par des theoriciens, et ceci pour un panel de températures, seul paramètre ajustable du problème. Une seconde partie est dédiée à l'étude d'observables qui sont succeptibles d'apporter des informations sur la localisation de la transtition de Mott et de la transition de phase classique qui apparait lorsque un nuage dans un état superfluide est chauffé. Notamment nous étudions l'évolution de la fraction condensée au cours de ces deux transtions.

Chapitre 5 : Corrélations à une particule dans un isolant de Mott

Dans un isolant de Mott parfait, c'est-à-dire lorsque $J/U = 0$, les atomes sont localisés au niveau des sites du réseau et le système est totalement incoherent. Lorsque J/U est faible mais fini, une cohérence à courte portée est restaurée par la présence "d'excitation" de type particule-trou. Cette cohérence est mise en évidence dans cette thèse par la modulation périodique présente dans la distribution en implusion d'un isolant de Mott qui dans la limite $J/U = 0$ est uniforme. L'évolution de la distribution en impulsion est mesurée [4] partant d'un isolant de Mott presque parfait et jusqu'au niveau de la transition, zone du diagramme de phase pour laquelle les théories existentes échouent à caractériser ces propriétés de cohérence à une particule.

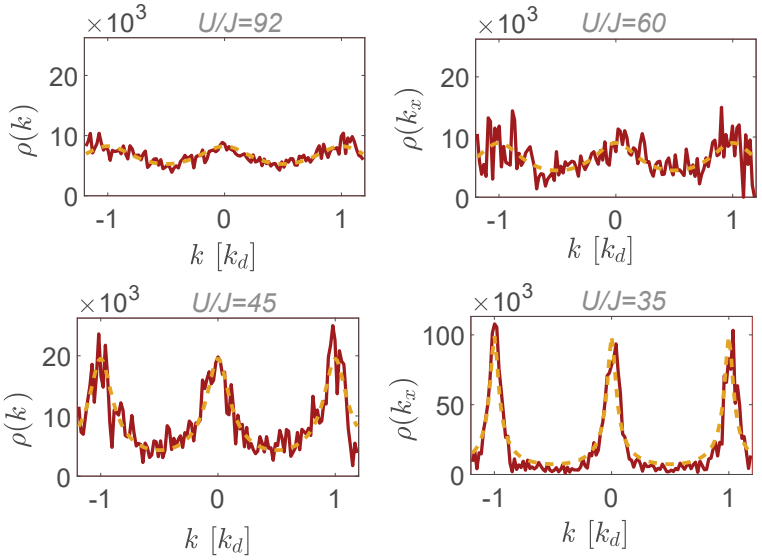

Figure 3: **Distribution en impulsion pour different gaz dans la phase isolante**.

Chapitre 6 : Corrélations dans un isolant de Mott

Les corrélations à plusieurs particules sont des observables qui permettent de rendre compte des mécanismes microscopiques à l'origine des propriétés macroscopiques observées dans les systèmes à N-corps. Un exemple de corrélations dont nous nous sommes interessés dans cette thèse sont les correlations de type HBT dans un isolant de Mott parfait. Un isolant de Mott parfait est un système incoherent régis par une statistique gaussienne, de manière similaire à un gaz thermique, ce qui a été confirmé experimentalement lors de ce travail [4]. Plus précisement, nous avons mesuré les correlations à deux et trois particules dans un isolant de Mott à $U/J = 100$ et vérifié de manière quantitative que les les signaux de corrélation étaient en accord avec un système régis par une statistique gaussienne.

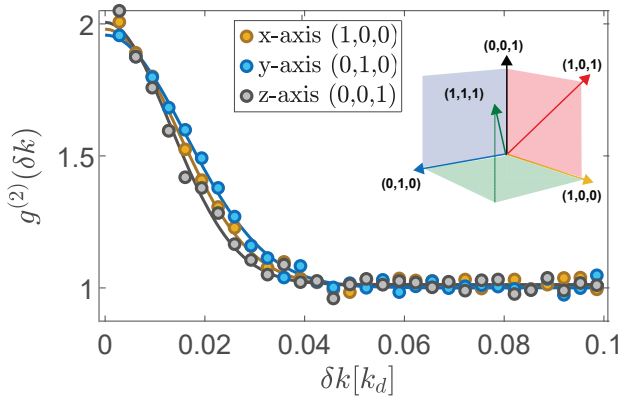

Figure 4: **Corrélation du second ordre $\mathbf{g^{(2)}(\delta k)}$ dans un isolant de Mott.**

[1] D. Jaksch, C. Bruder, J. I. Cirac, C. W. Gardiner, and P. Zoller, *Cold bosonic atoms in optical lattices*, Phys. Rev. Lett., vol. **81**, pp. 3108-3111, Oct 1998.

[2] H. Cayla, C. Carcy, Q. Bouton, R. Chang, G. Carleo, M. Mancini, and D. Clément,

Single atom- resolved probing of lattice gases in momentum space, Phys. Rev. A, vol. **97**, p.061609, Jun 2018.

[3] A. Tenart, C. Carcy, H. Cayla, T. Bourdel, M. Mancini and D. Clément, *Two-body collisions in the time-of-flight dynamics of lattice Bose superfluids*, arXiv:1909.13648 (2019).

[4] C. Carcy, H. Cayla, A. Tenart, A. Aspect, M. Mancini and D. Clément, *Momentum-space atom correlations in a Mott insulator*, Phys. Rev. X **9**, 041028 (2019).

université PARIS-SACLAY

ÉCOLE DOCTORALE
Ondes et Matière (EDOM)

Titre : Etude de la transition de Mott avec des atomes d'He*

Mots clés : Gaz sur réseau, Helium Métastable, Corrélations en impulsion, Transition de Mott, Interaction, Superfluidité

Résumé : Dans cette thèse, nous transférons un condensat de Bose-Einstein d'Hélium métastable dans un potentiel cubique 3D (réseau optique). Ce système constitue une réalisation expérimentale de l'Hamiltonien de Bose-Hubbard où interviennent deux échelles d'énergie: la force d'intéraction entre les atomes U et l'énergie cinétique J. Suivant le rapport U/J, l'état fondamental de ce système est soit un superfluide (SF), soit un isolant de Mott (MI). Ces deux phases sont séparées par une transition appelée transition de Mott dont nous avons étudié quelques propriétés au cours de cette thèse. Grâce à l'utilisation d'atomes d'Hélium dans un état métastable, il est possible de détecter ces atomes de manière individuelle et en 3D après un long temps de vol. Ainsi, on a accès à la distribution en impulsion du gaz piégé résolue à l'atome unique, ce qui permet de mesurer les fonctions de corrélation en impulsion à n'importe quel ordre. Nous avons démontré que les corrélations d'ordre 2 et 3 en impulsion sont celles d'un système décrit par une matrice densité gaussienne pour un isolant de Mott loin de la transition. Dans la phase MI, nous avons par ailleurs étudié l'augmentation de la cohérence à une particule en se rapprochant de la transition de Mott. Pour finir, nous avons comparé les distributions en impulsion mesurées experimentalement à des distributions numériques exactes calculées à partir de l'algorithme Monte Carlo et de nos paramètres expérimentaux pour un panel de températures. Ces comparaisons nous ont permis d'évaluer la temperature des nuages étudiés. Ces mesures de température ont servi lors de l'étude de la transition de phase entre un état SF et l'état thermique (NF) qui apparait lorsque le gaz est chauffé au delà d'une certaine température. En particulier, nous avons mesuré l'évolution de la fraction condensée le long des transitions de phases SF-MI et SF-NF. Nous avons montré que si l'évolution de la fraction condensée en fonction de la temperature permet de mesurer la position de la transition de phase SF-NF, l'inhomogénéité des nuages étudiés rend la mesure de la position de la transition de Mott plus compliquée. Dans ce cas, nous avons donc étudié d'autres observables.

Title : Investigation of the Mott transition with He* atoms

Keywords : Lattice gases, Metastable Helium, Momentum correlations, Mott transition, Interaction, Superfluidity

Abstract : In this work, we transfer a Bose-Einstein condensate of metastable Helium atoms to a 3D cubic lattice potential (optical lattice). This system is an experimental realization of the Bose-Hubbard Hamiltonian that depends on two parameters that are the interaction strength U between the atoms and the tunneling parameter J. Depending on the value of the ratio U/J, the ground state of the system is either a superfluid (SF) or a Mott insulator (MI). In the experiment, we investigated the Mott transition that separates the SF and the MI phases. Thanks to the use of He* atoms, one can detect the atoms individually and in 3D after a long time-of-flight. As a result, we access the in-trap momentum distribution of the lattice gases probed with a single atom sensitivity and one can compute the momentum correlations at any order. We demonstrate that the 2 and 3-particles correlations of a Mott insulator deep in the MI phase are the ones of a system described by a gaussian density operator. In the MI phase, we investigate the restoration of the first-order coherence on approaching the Mott transition. Finally, by comparing the momentum distributions measured in the experiment with Quantum Monte Carlo numerical simulations performed with the experimental parameters and calculated for a wide range of temperatures, we evaluated the temperature of the lattice gases probed, allowing us to investigate the transition between a SF and a thermal gas (NF) that occurs when increasing the temperature of the system. We notably have measured the condensate fraction across the SF-NF and the SF-MI transitions. We demonstrated that when probing trapped systems, if the condensate fraction is a good observable to locate the position of the SF-NF phase transition, it is not the case for the SF-MI transition. We thus probed different observables.

Université Paris-Saclay
Espace Technologique / Immeuble Discovery
Route de l'Orme aux Merisiers RD 128 / 91190 Saint-Aubin, France